

A Thesis Submitted for the Degree of PhD at the University of Warwick

Permanent WRAP URL:

<http://wrap.warwick.ac.uk/164659>

Copyright and reuse:

This thesis is made available online and is protected by original copyright.

Please scroll down to view the document itself.

Please refer to the repository record for this item for information to help you to cite it.

Our policy information is available from the repository home page.

For more information, please contact the WRAP Team at: wrap@warwick.ac.uk

Reconstitution of intracellular clathrin-coated vesicle formation

Cansu Kuey

Thesis submitted to the University of Warwick for the

degree of

Doctor of Philosophy



Warwick Medical School

University of Warwick

September 2021

Contents

List of Figures	iv
List of Tables	vi
List of Abbreviations	vii
Acknowledgements	x
Declaration	xi
Abstract	xii
1 Introduction	1
1.1 Clathrin-mediated vesicle formation	1
1.1.1 Clathrin-mediated endocytosis	1
1.1.2 Intracellular clathrin-mediated trafficking	11
1.2 Hot-wiring CME at the plasma membrane	16
1.3 Mitochondria	19
1.3.1 Lipid composition of mitochondrial membranes	20
1.3.2 Mitochondrial dynamics	21
1.3.3 Mitochondria-derived vesicles	22
1.4 Aims of this thesis	23
2 Materials and Methods	24
2.1 Molecular Biology	24
2.1.1 Constructs generated for this study	24
2.2 Cell Biology	29
2.2.1 Clathrin-coated vesicle formation by rapamycin induction .	30

2.2.2	Transferrin uptake	31
2.2.3	Actin depolymerisation	31
2.3	Immunofluorescence	32
2.4	Microscopy	33
2.4.1	Light Microscopy	33
2.4.2	Correlative Light Electron Microscopy (CLEM)	33
2.5	Data Analysis	34
3	Clathrin-coated vesicles can be formed synthetically at intracel- lular membranes	37
3.1	Introduction	37
3.2	Intracellular CCV formation can be induced at four different or- ganelles	38
3.3	Temporal and spatial characterisation of mitoPits	44
3.4	Endocytic hooks are more effective in forming mitoPits than in- tracellular hooks	49
3.5	Formation of mitoPits is clathrin dependent	50
3.6	mitoPits do not interact with σ subunits of AP-1, AP-2 and AP-3	52
3.7	Epsin2 and FCHo2 are recruited to mitoPits	54
3.8	Initiation, maturation and scission stages of CME are reconstituted at mitochondria	56
3.9	Discussion	59
4	MitoPits do not require a scission molecule for budding	61
4.1	Introduction	61
4.2	Dynamin is not involved in budding of mitoPits	61
4.3	Drp1 is not responsible for pinching off of the mitoPits	70
4.4	Vps4a do not have a role in MPDV formation	73
4.5	Actin is not involved in budding of mitoPits	75
4.6	Discussion	77
5	Discussion	80
	References	84

Appendix A	101
Appendix B	102
Appendix C	103

List of Figures

1.1	Stages of clathrin-mediated endocytosis.	2
1.2	The interaction network of proteins involved in clathrin-mediated endocytosis.	3
1.3	Clathrin-coated vesicle trafficking in the cell.	13
1.4	Subdomain organisation of adaptor protein complexes 1, 2 and 3 in their open conformations.	14
1.5	Synthetic CME was achieved by rerouting β 2 hook to plasma membrane upon rapamycin induction.	17
3.1	Rerouting of the clathrin hook to the mitochondria induces spot formation.	40
3.2	Rerouting of the hook to the ER induces spot formation.	41
3.3	Rerouting of the hook to the Golgi induces spot formation.	42
3.4	Rerouting of the hook to the lysosome induces spot formation.	43
3.5	Formation of mitoPits in real time.	44
3.6	Curved surfaces facilitate mitoPit formation.	45
3.7	mitoPits are surrounded by the WT β 2 hook.	47
3.8	mitoPit formation is not caused by transmembrane domain clustering.	48
3.9	Rerouting of FKBP- β 1-GFP, FKBP- β 2-GFP, FKBP-AP180c-GFP, and FKBP-epsin-GFP hooks to mitochondria forms mitoPits.	50
3.10	Clathrin colocalises with mitoPits.	51
3.11	Clathrin is necessary to form mitoPits.	52
3.12	AP-1, AP-2 and AP-3 σ subunits do not colocalise with mitoPits.	53

3.13	CME accessory proteins, amphiphysin 1, endophilin, Hip1R and SNX9 do not colocalise with mitoPits.	55
3.14	Epsin2 and FCHo2 are recruited to mitoPits.	56
3.15	Stages of CME reconstituted on mitochondria via inducible CCV formation.	58
3.16	mitoPits pinch off from the mitochondria.	58
4.1	Disruption of dynamin function by expressing a dominant-negative mutant does not change the ratio of free spots.	63
4.2	30 μ M Dynole is sufficient to inhibit dynamin activity in endocytosis.	65
4.3	Inhibition of dynamin with Dynole does not affect the ratio of free spots at mitochondria.	67
4.4	Inhibition of dynamin with Dynole affects the size and number of hot-wired CCVs.	68
4.5	Depletion of all three dynamin isoforms does not change the ratio of free spots.	70
4.6	Disruption of Drp1 function by expressing a dominant-negative mutant does not change the ratio of free spots.	72
4.7	Disruption of Vps4a function by expressing a dominant-negative mutant does not decrease the ratio of free spots.	74
4.8	1 μ M Latrunculin B is sufficient for actin depolymerisation.	76
4.9	Actin depolymerization does not change the ratio of free spots.	77

List of Tables

2.1	List of plasmids used in this study.	29
2.2	Antibodies and stains used in immunofluorescence.	32

List of Abbreviations

ANTH	AP180 N-Terminal homology
AP-1	Adaptor protein complex 1
AP-2	Adaptor protein complex 2
AP-3	Adaptor protein complex 3
AP-4	Adaptor protein complex 4
AP-5	Adaptor protein complex 5
AP180	Adaptor protein 180
Arf1	ADP ribosylation factor 1
ARFGEF2	Arf1 guanine nucleotide exchange-factor
ARG	Autosomal recessive hypercholesterolemia
ATP	Adenosine triphosphate
BAR	Bin/Amphiphysin/Rvs-homology
CALM	Clathrin-assembly lymphoid myeloid leukaemia protein
CBM	Clathrin binding motif
CCP	Clathrin-coated pit
CCV	Clathrin-coated vesicle
CD8	Cluster of differentiation 8
CHC	Clathrin heavy chain
CLC	Clathrin light chain
CLEM	Correlative light electron microscopy
CME	Clathrin-mediated endocytosis
COP	Coat protein
DNM TKO	Dynamin triple knock-out cells
Drp1	Dynamin-1-like protein

Dyn1	Dynamin 1
EM	Electron microscopy
ENTH	Epsin N-Terminal homology
Eps15	Epidermal growth factor receptor substrate 15
ER	Endoplasmic Reticulum
FCHo 1/2	Fer/Cip4 homology domain-only 1/2
FKBP	FK506 binding protein
FRB	FKBP and rapamycin-binding
GAK	G-associated kinase
GED	GTPase effector domain
GFP	Green Fluorescent Protein
GTP	Guanosine triphosphate
Hip1R	Hip1-related protein
Hsc70	70 kDa heat shock cognate protein
IMM	Inner mitochondrial membrane
LatB	Latrunculin B
LDL	Low density lipoprotein
LDLR	Low density lipoprotein receptor
MAPL	Mitochondria-anchored protein ligase
MDV	Mitochondria-derived vesicles
Mfn1	Mitofusin 1
mitoPit	Mitochondria-derived clathrin-coated pits
MPDV	MitoPit-derived vesicles
mTOR	Mammalian target of rapamycin
mTORC1	mTOR1 complex 1
OMM	Outer mitochondrial membrane
Opa1	Optic atrophy protein 1
PDH E2/E3	Pyruvate dehydrogenase E2/E3
PH	Pleckstrin homology
PI(4)P	Phosphatidylinositol-4-phosphate
PI(4,5)P₂	Phosphatidylinositol 4,5-bisphosphate

pol-TIRF	Polarized total internal reflection fluorescence microscopy
PRD	Proline-arginine domain
Rab	Ras-related protein
SH3	Src homology 3
SNARE	SNAP Receptor
TEM	Transmission electron microscopy
Tfn 647	Human transferrin conjugated to Alexa-647
TGN	Trans-Golgi network
TIM	Translocase of the inner membrane
TM	Transmembrane
TOM	Translocase of the outer membrane
WT	Wild type

Acknowledgements

Firstly, I would like to thank my supervisor Steve Royle for his superb mentorship throughout the PhD. He has been an excellent advisor and has given me the encouragement and support whenever I needed it. Thank you for helping me develop into a rigorous scientist.

I would like to thank my second supervisor Corinne Smith for her valuable feedback. I also thank SynBioCDT programme coordinator Chris Corre, and admin Nicola Glover for their support throughout the PhD. Saskia Bakker and Ian Hands-Portman of the Advanced Imaging RTP deserve a thank you for training me in EM.

I would like to thank all the past and current members of the Royle Lab and CMCB whom I worked with, who made the lab an enjoyable place to work.

A huge thank you to my parents who have always been there for me and given me the best support and opportunities they could give in life.

Finally, I thank my partner Patrick Capel, for sharing the hardest four years of our lives together. I could not have done this without you.

This work was generously funded by EPSRC and BBSRC.

Declaration

This thesis is submitted to the University of Warwick in support of my application for the degree of Doctor of Philosophy. It has been written by myself and has not been submitted in any previous application for any degree. The work presented has been carried out by me except for the generation of the FKBP-AP180c-GFP construct, which was done by Miguel Gonzalez Hernandez, and the CHC knockdown experiment and its data analysis which was carried out by Gabrielle Larocque.

I have given oral presentations of parts of this work at the UK Membrane Trafficking Meeting 2020 and the Gordon Research Conference on Molecular Membrane Biology 2021.

The poster including parts of this work, which I presented at the annual meeting of the American Society for Cell Biology & EMBO 2020, can be found in Appendix A.

Appendix B contains an article I contributed to as first author. I carried out all the experiments and data analysis with the SK-MEL2 cell line, except the ones done using HeLa cells in figures 1, 2 and 6.

Appendix C contains another article to which I have contributed. I generated four extra TPD mutants that has been needed after revisions, carried out the spatiotemporal variance analysis experiments with all mutants in figure 1, and mitochondrial aggregation experiments in figures 3C, D and 5C, D.

Work in Appendices B and C are not presented in this thesis.

Abstract

Clathrin-coated vesicle (CCV) formation is a major membrane remodelling process important for membrane traffic in eukaryotic cells. CCVs are formed at the plasma membrane during endocytosis, and at early/recycling endosomes and the trans-Golgi network during intracellular traffic. The plasma membrane is easier to access experimentally *in vivo* from the cell exterior, while intracellular compartments lack this advantage. To overcome this barrier and to study intracellular CCV dynamics and functional requirements, we have reconstituted intracellular CCV formation on-demand, using minimal machinery. The clathrin-binding region of the $\beta 2$ subunit of AP-2 was used as a ‘hook’ which can be attached inducibly to an ‘anchor’ protein on a membrane surface. Rerouting the hook to an anchor by chemical dimerisation was sufficient to form CCVs at mitochondria, ER, Golgi and lysosomes. As mitochondria are not part of canonical membrane trafficking, I investigated synthetic clathrin-coated pit formation on mitochondria in detail. CCPs on the mitochondria (termed mitoPits), form within minutes after induction. Electron microscopy and live cell imaging revealed that initiation, maturation and scission steps of CCV formation were faithfully reconstituted. MitoPits are double membraned invaginations that tend to form on surfaces with higher curvature. These observations suggests that enough force is generated by our synthetic system to deform both the inner and outer mitochondrial membranes and for budding of the mitoPits. Vesicle budding was shown not to depend on any scission molecule tested (dynamin, Drp1, Vps4a, actin), suggesting that intracellular CCVs do not need a scission factor. To conclude, unlike endocytosis, clathrin-coating may be sufficient for intracellular CCV budding. Given the differences in phospholipid profiles of mitochondrial membranes and plasma membrane, the phospholipid composition of the membrane may have a negligible role in CCV formation.

Chapter 1

Introduction

1.1 Clathrin-mediated vesicle formation

1.1.1 Clathrin-mediated endocytosis

Clathrin-mediated endocytosis (CME) is the major membrane trafficking process in eukaryotic cells to internalise a wide range of cargo, including hormones, proteins and metabolites, from the plasma membrane via clathrin-coated vesicles (CCVs). Coated pits were first identified in mosquito oocytes (Roth et al. 1964) using electron microscopy (EM). Coated vesicles were later found in nerve endings isolated from guinea pig brains revealing the polyhedral cage structure (Kanaseki et al. 1969). Then, Barbara Pearse identified the main protein component of these coated vesicles, and named it clathrin (Pearse 1976). Her works described the biochemical properties of clathrin, more specifically clathrin-heavy chain (CHC) and further confirmed the polyhedral structure of the coat (Pearse 1975; Pearse 1976). Later, coated areas on the plasma membrane of human cells were described in the work of Anderson et al. (1977). In this early study, low density lipoprotein (LDL) bound to its receptor was found in the coated areas of the plasma membrane, then internalised via the coated endocytic vesicles that bud off from these areas. Once inside the cell, vesicles were then uncoated, and eventually fused with lysosomes.

Clathrin is found as a triskelion, consisting of three heavy chains each interacting with one light chain (CLC). CHCs are organised such that their tripod

domain which is toward the C-terminus are in the centre of the triskelion, and their terminal domain toward the N-terminus are on the edges. The triskelia can self-polymerise into hexagonal lattices that cage membrane vesicles. These lattices need to have twelve pentagons to be able to form a closed cage. The smallest size of a clathrin cage could be composed of 36 or 60 triskelia forming the hexagonal barrel or soccer ball, respectively (Fotin et al. 2004). Although, the size of the cage ultimately depends on the size of the cargo (Stachowiak et al. 2013).

Clathrin itself is unable to bind to membrane or cargo hence it needs adaptor proteins for these interactions. CME starts with the initiation stage where adaptor protein complex 2 (AP-2) recognises and binds cargo, then recruits clathrin (Figure 1.1). Then in the maturation stage, membrane invaginates to form clathrin-coated pits (CCPs). Membrane bending is thought to be achieved by the help of accessory proteins and clathrin. Scission of the CCVs from the plasma membrane is accomplished by the large GTPase dynamin, that constricts at the necks of the CCPs and pinches them off. Now detached from the membrane CCVs, approximately 100 nm in size, are internalised and uncoated from their clathrin coat at the last stage of CME. Once uncoated, the vesicles fuse to form early endosomes. Then, their contents could be sent to lysosome for degradation or recycled back to plasma membrane (Robinson 2015; Kaksonen and Roux 2018). Stages of CME will be discussed in detail below.

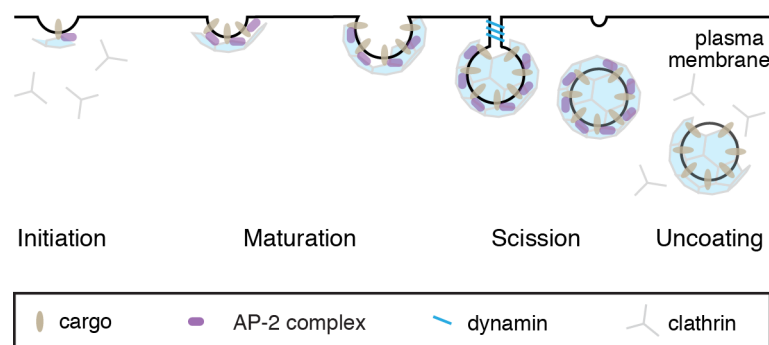


Figure 1.1: Stages of clathrin-mediated endocytosis. Diagram showing the four stages of CME. Cargo and clathrin bind to AP-2 at initiation and membrane starts to bend. Clathrin-coated pits form during maturation with invagination of the membrane. Finally in scission, clathrin-coated vesicles are pinched off from the membrane by dynamin. Internalised vesicles then start to lose their clathrin-coat. Diagram adapted from Smith et al. (2021) under Creative Commons Attribution License.

Accessory proteins are thought to be important for functional CME to take place *in vivo*. Until now, there have been more than 50 proteins associated with CME (Figure 1.2). Different proteins are involved in different stages of CME, some binding to membrane phospholipids, others binding to AP-2 and/or clathrin. Roles of specific accessory proteins will be covered in detail while describing each of the stage of CME below.

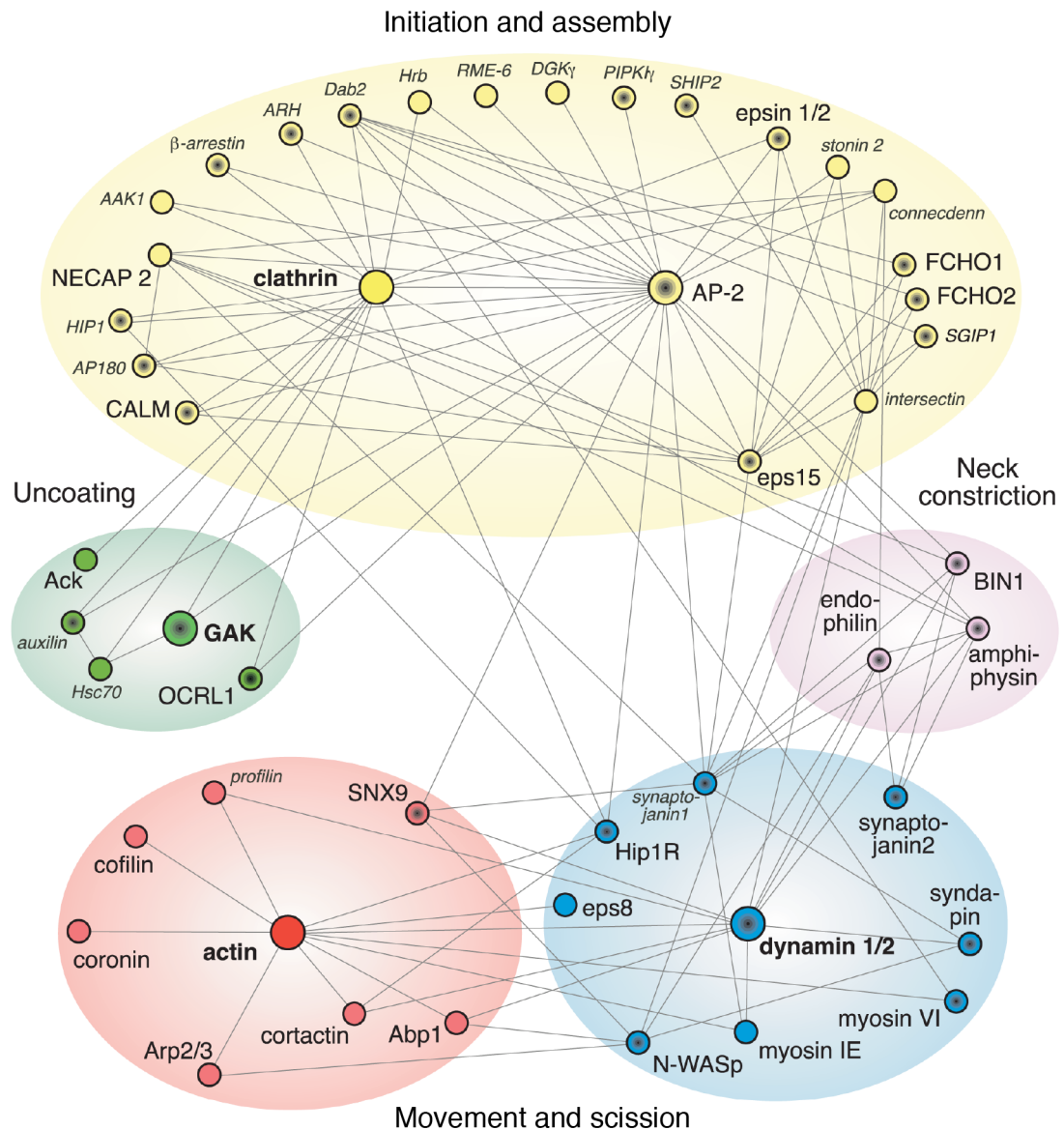


Figure 1.2: The interaction network of proteins involved in clathrin-mediated endocytosis. Schematic description of main hubs of CME. Proteins are represented in modules depicted in Taylor, Perrais, et al. (2011). Dots with black centres are binding partners of membrane lipid phosphatidylinositol 4,5-bisphosphate (PI(4,5)P₂). Figure is from Traub (2011), reproduced under Creative Commons Attribution License.

The prototypical example of CME is iron uptake. Transferrins are iron-binding glycoproteins that are recognised by the transferrin receptor on the plasma membrane and are constitutively internalised via CME. Recognition of YTRF sorting sequence at the cytoplasmic tail of the transferrin receptors by AP-2 initiates the process (Collawn et al. 1990; Ohno et al. 1995). Once the cargo is delivered, the receptors are recycled back to plasma membrane. Transferrin uptake has been used extensively as a tool to investigate receptor-mediated internalisation dynamics starting from the early days of the field (Wiley et al. 1982). Before fluorescent probes and imaging, it was not possible to quantify transferrin uptake by just visualising it; therefore, cell-free systems were used for biochemical analysis such as using perforated human cells incubated with radiolabeled transferrin (Smythe, Pypaert, et al. 1989). In this method, after initial binding of transferrin to its receptors at 4°C, cells would be scraped and then warmed up to at 37°C for the uptake to take place. Internalised transferrin would be collected in the supernatant by removal of the surface transferrin by centrifugation upon binding to the anti-transferrin antibody. This antibody inaccessibility assay was then used together with a similar assay that measures internalisation by resistance to a membrane impermeant-reducing agent, MesNa. This way it was possible to biochemically analyse the uptake in a stage-specific manner, as deeply invaginated coated pits would only be inaccessible to antibodies, but accessible to MesNa, and vesicles at scission and uncoating stages would be resistant to MesNa as well as being inaccessible to avidin (S. L. Schmid et al. 1991). Later, this stage-specific transferrin uptake assay was used to show that AP-2 prompts CCP formation and is required in the early stages of endocytosis together with a cytosolic clathrin pool (Smythe, Carter, et al. 1992).

Initiation

The first stage of CME includes cargo recognition, binding and recruitment of clathrin by AP-2 (Figure 1.1). The heterotetramer AP-2 consists of two large subunits, α and β 2 and two smaller subunits σ 2 and μ 2. AP-2 relies on the membrane phospholipid, PI(4,5)P₂, for its localisation to the plasma membrane. Its α , β 2 and μ 2 subunits carry binding sites for PI(4,5)P₂ (Collins et al. 2002;

Jackson et al. 2010). Recruitment to the plasma membrane promotes structural rearrangement on the complex resulting in an open conformation (Jackson et al. 2010, Figure 1.4). Cargo and clathrin binding sites of AP-2 are revealed after this early initiation event. It is also shown that the μ 2 subunit can bind to accessory proteins, Fer/Cip4 homology domain-only (FCHO) 1 and 2 and epidermal growth factor receptor substrate 15 (Eps15), and this binding might play a role in AP-2 activation (Hollopeter et al. 2014). In the open confirmation, the μ 2 subunit recognises the tyrosine YXX Φ (Φ is a bulky hydrophobic residue) motif of the cargo and binds to it (Ohno et al. 1995; Letourneur et al. 1992). Moreover, α/σ 2 heterodimer of the AP-2 can bind cargo via recognising the dileucine motif (Letourneur et al. 1992; Doray, I. Lee, et al. 2007). The β 2 subunit which is the clathrin recruiter also needs the open confirmation to be able to bind to clathrin via its clathrin binding motif (CBM), LLNLD on its hinge domain (Shih et al. 1995; Dell’Angelica et al. 1998; Kelly et al. 2014). Tyrosine residues at 815 (Y815) and at 888 (Y888) in the appendage of β 2 are the other clathrin binding sites that have been shown to be important functionally although to a lesser extent (Edeling et al. 2006; Wood et al. 2017; Smith et al. 2021). These sites are also important for binding of accessory proteins. Y815 site binds the alternative adaptor AP180, accessory proteins amphiphysin and Eps15 while Y888 site binds the alternative adaptor epsin, β -arrestin and autosomal recessive hypercholesterolemia (ARH) (Owen et al. 2000; E. M. Schmid et al. 2006). Moreover, the hinge and appendage of the β 2 subunit of AP-2 was shown to be sufficient to initiate CME on-demand on the plasma membrane, which will be discussed in detail in the following sections (Wood et al. 2017).

The accessory proteins epsin, AP180 and its non-neuronal homolog, clathrin-assembly lymphoid myeloid leukaemia protein (CALM) are also involved in CCP initiation. Epsin and AP180 interact with the appendage domain of β 2 localising them in close vicinity of AP-2 (Owen et al. 2000). They are also referred to as alternative clathrin adaptors emphasizing their clathrin binding ability (Figure 1.3). Epsin has two clathrin binding sites while AP180 has been shown to possess 12 copies of the clathrin binding motif DLL (Drake et al. 2000; Morgan et al. 2000). Moreover, epsin and AP180 can recognize cargo. They specifically

recognize SNAP receptor (SNARE) proteins via their N-terminal homology domains –ENTH and ANTH respectively–, and are involved in their internalisation (Miller, Collins, et al. 2007; Miller, Sahlender, et al. 2011). SNARE proteins are necessary for fusion of vesicles to their target membranes (Söllner et al. 1993); therefore they are essential parts of CCVs. Having exclusive adaptors for SNAREs ensures that they are always incorporated into CCVs regardless of other cargo. This in turn provides proper fusion of CCVs to their target membranes.

Maturation

The next step in CME is maturation. This is the stage where the plasma membrane invaginates and forms CCPs. Two different models have been proposed for membrane bending and pit formation, and this is a currently debated issue. The first model is called the constant area model which suggests clathrin-coated surfaces form flat on the plasma membrane first, then it is followed by membrane bending. This model was introduced by an early EM study that has shown flat regions of plasma membrane coated with hexagonal lattices and curved cages invaginating from these regions (Heuser 1980). In order to form a cage, pentagons would need to be inserted into the hexagonal array. However, this structural rearrangement is hypothesised to be an energetically unfavourable event (Kirchhausen 1993). This model gained support from a more recent correlative light electron microscopy (CLEM) study, showing that the area of the clathrin lattice is constant while the membrane curvature increases during invagination (Avinoam et al. 2015). The second model for membrane bending is the constant-curvature model which suggests that the clathrin coat is formed as a curved lattice from the beginning. As the CCP invaginates the area covered by the clathrin-coat increases. Two *in vitro* studies support this model. The first study showed that clathrin polymerises much faster on curved surfaces compared to planar ones (Dannhauser, Platen, et al. 2015). The second study found that clathrin prefers to be recruited to curved membranes (Zhao et al. 2017). This model is also supported by *in vivo* studies. One *in vivo* study showed that CCPs form and pinch off as CCVs while the flat clathrin lattices fail to form CCVs (Saffarian et al. 2009). Others visualised curvature generation by the CCPs in real time

and concluded that they do not undergo structural rearrangements suggested by the constant area model (Willy et al. 2021). Furthermore, a more inclusive approach has been proposed in recent years. In their study of membrane bending and clathrin-coat assembly using polarized total internal reflection fluorescence microscopy (pol-TIRF), Scott et al. (2018) suggested that both models can be plausible at different areas of the plasma membrane. The mode of curvature generation to be followed in CCP formation might be defined by the cooperation and competing forces, and various factors can affect the interplay between them, including membrane tension and lipid or protein content at the site (Scott et al. 2018). Another recent study demonstrated that the type of cargo could affect which mode of curvature is favoured in the cell. Maib et al. (2018) found out that phosphorylation of CLC is required for selective uptake of G-protein coupled receptors because it facilitates the transition of flat clathrin lattices to CCPs during maturation. On the other hand, constitutive uptake of transferrin did not depend on CLC phosphorylation, suggesting it might follow the constant curvature model (Maib et al. 2018).

Membrane bending is crucial for successful CME. It has been shown that clathrin can induce membrane curvature *in vitro* on liposomes in the presence of accessory proteins (Dannhauser and E. J. Ungewickell 2012), and clathrin or other proteins can act as scaffolds to bend the membrane (McMahon et al. 2005). Many accessory proteins promote the curvature themselves or recognise curved membranes. Epsin is one of the contributors to membrane curvature via binding of its ENTH domain to PI(4,5)P₂. Clathrin binding also helps epsin to further bend the membrane (Holkar et al. 2015). Another major role of epsin in CCP maturation is to help the recruitment of actin together with Hip1-related protein (Hip1R). Messa et al. (2014) showed that Hip1R, which binds to actin and clathrin, is not recruited to CCPs in epsin triple knock-out fibroblasts and epsin can bind actin directly. Other accessory proteins, amphiphysin, endophilin and SNX9 all contain Bin/Amphiphysin/Rvs-homology (BAR) domains recognising membrane curvature which helps them to be recruited to mature CCPs. Amphiphysin and SNX9 also bind to clathrin whereas endophilin does not. They all contain a Src homology 3 (SH3) domains which interact with the scission protein

dynamamin. However, only amphiphysin and endophilin were shown to be involved in the recruitment of dynamamin, as down regulation of SNX9 did not effect dynamamin levels at CME sites (Meinecke et al. 2013). This is consistent with results of a temporal CME dynamics study where it was shown that SNX9 recruitment peaks after scission (Taylor, Perrais, et al. 2011). Overall, membrane bending is an essential process in maturation of CCPs that involves various proteins.

Scission

Scission is the budding off of CCVs from the membrane, and the large GTPase dynamamin is the scission molecule for endocytosis. Once the plasma membrane invaginates and CCPs are matured, dynamamin is recruited to the neck of the pits, and promotes the budding of the vesicles (Figure 1.1). Dynamamin consists of an N-terminal GTPase domain, an α -helical middle domain, a pleckstrin homology (PH) domain for membrane insertion, a GTPase effector domain (GED) and a C-terminus proline-arginine domain (PRD) for interaction with SH3 domain containing proteins. In its active form, dynamamin self-assembles into dimers, in which the α -helical middle domain and GED interact with each other forming the “stalk” in between the membrane binding PH and GTPase head (Zhang et al. 2001). These dimers then assemble into polymers and into helical rings around the CCP neck, this structural reorganisation of dynamamin requires the force generated by GTP hydrolysis.

The mechanism of how dynamamin promotes scission of CCPs after conforming into a helix is still controversial. Three models have been proposed to explain this phenomenon. First one is the pinchase model, in which dynamamin is considered as a mechanoenzyme that catalyses fission by the force generated via GTP hydrolysis and constricts at the neck of the CCPs and pinches them off (McNiven 1998; Sweitzer et al. 1998). The second model supports dynamamin being a poppase rather than a pinchase. In this model, dynamamin uses the force from the GTP hydrolysis to stretch the membrane and pop the CCVs out (Stowell et al. 1999). The third model suggests that dynamamin acts as a switch. In this model GTP hydrolysis is not a force generator but rather a turning off mechanism for a switch. Dynamamin is thought to be active when its bound to GTP, and it promotes other scission

molecules recruitment to the necks of CCPs (Sever et al. 1999). Currently it is widely accepted that the constriction of dynamin oligomers happens in the presence of GTP, and that GTP hydrolysis is required for dynamin to catalyse membrane fission (Antonny et al. 2016).

The role of dynamin in endocytosis was first suggested in studies investigating *Drosophila* carrying a temperature sensitive mutant of *shibire*, the fly homologue for dynamin. At the non-permissive temperature, endocytic pits with electron dense structures at their necks accumulating at the nerve terminals was observed by EM (Kosaka et al. 1983). In mammalian cells, overexpression of a dominant-negative mutant of dynamin, dynamin K44A, lacking the ability to bind GTP, has been shown to inhibit endocytosis of transferrin and cause formation of CCPs with elongated necks demonstrating that a functional dynamin capable of GTP hydrolysis is essential for CCV fission (Bliek et al. 1993; Damke et al. 2001). Moreover, dynamin inhibitors such as Dynasore and Dynole 34-2 were shown to inhibit endocytosis demonstrated by transferrin uptake assays (Macia et al. 2006; Hill et al. 2009). Dynamin has three isoforms in human cells. Dynamin 2 is expressed ubiquitously while dynamin 1 and 3 are mostly expressed in the brain (Ferguson and De Camilli 2012). Dynamin triple knock-out (DNM TKO) cells also show the same phenotype of long necked CCPs as with dynamin K44A overexpression. Transferrin uptake was also inhibited in DNM TKO cells demonstrating the indispensable role of dynamin as the pinchose of CCVs (Park et al. 2013).

Just as dynamin could have regulatory roles in the early stages of CME (Mettlen et al. 2018), other proteins could be involved in scission. Actin, the driver of invagination and scission in yeast, has been shown to be recruited to CME sites in mammalian cells during invagination, neck constriction and scission (Kaksonen, Toret, et al. 2006). Actin depolymerisation reduced the scission of CCVs due to the decrease in dynamin recruitment in mammalian CME (Taylor, Lampe, et al. 2012). Moreover, actin is required together with CLC in constriction of the neck during CME when the plasma membrane is under high tension. Actin depolymerisation by Latrunculin treatment resulted in pits with wide necks and failure of dynamin recruitment on the apical membrane of polarised MDCK cells which

has higher tension whilst basolateral membrane was not affected (Boulant et al. 2011). Hip1R is a regulator of actin in CCPs. First, it is recruited to CCPs via binding to the CLC. Then it recruits actin to the CCPs by binding to it via its C-terminal THATCH domain. CLC and actin binding to Hip1R occur sequentially as CLC binding negatively regulates actin binding to Hip1R (Wilbur et al. 2008). Hip1R anchoring points at CCV sites have shown to be important for intracellular CCV budding from the trans-Golgi network (TGN) (Carreno et al. 2004). Recently it has been suggested that actin filaments attached to these anchor points might be creating a pulling and squeezing force that could facilitate CCV budding from membranes (Serwas et al. 2021).

Uncoating

The CCVs need to be uncoated in order to fuse with endosomes, so the cargo can continue their journey inside the cell. Uncoating relies on recruitment of auxilin/G-associated kinase (GAK) and ATP-dependent catalytic activity of 70 kDa heat shock cognate protein (Hsc70). Auxilin or GAK is recruited to CCVs for uncoating in neuronal and non-neuronal cells, respectively. Auxilin consists of an N-terminal domain, clathrin binding domain and a C-terminal J domain. All of these domains are also present as subdomains in the C-terminal of GAK (Greener et al. 2000). Auxilin arrives to CCVs after scission following the peak of dynamin and interacts with membrane lipids via its N-terminal PTEN-like domain (Guan et al. 2010). It binds to the clathrin cage first, then recruits Hsc70/ATP complex by binding to Hsc70 via its J domain (E. Ungewickell et al. 1995). Auxilin J domain promotes ATP hydrolysis in the Hsc70/ATP complex and activates it. There are several models explaining how Hsc70 disassembles the clathrin coat. The sequential model suggests that one auxilin and three Hsc70 proteins are required to disassociate one clathrin triskelion. According to this model, the first Hsc70/ATP complex is structurally rearranged after ATP hydrolysis. This allows the second Hsc70/ATP complex to bind to auxilin and undergo the same process. After the third ATP hydrolysis, the clathrin triskelion is thought to be released from the coat as Hsc70/ADP complexes could have a lower affinity for auxilin and higher affinity for free triskelion (Rothnie et al. 2011). A more recent study

supporting the collision pressure model suggests that the main mechanism of uncoating is collisions between the Hsc70s and the coat, and one Hsc70 molecule recruitment to the coat could generate sufficient force for dissociation. Multiple Hsc70 molecules could be recruited only if the force generated by one Hsc70 fails to initiate the collision (Sousa et al. 2016).

Uncoated vesicles fuse, then form early endosomes. Depending on the type of the cargo, the content of the vesicles have four fates: directly recycled to the plasma membrane (fast recycling), sent to recycling endosomes to be taken back to the cell surface (slow recycling), sent to late endosomes for transfer to TGN or sent to lysosomes for degradation. For example, transferrin receptors are recycled back to the plasma membrane via both fast and slow recycling pathways, the former being regulated by Rab4a latter by Rab4b and Rab11a (Sluijs et al. 1992; Perrin et al. 2013; Welz et al. 2014). Whereas, LDL and its receptor LDLR is directed to late endosomes where they dissociate due to lowered pH. They are sent to lysosomes for degradation and release of cholesterol, and finally LDLR is recycled back to the plasma membrane (Davis et al. 1987). Some of these intracellular trafficking events also require clathrin and other adaptor protein complexes for CCV formation, which will be discussed in detail in the next section.

1.1.2 Intracellular clathrin-mediated trafficking

Intracellular vesicle trafficking is the process of communication between membrane bound organelles within the eukaryotic cell. This communication is achieved by transport of coated vesicles encapsulating the cargo, such as proteins and lipids, from one organelle to the other. Vesicles with different coats are present in different trafficking pathways (Figure 1.3). CCVs are involved in transport of cargo between endosomes and TGN, and endosomes to lysosomes while vesicles transported from Golgi to ER carry the COPI coat, and vesicles transported from ER to Golgi have the COPII coat (Robinson 2015). COPI and COPII coats thought to contain proteins that are structurally similar to clathrin (Devos et al. 2004). Intracellular and endocytic coated vesicles are comparable to each other. Endocytic CCVs have a diameter around 100 nm, and intracellular CCVs were found to be similar in size (Kural et al. 2012). Moreover, COPI and COPII coated

vesicles have a diameter between 60-100 nm (Adolf, Rhiel, et al. 2019). Plasma membrane is easier to access experimentally *in vivo* while intracellular compartments lacks this advantage. This makes it hard to track the stages intracellular coated vesicles go through in real time and investigate the importance of their interaction partners in the process. Hence, formation of CCVs on-demand inside the cell could be a important tool to elucidate intracellular vesicle trafficking.

Intracellular clathrin adaptors

Just like endocytic CCVs, intracellular CCVs also depend on adaptor proteins for cargo binding and clathrin recruitment. The bidirectional transport of CCVs between early endosomes and TGN is the most studied intracellular CCV pathway (Hirst, Borner, et al. 2012), and it involves the heterotetramer adaptor protein complex 1 (AP-1) as the main clathrin adaptor. While transport of intracellular CCVs from endosomes to lysosomes is mediated by the adaptor protein complex 3 (AP-3). (Figure 1.3). Recently, adaptor protein complexes 4 and 5 (AP-4, AP-5) are also identified. AP-4 is involved in transportation of cargo from TGN to endosomes, and AP-5 is localised to late endosomes (Hirst, Irving, et al. 2013; Hirst, Itzhak, et al. 2018).

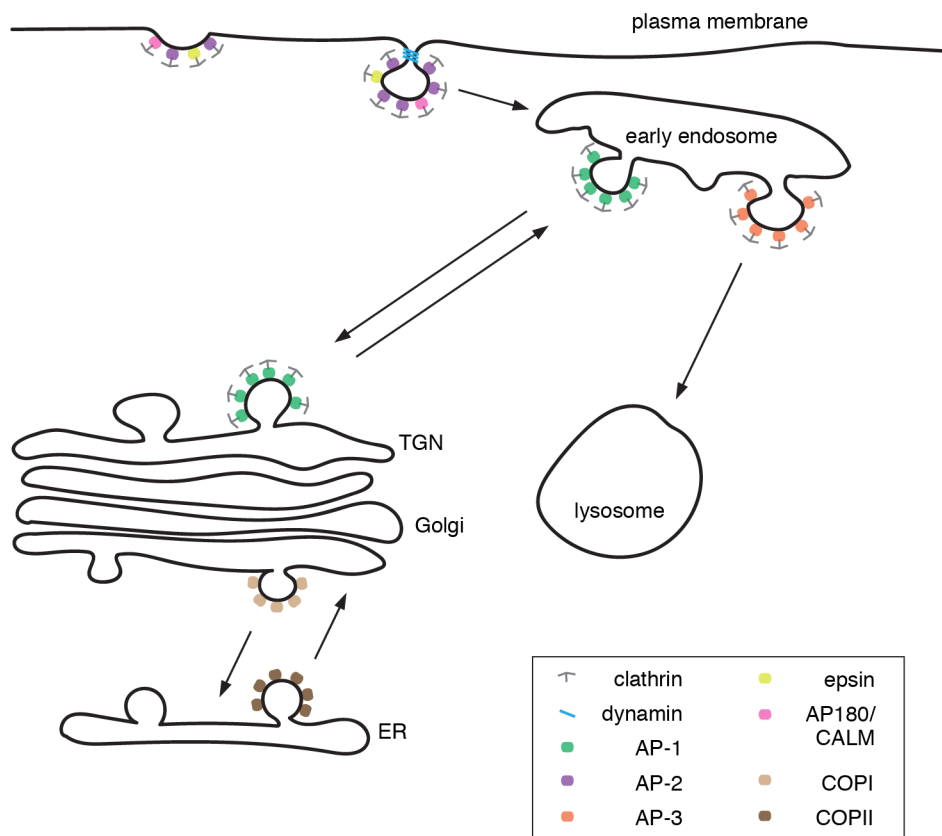


Figure 1.3: Clathrin-coated vesicle trafficking in the cell. Schematic description of endocytic and intracellular CCVs in the cell. AP-2 is the main adaptor for CCVs transported from plasma membrane to endosomes. Epsin and AP180/CALM are alternative endocytic clathrin adaptors. AP-1 and AP-3 are adaptors for CCVs transported from/to endosomes from/to TGN and from endosomes to lysosomes, respectively. Endocytic CCVs require dynamin for scission. Vesicles transported between ER and Golgi have COPI or COPII coats.

Adaptor protein complexes share similarity in their shape, structure and components. AP-1, AP-2 and AP-3 all have two large subunits with hinge and appendage domains γ and $\beta 1$, α and $\beta 2$ and δ and $\beta 3$, respectively. The appendages found on the C-terminus of the large subunits sit on the outer edges of the complex and are connected to the core via hinges. The core consists of N-terminal domains of the large subunits and the smaller subunits $\mu 1-3$, $\sigma 1-3$, respectively (Figure 1.4, Sanger et al. 2019). Subunits are not found separately in the cell but as a part of the complex (Robinson 2015).

Like AP-2, AP-1 and AP-3 also needs an open confirmation to be able to bind cargo, clathrin and other accessory proteins (Figure 1.4). AP-1 binds to phosphatidylinositol-4-phosphate (PI(4)P) for docking on the membranes of TGN and endosomes, which are rich in PI(4)P (Y. J. Wang et al. 2003; Di Paolo et al.

2006). However unlike AP-2, binding to its preferred membrane phospholipid is insufficient to initiate this structural rearrangement and activate AP-1. AP-1 requires ADP ribosylation factor 1 (Arf1) GTPase to be activated and recruited to intracellular membranes (Stamnes et al. 1993; Seaman et al. 1996). Study of the crystal structure of AP-1 in open conformation showed that, Arf1 interaction with $\beta 1$ and centre of γ subunits of AP-1 in a GTP-dependent manner is necessary for activation of AP-1 while a the third interaction of Arf1 with γ N-terminus is significant for recruitment (Ren et al. 2013). Like AP-1, AP-3 was also shown to require Arf1 interaction for its recruitment and activation (Ooi et al. 1998).

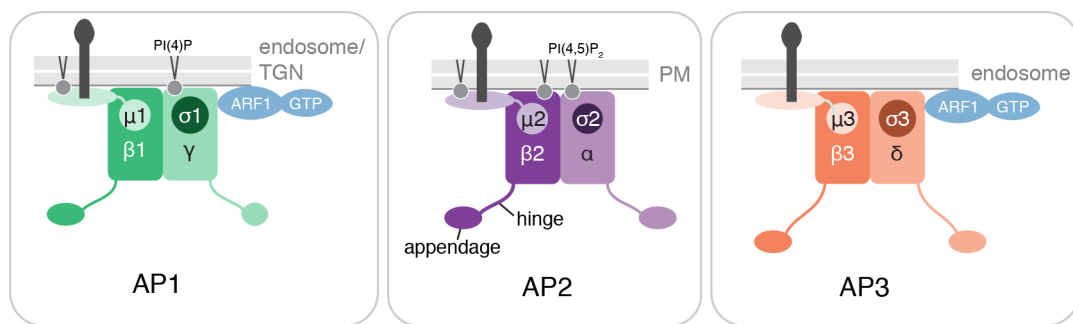


Figure 1.4: Subdomain organisation of adaptor protein complexes 1, 2 and 3 in their open conformations. Diagram showing subdomain organisations of adaptor protein complexes. AP-1 and AP-3 require Arf1 GTPase activity for open conformation while binding to PI(4,5)P₂ is sufficient for AP-2. μ subunits recognize the YXX Φ motif in cargoes. Diagram adapted from Smith et al. (2021) under Creative Commons Attribution License.

Once open, AP-1 recognises the same cargo signals, tyrosine YXX Φ or the dileucine motif, as AP-2 (Ohno et al. 1995; Carvajal-Gonzalez et al. 2012; Mattera et al. 2011). AP-3 has also been shown to possess the binding sites for these motifs by structural studies (Mardones et al. 2013; Mattera et al. 2011).

Unlike the α subunit of AP-2, its AP-1 counterpart γ can bind to clathrin via its hinge and appendage domain. The hinge domain includes two copies of a CBM variant, LLDLL, and the appendage domain has another binding site that facilitates the clathrin binding (Doray and Kornfeld 2001). On the other hand, the $\beta 1$ subunit of AP-1 is functionally and structurally very similar to $\beta 2$ of AP-2. Hinge domain of $\beta 1$ also contains the same CBM, LLNLD, as $\beta 2$ hinge, and its appendage domain shares more than 70% amino acid identity and binding partners – including clathrin – with the $\beta 2$ appendage (Dell’Angelica et al. 1998;

E. M. Schmid et al. 2006). The CBM sequence LLNLD was first identified in the $\beta 3$ subunit of AP-3 via pulldown experiments that indicated binding of the motif to CHC (Dell'Angelica et al. 1998). Yet, the mechanism of AP-3 clathrin interaction is not well understood. $\beta 3$ and $\sigma 3$ subunits of AP-3 has been shown to colocalise with clathrin in mammalian cells but not as much as AP-1 subunits (Peden, Oorschot, et al. 2004; Kural et al. 2012). However, a study done in mouse cells lacking $\beta 3$ has shown that $\beta 3$ lacking the CBM was able to rescue the mutant phenotype partially suggesting that like AP-2, AP-3 might also have other binding regions to clathrin for functional interaction (Peden, Rudge, et al. 2002). Finally, other adaptor proteins, AP-4 and AP-5 has not been associated with clathrin at all (Sanger et al. 2019).

What do the CCVs carry between TGN and endosomes? Hirst, Borner, et al. (2012) investigated this by removing AP-1 from the CCVs using rapamycin-induced rerouting. They compared the protein profiles of AP-1 depleted and control CCVs by mass spectrometry to elucidate the contents of the vesicles. They found that transport of SNARE proteins and some transmembrane proteins related with genetic diseases (ATP7A and ATP7B) from endosomes to TGN depended on AP-1 mediated CCV formation. Moreover, lysosomal hydrolases and hydrolase receptors requires the AP-1 pathway to be transported on the other direction, from TGN to endosomes. This study not only showed the bidirectionality of transport, but also pinpointed the accessory proteins involved in AP-1 mediated CCV formation. Along with clathrin, Arf1 GTPase, and Arf1 guanine nucleotide exchange-factor (ARFGEF2), actin interactor Hip1R, SNARE adaptor CALM, and uncoating protein GAK levels were found to change between the control and AP-1-depleted CCVs demonstrating a similarity between components of endocytic and intracellular CCV formation.

Intracellular scission mechanisms

COPI and COPII coated vesicles have been shown to not need a catalytic scission protein (Adolf, Herrmann, et al. 2013). By analogy to CCVs at the plasma membrane, it has been assumed that intracellular CCVs would require dynamin for scission; however this assumption has not been thoroughly tested. So far, no

scission molecule has been associated with budding of intracellular CCVs. One study tried to determine the requirement of scission molecules and has shown that dynamin does not colocalise with AP-1 or AP-3, and that AP-1 and AP-3 dynamics are not affected from dynamin inhibition (Kural et al. 2012). Though more work is needed to specifically address the formation of the vesicles themselves, rather than just the initiation mechanism. Considering the similarities between endocytic and intracellular vesicles, such as their clathrin coat, similar sizes, and stages they go through in formation, one could argue that they might require a catalytic protein or a facilitator for fission from organelle membranes.

Maturation and uncoating stages of intracellular CCVs have also not been researched specifically. Although, models proposed for these stages of CME could be true for intracellular CCVs as both vesicles have a clathrin coat, and the stages do not depend on membrane type or phospholipids. Endocytic CCVs can be tracked throughout their formation because external cargo can be provided, whereas the inaccessibility of intracellular CCVs from outside makes it harder to study their dynamics. Forming synthetic CCVs inside the cell on-demand may help us to understand more about intracellular CCVs.

1.2 Hot-wiring CME at the plasma membrane

CME is a multi-stage, intricate process that involves many proteins. AP-2 conducts clathrin recruitment and cargo binding, dynamin facilitates scission, and many accessory proteins contribute to CME at different levels. What are the crucial elements of endocytosis then? To answer this question, the minimal factors required for endocytosis was investigated previously in my lab by hot-wiring CME on the plasma membrane (Wood et al. 2017). Initiation of synthetic CME was achieved by targeting the hinge and appendage domain of AP-2 β 2 subunit to the plasma membrane on-demand, bypassing the requirements for initiation. This on-demand induction was done chemically and optogenetically providing temporal and spatiotemporal regulation of synthetic CME, respectively.

For chemical induction, β 2 hinge and appendage domain fused to FK506 binding protein (FKBP) was used as the hook to bind clathrin, and CD8, a trans-

membrane protein located on the plasma membrane fused to FKBP and the rapamycin-binding (FRB) domain was used as the anchor. Upon rapamycin induction, anchor and hook bound together and clathrin was recruited to the plasma membrane. Green spots, which were shown to include the CD8 anchor by antibody feeding, appeared on the plasma membrane, and then pinched off and trafficked within the cell localising with Rabs on the recycling pathway (Figure 1.5, Wood et al. 2017).

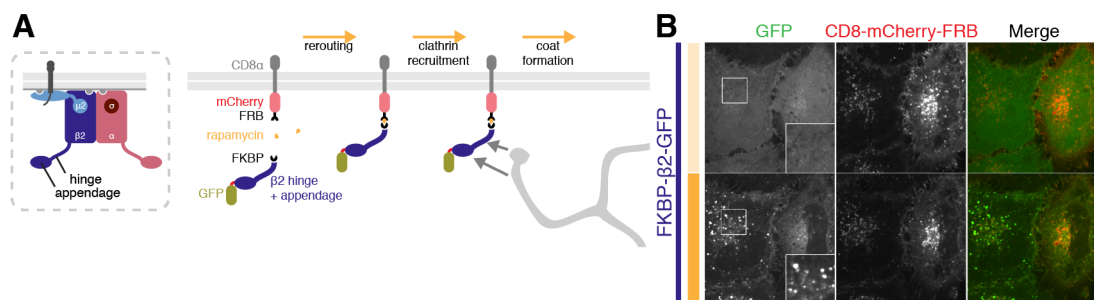


Figure 1.5: Synthetic CME was achieved by rerouting $\beta 2$ hook to plasma membrane upon rapamycin induction. Dimerisation of FKBP and FRB upon addition of 200 nM rapamycin attaches $\beta 2$ hinge and appendage to plasma membrane anchor CD8 resulting in recruitment of clathrin (A) and formation of green spots, synthetic CCVs (B). Figure is from Wood et al. (2017), used under the Creative Commons License, BY-NC-SA 4.0.

Chemical induction to initiate endocytosis on-demand was accomplished by binding of FKBP to FRB upon rapamycin induction. FKBP12 is an immunophilin that recognizes the natural immunosuppressant FK506, and dimerizes upon binding to it (Spencer et al. 1993). Rapamycin is a synthetic ligand of FKBP that also binds to the FRB domain of mammalian target of rapamycin (mTOR) after binding to FKBP creating the FKBP-FRB heterodimer (Chen et al. 1995). mTOR is a part of mTOR1 complex 1 (mTORC1) and rapamycin-FKBP complex binding to FRB inhibits mTORC1 by blocking substrate binding and reducing its kinase activity (Yang et al. 2013). As mTORC1 is a regulator of cell growth and proliferation, it is shown to be highly activated in some cancers and rapamycin and its analogs have been used as anticancer drugs as well as immunosuppressants (Guertin et al. 2009). Heterodimerisation of two different proteins using the FKBP-FRB binding upon rapamycin is one of the common chemically inducible dimerisation methods used as a tool to study various cellular mechanisms

(Karginov et al. 2010; Kapitein et al. 2010).

Synthetic CCVs were created in this work were indistinguishable from endogenous endocytic CCVs. CLEM showed the presence of extracellular antibody against CD8 within the synthetic CCVs. Generation of the synthetic CCVs depended on availability of two clathrin binding sites on the $\beta 2$ hinge and appendage, the CBM and tyrosine residue at 815, respectively. Recruiting the clathrin hook to the plasma membrane initiated spot formation which required clathrin as shown with CHC knockdown, but bypassed the requirements at initiation step of CME, such as AP-2 binding to PI(4,5)P₂, reducing the requirements for CME. This short-cut approach of creating synthetic CCVs was called hot-wiring. The minimum factor requirement of hot-wiring was also supported by the down regulation of the $\mu 2$ subunit of AP-2, which only inhibited endogenous CME and not the synthetic one. Moreover, with optogenetic dimerisation of the same hook and anchor, it was possible to initiate CME reversibly and with spatial control.

CME was hot-wired using peripheral membrane proteins as well. GAP43-FRB-mRFP and SH4-FRB-mRFP which are located to plasma membrane with palmitoylation were also successful anchors demonstrating that a transmembrane (TM) domain anchor is not a necessity (Wood et al. 2017).

Efficiency of different clathrin hooks to hot-wire CME was also investigated in this study. Parts of clathrin adaptors that contain the clathrin binding site were fused to FKBP-GFP to be used as hooks. The hinge and appendage from $\beta 1$ subunit of AP-1 and a fragment of monomeric clathrin adaptor epsin were both shown to recruit clathrin as hooks and hot-wire CME. Whereas, the hinge and appendage from $\beta 3$ subunit of AP-3 failed to initiate CME on-demand. The hinge and appendage from the $\beta 2$ subunit of AP-2 found to be the most potent hook. These experiments demonstrated that functional clathrin binding is essential for hot-wired CME (Wood et al. 2017). Hot-wiring can be a powerful tool to study clathrin hooks in detail. A recent study, investigated the functional significance of different clathrin binding sites of the $\beta 2$ hook via hot-wiring, and found out that two sites at the appendage domain of $\beta 2$ are not equally important for clathrin binding (Smith et al. 2021).

The model for synthetic CME is that CCVs are created *de novo*. However,

since hot-wiring is located at the plasma membrane there is a legitimate concern that $\beta 2$ is simply recruited to existing CME sites and not creating pits *de novo*. Although, the distinction of synthetic and endogenous CME was made clear by the knockdown of $\mu 2$ subunit of AP-2 only inhibiting the latter and extracellular antibody being present inside the cell, a more reductionist approach that would address this limitation could be to move hot-wired CCV formation to an intracellular location that is not a site of CME nor intracellular CCV formation. This way it would also be possible to study requirements for intracellular CCV formation, which is inaccessible from outside.

1.3 Mitochondria

In this thesis, I modified hot-wiring to investigate key differences between CME and intracellular CCV formation, focusing especially on mitochondria. Therefore, the key features of this organelle are briefly introduced here.

Mitochondria are primarily responsible for energy production in the cell by oxidative phosphorylation. They have prokaryotic origins; therefore, they are quite unique in their structure and function (Roger et al. 2017). Unlike other organelles in the cell, they are limited by two membranes and have their own genome (Osellame et al. 2012). Their double membrane is crucial for ATP production as it compartmentalizes the process. The outer mitochondrial membrane (OMM) allows passage of ions and small molecules via its pores. Large molecules require translocases for their transport through the OMM. On the other hand, the inner mitochondrial membrane (IMM) is much more restrictive, and ion and small molecule transport is facilitated via specific transport proteins. The IMM is loaded with protein complexes that function in the electron transport during oxidative phosphorylation. The inner membrane surface area is increased by the structures called cristae which invaginate into the matrix allowing more space for electrochemical reactions to take place. ATP production is driven by the proton gradient between the inter-membrane space and matrix and the ATP synthases on the IMM (Kühlbrandt 2015). The mitochondrial matrix resembles the cytoplasm of the cell, densely packed with proteins, the mitochondrial genome and

translation machinery. Most of the IMM and matrix preproteins are synthesized in the cytoplasm of the cell with an N-terminus presequence and transported into mitochondria via the translocases on the outer and inner membranes that recognizes the presequence. These translocases are called TOMs and TIMs, respectively. Once in the matrix, the presequences are cleaved by mitochondrial processing peptidases. The core TOM complex is composed of the transmembrane channel-forming TOM40 and three other smaller TOM proteins. TOM20 sits right next to the core complex and acts as the initial receptor for presequence recognition. On the other hand, noncleavable hydrophobic precursors are recognised by TOM70 which is loosely attached to the core complex (Wiedemann et al. 2017). TOM proteins are also useful to cell biologists to visualise or target proteins to the OMM. TOM20 is a common OMM marker, and TOM70 was used to create a mitochondrial trap by Robinson et al. (2010). In this work they inactivated adaptor protein complexes AP-1 and AP-2 by moving them to mitochondria using chemical dimerisation of FKBP and FRB. MitoTrap, a YFP-FRB fused to the import signal of the yeast TOM70p, was used as a target for binding of the FKBP tagged adaptor protein complex subunits (Robinson et al. 2010).

In recent years, the role of mitochondria has expanded from being “the powerhouse of the cell”. It has been shown to be involved in apoptosis, cell signaling, autophagy, stem cell differentiation and regulation of energy metabolism and immune response (Giacomello et al. 2020). Interaction with other organelles are crucial for some of these other functions. Hence different interaction mechanisms such as membrane contact sites with ER and vesicular transport to peroxisomes and lysosomes were discovered (Tubbs et al. 2017; Sugiura et al. 2014).

1.3.1 Lipid composition of mitochondrial membranes

As mitochondria have prokaryotic origins, they can synthesize some of their own proteins and membrane lipids. Mitochondrial membranes contain unique lipids that are exclusively synthesized in the organelle itself, along with common ones like phosphatidylcholine and phosphatidylethanolamine. Cardiolipin is one of the exclusive lipids that is mostly found in the IMM, making up 18% of its composition (Horvath et al. 2013). Cardiolipin has been shown to be involved

in various processes essential for mitochondria including maintenance of cristae morphology and regulation of mitochondrial dynamics (Paradies et al. 2019).

When compared, the lipid composition of mitochondrial membranes and plasma membrane are quite different from each other. Phosphoinositols make up 5% of mitochondrial membranes compared to 8% of plasma membrane in mammalian cells (Horvath et al. 2013). In a study that compared abundance of PI(4,5)P₂ at different membranes, PI(4,5)P₂ levels were found to be 4 fold lower in OMM compared to the plasma membrane. Moreover, mitochondria had even lesser PI(4,5)P₂ than cytosol, suggesting that mitochondria could be considered as a PI(4,5)P₂ free surface (Watt et al. 2002).

1.3.2 Mitochondrial dynamics

Mitochondria are not the small football-shaped organelles depicted in many textbooks. They are reticular and dynamic organelles that constantly undergo fusion and fission. These dynamics are crucial for proper function of mitochondria and for adaptation of its response to changing cellular needs. Fragmented mitochondria can be found before cell death and are usually a sign of mitochondrial dysfunction; however, fragmentation is also necessary for mitochondrial division, movement and quality control. Fusion of mitochondria ensures distribution of matrix proteins and is often linked to cell survival (Giacomello et al. 2020).

A member of the dynamin superfamily, dynamin-1-like protein (Drp1) is the GTPase responsible for the division of one mitochondrion into two daughter mitochondria. Drp1 is found in the cytoplasm until it is dephosphorylated by calcineurin and recruited to the fission sites on mitochondria by its receptors (Cereghetti et al. 2008). These fission sites are found where mitochondria contact ER and their constriction is promoted by actin polymerisation as well as Drp1 (Giacomello et al. 2020). Once recruited, Drp1 oligomerizes at the fission sites and catalyzes mitochondrial fragmentation. When Drp1 K38A dominant negative mutant, containing a point mutation in its GTP binding domain is overexpressed, cells show a hyperfused mitochondrial phenotype (Smirnova et al. 2001). Although it was previously argued that Drp1 is only a constrictor in the process and dynamin is the scission protein (J. E. Lee et al. 2016), in recent years

it has been shown that DNM TKO cells still have the ability to fragment mitochondria and fission was less potent only when Drp1 was knocked down (Fonseca et al. 2019), demonstrating the role of Drp1 as the catalytic scission protein.

Mitochondrial fusion is a relatively complicated process as it involves fusion of both outer and inner mitochondrial membranes. Mitofusin 1 (Mfn1) and optic atrophy protein 1 (Opa1) are the two GTPases that are responsible for fusion of OMM and IMM, respectively. First, Mfn1s from each mitochondrion bind to each other tethering two mitochondrion together. GTP hydrolysis is essential for Mfn1 activity, resulting in the fusion of two OMMs (Ishihara et al. 2004). Opa1 has two isoforms (long and short) that complement each other functionally in fusion of IMMs (Song et al. 2007). Interaction of the long isoform of Opa1 directly with membrane lipid cardiolipin is sufficient for the fusion of two IMMs (Ban et al. 2017).

1.3.3 Mitochondria-derived vesicles

As I aimed to make synthetic CCVs on mitochondria in this thesis, it is relevant to briefly introduce the endogenous vesicles derived from mitochondria here. Mitochondria-derived vesicles (MDVs) are a fairly new concept in mitochondrial biology. Their existence was first characterised in a work by Neuspiel et al. (2008) when they overexpressed an outer-membrane protein, mitochondria-anchored protein ligase (MAPL) in mammalian cells. MDVs were found to be 70-100 nm in size and occur as rarely as 5-7 MDV per cell on average. A subpopulation of them were found to be TOM20-positive while the rest were only MAPL positive. This encouraged the authors to claim that these two subpopulations carry different cargo hence should have different fates in the cell. Finally, MAPL positive MDVs were shown to fuse with a subset of peroxisomes while the TOM20-positive ones did not. As more work on this area was done by the same group, it was shown that TOM20-positive MDVs localised to multi-vesicular bodies, and oxidative stress-induced MDVs were transported to lysosomes (Soubannier, McLelland, et al. 2012). More recently, another type of stress-induced MDVs that are PINK1/parkin-dependent, were shown to use a mitochondrial SNARE, syntaxin-17 to fuse to endolysosomes (McLelland et al. 2016).

Both *in vitro* and *in vivo* EM studies revealed that MDVs can be single or double membraned, and 70-150 nm in size (Neuspiel et al. 2008; Soubannier, Rippstein, et al. 2012). The fission mechanism of MDVs were also investigated by GTP hydrolysis assay and overexpression of dominant negative version of Drp1, and it was concluded that Drp1 was not involved in scission of MDVs (Neuspiel et al. 2008; Soubannier, Rippstein, et al. 2012; Soubannier, McLelland, et al. 2012).

1.4 Aims of this thesis

Intracellular clathrin coated vesicles are experimentally inaccessible from outside of the cell *in vivo* unlike endocytic CCVs. This is a barrier to study the intracellular CCV dynamics and functional requirements. Therefore, the first aim of this thesis is to reconstitute intracellular CCVs on-demand, using minimal CME machinery that has been modified to target specific organelle membranes. This will pave the way to investigate properties, requirements and stages of intracellular CCV formation. Also, it will enable a comparison platform for intracellular and endocytic CCV formation. The second aim of this thesis is to focus on the scission stage and elucidate the vesicle budding mechanism for intracellular CCVs.

Chapter 2

Materials and Methods

2.1 Molecular Biology

To express proteins in human cells, DNA plasmids were constructed using standard methods (Green et al. 2012). If the gene of interest lacked the restriction sites required for digestion, it was first amplified by polymerase chain reaction (PCR) from the donor vector for addition of the sites. Then the PCR product or the donor vector was digested, along with the acceptor vector. Finally the insert and digested acceptor vector were ligated with Quick ligase (NEB, M2200) and transformed in DH5 α E. coli. Plasmid DNA was extracted from resulting colonies using GeneJET Plasmid Miniprep Kit (Thermo Scientific) and sent for sequencing to Source Bioscience (Nottingham, UK). The plasmid with the correct sequence was then cultured on a larger scale and DNA was extracted using GenElute Midiprep Kit (Merck). Each plasmid was assigned a unique accession number and entered into the lab database.

2.1.1 Constructs generated for this study

A number of plasmids were generated for this work which fell into four categories: i) anchor, ii) hook, iii) pinchase and iv) other plasmids.

Anchor Plasmids

To make the ER anchor (FRB-mCherry-Sec61 β), pAc-GFPC1-Sec61 β and FRB-mCherry-C1 vectors were cut with BglII and EcoRI, and Sec61 β was inserted into

the cut FRB-mCherry-C1 vector. The Golgi anchor (FRB-mCherry-Giantin) was generated by cutting out Giantin (3131-3259) from pmScarlet-Giantin-C1 with XhoI and BamHI and inserting into FRB-mCherry-C1. For the lysosome anchor (Lamp1-mCherry-FRB), Lamp1 was amplified using PCR from LAMP1-mGFP with addition of a BamHI site at the 3' end of the amplified fragment, using primers,

forward: 5'-gcgGAATTCAGGGACATGGCGGC-3',

reverse: 5'-gcgggatccttGATAGTCTGGTAGCCTGCGTG-3'). Then, TOM70p in pMito-mCherry-FRB was replaced with Lamp1 at EcoRI and BamHI sites.

Hook Plasmids

FKBP-AP180c-GFP was generated by Miguel Gonzalez Hernandez. Briefly, the C terminal region of AP180, residues 328-896 was amplified using PCR from AP180 plasmid with addition of BamHI and XmaI sites, using primers,

forward: 5'-atatatggatccccGTCGACATCTTTGCAACAGCATC-3',

reverse 5'-atatatccccgggagCAAGAAATCCTTGATGTTAAG-3'). Then, β 2 (616-951) was cut out from FKBP- β 2-GFP with BamHI and AgeI, resulting in a cut vector. Digested AP180 (328-896) PCR product, was ligated into the cut vector.

Pinchase Plasmids

Dyn1 WT-mCherry and Dyn1 K44A-mCherry were made replacing the GFP from WT Dyn1 pEGFP and K44A Dyn1 pEGFP, respectively, with mCherry from pmCherry-N1 using AgeI and NotI. mCherry-Drp1 K38A was made by site-directed mutagenesis (SDM) (W. Wang et al. 1999) using mCherry-Drp1 and following primers;

forward: 5'-GCAGAGCAGCGGAgcGAGCTCCGTGCTAG-3',

reverse: 5'-CTAGCACGGAGCTCgcTCCGCTGCTCTGC-3'. mCherry-Vps4a WT and mCherry-Vps4a E228Q were made replacing the GFP from GFP-Vps4wt and GFP-Vps4(Eqmut), respectively, with mCherry from pmCherry-N1 using AgeI and BsrGI.

Other Plasmids

To make the σ 1-mCherry and σ 3-mCherry, AP1S1 and AP3S1 gene sequences with XhoI and BamHI sites were ordered as G-blocks from Integrated DNA Technologies.

AP1S1 G block: ACTCAGATCTCGAGGCCACCATGATGCGGTTTCATGCTATTATTCAGCCGGCAGGGAAAACCTGCGGCTGCAAAAATGGTACCTGGCCACTTCGGACAAGGAACGGAAGAAGATGGTGCGCGAGCTCATGCAGGTTGTCCTGGCTCGAAAGCCCAAGATGTGCAGCTTCCTGGAGTGGAGGGACCTCAAAGTTGTCTATAAGAGATATGCCAGCCTCTACTTCTGCTGCGCCATCGAGGGCCAAGACAATGAGCTCATCACACTGGAGCTGATCCACCGATACGTGGAGCTCTTAGACAAATACTTTGGCAGTGTGTGCGAGCTGGACATCATCTTCAACTTTGAGAAGGCCTACTTCATCCTGATGAGTTTTTTGATGGGGGGGGATGTCCAGGACACCTCCAAGAAGAGTGTGCTGAAAGCCATCGAGCAGGCTGACCTACTGCAAGAGGAGGATGAGTCGCCACGGAGTGTGCTGGAGGAGATGGGTTTGGCATCCCGGATCCACCGGTTCG,

AP3S1 G block: ACTCAGATCTCGAGGCCACCATGATCAAGGCGATCCTAATCTTCAACAACCACGGGAAGCCGCGGCTCTCCAAGTTCTACCAGCCCTACAGTGAAGATACACAACAGCAAATCATCAGGGAGACTTTCCATTTGGTATCTAAGAGAGATGAAAATGTTTGTAAATTTCTAGAAAGGAGGATTATTAATTGGAGGATCTGACAACAAACTGATTTATAGACATTATGCAACGTTATATTTTGTCTTCTGTGTGGATTCTTCAGAAAGTGAACCTGGCATTTTAGATCTAATTCAAGTATTTGTGGAAACATTAGACAAATGTTTTGAAAATGTCTGTGAGCTGGATTTGATTTTCCATGTAGACAAGGTTTACAATATTCTTGCAGAAATGGTGTATGGGGGGAATGGTATTGGAGACAAATATGAATGAGATTGTTACACAAATTGATGCACAAAATAAGCTGGAAAATCTGAGGCTGGCTTAGCAGGAGCTCCAGCCCGTGCTGTATCAGCTGTAAAGAATATGAATCTTCTGAGATCCCAAGAAATATTAAACATTGGTGACATCAGTATAAAAGTGCCAAACCTGCCCTCTTTTAAATCCCGGGATCCACCGGTTCG.

σ 2-mCherry, which was available from previous work, and AP1S1 and AP3S1 G blocks were cut with XhoI and BamHI and σ 2 was replaced with σ 1 of AP-1 and

σ3 of AP-3, respectively.

Construct	ID	Insert	Vector	Method	Source
pMito-mCherry-FRB	681	MitoTrap	pMito	-	Royle lab
pMito-mCherry K70N-FRB	1581	MitoTrap K70N	pMito	-	Royle lab
pMito-mCherry- FRB-FRB	912	MitoTrap	pMito	-	Royle lab
CD8-mCherry-FRB	1237	CD8A	pMito	-	Royle lab
CD8-mCherry K70N-FRB	1253	-	pMito	-	Royle lab
FRB-mCherry-C1	1212	FRB	pmCherry-C1	-	Royle lab
pAc-GFP-C1-Sec61β	1625	Sec61β	pAcGFP1-C1	-	Addgene 15108
FRB-mCherry-Sec61β	2350	FRB	pmCherry-C1	BglII EcoRI	-
pmScarlet-Giantin-C1	2370	Giantin (3131-3259)	pmScarlet-C1	-	Addgene 85050
FRB-mCherry-Giantin	2418	Giantin (3131-3259)	pmCherry-C1	XhoI BamHI	-
LAMP1-mGFP	1118	LAMP1	pEGFP-N3	-	Addgene 34831
Lamp1-mCherry-FRB	2409	LAMP1	pMito	PCR EcoRI BamHI	-
GFP-FKBP	1969	FKBP	pEGFP	-	Royle lab
FKBP-α-GFP	1329	α (740-977)	pEGFP-N1	-	Royle lab
FKBP-β1-GFP	1330	β1 (617-949)	pEGFP-N1	-	Royle lab
FKBP-β2-GFP	1216	β2 (616-951)	pEGFP-N1	-	Royle lab
FKBP-β2 Y-A/ ΔCBM-GFP	1245	β2 (616-951, dCBM/ Y815A)	pEGFP-N1	-	Royle lab
FKBP-β2 Y815A/Y888V-GFP	1728	-	pEGFP-N1	-	Royle lab
FKBP-β3-GFP	1505	β3 (702-1094)	pEGFP-N1	-	Royle lab
FKBP-epsin-GFP	1458	Epsin1 (144-575)	pEGFP-N1	-	Royle lab

Construct	ID	Insert	Vector	Method	Source
AP180	314	Rat AP180 (328-896)	pBluescriptII SK(+)	-	EJ Unge- wickell
FKBP-AP180c-GFP	2146	Rat AP180 (328-896)	pEGFP-N1	PCR BamHI XmaI/AgeI	-
WT Dyn1 pEGFP	2425	Dyn1	pEGFP-N1	-	Addgene 34680
K44A Dyn1 pEGFP	2426	Dyn1 K44A	pEGFP-N1	-	Addgene 34681
Dyn1 WT-mCherry	2443	mCherry	pEGFP-N1	AgeI NotI	-
Dyn1 K44A-mCherry	2444	mCherry	pEGFP-N1	AgeI NotI	-
pmCherry-N1	351	Syn mCherry	pEGFP-N1	-	Royle lab
mCherry-Drp1	2428	Drp1	mCh-alpha tubulin	-	Addgene 49152
mCherry-Drp1 K38A	2438	-	mCh-alpha tubulin	SDM	-
GFP-Vps4wt	503	Vps4a	pEGFP	-	S Urbe
GFP-Vps4(Eqmut)	504	Vps4a (Eqmut)	pEGFP	-	S Urbe
mCherry-Vps4a WT	2508	mCherry	pEGFP	AgeI BsrGI	-
mCherry-Vps4a E228Q	2509	mCherry	pEGFP	AgeI BsrGI	-
σ 1-mCherry	2547	AP-1 σ 1	pmCherry-N1	PCR XhoI BamHI	-
σ 2-mCherry	561	AP-2 σ 2	pmCherry-N1	-	Royle lab
σ 3-mCherry	2548	AP-3 σ 3	pmCherry-N1	PCR XhoI BamHI	-
Endophilin-1-247-RFP	450	Rat Endophilin A1 SH3GL2	pcDNA3-1(-)	-	L Lagnado

Construct	ID	Insert	Vector	Method	Source
mCherry-epsin2	814	Mouse epsin2	pmCherry-C1	-	Addgene 27673
mCherry-FCHo2	827	Mouse FCHo2	pmCherry-C1	-	Addgene 27686
Hip1R-tDimer-RFP	841	Mouse Hip1R	pEGFP-N1	-	Addgene 27700
mCherry-amphi- physin 1	833	Mouse amphiphysin 1	pmCherry-N1	-	Addgene 27692
mCherry-SNX9	819	Mouse SNX9	pmCherry-C1	-	Addgene 27678

Table 2.1: List of plasmids used in this study. Constructs generated for this work include the method used for cloning. Rest is either used in cloning or imaging. ID indicates the ID number for lab database. Inserts are of human origin unless stated otherwise.

2.2 Cell Biology

HeLa cells (HPA/ECACC 93021013) were cultured in DMEM with GlutaMAX (Thermo Fisher) supplemented with 10% v/v foetal bovine serum, and 100 U/ml penicillin/streptomycin. DNM TKO cells (Ferguson, Raimondi, et al. 2009; Park et al. 2013), a kind gift from Pietro de Camilli, Yale School of Medicine, CT were cultured in DMEM+GlutaMAX (Thermo Fisher) supplemented with 10% v/v fetal bovine serum, 1% v/v L- glutamine, 3.5% v/v sodium bicarbonate and 1% penicillin/streptomycin. All cells were kept at 37 °C with 5% CO₂ in a humidified incubator.

For the conditional knock out of dynamin 1, 2, and 3, DNM TKO cells were plated 100,000 cells per well in 6-well dish and treated with 3 μ M 4-hydroxytamoxifen (Merck). After 48 h, Tamoxifen concentration was dropped to 300 nM, and cells were kept at this Tamoxifen concentration throughout the experiment until fixation which was 5-6 days later.

HeLa and DNM TKO cells were transfected with GeneJuice (Merck) or Fugene (Promega) according to the manufacturer’s instructions. In summary, cells

were plated in 60-70% confluency 24 h prior to DNA transfection on a cover-slip in a 12-well plate for fixed imaging or 4-well glass-bottom 3.5 cm dishes (Greiner Bio-One) for live imaging. For DNM TKO cells, cover slips were incubated with 10 $\mu\text{g}/\text{ml}$ Fibronectin for 45 min at 37°C and 5% CO_2 prior to cell seeding. 3 μL GeneJuice/Fugene was added to 100 μL Opti-MEM Reduced Serum Medium (Thermo Fisher) and incubated at room temperature for 5 min. A total of 1.2 μg DNA was added to the mix and incubated for 15 min. Anchor and hook plasmids (e.g., MitoTrap and FKBP- β 2-GFP), were transfected in a 1:2 ratio. Half or quarter of this mixture was added dropwise to each well of 12-well dish or 4-well dish, respectively. Transfection mixture was removed, and media refreshed within 18-24 h. Cells were imaged, fixed, or treated with drugs and fixed, 48 h after DNA transfection. Overall, transfection efficiency for multiple DNA constructs was around 60%.

Knockdown with siRNA transfections using Lipofectamine 2000 (Thermo Fisher) were performed by Gabrielle Larocque. HeLa cells were plated at \sim 50% confluency in a 6-well plate. They were transfected with GL2 (control) or CHC siRNA (target sequence 5'-3' TCCAATTCGAAGACCAATT) on day 2 and day 4 (Motley et al. 2003). Briefly, for 1 well, 250 μL Opti-MEM and 5 μL Lipofectamine 2000 was mixed together while 10 μL of 20 μM siRNA stock was mixed with 250 μL Opti-MEM. Both were incubated separately for 5 min, then together for 15 min. Total mixture was added to cells containing 1.5 mL media resulting in 100 nM final siRNA concentration. This was followed by DNA transfection as described above on day 4. Cells were seeded on cover slips on day 5 and fixed 24 h later.

2.2.1 Clathrin-coated vesicle formation by rapamycin induction

Rerouting of the hook to the anchor in the cell is based on heterodimerization of FKBP and FRB domains upon rapamycin addition which is exploited, to relocate proteins within the cell (Wood et al. 2017). When rapamycin enters the cell, it binds to its target FKBP, then the rapamycin-FKBP complex binds to FRB. If two proteins are tagged with FKBP and FRB, they bind together when exposed

to rapamycin. The hook plasmids contain part of proteins with clathrin binding regions fused to FKBP, and anchors are tagged with FRB. Therefore, in the presence of rapamycin, hook and anchor bind together, and clathrin is recruited to the location of the anchor. Within seconds of induction, spots start to form on the organelle that anchor sits. For fixed experiments, cells were incubated with 200 nM final concentration of rapamycin for 10-30 min, before fixation. For live cells, rerouting was triggered by addition of 400 μ l of 400 nM rapamycin to one compartment of the 4-well glass-bottom 3.5 cm dish containing 400 μ l media. This 2x rapamycin solution was added dropwise with a P1000 micropipette to promote even dilution of the drug resulting in 200 nM final rapamycin concentration during imaging. Spot formation was observed in 60% of rerouted and transfected cells.

2.2.2 Transferrin uptake

For transferrin uptake experiments, DNM TKO cells were serum-starved for a total of 30 min in serum-free media. Then for rerouting, they were exposed to 200 nM rapamycin (Alfa Aesar) and 100 μ g/ml Alexa Fluor 568 or 647-conjugated transferrin (Thermo Fisher) for the last 10 min of starvation. For HeLa cells, a dynamin inhibition step was added to the protocol where cells were treated with 30 μ M Dynole 34-2, dynamin I and dynamin II inhibitor, or negative control Dynole 31-2 (Abcam, ab120474) starting from 15-25 min after starvation, 15 min before rerouting and transferrin addition. All incubations were done in serum-free media at 37 °C with 5% CO₂ in a humidified incubator. Cells were then fixed as described in Immunofluorescence section.

2.2.3 Actin depolymerisation

For actin depolymerisation, HeLa cells were treated with 1 μ M Latrunculin B (Merck) or 0.02% v/v vehicle DMSO for 25 min, with addition of 200 nM rapamycin at the last 10 min. Cells were then fixed as described in Immunofluorescence section.

2.3 Immunofluorescence

Following drug treatments and 48 h after DNA transfection, cells were fixed at room temperature in 4% v/v formaldehyde, 4% w/v sucrose in mitochondria friendly buffer PEM (80 mM PIPES, 5 mM EGTA, and 2 mM MgCl₂, pH 6.8) for 10 min, washed three times with PBS, then permeabilised for 10 min in 0.1% Triton X-100 in PBS (Jimenez et al. 2020). Cells were blocked for 1 h in blocking solution, which was followed by an hour incubation with 1:1000 ratio of primary antibodies (Table 2.2). Cells were washed three times with PBS and incubated with 1:500 ratio of secondary antibodies for an hour, anti-mouse IgG Alexa Fluor 568 (Thermo Fisher, A11031) or anti-mouse IgG Alexa Fluor 647 (Thermo Fisher, A21235). When Acti-stain 555 was used to stain the actin cytoskeleton, it was added together with anti-mouse IgG Alexa Fluor 647 in 1:1000 ratio. After a final three washes with PBS, cover slips were dipped in MQ-grade water and left to dry. Cover slips were then mounted on slides with Mowiol.

When only fluorescently labelled proteins were imaged, fixation was carried out as described above omitting the antibody staining steps.

Primary anti-body/Stain	Supplier	Blocking Solution	Final Conc. (µg/ml)
Mouse anti-Pyruvate dehydrogenase E2/E3 (PDHE2/E3)	Abcam, ab110333	3% BSA + 5% goat serum in PBS	1
Mouse anti-clathrin heavy chain X22 (CHC, X22)	Hybridoma	3% BSA + 5% goat serum in PBS	N/A
Rabbit anti-TOMM20-Alexa Fluor 647	Abcam, ab209606	5% BSA + 5% goat serum in PBS	0.5
Acti-stain 555	Cytoskeleton Inc., PHDH1	3% BSA + 5% goat serum in PBS	N/A

Table 2.2: Antibodies and stains used in immunofluorescence.

2.4 Microscopy

2.4.1 Light Microscopy

For live cell imaging, HeLa cells were grown in 4-well glass-bottom 3.5 cm dishes and media exchanged for Liebovitz L-15 CO₂-independent medium (Gibco) before imaging. MitoTracker Deep Red FM (Thermo Fisher) was added in 1:15,000 to visualise mitochondria.

For CHC knockdown experiments cells were imaged using Ultraview Vox, (Perkin Elmer) with a 100X 1.4 NA oil objective (pixel size 0.069 μm) and a Hamamatsu ORCA-R2 camera after excitation with lasers at 488, 561, and 640 nm, operated by Volocity 6.0 software (Perkin Elmer). For the rest, Nikon CSU-W1 spinning disc confocal system with SoRa upgrade (Yokogawa) was used to image both live and fixed cells. A 60X 1.4 NA oil-immersion objective (Nikon) with 4X SoRa magnification (pixel size 0.045 μm) and 95B Prime (Photometrics) camera was used following excitation with 405, 488, 561 and 638 nm lasers. Images were acquired with NIS-Elements software (Nikon).

2.4.2 Correlative Light Electron Microscopy (CLEM)

HeLa cells plated onto gridded glass culture dishes (P35G- 1.5-14-CGRD, MatTek Corporation, Ashland, MA, USA) at 30,000 cells/dish. DNA transfection was carried out the next day with GeneJuice as described previously, using MitoTrap and FKBP- β 2-GFP, followed by live imaging on day 5 on a Nikon Ti-U epifluorescence microscope with CoolSnap MYO camera (Photometrics) using NIS-Elements software. Media was exchanged for Liebovitz L-15 CO₂-independent medium before imaging. Location of each cell of interest was recorded using the coordinates on the grid at 20X magnification with brightfield illumination. Then, cells were live imaged with epifluorescence at 100X magnification while rapamycin was added as described above. Once sufficient rerouting and spot formation was observed, cells were fixed in 3% glutaraldehyde, 0.5% formaldehyde in 0.05 M phosphate buffer, pH 7.4 for 1 h and washed with phosphate buffer three times afterwards. Cells were stained with 1% osmium tetroxide, 1.5% potassium ferrocyanide for 1 h, washed with distilled water for 4x5 min, stained with 1% tannic acid for 45

min to enhance the membrane contrast, washed with distilled water for 3x5 min and stained with 1% uranyl acetate overnight at 4 °C.

On day 6, cells were washed with distilled water for 3x5 min, dehydrated through ascending series of ethanol (30, 50, 70, 80, 90, 100%, 10 min each) and infiltrated in medium epoxy resin (TAAB) at 2:1, 1:1, 1:2 ethanol to resin ratios and finally in full resin, each for 30 min. Then, fresh full resin was added, and the gelatine capsule was placed over the grid with cell of interest. Resin was left to polymerise at 60 °C for 72 h.

On day 9, resin samples were dipped in liquid nitrogen briefly to remove the coverslip, extra plastic was removed with pliers, and samples were stored in 1.5 mL Eppendorf tubes. For trimming the resin block, cell of interest was located from 20X images previously taken and by looking at the resin grid-side, through a dissection microscope and labelled with razor marks. Extra resin was removed using a razorblade, creating a pyramid shape. Trimming was continued on the PTPCZ ultramicrotome (RMC Boeckeler) using a glass knife at 200 nm steps. 80 nm serial sections were taken using a diamond knife on the ultramicrotome and collected on Formvar coated Copper hexagonal 100 mesh grids (EM Resolutions). Sections were post-stained in 2% uranyl acetate for 2 min and in 3% Reynolds lead citrate (TAAB) for 2 min, washed with distilled water in between and after post-staining.

Electron micrographs were taken on a JEOL 2100Plus transmission electron micrograph (TEM) operating at 200kV using Gatan OneView IS camera with GMS3.0 and TEMCenter software. Cells were imaged at low magnification, 100-400X to locate and nanometre resolution images were taken at 25000X.

2.5 Data Analysis

For surface curvature analysis, an area of 150x150 pixels, where each mitochondrion and CCPs on it (mitoPits) were distinguishable, was selected and saved as region of interest (ROI). Spots that are free, on the edges or on the nodes (branch-points and endpoints) in this square area were counted using Cell Analyzer plugin in Fiji.

Channel intensity analyses was done using Fiji. For positions of the hook and the anchor in figure 3.7 a line perpendicular to a mitochondrion was drawn, crossing it and through the mitoPit and the intensity and distance for each channel over the length of the line was recorded. For TM density in figure 3.8 the line was drawn across mitoPits detached from the mitochondria. All images were registered before analysis with 200 nm beads image using NanoJ plugin for minimum distortion (Laine et al. 2019).

To quantify the spot formation efficiency with different hooks, NIS-Elements Advanced Research analysis software was used. Briefly, each cell was outlined manually and saved as an ROI. Total number of spots for each cell was counted using the “Spot Detection Binary” function at the hook channel with manual threshold. Spot size was adjusted to 3 pixels corresponding to 135 nm in scale. Then, the total number of spots for each cell was divided by the area of the cell ROI to give the number of spots per unit area.

For the CHC knockdown, total spots in a cell were counted in Fiji using “Analyze Particles”. Briefly, spots were isolated by applying manual threshold to images in the FKBP- β 2-GFP channel, and analysed particles with limits of 0.03-1.5 μ m in size and 0.4-1.0 circularity, counting the number of spots for each cell. This analysis was done by Gabrielle Larocque.

Colocalization analysis of spots, formed by rerouting of FKBP- β 2-GFP to mitochondria upon rapamycin induction, with clathrin, epsin and FCHO2 was done using the ComDet Plugin v0.5.5 in Fiji (Katrukha 2021). Spot on the FKBP- β 2-GFP were isolated by applying manual threshold to images. The maximum distance between FKBP- β 2-GFP and other proteins channels accepted as colocalisation was selected to be 2 pixels, and spot size was 3 pixels corresponding to 135 nm in scale to be able to distinguish singular spots.

To quantify how many of the spots are detached from the mitochondria with inhibition of various pinches in Chapter 4, total number of mitoPits, spots attached to mitochondria, for each cell was counted together with the total number of spots per cell. Counting was done using NIS-Elements Advanced Research analysis software. First, the cell ROI was saved as described above. Then, each mitochondrion in the cell was recognized by “Homogeneous Area Detection Bi-

nary” function using the mitochondrial matrix channel with a manual threshold and saved as an ROI. Total number of spots and total number of mitoPits within a cell was counted using “Spot Detection Binary” function at the hook channel within the cell ROI and the mitochondrial ROI, respectively. Thresholding while using the “Spot Detection Binary” function was done manually. Spot size was adjusted to 3 pixels corresponding to 135 nm in scale. Total number of mitoPits, spots counted from the mitochondrial ROI, was then subtracted from the total number of spots, spots counted from the cell ROI, in a cell to quantify number of detached or free spots. Percentage of free spots within the total spot population was calculated. Free spot analysis was done with the experimenter blind to the conditions of the experiment.

To quantify the size and abundance of hot-wired endocytic vesicles upon dynamin inhibition with Dynole 34-2, custom-written code for Fiji and Igor Pro 8 (Royle 2021) was used. Briefly, masks per cell were made via thresholding with IsoData method. Then, these masks were analysed using “Analyze Particles” function in Fiji, with limits of 0-1 μm in size and 0.3-1.0 in circularity, counting the number of spots for each cell and measuring the area of the spots. This analysis was done with the experimenter blind to the conditions of the experiment.

Image panels in figures were made with Fiji. Brightness and contrast (B & C) settings were identical for each image in a figure for all but Figure 3.1 and 3.6. In Figure 3.1, B & C settings were identical for each sample before and after rapamycin. Figures were assembled using Adobe Illustrator.

Null hypothesis statistical tests were done using Student’s t-test for comparing two groups, and one-way ANOVA and Dunnett’s or Tukey’s post-hoc test, for comparing three or more groups in Igor Pro 8.

Data were collected in Microsoft Excel and graphs were made with Igor Pro 8 (WaveMetrics). SuperPlots code in quantixed GitHub was used for graphs in Figure 3.10, Figure 3.14 and in all Figures in Chapter 4, but Figure 4.3D (Lord et al. 2020).

Chapter 3

Clathrin-coated vesicles can be formed synthetically at intracellular membranes

3.1 Introduction

Clathrin-coated vesicles are formed during endocytosis at the plasma membrane and at the endosomes and TGN during intracellular traffic. Clathrin, adaptor protein complexes and cargo are the main contributors to this process, but there are other factors involved, such as accessory proteins, phospholipid composition and curvature of the membrane. It is not understood how these factors affect CCV formation, how much, and under what conditions. It is not known, what the minimal factors are to form an intracellular CCV. Previously, our lab has shown that the hinge and appendage domain of $\beta 2$ subunit of AP-2 is sufficient to recruit clathrin to the plasma membrane and initiate endocytosis on-demand. This was achieved by targeting the hinge and appendage of the $\beta 2$ subunit to the plasma membrane using the CD8 anchor, by chemical heterodimerisation of FKBP and FRB upon rapamycin addition. (Wood et al. 2017). Upon induction, CCVs were shown to be internalised, meaning that all stages of CME were accomplished by the synthetic CME including the pinching off of vesicles. This synthetic system bypassed the dependency of CME on properties of the plasma membrane such as conformational changes on AP-2 triggered by $\text{PI}(4,5)\text{P}_2$ and was therefore termed

‘hot-wired’ CME (Wood et al. 2017). ‘Hot-wired’ CME occurs at the endogenous site of endocytosis, the plasma membrane, which makes it difficult to determine synthetic from endogenous factors that contribute to internalisation. As such, this study took a more reductionist approach and aimed to reconstitute CCV formation on intracellular membranes that have different lipid profiles, curvatures and lack endocytic proteins.

CCVs form on endosomes and TGN during intracellular trafficking as well. Although steps of CCV formation are similar at different membranes and size of CCVs are comparable, there are more than five different adaptor protein complexes operating on various membranes with different lipid profiles and accessory protein pools. We can follow the same principles and adapt our synthetic system to target other membranes to form CCPs on different organelles in the cell. Transmembrane proteins at different organelles are ideal candidates to be anchors. Several of these TM proteins – or sections of them – are commonly used as organelle markers, such as TOM70 for mitochondria, Sec61 β for ER, Giantin for Golgi and Lamp1 for lysosome. The first aim of this chapter was therefore to test whether rerouting β 2 to organelle membranes using rapamycin induction with membrane specific anchors is sufficient to form CCVs intracellularly.

3.2 Intracellular CCV formation can be induced at four different organelles

In order to initiate CCV formation on intracellular membranes in HeLa cells, we aimed to target mitochondria, ER, Golgi and lysosomes. The mitochondrial anchor used for targeting is termed ‘MitoTrap’ and has the TM domain of Tom70, a mitochondrial outer membrane protein fused to mCherry-FRB (Cheeseman et al. 2013). Other organelle specific membrane anchors were generated by fusing transmembrane domains of known organelle markers to mCherry-FRB. Sec61 β , Giantin TM domain (3131-3259) and LAMP1 were chosen for ER, Golgi and lysosome anchors, respectively. Next, a clathrin hook that can bind to the anchors upon rapamycin induction is required to be expressed together with the anchors. FKBP- β 2-GFP containing the hinge and appendage domains of β 2 subunit of AP-

2 was used as the hook. FKBP- β 2 Y-A/ Δ CBM-GFP was selected as a negative control as it cannot interact with clathrin functionally due to the deletion of the CBM on its hinge and the Y815A mutation on its appendage (Wood et al. 2017). As a second negative control, GFP-FKBP was used which has no clathrin-binding domains at all.

Before rapamycin addition, the WT β 2 hook (FKBP- β 2-GFP) is mostly cytoplasmic with some interacting with the clathrin on the plasma membrane. On the other hand, clathrin-binding deficient β 2 hook (FKBP- β 2 Y-A/ Δ CBM-GFP) and GFP-FKBP are solely cytoplasmic with no interaction with clathrin on the plasma membrane before induction (Figure 3.1). Upon rapamycin addition, WT β 2 hook, clathrin-binding deficient β 2 hook and the GFP-FKBP all rerouted successfully to the organelle specific anchors. Upon rerouting, formation of bright spots in the WT β 2 hook channel, resembling ones formed on the plasma membrane (Figure 1.5), were observed at mitochondria, ER, Golgi and lysosomes (Figure 3.1, 3.2, 3.3, 3.4). The respective anchors also concentrated at the same location as the spots, demonstrating the rerouting. No bright spots formed upon rerouting of the clathrin-binding deficient β 2 hook or the GFP-FKBP suggesting that those bright spots may be CCPs, requiring clathrin recruitment to form (Figure 3.1, 3.2, 3.3, 3.4). To conclude, our synthetic system was effective in forming CCVs at four different organelles.

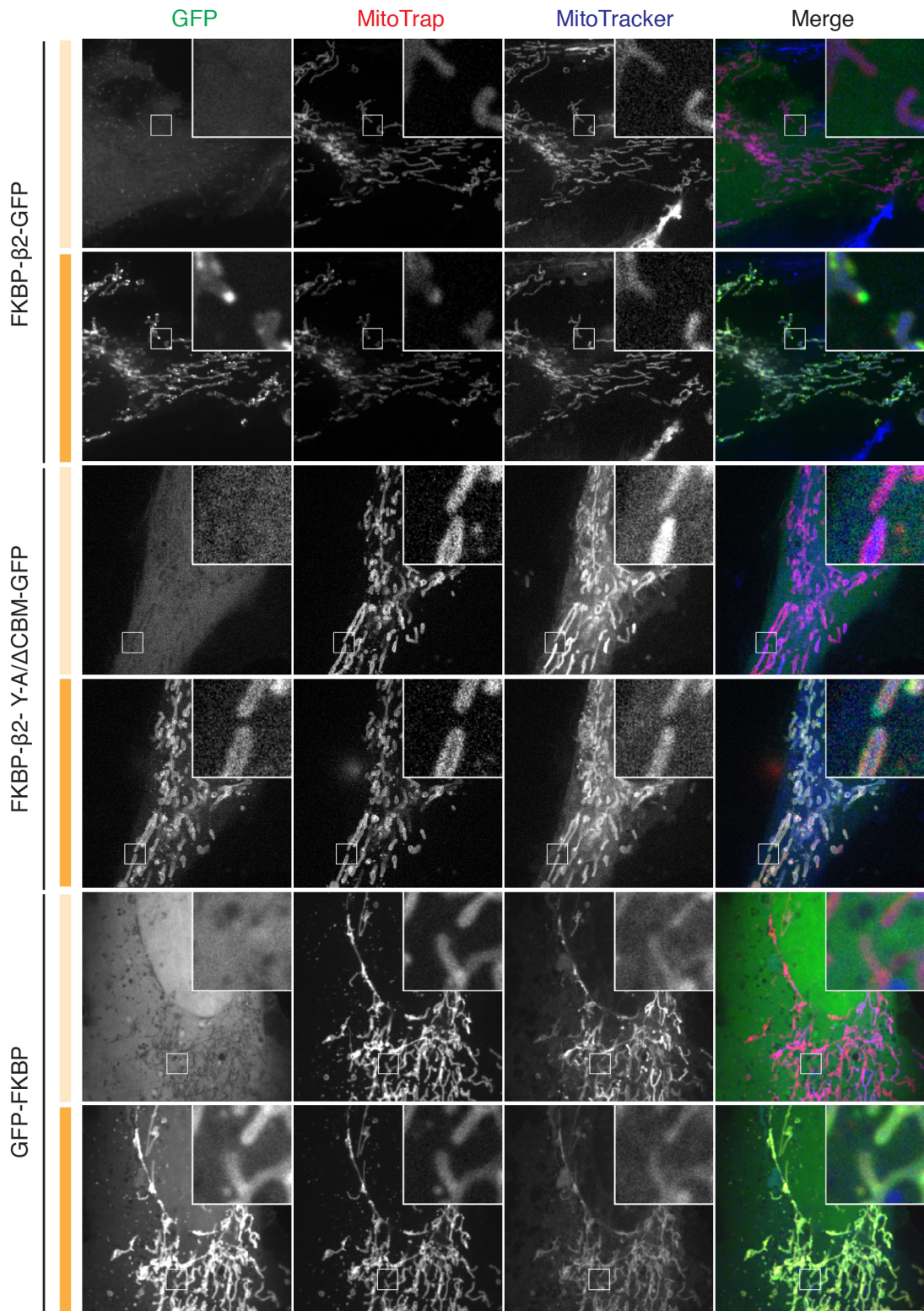


Figure 3.1: Rerouting of the clathrin hook to the mitochondria induces spot formation. Representative confocal micrographs of HeLa cells before (light orange bar) and 2 min after 200 nM rapamycin treatment (dark orange bar) showing the spot formation. Cells expressing WT hook, FKBP- β 2-GFP or clathrin binding-deficient double mutant, FKBP- β 2 Y-A/ Δ CBM-GFP or negative control GFP-FKBP together with MitoTrap, pMito-mCherry-FRB. Mitochondria labelled with far-red MitoTracker. Inset: 5X zoom. Scale bar: 10 μ m.

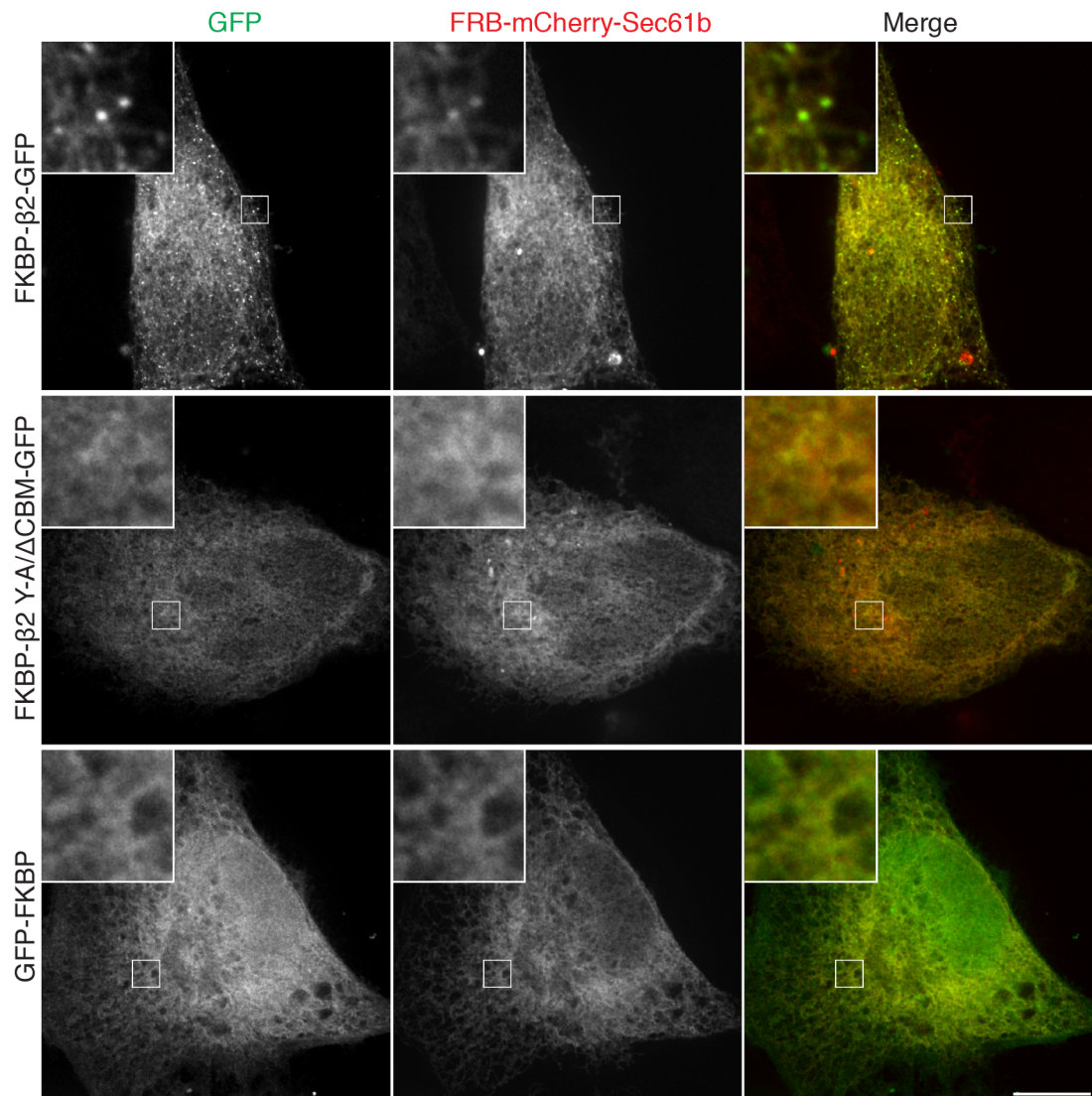


Figure 3.2: Rerouting of the hook to the ER induces spot formation. Representative confocal micrographs of HeLa cells showing the spot formation on ER. Cells expressing WT hook, FKBP-β2-GFP or clathrin binding-deficient double mutant, FKBP-β2 Y-A/ΔCBM-GFP or negative control GFP-FKBP together with ER anchor, FRB-mCherry-Sec61β. All cells are treated with 200 nM rapamycin. Inset: 5X zoom. Scale bar: 10 μm.

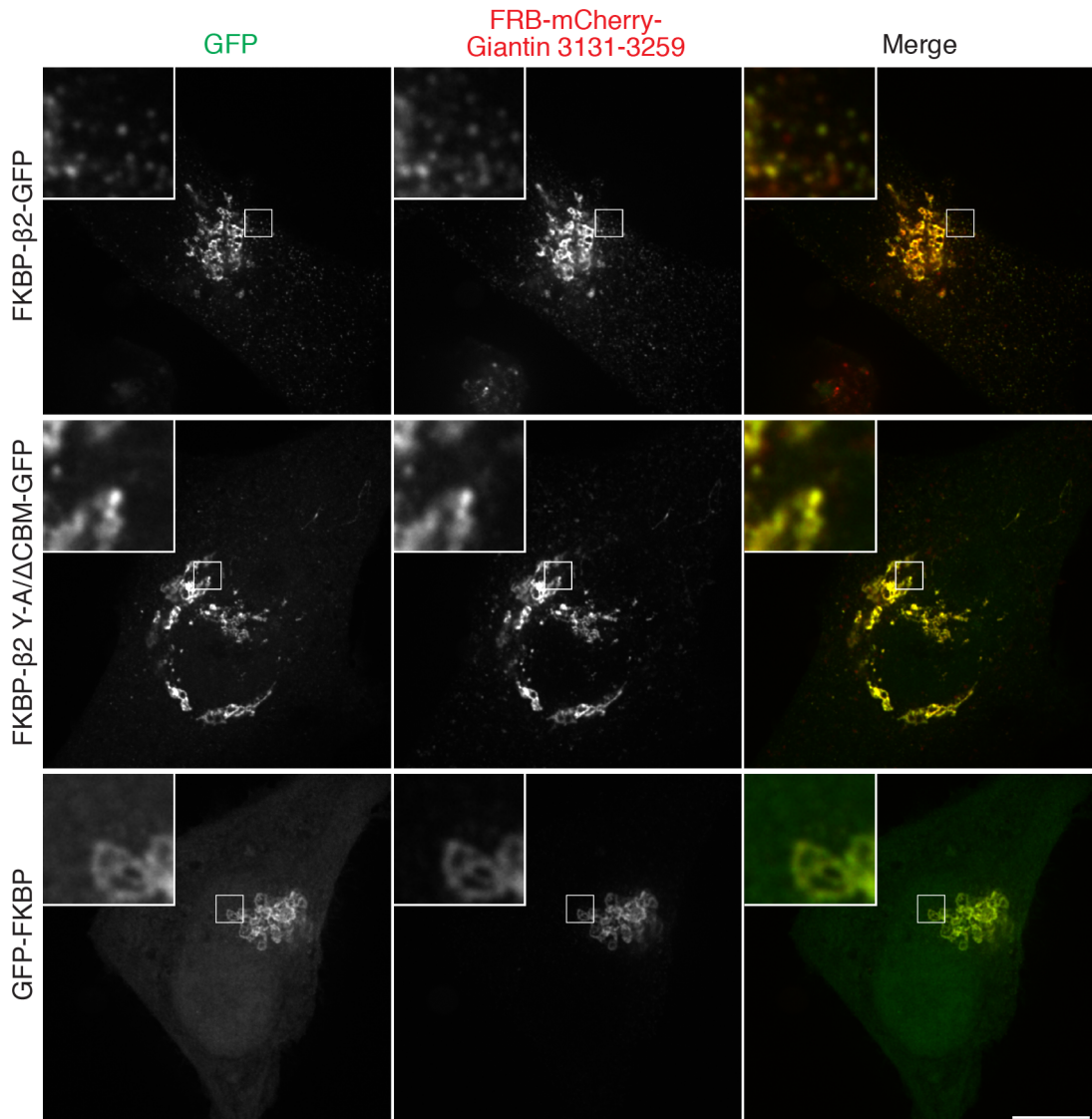


Figure 3.3: Rerouting of the hook to the Golgi induces spot formation. Representative confocal micrographs of HeLa cells showing the spot formation on Golgi. Cells expressing WT hook, FKBP- β 2-GFP or clathrin binding-deficient double mutant, FKBP- β 2 Y-A/ Δ CBM-GFP or negative control GFP-FKBP together with Golgi anchor, FRB-mCherry-Giantin 3131-3259. All cells are treated with 200 nM rapamycin. Inset: 5X zoom. Scale bar: 10 μ m.

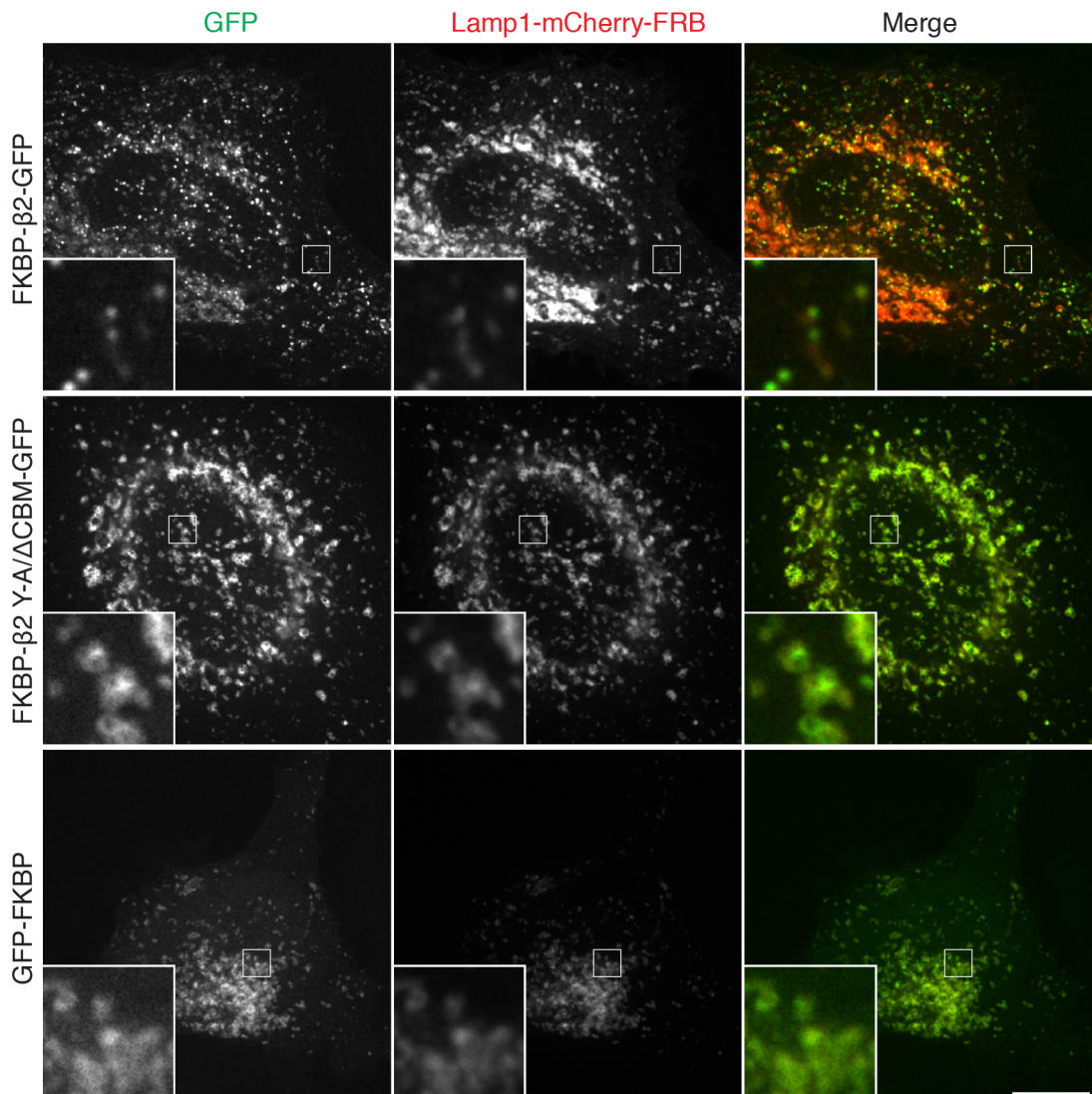


Figure 3.4: Rerouting of the hook to the lysosome induces spot formation. Representative confocal micrographs of HeLa cells showing the spot formation on lysosome. Cells expressing WT hook, FKBP- β 2-GFP or clathrin binding-deficient double mutant, FKBP- β 2 Y-A/ Δ CBM-GFP or negative control GFP-FKBP together with lysosome anchor, Lamp1-mCherry-FRB. All cells are treated with 200 nM rapamycin. Inset: 5X zoom. Scale bar: 10 μ m.

The most intriguing result was the formation of CCVs on mitochondria; as mitochondria are not part of canonical membrane trafficking unlike the other organelles targeted. Moreover, the lipid profile of the mitochondria is different from the plasma membrane and it includes very little PI(4,5)P₂ compared to the plasma membrane (Watt et al. 2002). Finally, mitochondria have a double membrane, meaning more force may be necessary to bend both membranes during invagination. Therefore, we focused our efforts on mitochondria and termed the CCPs forming here as ‘mitoPits’.

3.3 Temporal and spatial characterisation of mitoPits

We wanted to observe mitoPit formation live to investigate the temporal dynamics. Cells expressing WT $\beta 2$ hook and MitoTrap were stained with the live mitochondrial matrix dye MitoTracker and treated with rapamycin. The mitoPits start to form 12-16 sec after rapamycin addition (Figure 3.5) as seen on the WT $\beta 2$ channel at 22 sec. The bright spot of mitoPit is observed on the MitoTrap channel, too. This colocalisation of spots with the MitoTrap suggests that they are composed of mitochondrial membrane, whereas the mitochondrial matrix marker MitoTracker is absent from the spots. Moreover, it seems like that mitoPits tend to form at the tips of the mitochondria (Figure 3.5, arrowheads).

It can be concluded that mitoPit formation happens within seconds after rapamycin addition, and mitoPits involve the MitoTrap together with WT $\beta 2$ hook.

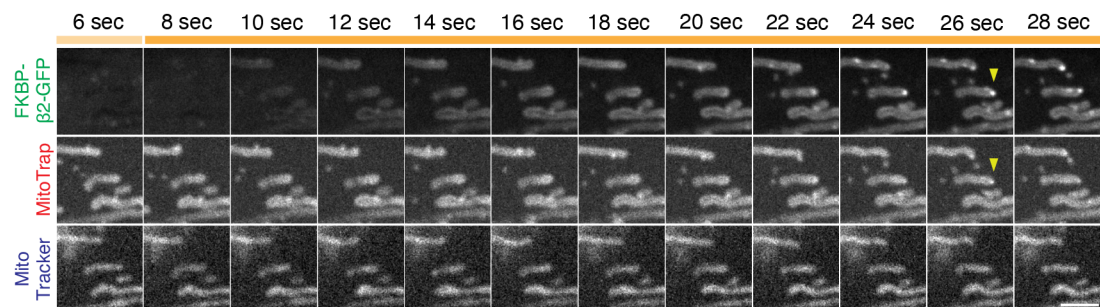


Figure 3.5: Formation of mitoPits in real time. Time course of representative confocal micrographs of a HeLa cell induced with 200 nM rapamycin at 8 sec, expressing the WT hook, FKBP- $\beta 2$ -GFP in green, and the anchor, MitoTrap in red. Mitochondria labelled with far-red MitoTracker. Arrows indicate a mitoPit. Scale bar: 10 μ m.

It was shown previously that clathrin lattices preferentially form on curved membranes over flat ones, and curved membranes are CME hotspots (Zhao et al. 2017), and I have observed mitoPit formation at the tips of mitochondria (Figure 3.5); therefore, we hypothesised that our mitoPits might also form preferentially on the mitochondrial nodes: endpoints and branchpoints, which have increased curvature. HeLa cells expressing the WT $\beta 2$ hook and MitoTrap were induced with rapamycin to form mitoPits. Areas of the cell containing mitochondria were

selected and the number of mitoPits were counted and classified according to their location on the mitochondrion. Less than 20% of the mitoPits occurred on the edges, the least curved surface of the mitochondria. Most of the mitoPits formed at the endpoints and branchpoints. Finally, 20% of the spots counted within the area were detached from the mitochondria (Figure 3.6), which will be discussed in detail later on. To conclude, mitoPits were shown to prefer curved surfaces over flat ones although formation on flat surfaces was not excluded.

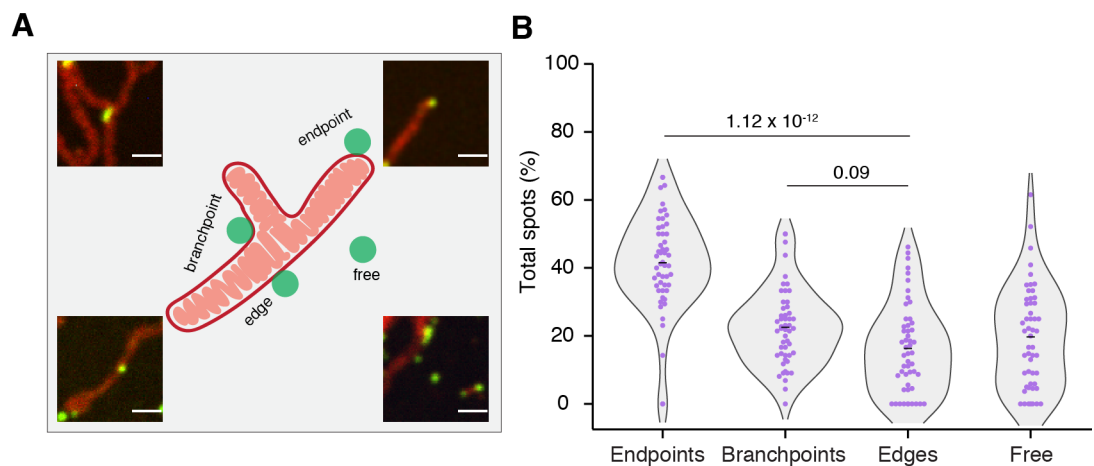


Figure 3.6: Curved surfaces facilitate mitoPit formation. (A) Schematic representation of mitochondria with representative micrographs of spots forming on various mitochondrial surfaces in HeLa cells expressing FKBP- β 2-GFP (green) and MitoTrap (red). All cells were treated with 200 nM rapamycin. Scale bar: 1 μ m. (B) Violin plot comparing abundance of mitoPits in different mitochondrial surfaces. 6.82 μ m x 6.82 μ m ROIs selected from each cell and mitoPits in each location was counted and graphed, each dot represents a cell, n=4. P-values from Tukey's post-hoc comparison.

According to our model for synthetic CCV formation, mitoPits should have MitoTrap surrounded by the WT β 2 hook (Figure 3.7, D). Therefore, the MitoTrap signal should spatially precede the WT β 2 signal. In order to test this, I used super-resolution imaging, confocal microscopy with SoRa upgrade (Figure 3.7, A). HeLa cells expressing the WT β 2 hook and MitoTrap were induced with rapamycin and stained for the mitochondrial matrix marker, PDHE2/E3 or the mitochondrial outer membrane marker TOM20. In order to minimise distortion, cell images were registered with 200 nm bead images using NanoJ plugin in Fiji (Laine et al. 2019). A line perpendicular to mitochondria was drawn across the mitochondria and through the mitoPits to quantify the positions of the WT β 2 hook, MitoTrap, the matrix marker and the mitochondrial outer membrane

marker, and channel intensity vs. distance was graphed (3.7B left, C). The peak of the MitoTrap precedes the WT $\beta 2$ hook by approximately 50 nm suggesting that MitoTrap resides closer to the surface of the mitochondria (Figure 3.7B middle). A shallower gradient of the left leg of the curve of MitoTrap corresponds to the weaker MitoTrap signal coming from the unbound anchors on mitochondria (Figure 3.7B left, C). Moreover, mitoPits were quantified to be around 135 nm in size referencing the peak width of $\beta 2$ (Figure 3.7B right). The matrix marker PDHE2/E3 signal peaks approximately 200 nm before the $\beta 2$ signal (Figure 3.7B middle) suggesting that there are undetectable levels of matrix in the mitoPits. This is in line with our previous results with MitoTracker (Figure 3.5). TOM20 on the other hand is a mitochondrial outer membrane protein, and therefore colocalisation of it with our mitoPits is expected; however, the TOM20 antibody signal was too weak to investigate this point (Figure 3.7C). Therefore, PDHE2/E3 was used in the rest of the study as the mitochondria marker. To conclude, the topology of mitoPits is as expected and they measured around 135 nm in diameter, which is comparable to CCPs.

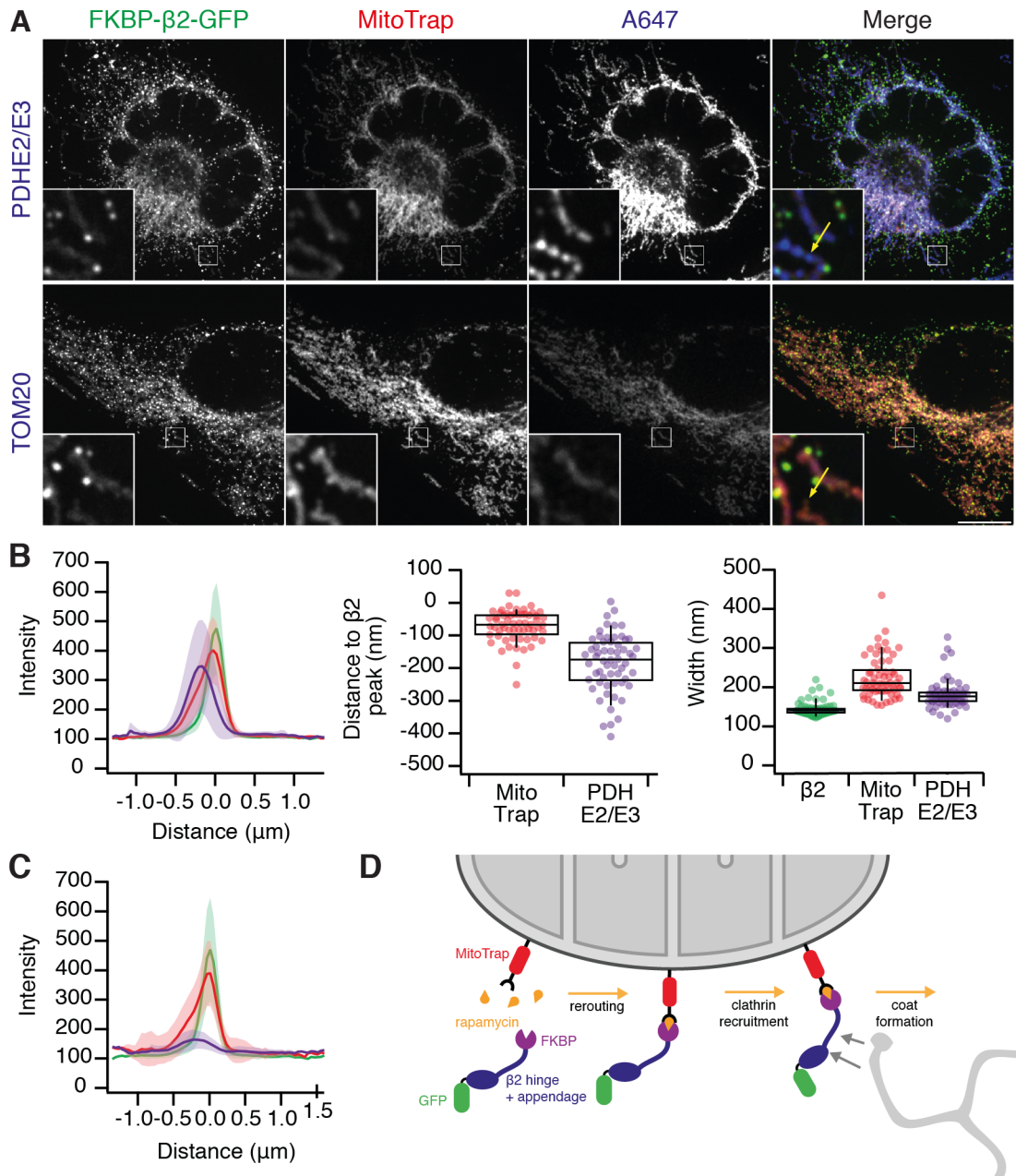


Figure 3.7: mitoPits are surrounded by the WT $\beta 2$ hook. (A) Representative confocal micrographs of HeLa cells forming mitoPits upon 200 nM rapamycin induction. Cells expressing FKBP- $\beta 2$ -GFP and MitoTrap stained with anti-PDHE2/E3, mitochondrial matrix or anti-TOM20, mitochondrial outer membrane marker, together with IgG Alexa Fluor 647. Inset: 5X zoom. Scale bar: 10 μm . Yellow arrows showing the direction of the line drawn for quantification. All images are corrected for distortion using 200 nm beads and NanoJ. Plots showing distance to the peak in fluorescence intensity for each channel (left), width of peaks (middle) and distance of MitoTrap and antibody to the mitoPits (right), for PDHE2/E3 (B) and TOM20 (C). Coloured lines are mean average of each channel, and clouds are the range of all cells. Dots represent single cells, box plots are median, IQR, 9th and 91st percentile, n=3. (D) Mechanism of inducible clathrin-coated vesicle formation on mitochondria.

Our model is that mitoPits form via clathrin recruitment and subsequent membrane bending. An alternative model is that clustering of transmembrane domains causes the membrane to bend via steric hindrance. Thus, I tested if mitoPits could form when the TM density per mitoPit is diluted. To do this, an anchor with two FRB domains, pMito-mCherry-FRB-FRB (2xFRB MitoTrap), was generated. When chemical dimerisation was induced via rapamycin addition, this anchor should bind twice the number of WT $\beta 2$ hooks diluting the TM domain per mitoPit. In figure 3.8A, mitoPits formed successfully with both regular 1xFRB MitoTrap and diluted 2xFRB MitoTrap anchors. Moreover, the difference between hook and anchor intensity is far greater with 2xFRB MitoTrap anchor demonstrating that more WT $\beta 2$ hook was bound per mitoPit, for same density of TM domains (Figure 3.8B, C). It can be concluded that TM clustering is not the reason for mitoPit formation, and clathrin might be driving the maturation of mitoPits.

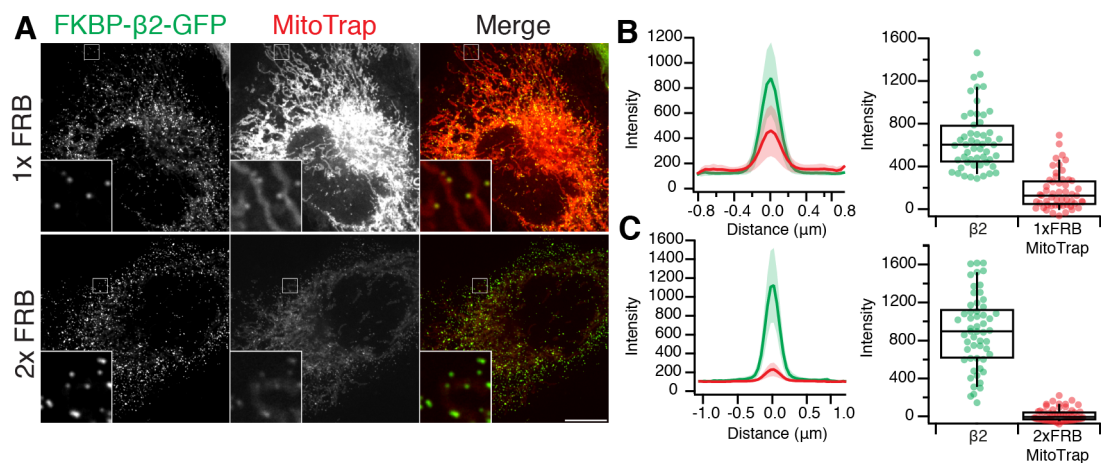


Figure 3.8: mitoPit formation is not caused by transmembrane domain clustering. (A) Representative confocal micrographs of HeLa cells expressing FKBP- $\beta 2$ -GFP and MitoTrap (1x FRB) or 2x FRB MitoTrap forming mitoPits upon 200 nM rapamycin induction. Cells with 2xFRB MitoTrap has less TM domain per mitoPit. Inset: 5X zoom. Scale bar: 10 μm . (B, C) Plots showing distance to the peak in fluorescence intensity for each channel (left) and comparison of the intensities between two channels (right) drawn from spatial fluorescence profile analysis data. Coloured lines are mean average of each channel, and clouds are the range of all cells. Dots represent single cells, box plots are median, IQR, 9th and 91st percentile, n=3.

3.4 Endocytic hooks are more effective in forming mitoPits than intracellular hooks

CME was shown to be hot-wired using different clathrin hooks (Wood et al. 2017). Therefore, we wanted to test whether this was also true for mitoPit formation. $\beta 1$ and $\beta 3$ subunits of intracellular clathrin adaptor complexes AP-1 and AP-3 as well as the monomeric endocytic clathrin adaptors epsin and AP180 can bind to clathrin. Therefore, we hypothesised that clathrin-binding regions of these proteins could be just as effective as hooks as $\beta 2$ and may be able to form mitoPits when rerouted to mitochondria by chemical dimerisation of FKBP to FRB. The $\beta 1$ and the $\beta 3$ hooks, FKBP- $\beta 1$ (617-949)-GFP and FKBP- $\beta 3$ (702-1094)-GFP, containing the CBMs; the epsin hook, FKBP-epsin1 (144-575)-GFP, lacking the PI(4,5)P₂ binding ENTH domain and containing the two CBMs; and the AP180 hook, FKBP-AP180c-GFP, lacking the ANTH, PI(4,5)P₂ binding domain and containing the clathrin binding domains were all expressed in HeLa cells together with MitoTrap. FKBP- α (740-977)-GFP was used as a negative control since neither hinge nor appendage domains of the α subunit of AP-2 can bind clathrin. When mitoPit formation was induced with rapamycin addition, cells expressing the $\beta 1$, $\beta 2$, epsin and AP180 hooks successfully formed mitoPits while α and $\beta 3$ hooks failed to initiate mitoPit formation upon rapamycin addition (Figure 3.9A, B). When the spot formation efficiency was quantified, AP180 was the most efficient hook to form spots while epsin, $\beta 2$ and $\beta 1$ followed it, respectively (Figure 3.9C). Overall endocytic hooks, $\beta 2$, epsin and AP180 were more potent in forming mitoPits than intracellular hooks, $\beta 1$ and $\beta 3$.

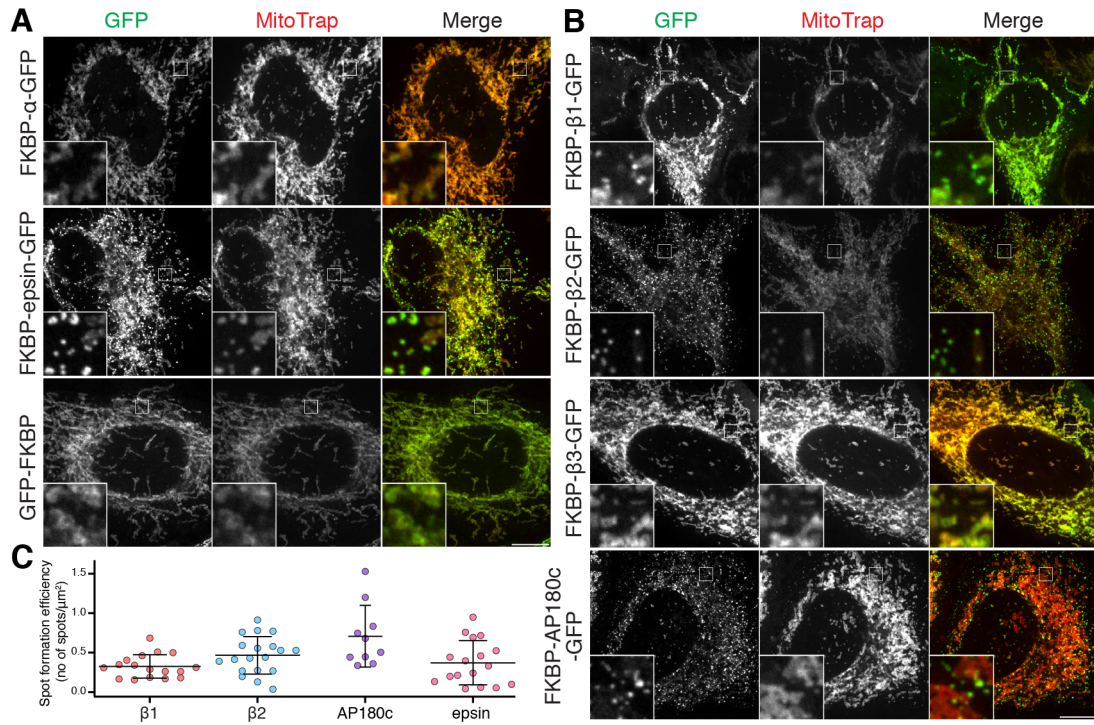


Figure 3.9: Rerouting of FKBP- β 1-GFP, FKBP- β 2-GFP, FKBP-AP180c-GFP, and FKBP-epsin-GFP hooks to mitochondria forms mitoPits. Representative confocal micrographs of mitoPit formation on HeLa cells with different hooks. Cells expressing FKBP- α -GFP, FKBP-epsin-GFP, GFP-FKBP (A), FKBP- β 1-GFP, FKBP- β 2-GFP, FKBP- β 3-GFP and FKBP-AP180c-GFP (B) together with MitoTrap. All cells were treated with 200 nM rapamycin. Inset: 5X zoom. Scale bar: 10 μ m. (C) Scatter dot plot comparing spot formation efficiency with different hooks. Each dot represents a cell. Bars indicate mean \pm 1 s.d.

3.5 Formation of mitoPits is clathrin dependent

We hypothesised that mitoPit formation should require clathrin. To test this hypothesis, endogenous clathrin localisation in HeLa cells was investigated while forming mitoPits via rerouting the WT hook, FKBP- β 2-GFP to the mitochondria (Figure 3.10). Clathrin-binding deficient hook, FKBP- β 2 Y-A/ Δ CBM-GFP, was a suitable additional negative control for this experiment as it has shown poor performance in spot formation efficiency (Figure 3.10B, bottom left). When mitoPits were formed upon rerouting of the WT β 2 hook, clathrin noticeably colocalised with them as detected with CHC antibody (Figure 3.10A). Quantification revealed that approximately 30% of the endogenous pitted clathrin colocalised with mitoPits. Moreover, more than 50% of the mitoPits had clathrin (Figure

3.10B, top graphs). As endogenous clathrin was found at similar levels between experimental and control samples (Figure 3.10B, bottom right), this colocalisation effect cannot occur as a result of excess clathrin production in the cell.

Another way to test the requirement of clathrin for mitoPit formation is to knockdown the endogenous clathrin in the cell. Clathrin detection with anti-CHC was greatly reduced in HeLa cells treated with siRNA against CHC compared to the control (Figure 3.11A). The knockdown of clathrin did not disrupt the rerouting of the WT $\beta 2$ hook to the mitochondria; however, it completely inhibited the formation of mitoPits (Figure 3.11B). Both the colocalisation experiment and the knockdown of clathrin support our hypothesis that mitoPit formation depends on recruitment of clathrin by the functional $\beta 2$ hook.

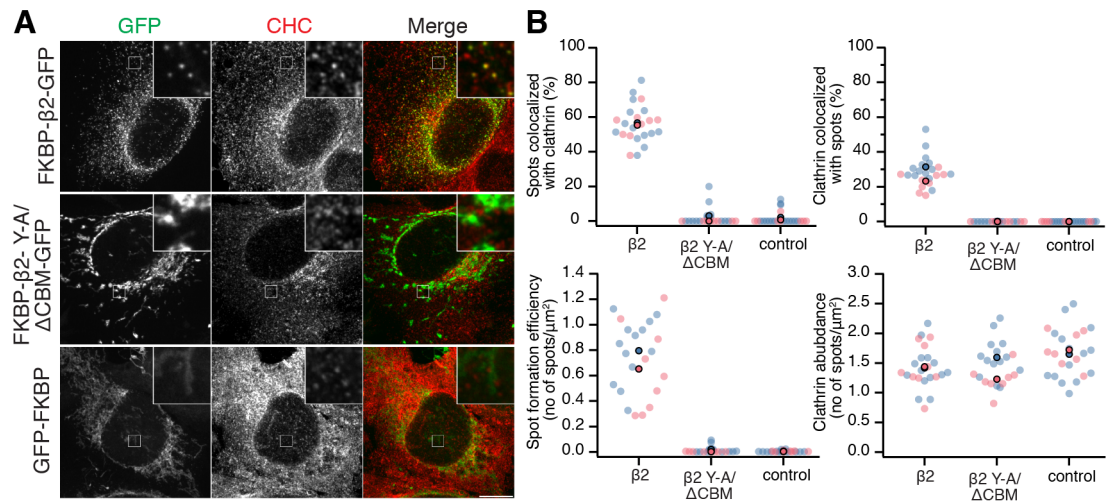


Figure 3.10: Clathrin colocalises with mitoPits. (A) Representative confocal micrographs of HeLa cells expressing WT hook, FKBP- $\beta 2$ -GFP or clathrin binding-deficient double mutant, FKBP- $\beta 2$ Y-A/ $\Delta 2$ CBM-GFP or negative control, GFP-FKBP together with dark MitoTrap. Clathrin stained with anti-CHC and IgG Alexa Fluor 568. All cells were treated with 200 nM rapamycin. Inset: 5X zoom. Scale bar: 10 μm . (B) SuperPlots comparing colocalisation of spots with clathrin (left top), colocalisation of clathrin with spots (right top), spot formation efficiency (left bottom) and clathrin abundance (right bottom) for each condition. Colours represent replicates. Each faded dot represents a cell, opaque dots represent means of replicates, n=2.

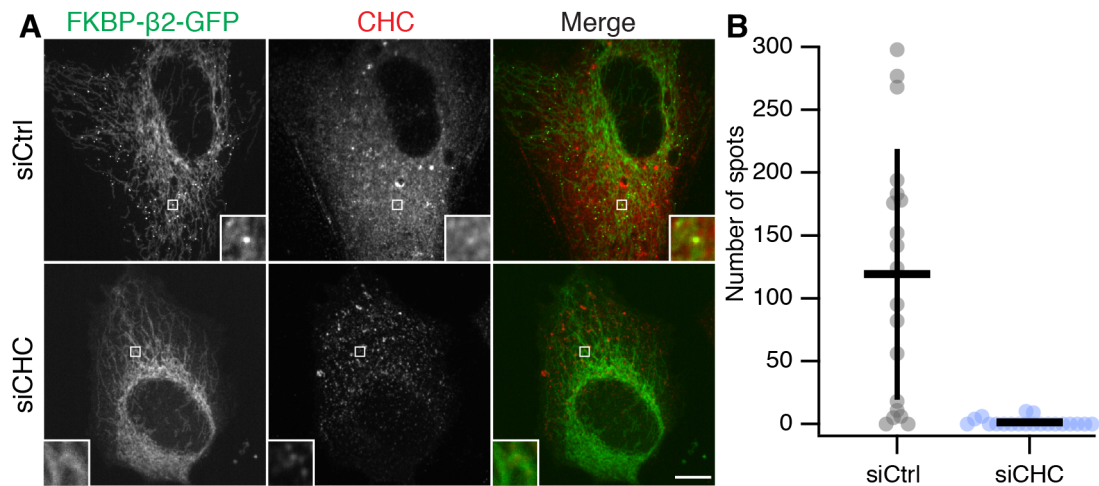


Figure 3.11: Clathrin is necessary to form mitoPits. (A) Representative confocal micrographs of HeLa cells showing no spot formation on CHC knockdown background. Cells expressing FKBP-β2-GFP and MitoTrap treated with control siRNA, siCtrl, or clathrin siRNA, siCHC, stained with anti-CHC and IgG Alexa Fluor 647. All cells were treated with 200 nM rapamycin. Inset: 5X zoom. Scale bar: 10 μm. (B) Scatter dot plot comparing number of spots between control and CHC knockdown. Each dot represents a cell, n=1.

3.6 mitoPits do not interact with σ subunits of AP-1, AP-2 and AP-3

The σ subunits of AP complexes do not have a direct role in clathrin recruitment and they do not bind to the hinge and appendage domains of β subunits. Therefore, we do not expect them to colocalise with mitoPits unless the endogenous AP complex is recruited to the mitoPit. To test this possibility, I expressed σ 1-mCherry, σ 2-mCherry or σ 3-mCherry together with dark MitoTrap and the WT β 2 hook in HeLa cells, and induced mitoPit formation with rapamycin. None of the σ subunits colocalised with mitoPits (Figure 3.12). Hence, mitoPit formation does not promote recruitment of endogenous AP-1, AP-2 or AP-3 to mitochondria. These results underline that clathrin recruitment is driven by the clathrin hook alone. The mitoPits do not form due to any endogenous adaptor protein complexes nor do they form at pre-existing sites of CCV formation in the cell.

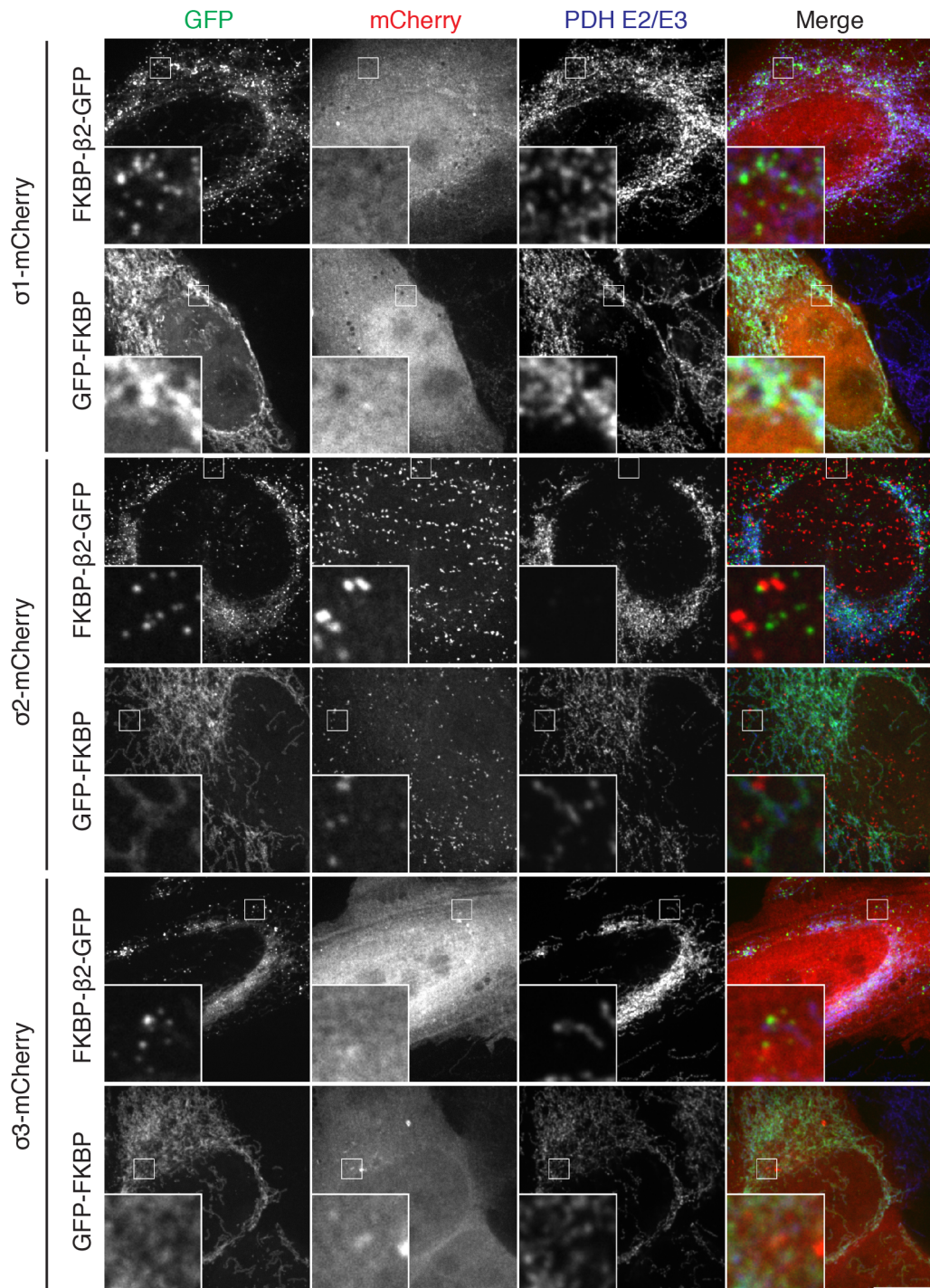


Figure 3.12: AP-1, AP-2 and AP-3 σ subunits do not colocalise with mito-Pits. Representative confocal micrographs of HeLa cells expressing σ 1-mCherry, σ 2-mCherry or σ 3-mCherry together with dark MitoTrap and WT hook, FKBP- β 2-GFP or negative control GFP-FKBP, stained with anti-PDHE2/E3, mitochondrial matrix marker and IgG Alexa Fluor 647. All cells were treated with 200 nM rapamycin. Inset: 5X zoom. Scale bar: 10 μ m.

3.7 Epsin2 and FCHO2 are recruited to mitoPits

It is possible that our synthetic intracellular CCP system attracts other proteins involved in CME. In order to investigate whether any accessory proteins accompany mitoPit formation, mCherry- or RFP-tagged accessory proteins, amphiphysin 1, endophilin, Hip1R, SNX9, epsin2 and FCHO2 were expressed in HeLa cells. Once mitoPit formation was induced, cells were fixed and stained for the mitochondrial matrix marker, PDHE2/E3. Overexpressed amphiphysin 1, endophilin, and SNX9 were found in cytoplasm while Hip1R also localised to CCVs at the plasma membrane. Their localisation was unchanged due to mitoPit formation and none were recruited to mitoPits (Figure 3.13). Yet both epsin2 and FCHO2 colocalised with mitoPits (Figure 3.14A, C top panels). Approximately 50% of overexpressed epsin2 was recruited to around 80% of mitoPits (Figure 3.14B top graphs). Within the tested accessory proteins, epsin2 is unique in its ability to bind both clathrin and $\beta 2$; therefore, to elucidate its route of recruitment, FKBP- $\beta 2$ Y815A/Y888V-GFP, a $\beta 2$ hook with both of its accessory protein binding sites at the appendage domain mutated, was used (Edeling et al. 2006). These mutations are also likely to affect clathrin binding (Smith et al. 2021), although the presence of CBM may mean that some mitoPits can form. As seen in figure 3.14B bottom left graph, mitoPit formation efficiency was decreased but not completely diminished, suggesting epsin2 is recruited to mitoPits by both clathrin and $\beta 2$ hook. Although FCHO2 colocalisation, was less efficient than epsin2 – only around 20% of overexpressed FCHO2 was recruited to around 20% of mitoPits (Figure 3.14D, top graphs) – this was surprising as neither $\beta 2$ nor clathrin is a binding partner of FCHO2. Furthermore, when a binding-deficient $\beta 2$ hook was induced to form mitoPits in FCHO2 overexpressed HeLa cells, the efficiency of spot formation dropped and the colocalisation of FCHO2 with mitoPits diminished (Figure 3.14D, left). To conclude, out of six accessory proteins, only epsin2 and FCHO2 were recruited to mitoPits, epsin2 via its binding to clathrin and the WT $\beta 2$ hook, FCHO2 via an unknown binding partner of $\beta 2$.

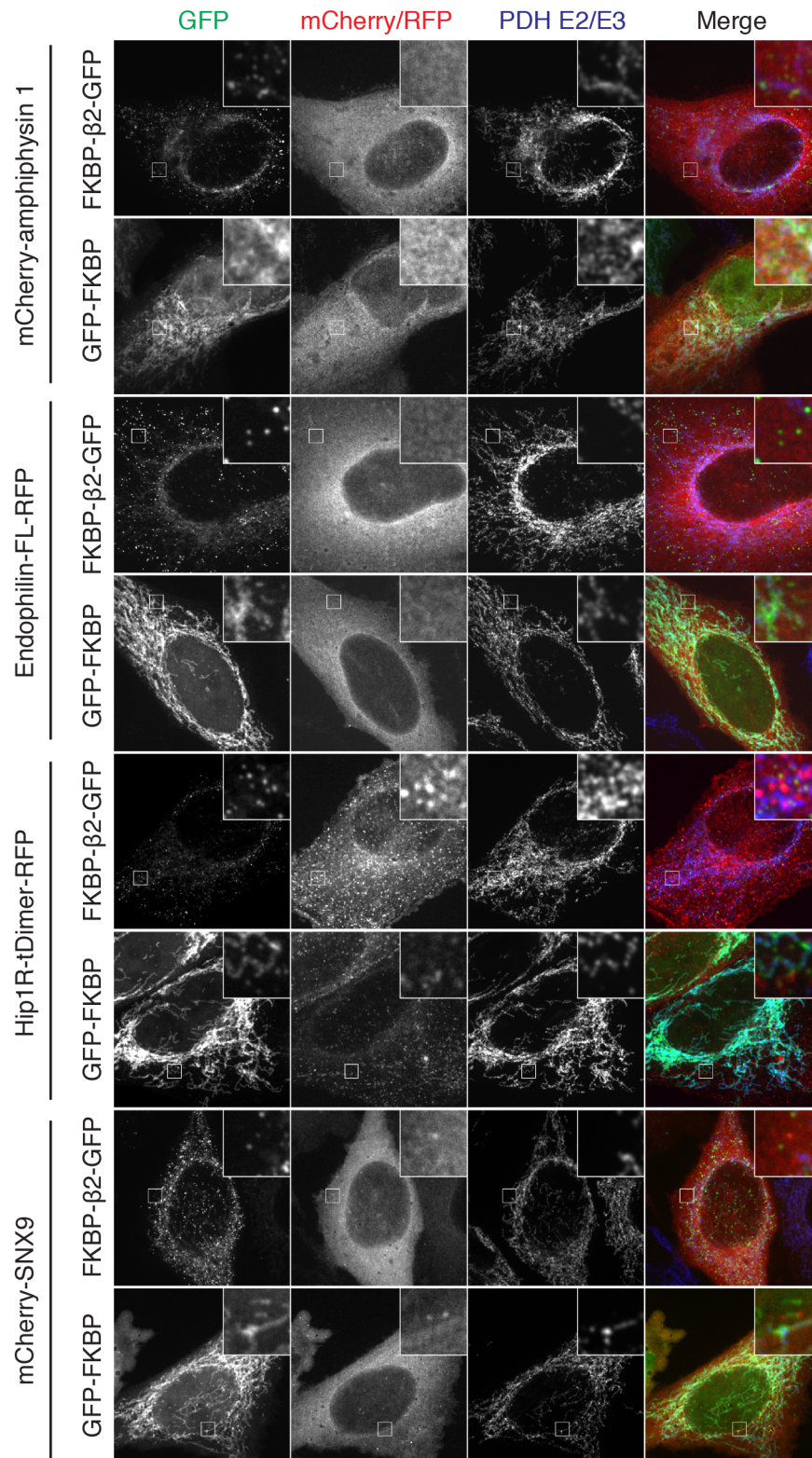


Figure 3.13: CME accessory proteins, amphiphysin 1, endophilin, Hip1R and SNX9 do not colocalise with mitoPits. Representative confocal micrographs of HeLa cells expressing mCherry-amphiphysin 1, Endophilin-FL-RFP, Hip1R-tDimer-RFP or mCherry-SNX9 together with WT hook, FKBP- β 2-GFP or negative control GFP-FKBP, stained with anti-PDHE2/E3, mitochondrial matrix marker and IgG Alexa Fluor 647. All cells were treated with 200 nM rapamycin. Inset: 5X zoom. Scale bar: 10 μ m.

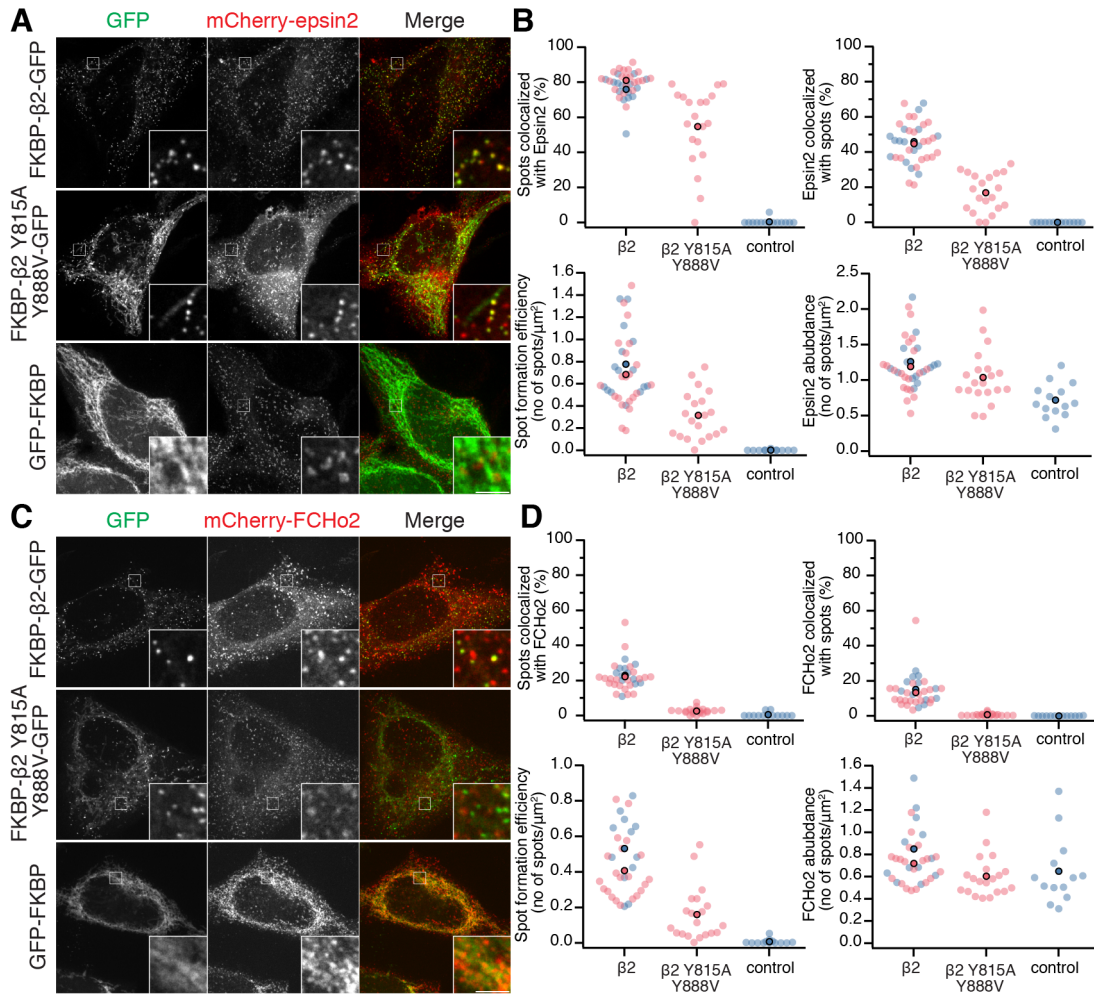


Figure 3.14: Epsin2 and FCHo2 are recruited to mitoPits. Representative confocal micrographs of HeLa cells showing epsin2 (A) and FCHo2 (C) colocalization with mitoPits. Cells expressing dark MitoTrap, WT hook, FKBP- β -GFP or binding deficient mutant, FKBP- β Y815A/Y888V-GFP or negative control GFP-FKBP together with mCherry-epsin2 or mCherry-FCHo2. All cells were treated with 200 nM rapamycin. Inset: 5X zoom. Scale bar: 10 μ m. SuperPlots comparing colocalization of spots with epsin2 (B) or FCHo2 (D) (left top), colocalization of epsin2 or FCHo2 with spots (right top), spot formation efficiency (left bottom) and epsin2 or FCHo2 abundance (right bottom) for each condition. Colours represent replicates. Each faded dot represents a cell, opaque dots represent means of replicates, n=2.

3.8 Initiation, maturation and scission stages of CME are reconstituted at mitochondria

The defining feature of endocytic vesicles is the electron dense clathrin coat structure encapsulating them. We need to ensure that what was observed as the colocalisation of mitoPits and clathrin in figure 3.10 are proper CCVs and not aggregates of clathrin. To do this, I used CLEM and observed the clathrin coat

at the ultrastructural level. First, mitoPit formation upon rapamycin induction in HeLa cells expressing the WT β 2 hook and MitoTrap was visualised live on gridded dishes (Figure 3.15A), then the cells were fixed and processed for TEM. The same cells with mitoPits were found within the resin and sectioned for TEM. As seen in figure 3.15C darker electron-dense coated pits and vesicles with a double membrane were invaginated from the mitochondria. The double membrane structure of mitoPits and mitoPit-derived vesicles (MPDVs) could account for their diameter measuring larger than 100 nm. Moreover, imaging mitoPits under TEM revealed that all stages of CME, initiation, maturation and even scission were reconstituted at the mitochondria via our synthetic CCV formation system (Figure 3.15C). MPDVs that are seen as unattached in 2D TEM images may be attached to the mitochondria in another z-plane. Therefore, I also used live confocal imaging to catch the scission of mitoPits from the mitochondria. In figure 3.16, a HeLa cell expressing the WT β 2 hook, and MitoTrap anchor is shown after rapamycin addition at 8 seconds of recording. At 26 seconds mitoPit formation is clearly visible on the tips, edges and branchpoints of the mitochondria. At 52 seconds, the mitoPit is mature enough to break off of the mitochondria, and between 54-62 seconds the pinched off mitoPit can be seen to move freely. This observation taken together with the TEM images, shows that mitoPits undergo the same stages as endocytic vesicles: initiation, where the clathrin coat starts to form, maturation of the pit by invagination and scission, budding off the vesicle.

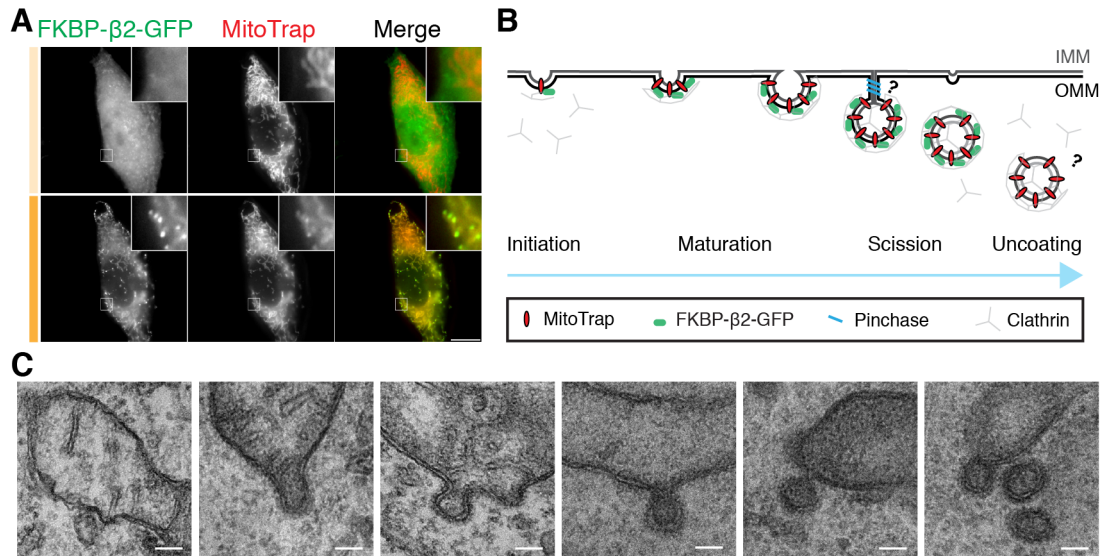


Figure 3.15: Stages of CME reconstituted on mitochondria via inducible CCV formation. (A) HeLa cells expressing FKBP- β 2-GFP and MitoTrap were treated with 200 nM rapamycin (dark orange bar) on gridded dishes, and the same cell was subsequently imaged by TEM. (B) Diagram of inducible CCV formation on mitochondria, adapted from Smith et al. (2021) under Creative Commons Attribution License. (C) Electron micrographs of mitoPits in cells expressing FKBP- β 2-GFP and MitoTrap induced with rapamycin. Scale bar: 100 nm.

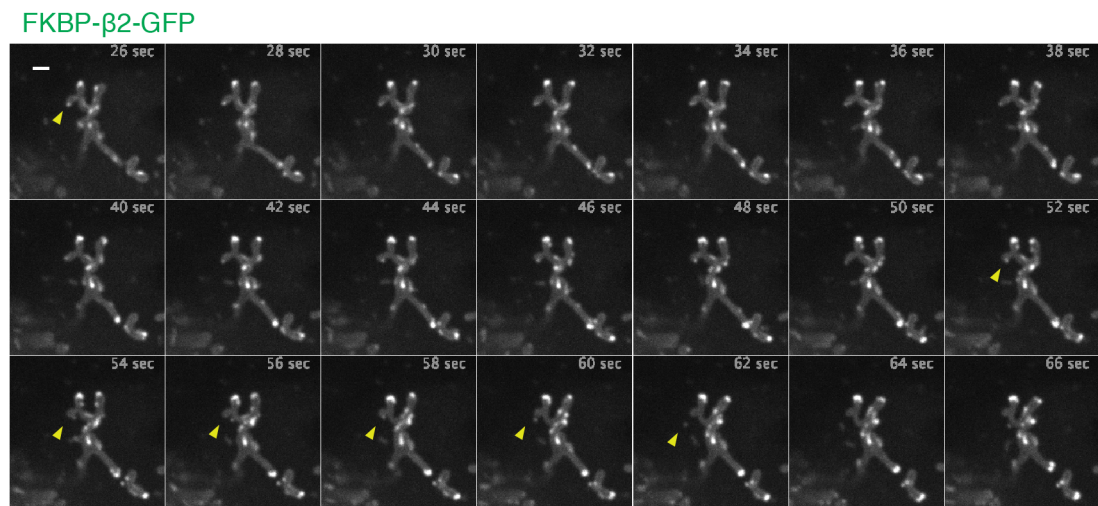


Figure 3.16: mitoPits pinch off from the mitochondria. Time course of representative confocal micrographs showing mitoPits can bud off from mitochondria in HeLa cells expressing FKBP- β 2-GFP and MitoTrap induced with 200 nM rapamycin at 8 sec. Arrows indicate the mitoPit, its pinching off and movement of the MPDV. FKBP- β 2-GFP channel is shown. Scale bar: 1 μ m.

3.9 Discussion

Rerouting the $\beta 2$ clathrin hook to mitochondria, ER, Golgi and lysosome was sufficient to reconstitute intracellular CCPs on these organelles, on-demand. The mitoPits are fully synthetic and were most interesting to study since mitochondria is not a part of canonical membrane trafficking. Given the differences in lipid composition of mitochondrial membranes to plasma membrane, especially how little PI(4,5)P₂ there is, phospholipid composition may not be critical for CCV formation.

The mitoPit formation is driven by clathrin. This is demonstrated by the absence of mitoPits when the clathrin-binding deficient $\beta 2$ hook was used, and when CHC was downregulated by siRNA. Moreover, colocalisation of clathrin with mitoPits showed the involvement of clathrin in the formation of intracellular synthetic CCPs. Also, the mitoPit formation was initiated with other hooks that effectively bind clathrin such as $\beta 1$, epsin and AP180. The WT $\beta 2$ hook and clathrin-binding deficient one are identical except the ability to bind clathrin suggesting that membrane bending is not driven by liquid-liquid condensates (Yuan et al. 2021), but depends on clathrin presence at the pits. It was also evident that the TM clustering is not the cause of mitoPit formation. Lack of colocalisation between mitoPits and the σ subunits of AP-1, AP-2 and AP-3 underline that clathrin recruitment is driven by the hook alone, and the mitoPits do not form due to the presence of any other endogenous adaptor protein complexes and their formation is at sites normally devoid of CCPs. The TEM imaging not only demonstrated the electron-dense clathrin-coat on the mitoPits at ultrastructural level, but also revealed that stages of CME are reconstituted at the mitochondria implying that enough force is generated by our synthetic system to deform both the inner and outer mitochondrial membranes and even to pinch off the mitoPits.

With our synthetic CCP system, mitoPits started forming seconds after the rapamycin induction. They were enclosed by the WT $\beta 2$ hook which was preceded by the MitoTrap. Yet, no mitochondrial matrix was observed. MitoPits might include a low concentration of matrix that is impossible to visualise due to the resolution limit of confocal microscopy. MitoPits were also found to favour forming on surfaces with higher curvature suggesting that clathrin might have a

higher affinity for curved membranes, supporting the constant-curvature model for membrane bending during CME. The mitoPit formation efficiency was higher when endocytic clathrin hooks, AP180 being the top performer possibly due to its multiple clathrin binding sites (Morgan et al. 2000). On the other hand, our results suggests that even though the $\beta 3$ hinge and appendage domains carry clathrin binding sites (Dell'Angelica et al. 1998), they may not be interacting with clathrin effectively, as no mitoPits were formed with the $\beta 3$ intracellular hook. This was in line with the previous work in the lab, which has shown that a $\beta 3$ hook was not able to induce synthetic CME on the plasma membrane either (Wood et al. 2017), emphasising the requirement for functional interactions between the hook and clathrin for on-demand CCV formation. Out of six proteins involved in CME only two, epsin and FCHo2, were found to colocalise with mitoPits. The recruitment of epsin to our mitoPits was much potent than FCHo2 as epsin was shown to be recruited to the mitoPits via binding to both clathrin and WT $\beta 2$ hook which is in line with the literature (Owen et al. 2000; Drake et al. 2000). FCHo2 lacks the CBM and has not been shown to interact with WT $\beta 2$ hook before, thus could have been recruited indirectly via an unknown binding partner of $\beta 2$ which is also supported by the fact that FCHo2 recruitment is less compared to epsin.

Chapter 4

MitoPits do not require a scission molecule for budding

4.1 Introduction

I have shown successful reconstitution of clathrin-coated vesicle formation at the mitochondria in Chapter 3 and revealed that the mitoPits are pinched off from the mitochondrial outer membrane via electron microscopy and live imaging. Moreover, approximately 20% of the spots observed upon rapamycin induction were completely detached from the organelle. Yet the mechanism of pinching off is unknown. Thus, the aim of this chapter is to elucidate the scission mechanism of MPDVs.

A limited number of proteins have the potential to cause scission of MPDVs. These candidates are: dynamin, the pinchase in endocytosis; Drp-1, the mitochondrial fission factor; Vps4a, protein involved in opposite topology scission; and actin, via an indirect activity. Therefore, we aimed to investigate whether any of these proteins are involved in MPDV scission.

4.2 Dynamin is not involved in budding of mitoPits

Dynamin constricts at the neck of CCPs and facilitates their scission from the plasma membrane during CME; therefore, it is the primary pinchase candidate

for mitoPits. We hypothesised that if dynamin catalyses MPDV formation from the mitochondrial outer membrane, there will be a smaller number of MPDVs when dynamin function is disrupted or inhibited. I used three strategies to inhibit dynamin function: mutation, chemical inhibition and conditional knockout.

To disrupt the function of dynamin, dominant-negative mutant Dyn1 K44A was overexpressed in HeLa cells that are also expressing WT β 2 hook and dark MitoTrap anchor, and compared to no co-expression of dynamin and overexpression of dynamin WT. MitoPit formation was induced by rapamycin treatment. When overexpressed, Dyn1 K44A-mCherry accumulated on CME sites on the plasma membrane, blocking the endogenous CCP internalisation. (Figure 4.1A). This was in line with classic work showing that this well-established dominant-negative mutant of dynamin causes inhibition of transferrin uptake (Blick et al. 1993). If dynamin is the pinchase for mitoPits, there should be almost no MPDVs in Dyn1 K44A-mCherry overexpressed cells and more MPDVs in Dyn1 WT-mCherry overexpressed cells. To test this, the percentage of free spots (MPDVs) was calculated for each condition by subtracting the number of attached spots, mitoPits, from the total number of spots in the cell (Figure 4.1B). The percentage of MPDVs was the same in the WT dynamin overexpressed and the dominant negative dynamin overexpressed cells compared to control, suggesting that dynamin is not involved in the scission of mitoPits.

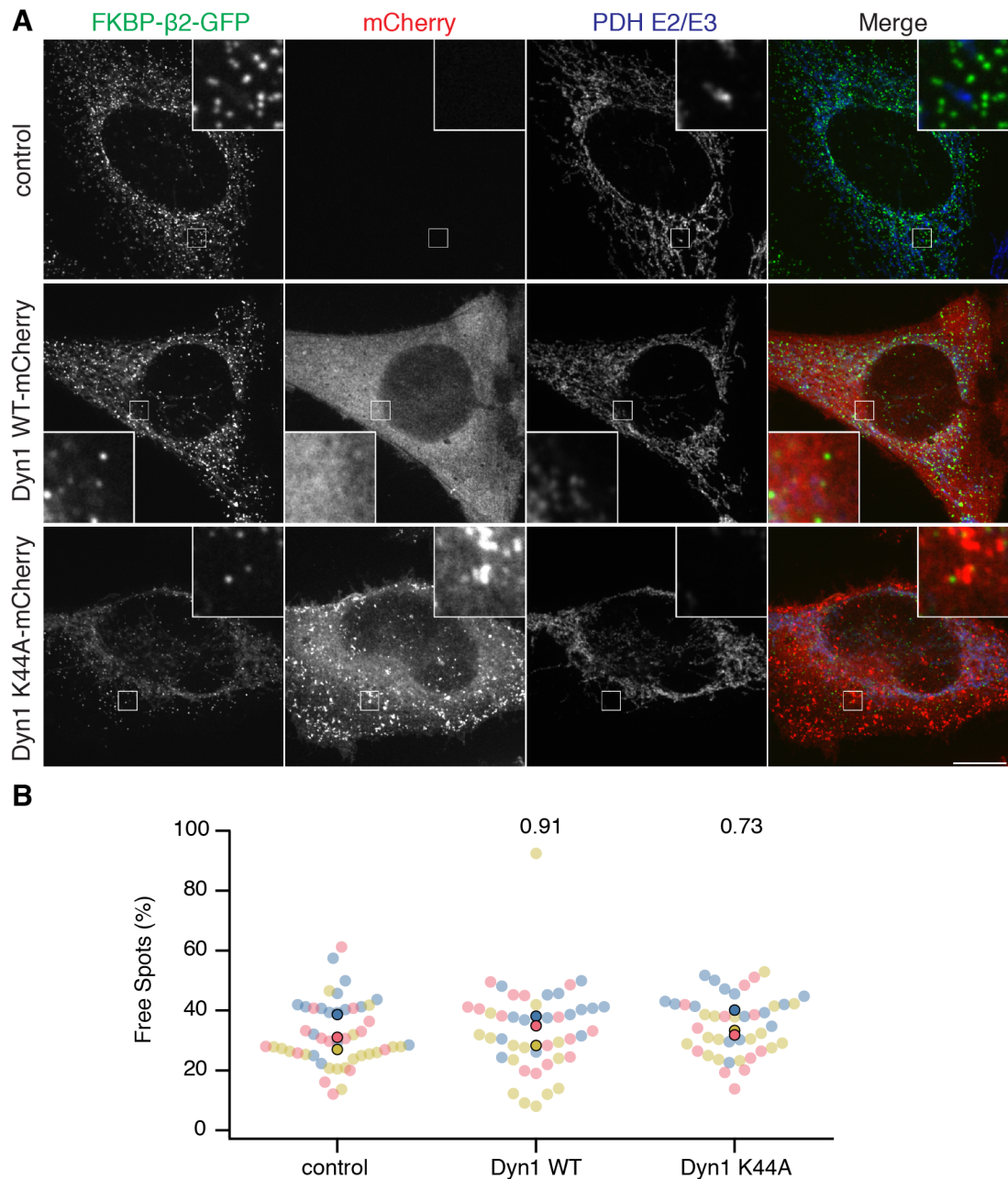


Figure 4.1: Disruption of dynamin function by expressing a dominant-negative mutant does not change the ratio of free spots. (A) Representative confocal micrographs of HeLa cells expressing dark MitoTrap, FKBP- β 2-GFP alone or in combination with either Dyn1 WT-mCherry WT or Dyn1 K44A-mCherry. All cells were treated with 200 nM rapamycin for 30 min, fixed and stained with anti-PDHE2/E3, mitochondrial matrix marker and IgG Alexa Fluor 647. Insets (5X) showing free spots, pinched off from mitochondria. Scale bar: 10 μ m. (B) SuperPlot showing the percentage of free spots for each condition. Colours represent replicates. Each faded dot represents a cell, opaque dots represent means of replicates, n=3. P-values from Dunnett's post-hoc comparison.

Another well established strategy to disrupt dynamin function is the usage of chemical compounds that directly inhibit dynamin. Next, we aimed to inhibit endogenous dynamin using a dynamin 1 and 2 inhibitor, Dynole 34-2. The dose-response relationship between Dynole 34-2 and the mitoPit-forming cells was determined first, by treating the cells with increasing amounts of the inhibitor and analysing the CME inhibition via imaging transferrin uptake. 30 μM Dynole 34-2 was sufficient to fully inhibit CME without damaging mitochondrial morphology as seen in transferrin and PDHE2/E3 channels, respectively (Figure 4.2).

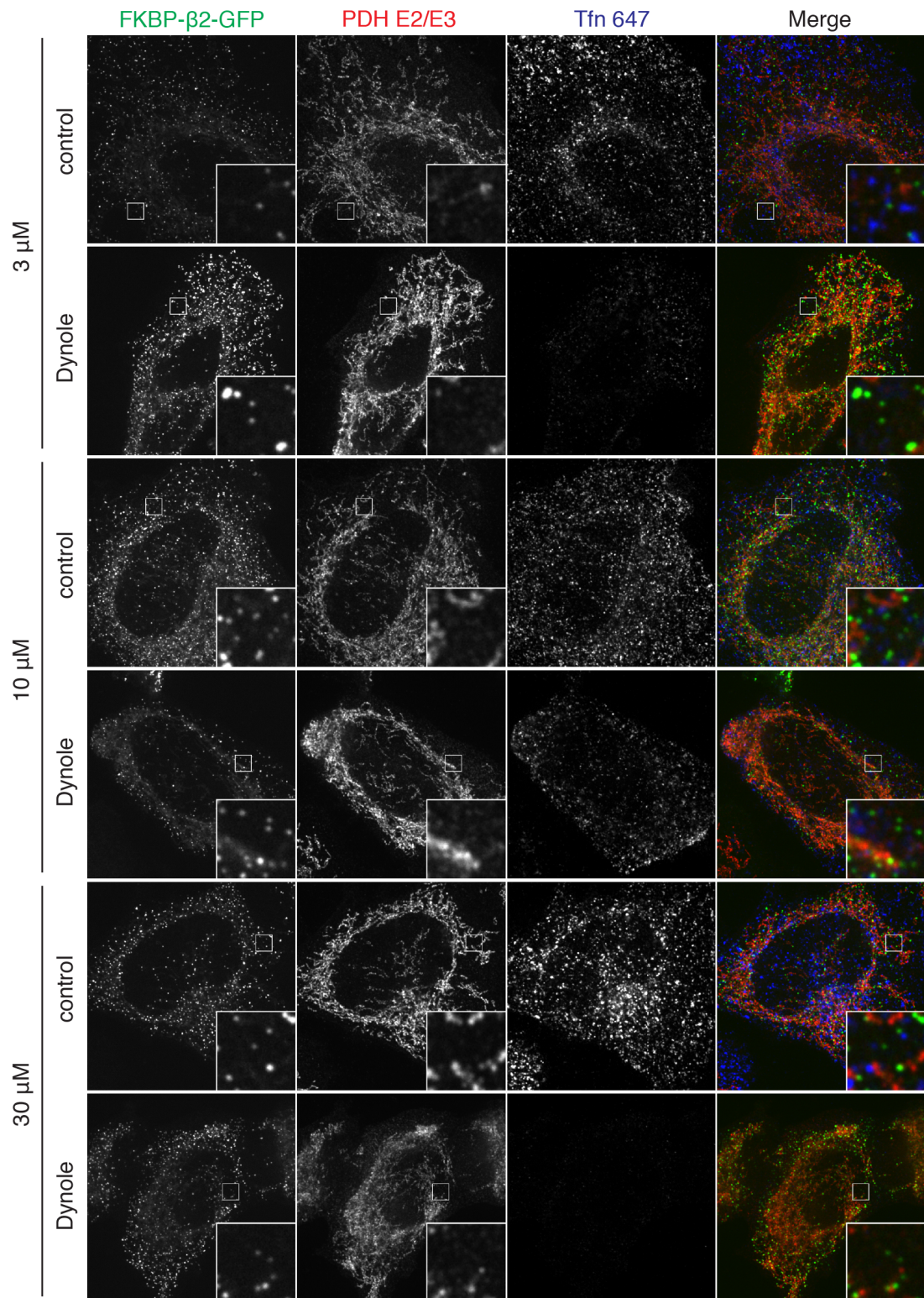


Figure 4.2: 30 μM Dynole is sufficient to inhibit dynamin activity in endocytosis. Representative confocal micrographs of transferrin uptake in HeLa cells expressing dark MitoTrap and FKBP-β2-GFP, treated with 3 μM, 10 μM, 30 μM control (Dynole 31-2) or Dynole 34-2 for 25 min and with 200 nM rapamycin for the last 10 min of incubation. Alexa 647 conjugated human transferrin (Tfn 647) indicates endocytic vesicles. Mitochondrial matrix stained with anti-PDHE2/E3 and IgG Alexa Fluor 568. Inset: 5X zoom. Scale bar: 10 μm.

Next, HeLa cells expressing WT $\beta 2$ hook and dark MitoTrap anchor were treated with 30 μM Dynole 34-2 prior to and during mitoPit formation with rapamycin induction. Lack of transferrin uptake in Dynole 34-2 treated cells demonstrated that dynamin inhibition was successful; however MPDVs were still observed in dynamin inhibited cells (Figure 4.3A). The fraction of MPDVs in the whole spot population was no different between Dynole 34-2 treated cells and control (Figure 4.3B), which suggests that chemical inhibition of dynamin that is sufficient to inhibit CME, does not inhibit the scission of mitoPits from the mitochondria.

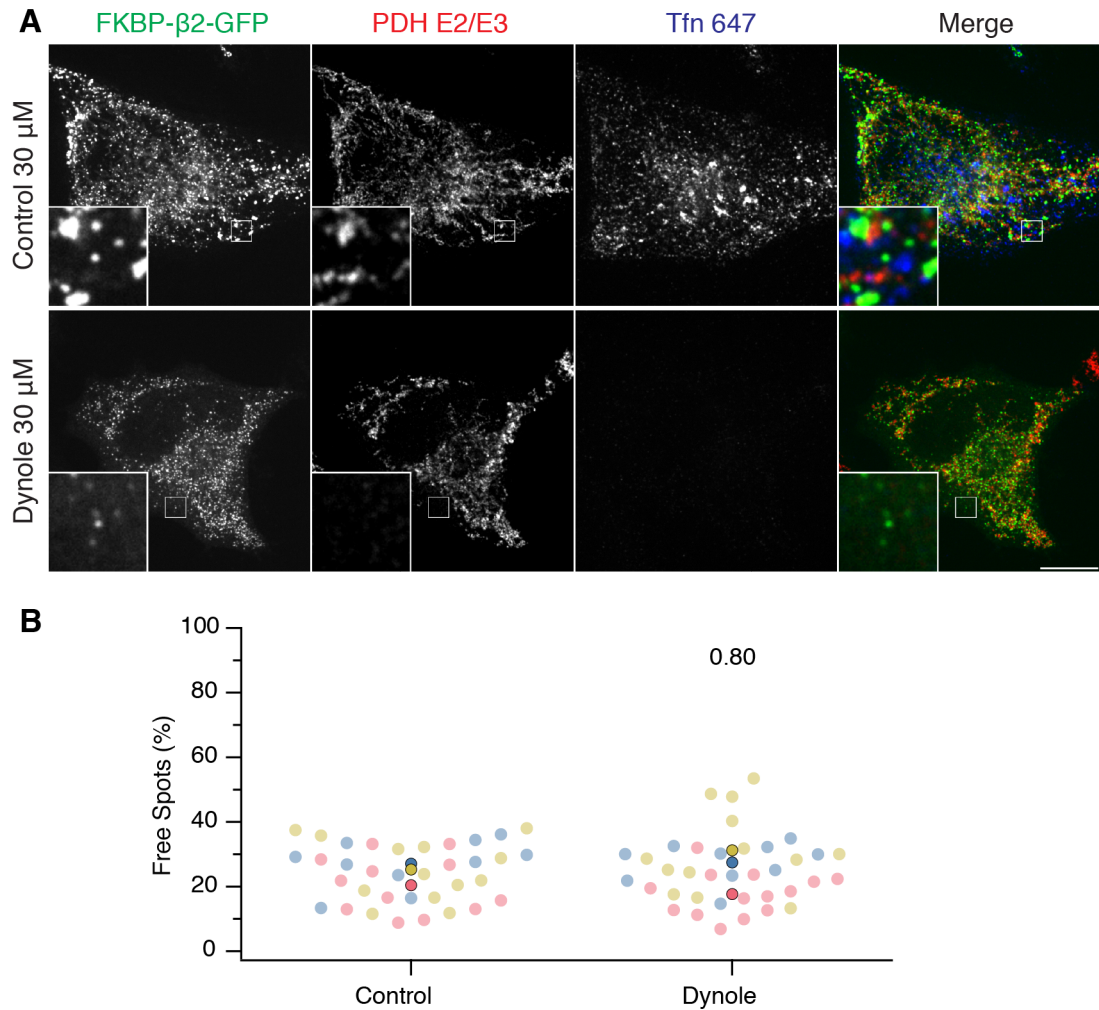


Figure 4.3: Inhibition of dynamin with Dynole does not affect the ratio of free spots at mitochondria. (A) Representative confocal micrographs of HeLa cells expressing dark MitoTrap and FKBP- β 2-GFP, treated with 30 μ M control (Dynole 31-2) or Dynole 34-2 for 25 min and with 200 nM rapamycin for the last 10 min of incubation. Alexa 647 conjugated human transferrin (Tfn 647) indicates endocytic vesicles. Mitochondrial matrix stained with anti-PDHE2/E3 and IgG Alexa Fluor 568. Insets (5X) showing free spots, pinched off from mitochondria. Scale bar: 10 μ m. (B) SuperPlot showing the percentage of free spots for each condition. Colours represent replicates. Each faded dot represents a cell, opaque dots represent means of replicates, n=3. P-value from Student's t-test.

Having found no effect on scission of mitoPits via overexpression of the dominant negative K44A mutant or treatment with Dynole 34-2, we questioned whether our synthetic system itself simply bypasses dynamin. Therefore, I looked at the requirement of dynamin for hot-wired CME. Hot-wired endocytosis on the plasma membrane was induced with rapamycin in HeLa cells expressing WT β 2 hook and dark CD8 anchor and treated with Dynole 34-2. Enlarged CME sites

on the plasma membrane was observed in Dynole 34-2 treated cells compared to control (Figure 4.4A), and this was quantified by measuring the total spot area per cell. Dynole 34-2 treated cells not only had larger spots, but also had fewer number of CME sites compared to control (Figure 4.4B) suggesting that dynamin is the pinchase for hot-wired CME. Hence it can be concluded that the lack of effect of dynamin inhibition in mitoPit fission is not caused by our synthetic induction system itself bypassing dynamin.

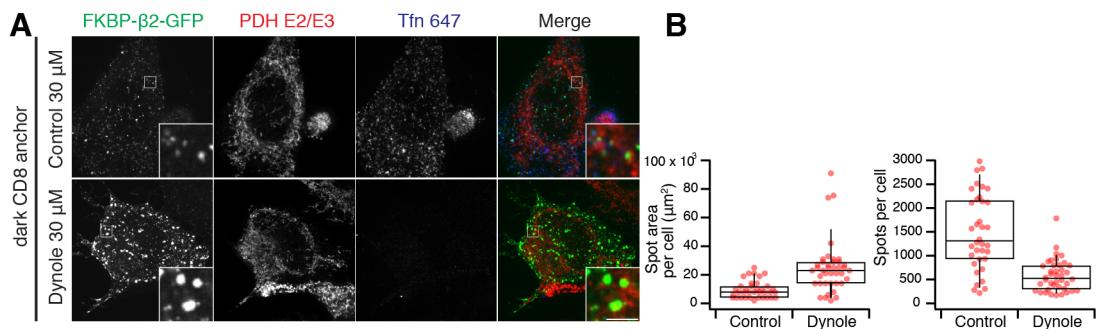


Figure 4.4: Inhibition of dynamin with Dynole affects the size and number of hot-wired CCVs. (A) Representative confocal micrographs of HeLa cells expressing dark CD8 anchor and FKBP-β2-GFP, treated with 30 μM control (Dynole 31-2) or Dynole 34-2 for 25 min and with 200 nM rapamycin for the last 10 min of incubation. Alexa 647 conjugated human transferrin (Tfn 647) indicates endocytic vesicles. Mitochondrial matrix stained with anti-PDHE2/E3 and IgG Alexa Fluor 568. Insets (5X) showing enlarged hot-wired plasma membrane spots. Scale bar: 10 μm. (B) Scatter dot plot comparing the total spot area per cell (left) and number of spots per cell between control and Dynole (right). Each dot is a cell, box plots are median, IQR, 9th and 91st percentile, n=3.

Dynamin has three isoforms; therefore, redundancy might be a confounding factor when inhibiting dynamin for example by overexpression of dynamin 1 K44A. To circumvent this issue, I used a DNM TKO cell line, to investigate whether dynamin has a scission function in MPDV formation (Ferguson, Raimondi, et al. 2009; Park et al. 2013). Conditional knockout of dynamin 1, 2 and 3 was induced in mouse fibroblasts by treating them with 3 μM Tamoxifen for 2 days prior to transfection with WT β2 hook and dark MitoTrap anchor. MPDV formation was induced with rapamycin in both control and Tamoxifen treated cells. Free spots were observed in Tamoxifen treated cells (Figure 4.5A), and there was no significant difference in percentage of MPDVs formed between the

control and Tamoxifen treated cells (Figure 4.5B). Transferrin uptake was performed alongside to assess if endogenous CME was inhibited in Tamoxifen treated cells. Compared to the control, Tamoxifen treated cells showed no transferrin uptake confirming the depletion of dynamin isoforms (Figure 4.5A). Together the results show that overexpression of dominant negative dynamin, chemical inhibition by Dynole and depletion of all three isoforms of dynamin with conditional knockout did not affect percentage of free spots pinched off of mitochondria, even though all the dynamin inhibition methods were sufficient to inhibit endogenous CME or hot-wired CME. To conclude our results suggests that dynamin may not be responsible for scission of mitoPits.

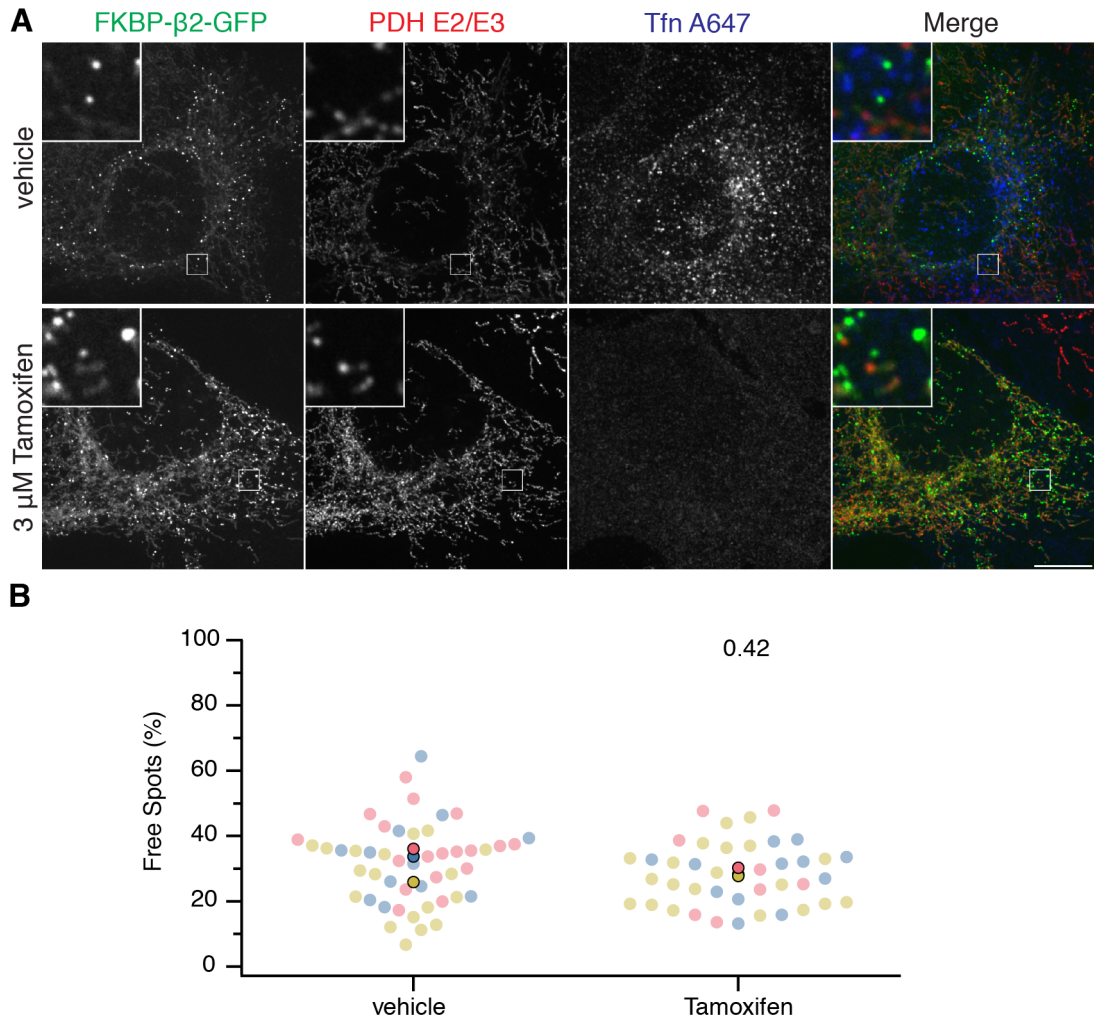


Figure 4.5: Depletion of all three dynamin isoforms does not change the ratio of free spots. (A) Representative confocal micrographs of transferrin uptake in dynamin triple knock-out mouse fibroblasts expressing dark MitoTrap and FKBP- β 2-GFP, treated with vehicle (EtOH) or 3 μ M Tamoxifen for 2 days prior to transfection for dynamin depletion and with 200 nM rapamycin for 10 min for CCP induction. Alexa 647 conjugated human transferrin (Tfn 647) indicates endocytic vesicles. Mitochondrial matrix stained with anti-PDHE2/E3 and IgG Alexa Fluor 568. Inset: 5X zoom. Scale bar: 10 μ m. (B) SuperPlot showing the percentage of free spots for each condition. Colours represent replicates. Each faded dot represents a cell, opaque dots represent means of replicates, n=3. P-value from Student's t-test.

4.3 Drp1 is not responsible for pinching off of the mitoPits

Drp1 has high homology with dynamin and is abundant in the vicinity of MPDV formation as it is the mitochondrial fission factor. Thus we hypothesised that it could be the pinchase for MPDV scission. MitoPit formation was induced by

rapamycin addition in HeLa cells expressing an mCherry tagged WT Drp1 or dominant negative version (mCherry-Drp1 K38A) together with WT β 2 hook and dark MitoTrap anchor. Overexpression of WT Drp1 and Drp1 K38A resulted in fragmented and hyperfused mitochondria respectively, demonstrating that the mutant worked as expected and that Drp1 has a role in mitochondrial fission (Figure 4.6A). If Drp1 is responsible for budding the MPDVs, it should be expected to see almost no free spots in mCherry-Drp1 K38A overexpressed cells; however, as seen in figure 4.6B, the percentage of MPDVs was similar to the control. In fact, I measured a small *increase* in the ratio of MPDVs in Drp1 WT expressing cells that is statistically significant. This can be explained by excess fragmentation of mitochondria due to overexpression of WT Drp1, since I showed in Chapter 3 that mitoPits form preferentially at nodes and there are simply more mitochondrial nodes with increased fission. However, the result that there is no difference between the dominant-negative mutant and control suggests that Drp1 is not involved in budding of mitoPits.

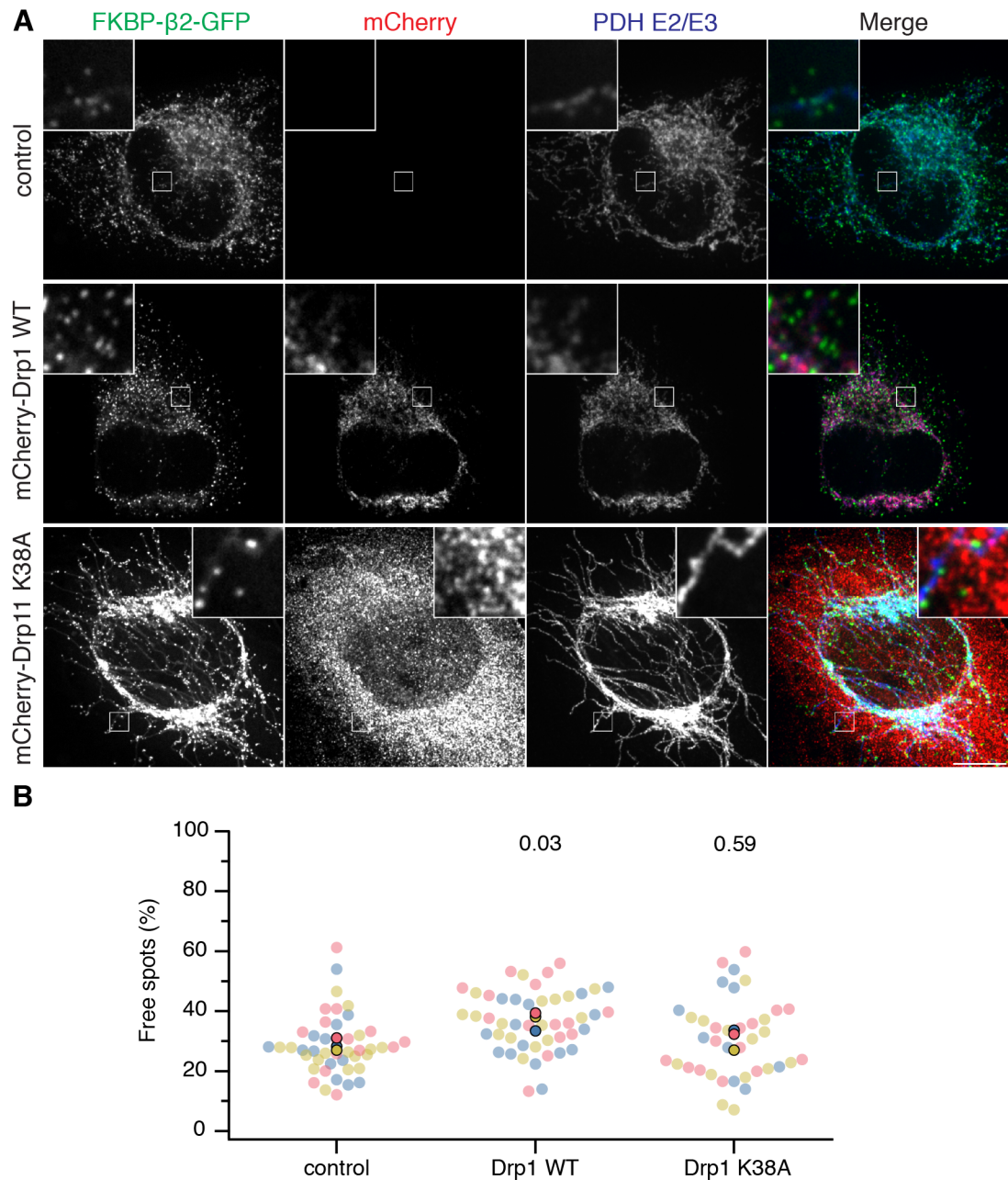


Figure 4.6: Disruption of Drp1 function by expressing a dominant-negative mutant does not change the ratio of free spots. (A) Representative confocal micrographs of HeLa cells expressing dark MitoTrap, FKBP- β 2-GFP alone or in combination with either mCherry-Drp1 WT or mCherry-Drp1 K38A. All cells were treated with 200 nM rapamycin for 30 min, fixed and stained with anti-PDH E2/E3, mitochondrial matrix marker and IgG Alexa Fluor 647. Insets (5X) showing free spots, pinched off from mitochondria. Scale bar: 10 μ m. (B) SuperPlot showing the percentage of free spots for each condition. Colours represent replicates. Each faded dot represents a cell, opaque dots represent means of replicates, n=3. P-values from Dunnett's post-hoc comparison.

4.4 Vps4a do not have a role in MPDV formation

Vps4a is an AAA-ATPase involved in membrane fission of intraluminal vesicles at multivesicular bodies and was thus selected as our next pinchase candidate. Similar to the approach taken with dynamin and Drp1, WT Vps4a and the dominant negative form, Vps4a E228Q, was tagged with mCherry and overexpressed in HeLa cells also expressing WT β 2 hook and dark MitoTrap anchor. The formation of the mitoPits was induced by rapamycin treatment. Overexpressed mCherry-Vps4a E228Q localised to enlarged endosomes, demonstrating the loss of function; however, MPDVs were still present in the cell (Figure 4.7A). Quantification of the percentage of MDPVs by free spot analysis showed that their ratio had not changed when WT Vps4a was overexpressed. Moreover, no decrease in the percentage of free spots was observed upon Vps4a E228Q overexpression (Figure 4.7B), suggesting that Vps4a is not the pinchase for MPDVs.

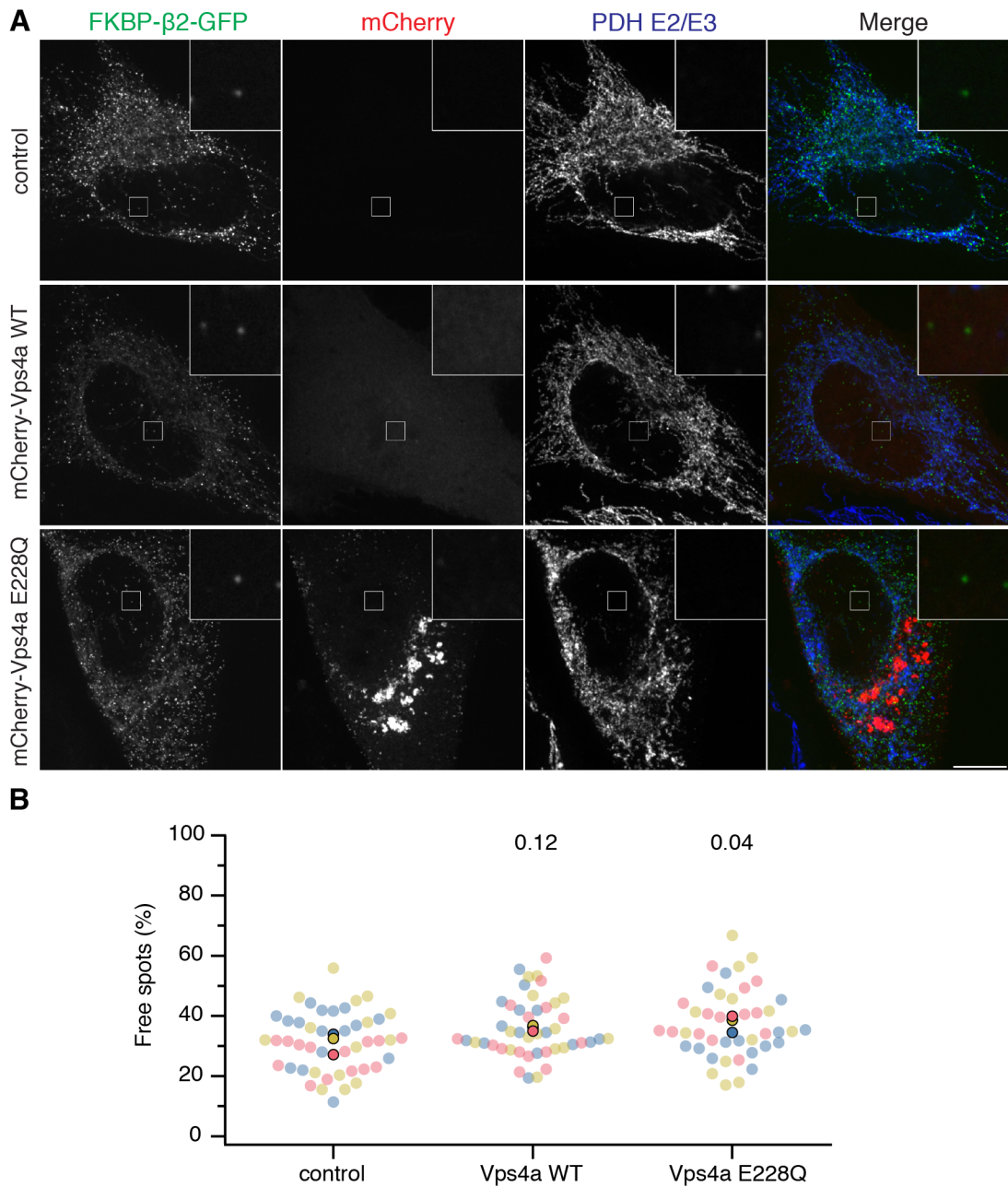


Figure 4.7: Disruption of Vps4a function by expressing a dominant-negative mutant does not decrease the ratio of free spots. (A) Representative confocal micrographs of HeLa cells expressing dark MitoTrap, FKBP- β 2-GFP alone or in combination with either mCherry-Vps4a WT or mCherry-Vps4a E228Q. All cells were treated with 200 nM rapamycin for 30 min, fixed and stained with anti-PDH E2/E3, mitochondrial matrix marker and IgG Alexa Fluor 647. Insets (5X) showing free spots, pinched off from mitochondria. Scale bar: 10 μ m. (B) SuperPlot showing the percentage of free spots for each condition. Colours represent replicates. Each faded dot represents a cell, opaque dots represent means of replicates, n=3. P-values from Dunnett's post-hoc comparison.

4.5 Actin is not involved in budding of mitoPits

It was previously reported that actin is important for endocytosis in systems where membrane tension is high (Aghamohammadzadeh et al. 2009; Boulant et al. 2011; Kaur et al. 2014). Although we do not know the tension at the mitoPits, the invagination of a double membrane may be increasing the membrane tension. Thus we hypothesised that actin might be recruited to mitoPits to facilitate pit closure hence assist pinching off. In order to test this, actin polymerisation was inhibited using Latrunculin B (Lat B), a toxin from *Latruncula magnifica*. First, the dose of Lat B that causes sufficient actin depolymerisation without affecting mitochondrial morphology was determined in HeLa cells expressing the dark MitoTrap and the WT $\beta 2$ hook induced with rapamycin to form mitoPits. A dosage of $1 \mu\text{M}$ for 25 min was shown to be the highest dose that is harmless to mitochondrial morphology and effective in disrupting the actin filaments at the same time (Figure 4.8). Then, to determine if actin is involved in mitoPit budding, free spot analysis was performed on HeLa cells expressing the dark MitoTrap and WT $\beta 2$ hook treated with $1 \mu\text{M}$ LatB for 25 min, with addition of 200 nM rapamycin at the last 10 min for induction of mitoPit formation (Figure 4.9). When actin was depolymerised, pinched off mitoPits were still present in the cell (Figure 4.9A), and the percentage of free spots was no different from the control (Figure 4.9B). Surprisingly, the depolymerised actin structure did not affect mitoPit formation suggesting that invagination is not disrupted in the absence of actin fibers. Since budding of mitoPits persisted under conditions of no filamentous actin, these results demonstrate that actin does not have a role in mitoPit scission nor any influence on mitoPit formation.

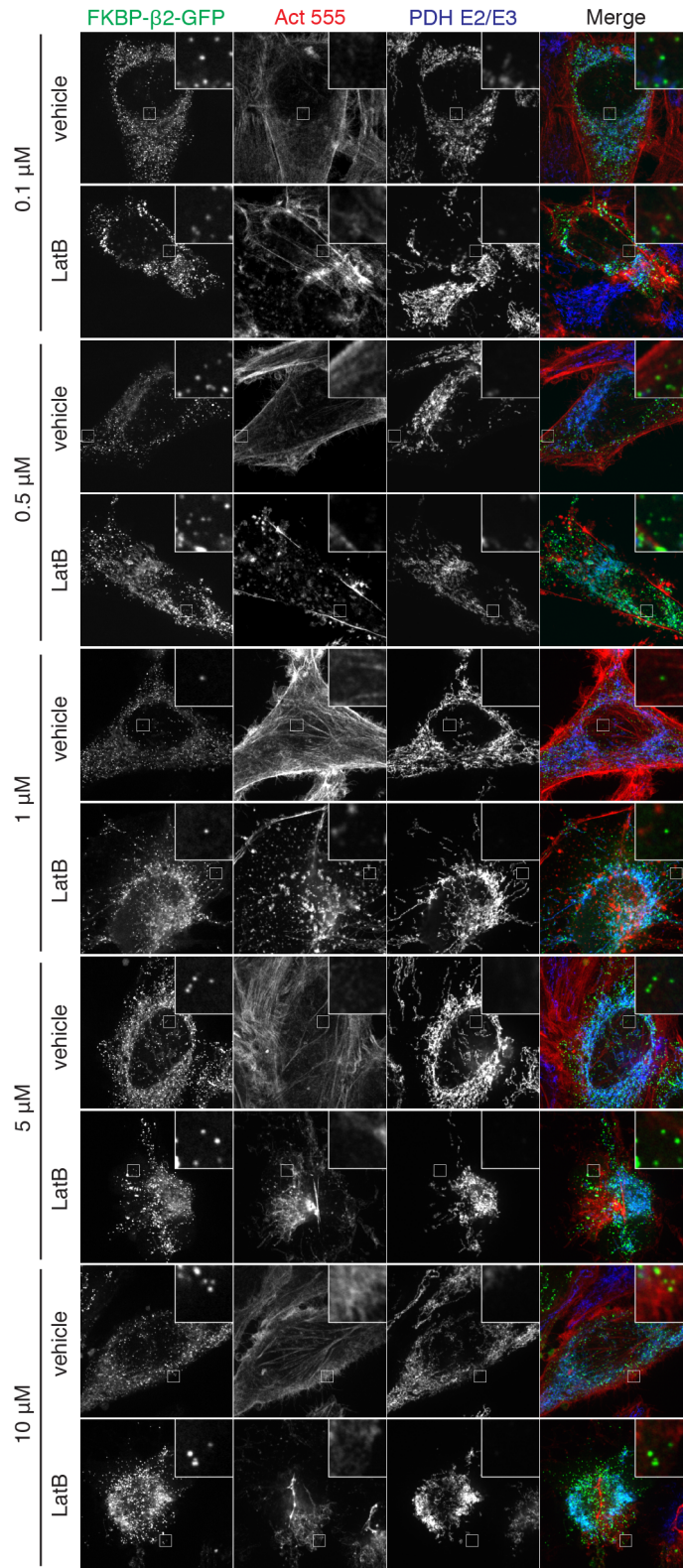


Figure 4.8: 1 μM Latrunculin B is sufficient for actin depolymerisation. Representative confocal micrographs of HeLa cells expressing dark MitoTrap and FKBP- β 2-GFP, treated with vehicle (DMSO) or 0.1 μM , 0.5 μM , 1 μM , 5 μM , 10 μM Latrunculin B for 25 min and with 200 nM rapamycin for last 10 min of incubation. Cells were stained with Act 555, actin marker and anti-PDHE2/E3, mitochondrial matrix marker, IgG Alexa Fluor 647. Inset: 5X zoom. Scale bar: 10 μm .

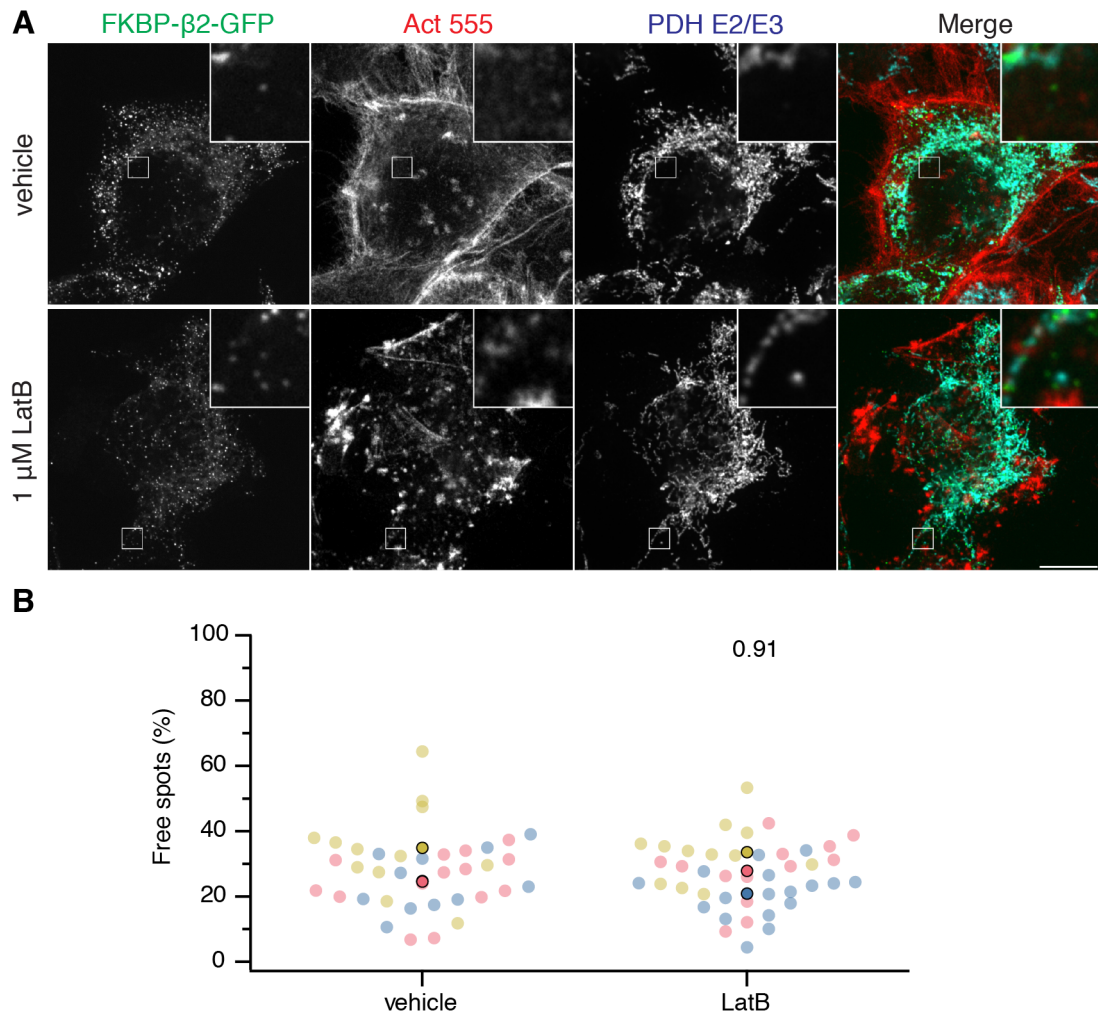


Figure 4.9: Actin depolymerization does not change the ratio of free spots. Representative confocal micrographs of HeLa cells expressing dark MitoTrap and FKBP- β 2-GFP, treated with vehicle (DMSO) or 1 μ M Latrunculin B for 25 min and with 200 nM rapamycin for the last 10 min of incubation. Cells were stained with Act 555, actin marker and anti-PDHE2/E3, mitochondrial matrix marker, IgG Alexa Fluor 647. Inset: 5X zoom. Scale bar: 10 μ m. (B) SuperPlot showing the percentage of free spots for each condition. Colours represent replicates. Each faded dot represents a cell, opaque dots represent means of replicates, n=3. P-value from Student's t-test.

4.6 Discussion

Four candidates – the endocytic pinchase, dynamin; the mitochondrial fission factor, Drp1; an endosomal pinchase, Vps4a; the endocytic scission molecule in yeast, actin – that might be responsible for scission of mitoPits from mitochondria were tested using variety of approaches including overexpression of dominant-negative mutant forms, chemical inhibition and conditional knockout. The amount of

MPDVs, spots detached from mitochondria, was quantified by a method where spots attached to mitochondria, mitoPits, were determined by the presence of mitochondrial marker, and counted. Then, the number of MPDVs were subtracted from the total number of spots in the cell. If there was any inhibition of scission, the percentage of the MPDVs within the total number of spots should have dropped significantly as more mitoPits would accumulate on the mitochondria. This was not observed with any of the candidates, which suggests that none of them are involved in mitoPit scission.

The quantification method relies on the fact that mitoPits and MPDVs are coated with the GFP-tagged clathrin hook anchored by MitoTrap. There is a possibility that other small, similarly-sized mitochondrial structures could be coated with the hook and misidentified as MPDVs. However, fragmented mitochondria are much larger than mitoPits, so they would not be included in our detection threshold of 135 nm. Another potential confounding factor are endogenous MDVs, which could fit the size scale. However, occurrence of MDVs is very rare with only 5-7 MDVs per cell on average (Neuspiel et al. 2008), whereas with our synthetic system creates hundreds of MPDVs per cell. Thus, even if MDVs were counted in our quantification, they would not affect the results significantly.

The method of quantification developed here to determine pinched off vesicles from pits is useful for the study of intracellular vesicle formation. It is not possible to use this method with synthetic, or endogenous, CME because the plasma membrane cannot easily be separated from the cell interior by marker staining. However, CME does not require this method because antibody-feeding experiments can be used to visualise and quantify the internalised vesicles (Wood et al. 2017). Intracellular clathrin-mediated vesicle formation on the other hand is inaccessible from outside of the cell, and requires this method to classify the vesicles that are formed. Therefore, our method of creating synthetic intracellular CCVs with trackable clathrin hooks and spatially quantifying them within the cell is a valuable tool to study intracellular clathrin-mediated vesicle formation dynamics.

MitoPit scission was shown not to be affected by inhibition of any of the candidate scission molecules suggesting synthetic intracellular CCVs might not

require a facilitator or pinchase, and that the clathrin cage might be sufficient for budding of the mitoPits from the mitochondria. GTP hydrolysing scission molecules may not be essential for intracellular budding events generally, which is evidenced by other studies for the scission of COPI- and COPII-coated vesicles (Adolf, Herrmann, et al. 2013) and endogenous mitochondrial vesicle budding (Neuspiel et al. 2008; Soubannier, McLelland, et al. 2012; Soubannier, Rippstein, et al. 2012). Finally, these results suggest that requirement of a scission molecule for CCV budding might be exclusive to plasma membrane.

Chapter 5

Discussion

This thesis shows that clathrin-coated vesicles can be formed on-demand at various intracellular membranes using minimal molecular machinery: a clathrin hook and a membrane-specific anchor. Rerouting of $\beta 2$ hinge and appendage domains containing two clathrin-binding regions to target intracellular membranes was sufficient to induce CCP formation. Clathrin recruitment with a potent hook is crucial for initiation. Endocytic clathrin hooks performed better than intracellular hooks, suggesting endocytosis might require a more robust clathrin recruitment than intracellular CCV trafficking.

Initiation, maturation and scission stages of CCV lifecycle are recapitulated at mitochondria following the inducible binding of clathrin hook to the mitochondrial anchor. Our synthetic system is capable of not only deforming both inner and outer membranes of the mitochondria, but also budding off of the mitoPits. It has been shown that intracellular vesicle formation, such as budding of COPI- and COPII-coated vesicles or endogenous mitochondrial vesicles, does not seem to require a scission factor (Adolf, Herrmann, et al. 2013; Neuspiel et al. 2008; Soubannier, McLelland, et al. 2012; Soubannier, Rippstein, et al. 2012). This could be the case for intracellular CCVs generally. Previously, one imaging study has suggested that dynamin is not associated with intracellular CCVs (Kural et al. 2012). In fact, the plasma membrane may even be unique in its requirement for a scission molecule, as CME and some clathrin-independent small scale endocytosis processes all require dynamin for vesicle scission (Mayor et al. 2014).

MitoPits did not recruit the σ subunits of AP-1 and AP-3, nor of AP-2,

suggesting the complexes are not recruited to synthetic intracellular CCP sites, and not needed in mitoPit formation. Mitochondria are not involved in canonical membrane trafficking pathways and endogenous mitochondria-derived vesicles do not have clathrin coats (Sugiura et al. 2014). Therefore, it would be unusual to find any CCV formation machinery in the vicinity of mitochondrial outer membrane, unless they are recruited by our minimal machinery.

The prerequisite of AP-2 binding to PI(4,5)P₂ in endocytic CCV formation is bypassed using minimal machinery which allows on-demand CCP formation at mitochondria. In any case, the outer mitochondrial membrane contains very little PI(4,5)P₂ (Watt et al. 2002). Formation of CCPs on a practically PI(4,5)P₂-free membrane suggests that it is highly unlikely that other factors, which depend on PI(4,5)P₂-binding for their function, would be involved in mitoPit formation. These proteins include accessory factors containing ENTH and BAR domains. Overall, this suggests that phospholipid composition of the membrane might not be essential for CCV formation, at least after the initial clathrin recruitment steps have been bypassed.

Accessory proteins epsin and FCHo2, which are involved in membrane bending during maturation of CCPs in endocytosis, were recruited to mitoPits formed using the endocytic β 2 hook. Epsin was found to be recruited via binding to clathrin and β 2. FCoH2 on the other hand, must be recruited indirectly by a binding partner of β 2. This protein could be Eps15 as that is recruited to CCPs at the same time as FCHo2, and the only protein that interacts with both β 2 and FCHo2 (Taylor, Perrais, et al. 2011). Do mitoPits require epsin and FCHo2 to form, then? MitoPit formation could be also induced using the β 1 subunit of AP-1 as a clathrin hook. Epsin and FCHo2 are not involved in intracellular CCV trafficking and do not bind to the intracellular clathrin adaptor AP-1; therefore it is unlikely that they would contribute to mitoPit formation. Epsin is recruited by clathrin as well, so epsin could colocalise with mitoPits formed with β 1 hook in theory, but it would not mean that it has a crucial role. Curvature-sensing accessory proteins with SH3 domains, amphiphysin, endophilin and SNX9 were absent from mitoPits. They are binding partners of dynamin and have shown to be recruited to mature CCPs briefly during or after scission (Taylor, Perrais, et al.

2011). Multiple SH3 domain binding was shown to be necessary for recruitment and function of dynamin (Rosendale et al. 2019). The lack of accessory proteins with SH3-domains recruited to mitoPits further supports the independence of mitoPit scission from dynamin.

Other components of mitoPits could be identified in the future by modifying the mitoID approach (Gillingham et al. 2019). The $\beta 2$ hook can be tagged by BioID2 which is a promiscuous biotin ligase that would biotinylate proteins in close proximity to the hook, including proteins directly or indirectly interacting with it (Kim et al. 2016). Then the biotinylated proteins can be isolated from the lysate with streptavidin beads, and identified by mass spectrometry. This way it could be possible to identify other accessory proteins that are not tested with colocalisation experiments. What cargoes do MPDVs or other synthetic intracellular CCVs carry? This question can be addressed by using GFP-trap against $\beta 2$ hook to immunoprecipitate the synthetic vesicles. Isolating the MPDVs and synthetic intracellular CCVs derived from ER, Golgi and lysosome this way and analysing their contents via mass spectrometry could identify common components and kind of cargo they carry.

On-demand CCV formation, could have many potential uses in the future. Particular proteins could be packaged into synthetic CCVs and sent to different cellular compartments. These proteins can be intracellular or plasma membrane TM proteins that will act as anchors or ligands of TM receptors. Although, investigation of the fate of MPDVs or other synthetic CCVs in detail is required first, to determine the destination of the cargo. MitoPits are also useful to investigate stages of CCP formation in detail such as examining the factors that contribute to different stages. The “free spot analysis” I developed in this work to identify detached MPDVs can be modified in the future to investigate later stages of CCVs. For example, it could be combined with clathrin colocalisation to identify uncoated MPDVs. MitoPits can be formed in cells that are stained for endogenous clathrin with anti-CHC antibody. After identifying the MPDVs with free spot analysis, their colocalisation with clathrin will reflect the percentage of MPDVs that are still coated, and rest will give the number of uncoated vesicles. This analysis can also be combined with colocalisation with specific endosomal

or lysosomal markers to identify fusion and their fate. Finally, synthetic intracellular CCVs can be a useful tool for developing inhibitors of intracellular CCV formation. It can be used to test their effectiveness similar to how transferrin uptake assay used as a measure of CME.

References

- Adolf, F., A. Herrmann, A. Hellwig, R. Beck, B. Brügger, and F. T. Wieland (2013). “Scission of COPI and COPII vesicles is independent of GTP hydrolysis”. *Traffic (Copenhagen, Denmark)* 14.8, pp. 922–932. DOI: 10.1111/tra.12084.
- Adolf, F., M. Rhiel, B. Hessling, Q. Gao, A. Hellwig, J. Béthune, and F. T. Wieland (2019). “Proteomic Profiling of Mammalian COPII and COPI Vesicles”. *Cell Reports* 26.1, 250–265.e5. DOI: 10.1016/j.celrep.2018.12.041.
- Aghamohammadzadeh, S. and K. R. Ayscough (2009). “Differential requirements for actin during yeast and mammalian endocytosis”. *Nature Cell Biology* 11.8, pp. 1039–1042. DOI: 10.1038/ncb1918.
- Anderson, R. G., M. S. Brown, and J. L. Goldstein (1977). “Role of the coated endocytic vesicle in the uptake of receptor-bound low density lipoprotein in human fibroblasts”. *Cell* 10.3, pp. 351–364. DOI: 10.1016/0092-8674(77)90022-8.
- Antonny, B., C. Burd, P. De Camilli, E. Chen, O. Daumke, K. Faelber, M. Ford, V. A. Frolov, A. Frost, J. E. Hinshaw, T. Kirchhausen, M. M. Kozlov, M. Lenz, H. H. Low, H. McMahon, C. Merrifield, T. D. Pollard, P. J. Robinson, A. Roux, and S. Schmid (2016). “Membrane fission by dynamin: what we know and what we need to know”. *The EMBO journal* 35.21, pp. 2270–2284. DOI: 10.15252/embj.201694613.
- Avinoam, O., M. Schorb, C. J. Beese, J. A. G. Briggs, and M. Kaksonen (2015). “Endocytic sites mature by continuous bending and remodeling of the clathrin coat”. *Science* 348.6241, pp. 1369–1372. DOI: 10.1126/science.aaa9555.
- Ban, T., T. Ishihara, H. Kohno, S. Saita, A. Ichimura, K. Maenaka, T. Oka, K. Mihara, and N. Ishihara (2017). “Molecular basis of selective mitochondrial

- fusion by heterotypic action between OPA1 and cardiolipin”. *Nature Cell Biology* 19.7, pp. 856–863. DOI: 10.1038/ncb3560.
- Blik, A. M. van der, T. E. Redelmeier, H. Damke, E. J. Tisdale, E. M. Meyerowitz, and S. L. Schmid (1993). “Mutations in human dynamin block an intermediate stage in coated vesicle formation”. *Journal of Cell Biology* 122.3, pp. 553–563. DOI: 10.1083/jcb.122.3.553.
- Boulant, S., C. Kural, J.-C. Zeeh, F. Ubelmann, and T. Kirchhausen (2011). “Actin dynamics counteract membrane tension during clathrin-mediated endocytosis”. *Nature Cell Biology* 13.9, pp. 1124–1131. DOI: 10.1038/ncb2307.
- Carreno, S., Å. E. Engqvist-Goldstein, C. X. Zhang, K. L. McDonald, and D. G. Drubin (2004). “Actin dynamics coupled to clathrin-coated vesicle formation at the trans-Golgi network”. *Journal of Cell Biology* 165.6, pp. 781–788. DOI: 10.1083/jcb.200403120.
- Carvajal-Gonzalez, J. M., D. Gravotta, R. Mattera, F. Diaz, A. Perez Bay, A. C. Roman, R. P. Schreiner, R. Thuenauer, J. S. Bonifacino, and E. Rodriguez-Boulan (2012). “Basolateral sorting of the coxsackie and adenovirus receptor through interaction of a canonical YXX Φ motif with the clathrin adaptors AP-1A and AP-1B”. *Proceedings of the National Academy of Sciences of the United States of America* 109.10, pp. 3820–3825. DOI: 10.1073/pnas.1117949109.
- Cereghetti, G. M., A. Stangherlin, O. M. de Brito, C. R. Chang, C. Blackstone, P. Bernardi, and L. Scorrano (2008). “Dephosphorylation by calcineurin regulates translocation of Drp1 to mitochondria”. *Proceedings of the National Academy of Sciences of the United States of America* 105.41, pp. 15803–15808. DOI: 10.1073/pnas.0808249105.
- Cheeseman, L. P., E. F. Harry, A. D. McAinsh, I. A. Prior, and S. J. Royle (2013). “Specific removal of TACC3–ch-TOG–clathrin at metaphase deregulates kinetochore fiber tension”. *Journal of Cell Science* 126.9, pp. 2102–2113. DOI: 10.1242/jcs.124834.
- Chen, J., X. F. Zheng, E. J. Brown, and S. L. Schreiber (1995). “Identification of an 11-kDa FKBP12-rapamycin-binding domain within the 289-kDa FKBP12-rapamycin-associated protein and characterization of a critical ser-

- ine residue”. *Proceedings of the National Academy of Sciences of the United States of America* 92.11, pp. 4947–4951. DOI: 10.1073/pnas.92.11.4947.
- Collawn, J. F., M. Stangel, L. A. Kuhn, V. Esekogwu, S. Q. Jing, I. S. Trowbridge, and J. A. Tainer (1990). “Transferrin receptor internalization sequence YXRF implicates a tight turn as the structural recognition motif for endocytosis”. *Cell* 63.5, pp. 1061–1072. DOI: 10.1016/0092-8674(90)90509-d.
- Collins, B. M., A. J. McCoy, H. M. Kent, P. R. Evans, and D. J. Owen (2002). “Molecular Architecture and Functional Model of the Endocytic AP2 Complex”. *Cell* 109.4, pp. 523–535. DOI: 10.1016/S0092-8674(02)00735-3.
- Damke, H., D. D. Binns, H. Ueda, S. L. Schmid, and T. Baba (2001). “Dynamamin GTPase Domain Mutants Block Endocytic Vesicle Formation at Morphologically Distinct Stages”. *Molecular Biology of the Cell* 12.9, pp. 2578–2589. DOI: 10.1091/mbc.12.9.2578.
- Dannhauser, P. N., M. Platen, H. Böning, H. Ungewickell, I. A. T. Schaap, and E. J. Ungewickell (2015). “Effect of Clathrin Light Chains on the Stiffness of Clathrin Lattices and Membrane Budding”. *Traffic* 16.5, pp. 519–533. DOI: 10.1111/tra.12263.
- Dannhauser, P. N. and E. J. Ungewickell (2012). “Reconstitution of clathrin-coated bud and vesicle formation with minimal components”. *Nature Cell Biology* 14.6, pp. 634–639. DOI: 10.1038/ncb2478.
- Davis, C. G., J. L. Goldstein, T. C. Südhof, R. G. W. Anderson, D. W. Russell, and M. S. Brown (1987). “Acid-dependent ligand dissociation and recycling of LDL receptor mediated by growth factor homology region”. *Nature* 326.6115, pp. 760–765. DOI: 10.1038/326760a0.
- Dell’Angelica, E. C., J. Klumperman, W. Stoorvogel, and J. S. Bonifacino (1998). “Association of the AP-3 Adaptor Complex with Clathrin”. *Science* 280.5362, pp. 431–434. DOI: 10.1126/science.280.5362.431.
- Devos, D., S. Dokudovskaya, F. Alber, R. Williams, B. T. Chait, A. Sali, and M. P. Rout (2004). “Components of Coated Vesicles and Nuclear Pore Complexes Share a Common Molecular Architecture”. *PLoS Biology* 2.12, e380. DOI: 10.1371/journal.pbio.0020380.

- Di Paolo, G. and P. De Camilli (2006). “Phosphoinositides in cell regulation and membrane dynamics”. *Nature* 443.7112, pp. 651–657. DOI: 10.1038/nature05185.
- Doray, B. and S. Kornfeld (2001). “ γ Subunit of the AP-1 Adaptor Complex Binds Clathrin: Implications for Cooperative Binding in Coated Vesicle Assembly”. *Molecular Biology of the Cell* 12.7, pp. 1925–1935. DOI: 10.1091/mbc.12.7.1925.
- Doray, B., I. Lee, J. Knisely, G. Bu, and S. Kornfeld (2007). “The $\gamma/\sigma 1$ and $\alpha/\sigma 2$ Hemicomplexes of Clathrin Adaptors AP-1 and AP-2 Harbor the Dilucine Recognition Site”. *Molecular Biology of the Cell* 18.5, pp. 1887–1896. DOI: 10.1091/mbc.E07-01-0012.
- Drake, M. T., M. A. Downs, and L. M. Traub (2000). “Epsin binds to clathrin by associating directly with the clathrin-terminal domain. Evidence for cooperative binding through two discrete sites”. *Journal of Biological Chemistry* 275.9, pp. 6479–6489. DOI: 10.1074/jbc.275.9.6479.
- Edeling, M. A., S. K. Mishra, P. A. Keyel, A. L. Steinhauser, B. M. Collins, R. Roth, J. E. Heuser, D. J. Owen, and L. M. Traub (2006). “Molecular Switches Involving the AP-2 $\beta 2$ Appendage Regulate Endocytic Cargo Selection and Clathrin Coat Assembly”. *Developmental Cell* 10.3, pp. 329–342. DOI: 10.1016/j.devcel.2006.01.016.
- Ferguson, S. M. and P. De Camilli (2012). “Dynamamin, a membrane remodelling GTPase”. *Nature Reviews Molecular Cell Biology* 13.2, pp. 75–88. DOI: 10.1038/nrm3266.
- Ferguson, S. M., A. Raimondi, S. Paradise, H. Shen, K. Mesaki, A. Ferguson, O. Destaing, G. Ko, J. Takasaki, O. Cremona, E. O’ Toole, and P. De Camilli (2009). “Coordinated actions of actin and BAR proteins upstream of dynamamin at endocytic clathrin-coated pits”. *Developmental cell* 17.6, pp. 811–822. DOI: 10.1016/j.devcel.2009.11.005.
- Fonseca, T. B., Á. Sánchez-Guerrero, I. Milosevic, and N. Raimundo (2019). “Mitochondrial fission requires DRP1 but not dynamins”. *Nature* 570.7761, E34–E42. DOI: 10.1038/s41586-019-1296-y.

- Fotin, A., Y. Cheng, P. Sliz, N. Grigorieff, S. C. Harrison, T. Kirchhausen, and T. Walz (2004). “Molecular model for a complete clathrin lattice from electron cryomicroscopy”. *Nature* 432.7017, pp. 573–579. DOI: 10.1038/nature03079.
- Giacomello, M., A. Pyakurel, C. Glytsou, and L. Scorrano (2020). “The cell biology of mitochondrial membrane dynamics”. *Nature Reviews Molecular Cell Biology* 21.4, pp. 204–224. DOI: 10.1038/s41580-020-0210-7.
- Gillingham, A. K., J. Bertram, F. Begum, and S. Munro (2019). “In vivo identification of GTPase interactors by mitochondrial relocalization and proximity biotinylation”. *eLife* 8, e45916. DOI: 10.7554/eLife.45916.
- Green, M. R. and J. Sambrook (2012). *Molecular Cloning: A Laboratory Manual, Fourth Edition*. 4th edition. Cold Spring Harbor, N.Y: Cold Spring Harbor Press. 2028 pp.
- Greener, T., X. Zhao, H. Nojima, E. Eisenberg, and L. E. Greene (2000). “Role of Cyclin G-associated Kinase in Uncoating Clathrin-coated Vesicles from Non-neuronal Cells”. *Journal of Biological Chemistry* 275.2, pp. 1365–1370. DOI: 10.1074/jbc.275.2.1365.
- Guan, R., H. Dai, D. Han, S. C. Harrison, and T. Kirchhausen (2010). “Structure of the PTEN-like region of auxilin, a detector of clathrin-coated vesicle budding”. *Structure* 18.9, pp. 1191–1198. DOI: 10.1016/j.str.2010.06.016.
- Guertin, D. A. and D. M. Sabatini (2009). “The pharmacology of mTOR inhibition”. *Science Signaling* 2.67, pe24. DOI: 10.1126/scisignal.267pe24.
- Heuser, J. (1980). “Three-dimensional visualization of coated vesicle formation in fibroblasts.” *Journal of Cell Biology* 84.3, pp. 560–583. DOI: 10.1083/jcb.84.3.560.
- Hill, T. A., C. P. Gordon, A. B. McGeachie, B. Venn-Brown, L. R. Odell, N. Chau, A. Quan, A. Mariana, J. A. Sakoff, M. Chircop, P. J. Robinson, and A. McCluskey (2009). “Inhibition of dynamin mediated endocytosis by the dynoles—synthesis and functional activity of a family of indoles”. *Journal of Medicinal Chemistry* 52.12, pp. 3762–3773. DOI: 10.1021/jm900036m.
- Hirst, J., G. H. H. Borner, R. Antrobus, A. A. Peden, N. A. Hodson, D. A. Sahlender, and M. S. Robinson (2012). “Distinct and overlapping roles for

- AP-1 and GGAs revealed by the "knocksideways" system". *Current Biology* 22.18, pp. 1711–1716. DOI: 10.1016/j.cub.2012.07.012.
- Hirst, J., C. Irving, and G. H. H. Borner (2013). "Adaptor protein complexes AP-4 and AP-5: new players in endosomal trafficking and progressive spastic paraplegia". *Traffic (Copenhagen, Denmark)* 14.2, pp. 153–164. DOI: 10.1111/tra.12028.
- Hirst, J., D. N. Itzhak, R. Antrobus, G. H. H. Borner, and M. S. Robinson (2018). "Role of the AP-5 adaptor protein complex in late endosome-to-Golgi retrieval". *PLOS Biology* 16.1, e2004411. DOI: 10.1371/journal.pbio.2004411.
- Holkar, S. S., S. C. Kamerkar, and T. J. Pucadyil (2015). "Spatial Control of Epsin-induced Clathrin Assembly by Membrane Curvature". *Journal of Biological Chemistry* 290.23, pp. 14267–14276. DOI: 10.1074/jbc.M115.653394.
- Hollopeter, G., J. J. Lange, Y. Zhang, T. N. Vu, M. Gu, M. Ailion, E. J. Lambie, B. D. Slaughter, J. R. Unruh, L. Florens, and E. M. Jorgensen (2014). "The membrane-associated proteins FCHo and SGIP are allosteric activators of the AP2 clathrin adaptor complex". *eLife* 3, e03648. DOI: 10.7554/eLife.03648.
- Horvath, S. E. and G. Daum (2013). "Lipids of mitochondria". *Progress in Lipid Research* 52.4, pp. 590–614. DOI: 10.1016/j.plipres.2013.07.002.
- Ishihara, N., Y. Eura, and K. Mihara (2004). "Mitofusin 1 and 2 play distinct roles in mitochondrial fusion reactions via GTPase activity". *Journal of Cell Science* 117.26, pp. 6535–6546. DOI: 10.1242/jcs.01565.
- Jackson, L. P., B. T. Kelly, A. J. McCoy, T. Gaffry, L. C. James, B. M. Collins, S. Höning, P. R. Evans, and D. J. Owen (2010). "A Large-Scale Conformational Change Couples Membrane Recruitment to Cargo Binding in the AP2 Clathrin Adaptor Complex". *Cell* 141.7, pp. 1220–1229. DOI: 10.1016/j.cell.2010.05.006.
- Jimenez, A., K. Friedl, and C. Leterrier (2020). "About samples, giving examples: Optimized Single Molecule Localization Microscopy". *Methods* 174, pp. 100–114. DOI: 10.1016/j.ymeth.2019.05.008.

- Kaksonen, M. and A. Roux (2018). “Mechanisms of clathrin-mediated endocytosis”. *Nature Reviews Molecular Cell Biology* 19.5, pp. 313–326. DOI: 10.1038/nrm.2017.132.
- Kaksonen, M., C. P. Toret, and D. G. Drubin (2006). “Harnessing actin dynamics for clathrin-mediated endocytosis”. *Nature Reviews Molecular Cell Biology* 7.6, pp. 404–414. DOI: 10.1038/nrm1940.
- Kanaseki, T. and K. Kadota (1969). “The ”vesicle in a basket”. A morphological study of the coated vesicle isolated from the nerve endings of the guinea pig brain, with special reference to the mechanism of membrane movements”. *Journal of Cell Biology* 42.1, pp. 202–220. DOI: 10.1083/jcb.42.1.202.
- Kapitein, L. C., M. A. Schlager, W. A. van der Zwan, P. S. Wulf, N. Keijzer, and C. C. Hoogenraad (2010). “Probing Intracellular Motor Protein Activity Using an Inducible Cargo Trafficking Assay”. *Biophysical Journal* 99.7, pp. 2143–2152. DOI: 10.1016/j.bpj.2010.07.055.
- Karginov, A. V., F. Ding, P. Kota, N. V. Dokholyan, and K. M. Hahn (2010). “Engineered allosteric activation of kinases in living cells”. *Nature Biotechnology* 28.7, pp. 743–747. DOI: 10.1038/nbt.1639.
- Katruxha, E. (2021). *ComDet*. Version <https://github.com/ekatruxha/ComDet>.
- Kaur, S., A. B. Fielding, G. Gassner, N. J. Carter, and S. J. Royle (2014). “An unmet actin requirement explains the mitotic inhibition of clathrin-mediated endocytosis”. *eLife* 3, e00829. DOI: 10.7554/eLife.00829.
- Kelly, B. T., S. C. Graham, N. Liska, P. N. Dannhauser, S. Höning, E. J. Ungewickell, and D. J. Owen (2014). “Clathrin adaptors. AP2 controls clathrin polymerization with a membrane-activated switch”. *Science* 345.6195, pp. 459–463. DOI: 10.1126/science.1254836.
- Kim, D. I., S. C. Jensen, K. A. Noble, B. KC, K. H. Roux, K. Motamedchaboki, and K. J. Roux (2016). “An improved smaller biotin ligase for BioID proximity labeling”. *Molecular Biology of the Cell* 27.8, pp. 1188–1196. DOI: 10.1091/mbc.E15-12-0844.
- Kirchhausen, T. (1993). “Coated pits and coated vesicles — sorting it all out”. *Current Opinion in Structural Biology* 3.2, pp. 182–188. DOI: 10.1016/S0959-440X(05)80150-2.

- Kosaka, T. and K. Ikeda (1983). “Possible temperature-dependent blockage of synaptic vesicle recycling induced by a single gene mutation in *Drosophila*”. *Journal of Neurobiology* 14.3, pp. 207–225. DOI: 10.1002/neu.480140305.
- Kühlbrandt, W. (2015). “Structure and function of mitochondrial membrane protein complexes”. *BMC Biology* 13.1, p. 89. DOI: 10.1186/s12915-015-0201-x.
- Kural, C., S. K. Tacheva-Grigorova, S. Boulant, E. Cocucci, T. Baust, D. Duarte, and T. Kirchhausen (2012). “Dynamics of Intracellular Clathrin/AP1- and Clathrin/AP3-Containing Carriers”. *Cell Reports* 2.5, pp. 1111–1119. DOI: 10.1016/j.celrep.2012.09.025.
- Laine, R. F., K. L. Tosheva, N. Gustafsson, R. D. M. Gray, P. Almada, D. Albrecht, G. T. Risa, F. Hurtig, A.-C. Lindås, B. Baum, J. Mercer, C. Leterrier, P. M. Pereira, S. Culley, and R. Henriques (2019). “NanoJ: a high-performance open-source super-resolution microscopy toolbox”. *Journal of Physics D: Applied Physics* 52.16, p. 163001. DOI: 10.1088/1361-6463/ab0261.
- Lee, J. E., L. M. Westrate, H. Wu, C. Page, and G. K. Voeltz (2016). “Multiple dynamin family members collaborate to drive mitochondrial division”. *Nature* 540.7631, pp. 139–143. DOI: 10.1038/nature20555.
- Letourneur, F. and R. D. Klausner (1992). “A novel di-leucine motif and a tyrosine-based motif independently mediate lysosomal targeting and endocytosis of CD3 chains”. *Cell* 69.7, pp. 1143–1157. DOI: 10.1016/0092-8674(92)90636-q.
- Lord, S. J., K. B. Velle, R. D. Mullins, and L. K. Fritz-Laylin (2020). “SuperPlots: Communicating reproducibility and variability in cell biology”. *Journal of Cell Biology* 219.6, e202001064. DOI: 10.1083/jcb.202001064.
- Macia, E., M. Ehrlich, R. Massol, E. Boucrot, C. Brunner, and T. Kirchhausen (2006). “Dynasore, a Cell-Permeable Inhibitor of Dynamin”. *Developmental Cell* 10.6, pp. 839–850. DOI: 10.1016/j.devcel.2006.04.002.
- Maib, H., F. Ferreira, S. Vassilopoulos, and E. Smythe (2018). “Cargo regulates clathrin-coated pit invagination via clathrin light chain phosphorylation”. *Journal of Cell Biology* 217.12, pp. 4253–4266. DOI: 10.1083/jcb.201805005.

- Mardones, G. A., P. V. Burgos, Y. Lin, D. P. Kloer, J. G. Magadán, J. H. Hurley, and J. S. Bonifacino (2013). “Structural basis for the recognition of tyrosine-based sorting signals by the μ 3A subunit of the AP-3 adaptor complex”. *Journal of Biological Chemistry* 288.13, pp. 9563–9571. DOI: 10.1074/jbc.M113.450775.
- Mattera, R., M. Boehm, R. Chaudhuri, Y. Prabhu, and J. S. Bonifacino (2011). “Conservation and Diversification of Dilucine Signal Recognition by Adaptor Protein (AP) Complex Variants”. *Journal of Biological Chemistry* 286.3, pp. 2022–2030. DOI: 10.1074/jbc.M110.197178.
- Mayor, S., R. G. Parton, and J. G. Donaldson (2014). “Clathrin-Independent Pathways of Endocytosis”. *Cold Spring Harbor Perspectives in Biology* 6.6, a016758. DOI: 10.1101/cshperspect.a016758.
- McLelland, G.-L., S. A. Lee, H. M. McBride, and E. A. Fon (2016). “Syntaxin-17 delivers PINK1/parkin-dependent mitochondrial vesicles to the endolysosomal system”. *Journal of Cell Biology* 214.3, pp. 275–291. DOI: 10.1083/jcb.201603105.
- McMahon, H. T. and J. L. Gallop (2005). “Membrane curvature and mechanisms of dynamic cell membrane remodelling”. *Nature* 438.7068, pp. 590–596. DOI: 10.1038/nature04396.
- McNiven, M. A. (1998). “Dynamin: A Molecular Motor with Pinchase Action”. *Cell* 94.2, pp. 151–154. DOI: 10.1016/S0092-8674(00)81414-2.
- Meinecke, M., E. Boucrot, G. Camdere, W.-C. Hon, R. Mittal, and H. T. McMahon (2013). “Cooperative recruitment of dynamin and BIN/amphiphysin/Rvs (BAR) domain-containing proteins leads to GTP-dependent membrane scission”. *Journal of Biological Chemistry* 288.9, pp. 6651–6661. DOI: 10.1074/jbc.M112.444869.
- Messa, M., R. Fernández-Busnadiego, E. W. Sun, H. Chen, H. Czapla, K. Wrasman, Y. Wu, G. Ko, T. Ross, B. Wendland, and P. De Camilli (2014). “Epsin deficiency impairs endocytosis by stalling the actin-dependent invagination of endocytic clathrin-coated pits”. *eLife* 3, e03311. DOI: 10.7554/eLife.03311.

- Mettlen, M., P.-H. Chen, S. Srinivasan, G. Danuser, and S. L. Schmid (2018). “Regulation of Clathrin-Mediated Endocytosis”. *Annual Review of Biochemistry* 87, pp. 871–896. DOI: 10.1146/annurev-biochem-062917-012644.
- Miller, S. E., B. M. Collins, A. J. McCoy, M. S. Robinson, and D. J. Owen (2007). “A SNARE–adaptor interaction is a new mode of cargo recognition in clathrin-coated vesicles”. *Nature* 450.7169, pp. 570–574. DOI: 10.1038/nature06353.
- Miller, S. E., D. A. Sahlender, S. C. Graham, S. Höning, M. S. Robinson, A. A. Peden, and D. J. Owen (2011). “The molecular basis for the endocytosis of small R-SNAREs by the clathrin adaptor CALM”. *Cell* 147.5, pp. 1118–1131. DOI: 10.1016/j.cell.2011.10.038.
- Morgan, J. R., K. Prasad, W. Hao, G. J. Augustine, and E. M. Lafer (2000). “A Conserved Clathrin Assembly Motif Essential for Synaptic Vesicle Endocytosis”. *Journal of Neuroscience* 20.23, pp. 8667–8676. DOI: 10.1523/JNEUROSCI.20-23-08667.2000.
- Motley, A., N. A. Bright, M. N. Seaman, and M. S. Robinson (2003). “Clathrin-mediated endocytosis in AP-2–depleted cells”. *Journal of Cell Biology* 162.5, pp. 909–918. DOI: 10.1083/jcb.200305145.
- Neuspiel, M., A. C. Schauss, E. Braschi, R. Zunino, P. Rippstein, R. A. Rachubinski, M. A. Andrade-Navarro, and H. M. McBride (2008). “Cargo-selected transport from the mitochondria to peroxisomes is mediated by vesicular carriers”. *Current Biology* 18.2, pp. 102–108. DOI: 10.1016/j.cub.2007.12.038.
- Ohno, H., J. Stewart, M. C. Fournier, H. Bosshart, I. Rhee, S. Miyatake, T. Saito, A. Gallusser, T. Kirchhausen, and J. S. Bonifacino (1995). “Interaction of tyrosine-based sorting signals with clathrin-associated proteins”. *Science* 269.5232, pp. 1872–1875. DOI: 10.1126/science.7569928.
- Ooi, C. E., E. C. Dell’Angelica, and J. S. Bonifacino (1998). “ADP-Ribosylation Factor 1 (ARF1) Regulates Recruitment of the AP-3 Adaptor Complex to Membranes”. *Journal of Cell Biology* 142.2, pp. 391–402. DOI: 10.1083/jcb.142.2.391.
- Osellame, L. D., T. S. Blacker, and M. R. Duchen (2012). “Cellular and molecular mechanisms of mitochondrial function”. *Best Practice & Research. Clinical*

- Endocrinology & Metabolism* 26.6, pp. 711–723. DOI: 10.1016/j.beem.2012.05.003.
- Owen, D., Y. Vallis, B. Pearse, H. McMahon, and P. Evans (2000). “The structure and function of the β 2-adaptin appendage domain”. *The EMBO Journal* 19.16, pp. 4216–4227. DOI: 10.1093/emboj/19.16.4216.
- Paradies, G., V. Paradies, F. M. Ruggiero, and G. Petrosillo (2019). “Role of Cardiolipin in Mitochondrial Function and Dynamics in Health and Disease: Molecular and Pharmacological Aspects”. *Cells* 8.7, p. 728. DOI: 10.3390/cells8070728.
- Park, R. J., H. Shen, L. Liu, X. Liu, S. M. Ferguson, and P. De Camilli (2013). “Dynamamin triple knockout cells reveal off target effects of commonly used dynamamin inhibitors”. *Journal of Cell Science* 126.22, pp. 5305–5312. DOI: 10.1242/jcs.138578.
- Pearse, B. M. (1975). “Coated vesicles from pig brain: Purification and biochemical characterization”. *Journal of Molecular Biology* 97.1, pp. 93–98. DOI: 10.1016/S0022-2836(75)80024-6.
- (1976). “Clathrin: a unique protein associated with intracellular transfer of membrane by coated vesicles.” *Proceedings of the National Academy of Sciences of the United States of America* 73.4, pp. 1255–1259. DOI: 10.1073/pnas.73.4.1255.
- Peden, A. A., V. Oorschot, B. A. Hesser, C. D. Austin, R. H. Scheller, and J. Klumperman (2004). “Localization of the AP-3 adaptor complex defines a novel endosomal exit site for lysosomal membrane proteins”. *The Journal of Cell Biology* 164.7, pp. 1065–1076. DOI: 10.1083/jcb.200311064.
- Peden, A. A., R. E. Rudge, W. W. Lui, and M. S. Robinson (2002). “Assembly and function of AP-3 complexes in cells expressing mutant subunits”. *Journal of Cell Biology* 156.2, pp. 327–336. DOI: 10.1083/jcb.200107140.
- Perrin, L., S. Lacas-Gervais, J. Gilleron, F. Ceppo, F. Prodon, A. Benmerah, J.-F. Tanti, and M. Cormont (2013). “Rab4b controls an early endosome sorting event by interacting with the γ -subunit of the clathrin adaptor complex 1”. *Journal of Cell Science* 126.21, pp. 4950–4962. DOI: 10.1242/jcs.130575.

- Ren, X., G. G. Farias, B. J. Canagarajah, J. S. Bonifacino, and J. H. Hurley (2013). “Structural Basis for Recruitment and Activation of the AP-1 Clathrin Adaptor Complex by Arf1”. *Cell* 152.4, pp. 755–767. DOI: 10.1016/j.cell.2012.12.042.
- Robinson, M. S. (2015). “Forty Years of Clathrin-coated Vesicles”. *Traffic* 16.12, pp. 1210–1238. DOI: 10.1111/tra.12335.
- Robinson, M. S., D. A. Sahlender, and S. D. Foster (2010). “Rapid Inactivation of Proteins by Rapamycin-Induced Rerouting to Mitochondria”. *Developmental Cell* 18.2, pp. 324–331. DOI: 10.1016/j.devcel.2009.12.015.
- Roger, A. J., S. A. Muñoz-Gómez, and R. Kamikawa (2017). “The Origin and Diversification of Mitochondria”. *Current Biology* 27.21, R1177–R1192. DOI: 10.1016/j.cub.2017.09.015.
- Rosendale, M., T. N. N. Van, D. Grillo-Bosch, S. Sposini, L. Claverie, I. Gauthereau, S. Claverol, D. Choquet, M. Sainlos, and D. Perrais (2019). “Functional recruitment of dynamin requires multimeric interactions for efficient endocytosis”. *Nature Communications* 10.1, p. 4462. DOI: 10.1038/s41467-019-12434-9.
- Roth, T. F. and K. R. Porter (1964). “YOLK PROTEIN UPTAKE IN THE OOCYTE OF THE MOSQUITO AEDES AEGYPTI. L”. *Journal of Cell Biology* 20, pp. 313–332. DOI: 10.1083/jcb.20.2.313.
- Rothnie, A., A. R. Clarke, P. Kuzmic, A. Cameron, and C. J. Smith (2011). “A sequential mechanism for clathrin cage disassembly by 70-kDa heat-shock cognate protein (Hsc70) and auxilin”. *Proceedings of the National Academy of Sciences of the United States of America* 108.17, pp. 6927–6932. DOI: 10.1073/pnas.1018845108.
- Royle, S. (2021). *p054p031*. Version <https://github.com/quantixed/p054p031>.
- Saffarian, S., E. Cocucci, and T. Kirchhausen (2009). “Distinct Dynamics of Endocytic Clathrin-Coated Pits and Coated Plaques”. *PLoS Biology* 7.9, e1000191. DOI: 10.1371/journal.pbio.1000191.
- Sanger, A., J. Hirst, A. K. Davies, and M. S. Robinson (2019). “Adaptor protein complexes and disease at a glance”. *Journal of Cell Science* 132.20. DOI: 10.1242/jcs.222992.

- Schmid, E. M., M. G. J. Ford, A. Burtsey, G. J. K. Praefcke, S.-Y. Peak-Chew, I. G. Mills, A. Benmerah, and H. T. McMahon (2006). “Role of the AP2 β -Appendage Hub in Recruiting Partners for Clathrin-Coated Vesicle Assembly”. *PLoS Biology* 4.9, e262. DOI: 10.1371/journal.pbio.0040262.
- Schmid, S. L. and E. Smythe (1991). “Stage-specific assays for coated pit formation and coated vesicle budding in vitro”. *Journal of Cell Biology* 114.5, pp. 869–880. DOI: 10.1083/jcb.114.5.869.
- Scott, B. L., K. A. Sochacki, S. T. Low-Nam, E. M. Bailey, Q. Luu, A. Hor, A. M. Dickey, S. Smith, J. G. Kerkvliet, J. W. Taraska, and A. D. Hoppe (2018). “Membrane bending occurs at all stages of clathrin-coat assembly and defines endocytic dynamics”. *Nature Communications* 9.1, p. 419. DOI: 10.1038/s41467-018-02818-8.
- Seaman, M. N., P. J. Sowerby, and M. S. Robinson (1996). “Cytosolic and membrane-associated proteins involved in the recruitment of AP-1 adaptors onto the trans-Golgi network”. *Journal of Biological Chemistry* 271.41, pp. 25446–25451. DOI: 10.1074/jbc.271.41.25446.
- Serwas, D., M. Akamatsu, A. Moayed, K. Vegesna, R. Vasan, J. M. Hill, J. Schöneberg, K. M. Davies, P. Rangamani, and D. G. Drubin (2021). “Actin force generation in vesicle formation: mechanistic insights from cryo-electron tomography”. *bioRxiv*, p. 2021.06.28.450262. DOI: 10.1101/2021.06.28.450262.
- Sever, S., A. B. Muhlberg, and S. L. Schmid (1999). “Impairment of dynamin’s GAP domain stimulates receptor-mediated endocytosis”. *Nature* 398.6727, pp. 481–486. DOI: 10.1038/19024.
- Shih, W., A. Gallusser, and T. Kirchhausen (1995). “A clathrin-binding site in the hinge of the beta 2 chain of mammalian AP-2 complexes”. *Journal of Biological Chemistry* 270.52, pp. 31083–31090. DOI: 10.1074/jbc.270.52.31083.
- Sluijs, P. v. d., M. Hull, P. Webster, P. Mâle, B. Goud, and I. Mellman (1992). “The small GTP-binding protein rab4 controls an early sorting event on the endocytic pathway”. *Cell* 70.5, pp. 729–740. DOI: 10.1016/0092-8674(92)90307-X.

- Smirnova, E., L. Griparic, D.-L. Shurland, and A. M. van der Bliek (2001). “Dynamamin-related Protein Drp1 Is Required for Mitochondrial Division in Mammalian Cells”. *Molecular Biology of the Cell* 12.8, pp. 2245–2256. DOI: 10.1091/mbc.12.8.2245.
- Smith, S. M., G. Larocque, K. M. Wood, K. L. Morris, A. M. Roseman, R. B. Sessions, S. J. Royle, and C. J. Smith (2021). “Multi-modal adaptor-clathrin contacts drive coated vesicle assembly”. *The EMBO journal*, e108795. DOI: 10.15252/embj.2021108795.
- Smythe, E., L. L. Carter, and S. L. Schmid (1992). “Cytosol- and clathrin-dependent stimulation of endocytosis in vitro by purified adaptors”. *Journal of Cell Biology* 119.5, pp. 1163–1171. DOI: 10.1083/jcb.119.5.1163.
- Smythe, E., M. Pypaert, J. Lucocq, and G. Warren (1989). “Formation of coated vesicles from coated pits in broken A431 cells.” *Journal of Cell Biology* 108.3, pp. 843–853. DOI: 10.1083/jcb.108.3.843.
- Söllner, T., S. W. Whiteheart, M. Brunner, H. Erdjument-Bromage, S. Geromanos, P. Tempst, and J. E. Rothman (1993). “SNAP receptors implicated in vesicle targeting and fusion”. *Nature* 362.6418, pp. 318–324. DOI: 10.1038/362318a0.
- Song, Z., H. Chen, M. Fiket, C. Alexander, and D. C. Chan (2007). “OPA1 processing controls mitochondrial fusion and is regulated by mRNA splicing, membrane potential, and Yme1L”. *Journal of Cell Biology* 178.5, pp. 749–755. DOI: 10.1083/jcb.200704110.
- Soubannier, V., G.-L. McLelland, R. Zunino, E. Braschi, P. Rippstein, E. A. Fon, and H. M. McBride (2012). “A vesicular transport pathway shuttles cargo from mitochondria to lysosomes”. *Current Biology* 22.2, pp. 135–141. DOI: 10.1016/j.cub.2011.11.057.
- Soubannier, V., P. Rippstein, B. A. Kaufman, E. A. Shoubridge, and H. M. McBride (2012). “Reconstitution of Mitochondria Derived Vesicle Formation Demonstrates Selective Enrichment of Oxidized Cargo”. *PLOS One* 7.12, e52830. DOI: 10.1371/journal.pone.0052830.
- Sousa, R., H.-S. Liao, J. Cuéllar, S. Jin, J. M. Valpuesta, A. J. Jin, and E. M. Lafer (2016). “Clathrin-coat disassembly illuminates the mechanisms of Hsp70

- force generation”. *Nature Structural & Molecular Biology* 23.9, pp. 821–829. DOI: 10.1038/nsmb.3272.
- Spencer, D. M., T. J. Wandless, S. L. Schreiber, and G. R. Crabtree (1993). “Controlling signal transduction with synthetic ligands”. *Science* 262.5136, pp. 1019–1024. DOI: 10.1126/science.7694365.
- Stachowiak, J. C., F. M. Brodsky, and E. A. Miller (2013). “A cost–benefit analysis of the physical mechanisms of membrane curvature”. *Nature Cell Biology* 15.9, pp. 1019–1027. DOI: 10.1038/ncb2832.
- Stammes, M. A. and J. E. Rothman (1993). “The binding of AP-1 clathrin adaptor particles to Golgi membranes requires ADP-ribosylation factor, a small GTP-binding protein”. *Cell* 73.5, pp. 999–1005. DOI: 10.1016/0092-8674(93)90277-w.
- Stowell, M. H., B. Marks, P. Wigge, and H. T. McMahon (1999). “Nucleotide-dependent conformational changes in dynamin: evidence for a mechanochemical molecular spring”. *Nature Cell Biology* 1.1, pp. 27–32. DOI: 10.1038/8997.
- Sugiura, A., G.-L. McLelland, E. A. Fon, and H. M. McBride (2014). “A new pathway for mitochondrial quality control: mitochondrial-derived vesicles”. *The EMBO Journal* 33.19, pp. 2142–2156. DOI: 10.15252/embj.201488104.
- Sweitzer, S. M. and J. E. Hinshaw (1998). “Dynamin Undergoes a GTP-Dependent Conformational Change Causing Vesiculation”. *Cell* 93.6, pp. 1021–1029. DOI: 10.1016/S0092-8674(00)81207-6.
- Taylor, M. J., M. Lampe, and C. J. Merrifield (2012). “A Feedback Loop between Dynamin and Actin Recruitment during Clathrin-Mediated Endocytosis”. *PLOS Biology* 10.4, e1001302. DOI: 10.1371/journal.pbio.1001302.
- Taylor, M. J., D. Perrais, and C. J. Merrifield (2011). “A High Precision Survey of the Molecular Dynamics of Mammalian Clathrin-Mediated Endocytosis”. *PLOS Biology* 9.3, e1000604. DOI: 10.1371/journal.pbio.1000604.
- Traub, L. M. (2011). “Regarding the Amazing Choreography of Clathrin Coats”. *PLOS Biology* 9.3, e1001037. DOI: 10.1371/journal.pbio.1001037.
- Tubbs, E. and J. Rieusset (2017). “Metabolic signaling functions of ER – mitochondria contact sites: role in metabolic diseases”. *Journal of Molecular Endocrinology* 58.2, R87–R106. DOI: 10.1530/JME-16-0189.



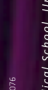
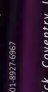
- Ungewickell, E., H. Ungewickell, S. E. Holstein, R. Lindner, K. Prasad, W. Barouch, B. Martin, L. E. Greene, and E. Eisenberg (1995). “Role of auxilin in uncoating clathrin-coated vesicles”. *Nature* 378.6557, pp. 632–635. DOI: 10.1038/378632a0.
- Wang, W. and B. A. Malcolm (1999). “Two-stage PCR protocol allowing introduction of multiple mutations, deletions and insertions using QuikChange Site-Directed Mutagenesis”. *BioTechniques* 26.4, pp. 680–682. DOI: 10.2144/99264st03.
- Wang, Y. J., J. Wang, H. Q. Sun, M. Martinez, Y. X. Sun, E. Macia, T. Kirchhausen, J. P. Albanesi, M. G. Roth, and H. L. Yin (2003). “Phosphatidylinositol 4 phosphate regulates targeting of clathrin adaptor AP-1 complexes to the Golgi”. *Cell* 114.3, pp. 299–310. DOI: 10.1016/s0092-8674(03)00603-2.
- Watt, S. A., G. Kular, I. N. Fleming, C. P. Downes, and J. M. Lucocq (2002). “Subcellular localization of phosphatidylinositol 4,5-bisphosphate using the pleckstrin homology domain of phospholipase C $\delta 1$ ”. *Biochemical Journal* 363.3, pp. 657–666. DOI: 10.1042/bj3630657.
- Welz, T., J. Wellbourne-Wood, and E. Kerkhoff (2014). “Orchestration of cell surface proteins by Rab11”. *Trends in Cell Biology* 24.7, pp. 407–415. DOI: 10.1016/j.tcb.2014.02.004.
- Wiedemann, N. and N. Pfanner (2017). “Mitochondrial Machineries for Protein Import and Assembly”. *Annual Review of Biochemistry* 86, pp. 685–714. DOI: 10.1146/annurev-biochem-060815-014352.
- Wilbur, J. D., C.-Y. Chen, V. Manalo, P. K. Hwang, R. J. Fletterick, and F. M. Brodsky (2008). “Actin Binding by Hip1 (Huntingtin-interacting Protein 1) and Hip1R (Hip1-related Protein) Is Regulated by Clathrin Light Chain”. *Journal of Biological Chemistry* 283.47, pp. 32870–32879. DOI: 10.1074/jbc.M802863200.
- Wiley, H. S. and D. D. Cunningham (1982). “The endocytotic rate constant. A cellular parameter for quantitating receptor-mediated endocytosis”. *Journal of Biological Chemistry* 257.8, pp. 4222–4229.
- Willy, N. M., J. P. Ferguson, A. Akatay, S. Huber, U. Djakbarova, S. Silahli, C. Cakez, F. Hasan, H. C. Chang, A. Travasset, S. Li, R. Zandi, D. Li, E. Betzig,

- E. Cocucci, and C. Kural (2021). “De novo endocytic clathrin coats develop curvature at early stages of their formation”. *Developmental Cell* 56.22, 3146–3159.e5. DOI: 10.1016/j.devcel.2021.10.019.
- Wood, L. A., G. Larocque, N. I. Clarke, S. Sarkar, and S. J. Royle (2017). “New tools for “hot-wiring” clathrin-mediated endocytosis with temporal and spatial precision”. *Journal of Cell Biology* 216.12, pp. 4351–4365. DOI: 10.1083/jcb.201702188.
- Yang, H., D. G. Rudge, J. D. Koos, B. Vaidialingam, H. J. Yang, and N. P. Pavletich (2013). “mTOR kinase structure, mechanism and regulation by the rapamycin-binding domain”. *Nature* 497.7448, pp. 217–223. DOI: 10.1038/nature12122.
- Yuan, F., H. Alimohamadi, B. Bakka, A. N. Trementozzi, K. J. Day, N. L. Fawzi, P. Rangamani, and J. C. Stachowiak (2021). “Membrane bending by protein phase separation”. *Proceedings of the National Academy of Sciences of the United States of America* 118.11.
- Zhang, P. and J. E. Hinshaw (2001). “Three-dimensional reconstruction of dynamin in the constricted state”. *Nature Cell Biology* 3.10, pp. 922–926. DOI: 10.1038/ncb1001-922.
- Zhao, W., L. Hanson, H.-Y. Lou, M. Akamatsu, P. D. Chowdary, F. Santoro, J. R. Marks, A. Grassart, D. G. Drubin, Y. Cui, and B. Cui (2017). “Nanoscale manipulation of membrane curvature for probing endocytosis in live cells”. *Nature Nanotechnology* 12.8, pp. 750–756. DOI: 10.1038/nnano.2017.98.

Appendix A

Reconstituting clathrin-mediated vesicle formation at mitochondria
 Cansu Küey, Gabrielle Larocque*, Miguel Hernández-González*, Stephen J Royle

Centre for Mechanochemical Cell Biology, Warwick Medical School, University of Warwick, Coventry, Warwick, UK
 Present address: The Francis Crick Institute, London, UK

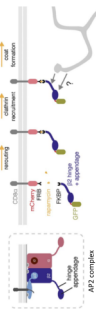





0000-0002-3993-3523 0000-0001-8295-9378 0000-0003-5562-7076 0000-0001-8977-6967

Key players in Clathrin Mediated Endocytosis (CME)

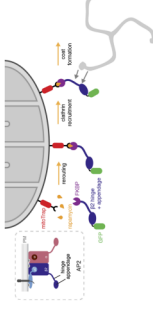
- There are more than 50 proteins involved in CME
- AP2 complex binds to cargo and PP2, then to clathrin, to its $\beta 2$ subunit
- CCVs pinch off as dynamin and forces generated by actin polymerisation

What are the minimal factors required for CME? Hot-wiring CME on Plasma Membrane (PM)



Hot-wiring was sufficient to initiate endocytosis on demand which manifests as bright spots that form on PM, then internalised

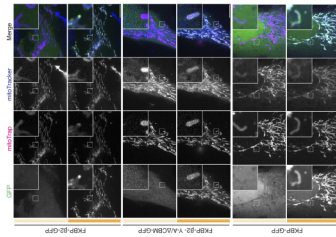
Can we answer this question in more detail by doing hot-wiring on mitochondria?



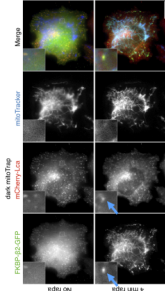
Why mitochondria?

- It is like a cell inside the cell with a double membrane
- Not involved in canonical membrane trafficking
- Have a different lipid profile to its membrane than PM, no PIPs

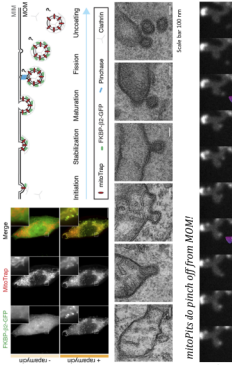
Formation of the mitoPIts on MOM require clathrin



mitoPIts colocalise with clathrin

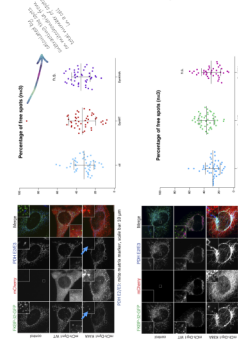


Stages of CME mimicked on mitochondria via hot-wiring

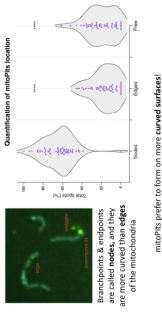


What is responsible for pinching off of the mitoPIts? Dynamin? Dp11?

If so, then there should be almost no free spots when their respective dominant negative forms, Dyn K44A or Dp11 K38A, are overexpressed



Do mitoPIts form on specific regions on mitochondria?



Conclusions

- Successfully mimicked CCV formation at MOM
- Electron microscopy and live cell imaging reveal that all steps of CCV formation from initiation to maturation and scission were reconstituted
- Mitochondria are not involved in canonical membrane trafficking
- Mitochondria recruited by our synthetic system to deform both the inner and outer mitochondrial membrane, and even to pinch off the mitoPIts
- Given the differences in lipid composition of mitochondria and PM, our system suggests that phospholipid composition is not essential for CCV formation
- PIPs and clathrin molecules (pinchpoints) are not necessarily needed for intracellular budding
- Mitochondria favour forming on mitochondrial surfaces with higher curvature

References

Wood, L. A., Larocque, G., Chikhe, N. L., Sarker, S. J. (2017). Hot-wiring clathrin-mediated endocytosis with response and control proteins. *J. Cell Biol.* 216, 4057-4065. doi:10.1093/jcb/133/17/4057



Appendix B

TOOLS AND RESOURCES

Unintended perturbation of protein function using GFP nanobodies in human cells

Cansu Küey, Gabrielle Larocque, Nicholas I. Clarke and Stephen J. Royle*

ABSTRACT

Tagging a protein of interest with GFP using genome editing is a popular approach to study protein function in cell and developmental biology. To avoid re-engineering cell lines or organisms in order to introduce additional tags, functionalized nanobodies that bind GFP can be used to extend the functionality of the GFP tag. We developed functionalized nanobodies, which we termed ‘dongles’, that could add, for example, an FKBP tag to a GFP-tagged protein of interest, enabling knocksideways experiments in GFP knock-in cell lines. The power of knocksideways is that it allows investigators to rapidly switch the protein from an active to an inactive state. We show that dongles allow for effective knocksideways of GFP-tagged proteins in genome-edited human cells. However, we discovered that nanobody binding to dynamin-2–GFP caused inhibition of dynamin function prior to knocksideways. The function of GFP-tagged tumor protein D54 (TPD54, also known as TPD52L2) in anterograde traffic was also perturbed by dongles. While these issues potentially limit the application of dongles, we discuss strategies for their deployment as cell biological tools.

This article has an associated First Person interview with the first author of the paper.

KEY WORDS: Clathrin-mediated endocytosis, Dynamin, Nanobody, GFP-binding protein, Knocksideways

INTRODUCTION

Fluorescent proteins revolutionized cell biology. The green fluorescent protein (GFP) or its relatives can be attached to virtually any protein of interest and allow the direct visualization of that protein by light microscopy or flow cytometry (Wang and Hazelrigg, 1994). Whole genome GFP-tagging projects have been completed in yeast (Huh et al., 2003), plants (Tian et al., 2004), bacteria (Kitagawa et al., 2005) and fly (Nagarkar-Jaiswal et al., 2015). The advent of genome engineering, particularly via CRISPR/Cas9, has allowed the creation of GFP knock-in mammalian cell lines in labs around the world (Jinek et al., 2013), with centralized efforts to systematically tag genes in human induced pluripotent stem cells (Roberts et al., 2017). While these

resources are incredibly useful, additional tags would further enhance our ability to probe protein function in single cells.

Of particular interest is the ability to rapidly modulate protein function. Inducible methods such as relocation (Haruki et al., 2008; Robinson et al., 2010) and degradation (Nishimura et al., 2009) allow investigators to study the effect of inactivating a protein of interest in live cells. For example, we have used the knocksideways method to study protein function at distinct stages of mitosis, without perturbing interphase function (Cheeseman et al., 2013). Here, a protein of interest has an FKBP tag that allows inducible binding to a mitochondrially targeted protein containing an FRB tag (MitoTrap) via the heterodimerization of FKBP and FRB by rapamycin (Robinson et al., 2010). The power of these methods lies in the comparison of the active and inactive states of the protein of interest.

The development of camelid nanobodies that bind GFP have been very useful as affinity purification tools (Rothbauer et al., 2008). Since these nanobodies can be readily expressed in cells, it is possible to use them as ‘dongles’ to extend the functionality of GFP by attaching a new protein domain to the GFP-tagged protein of interest via fusion with the nanobody. This approach has been exploited to degrade proteins of interest (Caussinus et al., 2011; Kanner et al., 2017; Daniel et al., 2018; Yamaguchi et al., 2019), to introduce additional tags (Rothbauer et al., 2008; Ariotti et al., 2015; Derivery et al., 2017; Zhao et al., 2019), or to constitutively relocalize GFP-tagged proteins (Schornack et al., 2009; Derivery et al., 2015). Recently a suite of functionalized nanobodies to GFP or RFP were generated, enabling recoloring, inactivation, ectopic recruitment and calcium sensing (Prole and Taylor, 2019). The dongle approach holds much promise because it is flexible and saves investigators from re-engineering knock-in cell lines to introduce additional tags.

Some time ago, we developed dongles to allow knocksideways experiments in GFP knock-in cell lines. The approach certainly works and we demonstrate this using two different genome-edited human cell lines. However, we discovered during the course of development that nanobody binding to dynamin-2–GFP causes inhibition of dynamin function, prior to any induced inactivation. Since the purpose of knocksideways is to compare active and inactive states, the dongles could not be used in this way. The aim of this paper is to alert other labs to the possibility that nanobodies against GFP can perturb the function of the target GFP-tagged protein. We discuss what strategies investigators might pursue as alternatives and outline possible applications of dongles despite this limitation.

RESULTS

Testing fluorescent protein selectivity of dongles in cells

Most experimental applications of dongles would involve two different fluorescent proteins, one as a target for the dongle and a second as an experimental readout. We therefore wanted to assess the fluorescent protein selectivity of the GFP nanobody in cells. To

Centre for Mechanochemical Cell Biology, Warwick Medical School, University of Warwick, Gibbet Hill Road, Coventry CV4 7AL, UK.

*Author for correspondence (s.j.royle@warwick.ac.uk)

© C.K., 0000-0002-7992-3523; G.L., 0000-0001-8295-9378; N.I.C., 0000-0003-3297-8604; S.J.R., 0000-0001-8927-6967

This is an Open Access article distributed under the terms of the Creative Commons Attribution License (<https://creativecommons.org/licenses/by/4.0>), which permits unrestricted use, distribution and reproduction in any medium provided that the original work is properly attributed.

Received 31 May 2019; Accepted 3 October 2019

do this, we used a visual screening method in HeLa cells by expressing a GFP nanobody (GFP-binding protein enhancer, GBPen) that was constitutively attached to the mitochondria (DongleTrap, see Materials and Methods) along with a suite of twenty-five different fluorescent proteins. Affinity of the fluorescent protein for the DongleTrap resulted in a steady-state relocation to the mitochondria, while lack of interaction meant that the fluorescent protein remained cytoplasmic (Fig. 1). We observed relocation for mAzurite, EBFP2, sfGFP, mEmerald, EGFP, Clover, EYFP, mVenus and mCitrine. The following fluorescent proteins remained cytoplasmic in all cells examined: TagBFP2, ECFP, mCerulean3, mTurquoise2, mAzamiGreen, mNeonGreen, mOrange2, mKO2, DsRed, mRuby2, mScarlet, mRFP, mCherry, mNeptune2, mMaroon and TagRFP657. All of the fluorescent proteins that DongleTrap binds are derivatives of avGFP (GFP from *Aequorea victoria*), while it did not bind proteins from other lineages, e.g. dsRed, eqFP578, and LanYFP (Lambert, 2019). The GBPen has

further specificity besides lineage, since DongleTrap did not bind other avGFP descendants ECFP, mCerulean3 and mTurquoise2 (Kubala et al., 2010). These experiments demonstrated which tags could be manipulated by dongles in cells (e.g. GFP), but also which fluorescent proteins can be used simultaneously with these tools, without interference (e.g. mCherry).

Dongles can be used to extend the function of GFP

Knocksideways is a useful tool to rapidly inactivate proteins by sequestering them onto mitochondria using heterodimerization of FKBP and FRB domains (Robinson et al., 2010). Typically, the FKBP domain is fused to the protein of interest (usually along with GFP for visualization) and the FRB domain is part of MitoTrap (Fig. 2). To demonstrate the usual application of this method, we rerouted the membrane trafficking protein tumor protein D54 (TPD54, also known as TPD52L2) to mitochondria (for detailed analysis of TPD54 rerouting see Larocque et al., 2019). To do this,

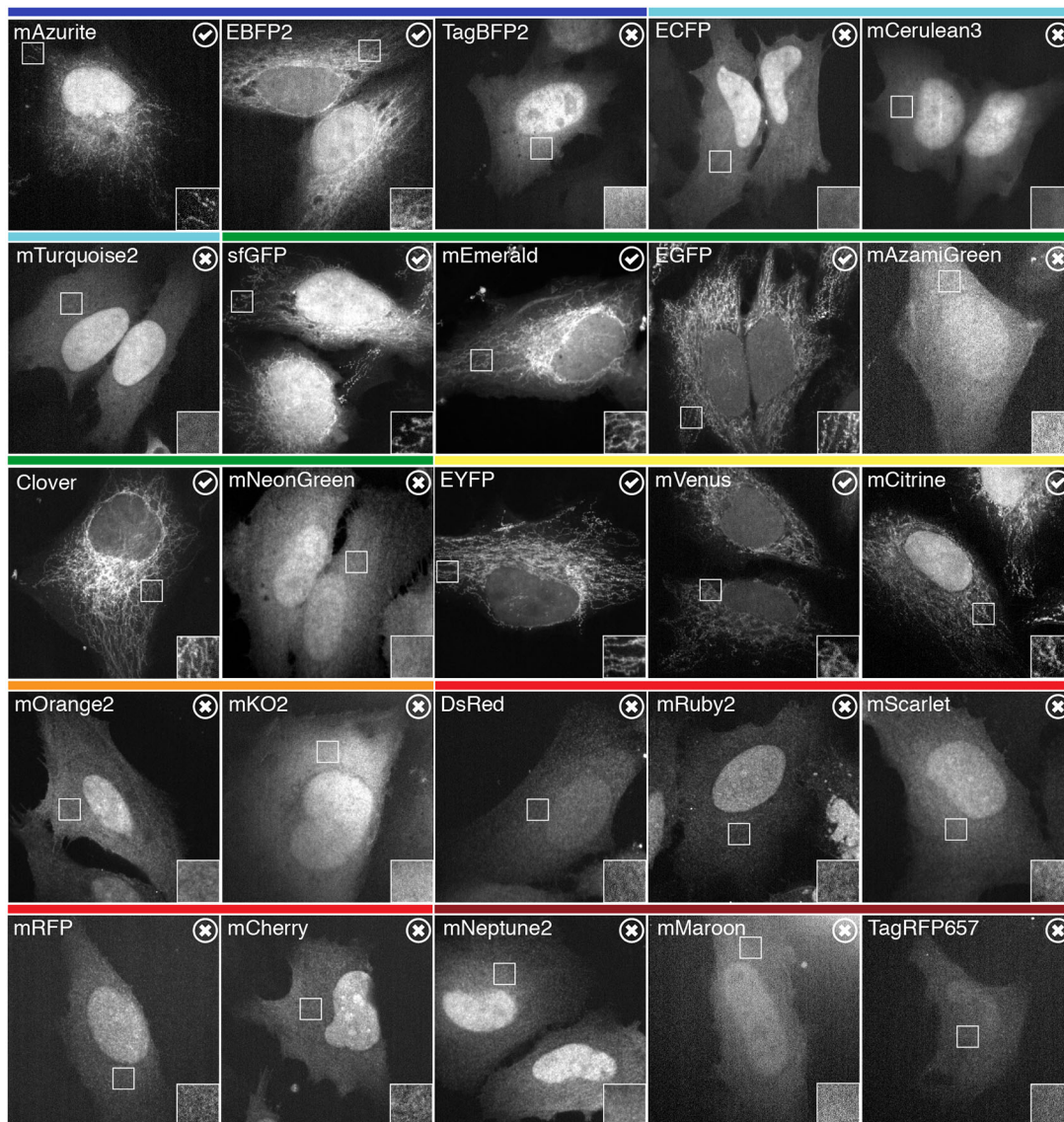


Fig. 1. Selectivity of dongles for fluorescent proteins. Representative images of HeLa cells expressing DongleTrap (pMito–GBPen) and the indicated fluorescent protein. Binding to DongleTrap results in mitochondrial localization of the fluorescent protein and is indicated by a tick (check mark). Fluorescent proteins that do not bind to the DongleTrap remain cytoplasmic and are indicated by a cross. Insets show a 2× zoom of the indicated region of interest. Colored bars above indicate the approximate emission of the fluorescent proteins tested.

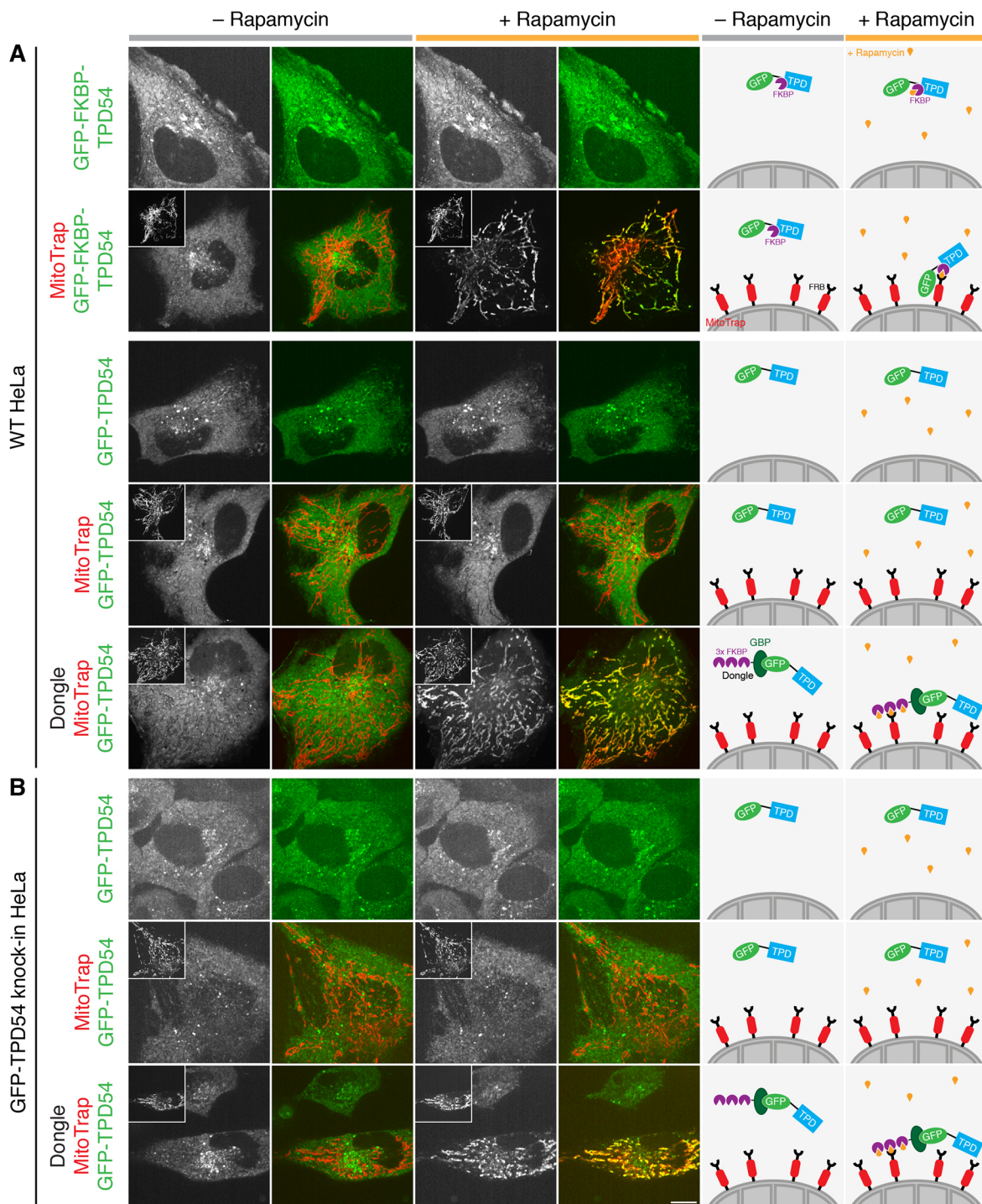


Fig. 2. Dogle allows for knocksideways of GFP-tagged proteins that have no FKBP tag. Representative confocal images of live cells taken before (gray bar) or after (orange bar) addition of 200 nM rapamycin. (A) GFP-FKBP-TPD54 or GFP-TPD54 were expressed in wild-type (WT) HeLa cells, along with MitoTrap (pMito-mCherry-FRB) alone or together with the dogle as indicated. If MitoTrap (red in merge) was co-expressed, the red channel is shown in the inset at half size. (B) In GFP-TPD54 knock-in HeLa cells, MitoTrap or MitoTrap+dogle were expressed as indicated. Scale bar: 10 μ m. Schematic diagrams to the right illustrate the experimental conditions and the respective result.

we expressed GFP-FKBP-TPD54 in HeLa cells either alone or together with MitoTrap. Application of 200 nM rapamycin caused the relocation of GFP-FKBP-TPD54 to mitochondria in seconds, only when MitoTrap was present (Fig. 2A).

We wanted to use knocksideways on proteins that have a GFP tag, but no FKBP. To enable this we designed a dogle comprising three copies of FKBP fused to the N-terminus of GBPen, which

can be co-expressed in cells along with MitoTrap (see Materials and Methods). When expressed transiently in cells along with GFP-TPD54, application of rapamycin (200 nM) caused GFP-TPD54 to become rapidly rerouted to mitochondria (Fig. 2A). Mitochondrial rerouting was dependent on the presence of the dogle, since no rerouting was seen in rapamycin-treated cells expressing GFP-TPD54 and MitoTrap. The effect was indistinguishable from

rerouting of GFP–FKBP–TPD54 to MitoTrap in response to rapamycin (Fig. 2A).

Given these encouraging results, we next tested whether dongles could be used to reroute endogenous proteins, tagged with GFP, to the mitochondria. To do this, we expressed the dongle and MitoTrap in cells where endogenous TPD54 was tagged with GFP (Larocque et al., 2019). We found that GFP–TPD54 was rerouted when the dongle and MitoTrap were present and rapamycin was added (Fig. 2B). Knocksideways was qualitatively similar to GFP–FKBP–TPD54 or GFP–TPD54 and dongle, expressed with MitoTrap in wild-type HeLa cells (Fig. 2). These experiments indicate that the dongles can be used to extend the function of GFP and to permit knocksideways experiments in GFP knock-in cell lines without an FKBP tag. We termed this method ‘dongle-knocksideways’.

Knocksideways of dynamin-2 in gene-edited human cells

We next wanted to use the dongle-knocksideways method to switch off endocytosis on demand. A direct approach would be to inactivate the large GTPase dynamin, which is essential for vesicle scission during endocytosis (Antonny et al., 2016). We therefore tested dongle-knocksideways in SK-MEL-2 hDNM2^{EN-all} cells, where both alleles of dynamin-2 are tagged with GFP (Doyon et al., 2011). Confocal imaging revealed rapid and efficient rerouting of dynamin-2–GFP (DNM2–GFP) to mitochondria using 200 nM rapamycin in cells co-expressing the dongle and MitoTrap (Fig. 3A; Movie 1).

The dongle used for knocksideways has three FKBP domains in tandem, attached to GBPen (3×FKBP dongle). For reasons that will become clear below, we also generated a dongle with a single FKBP domain (1×FKBP dongle). Using this construct for dongle-knocksideways of DNM2–GFP in SK-MEL-2 hDNM2^{EN-all} cells was similar to experiments that used 3×FKBP dongle (Fig. 3B). Therefore, dynamin-2–GFP can be rerouted efficiently to mitochondria using dongle-knocksideways.

Inhibition of clathrin-mediated endocytosis using dongles

Does dongle-knocksideways of dynamin-2–GFP cause an inhibition of clathrin-mediated endocytosis (CME)? To answer this question we analyzed the cellular uptake of fluorescently labelled transferrin, an established assay for CME. We first verified that chronic inhibition of CME could be achieved by expression of DongleTrap (Fig. S1). Then we tested the effect of dongle-knocksideways (rapamycin versus vehicle) and compared this to inhibition of endocytosis (sucrose) using hypertonic media (Hansen et al., 1993). To our surprise, we found that expression of the dongle was sufficient to inhibit CME in SK-MEL-2 hDNM2^{EN-all} cells (Fig. 4). The amount of transferrin uptake in cells expressing MitoTrap together with 3×FKBP dongle was significantly reduced compared to untransfected cells or those expressing MitoTrap alone (Fig. 4). This unintended inhibition of CME was similar to treatment with hypertonic media, a classical method to inhibit endocytosis. We wondered whether the size of 3×FKBP dongle caused this inhibition and so we generated a 1×FKBP dongle, which was approximately half the size (3×FKBP dongle, 49.8 kDa; 1×FKBP dongle, 25.9 kDa), and verified that the 1×FKBP dongle was fully functional for rerouting experiments (Fig. 3B). Again, this dongle caused inhibition of CME by expression in SK-MEL-2 hDNM2^{EN-all} cells, similar to that seen for 3×FKBP dongle (Fig. 4). Similar results were seen using SK-MEL-2 hCLTA^{EN}/hDNM2^{EN} cells, which indicated that this effect was not specific to the hDNM2^{EN-all} cell line used (Fig. S2).

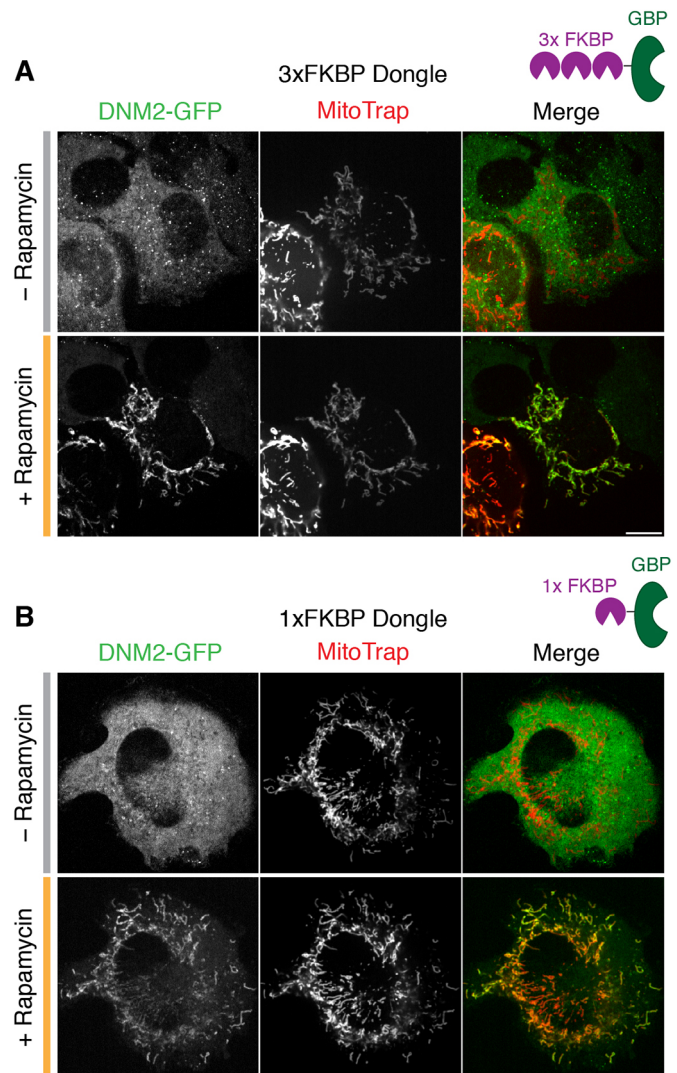


Fig. 3. Dongle-knocksideways efficiently reroutes dynamin-2–GFP to mitochondria. Still confocal images from dongle-knocksideways experiments showing a cell before and after application of 200 nM rapamycin. SK-MEL-2 hDNM2^{EN-all} cells expressing GFP-tagged dynamin-2 (DNM2–GFP), MitoTrap and either (A) 3×FKBP dongle or (B) 1×FKBP dongle. Scale bars: 10 μm.

Note that with either dongle and either cell line, no further inhibition of CME was observed by sucrose treatment nor by rapamycin addition causing dongle-knocksideways. These observations mean that the dongle method cannot be used in this way to inhibit endocytosis on demand, since the active state is inhibited unintentionally.

Our results suggested that the unintentional inhibition of CME is caused by dongles binding to dynamin-2–GFP and inhibiting its function. An alternative hypothesis is that the dongles inhibit CME via some unknown mechanism and the effect in cells with dynamin-2–GFP was coincidental. To test whether dongles inhibited CME directly, we measured transferrin uptake in HeLa cells with no dynamin-2–GFP, which expressed either the 3×FKBP or 1×FKBP dongles with MitoTrap (Fig. 5). We found that transferrin uptake in these cells was similar to that in cells expressing MitoTrap alone or to untransfected controls (Fig. 5). CME in cells expressing either dongle could be inhibited by sucrose and not by rapamycin treatment, which is to be expected if there is no direct inhibition of CME caused by the

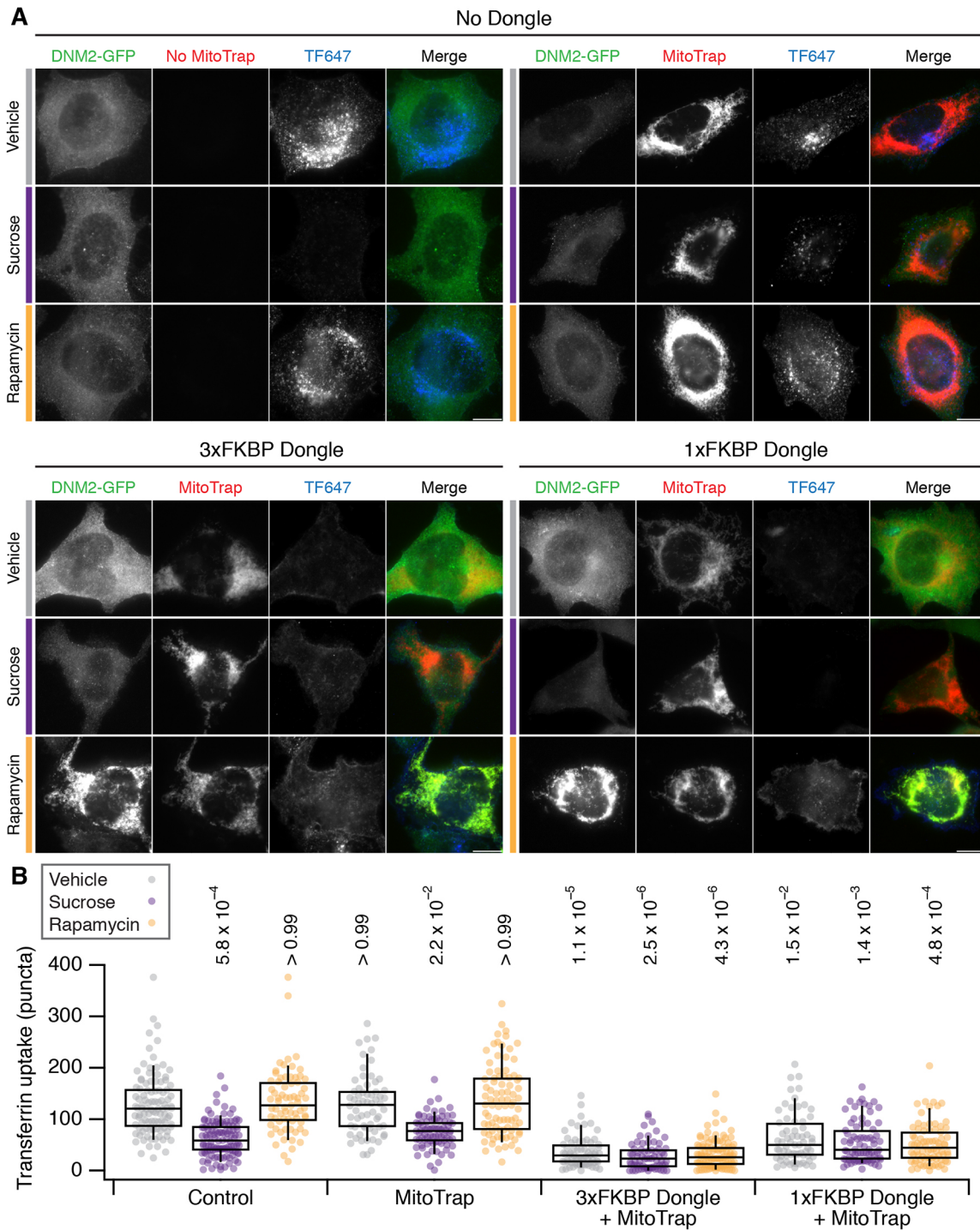


Fig. 4. Effect of dongle expression on transferrin uptake in SK-MEL-2 hDNM2^{EN-all} cells. (A) Micrographs of SK-MEL-2 hDNM2^{EN-all} cells treated with vehicle (gray bar), sucrose (purple bar) or 200 nM rapamycin (orange bar). Cells were untransfected (No Dongle, No Mitotrap), or expressed MitoTrap alone, or MitoTrap with 3xFKBP dongle or 1xFKBP dongle. DNM2-GFP (green), MitoTrap (red) and transferrin-Alexa Fluor 647 (TF647, blue) are displayed using the same minimum and maximum value per channel for all images in the figure. Scale bars: 10 μm. (B) Box plot to show quantification of transferrin uptake. Expression and treatments are as indicated and colored as in A. Dots represent individual cells from multiple experiments. Box represents the interquartile range (IQR), the line the median and the whiskers the 9th and 91st percentile. $n_{\text{cell}}=64-114$, $n_{\text{exp}}=7$. Two-way ANOVA on experimental means, within subject; Factor A=expression, $DF=2$, $F=12.44$, $F_c=8.77$, $P<0.001$; Factor B=treatment, $DF=3$, $F=35.02$, $F_c=7.05$, $P<0.001$; AxB, $DF=6$, $F=3.17$, $F_c=5.12$, $P<0.001$. P -values from Dunnett's post hoc test are shown above each plot (Control vehicle as the control group).

dongle. These experiments ruled out an inhibitory effect of dongles on CME, and implicate the inhibition seen in cells expressing dynamin-2-GFP as being due to binding of dynamin-2-GFP with the nanobody.

Unintended perturbation of GFP-TPD54 function with dongles
The dongle-mediated inhibition of dynamin-2-GFP function might be particular to dynamin-2. We therefore tested whether the function of GFP-TPD54 was also affected by dongle expression. TPD54 is

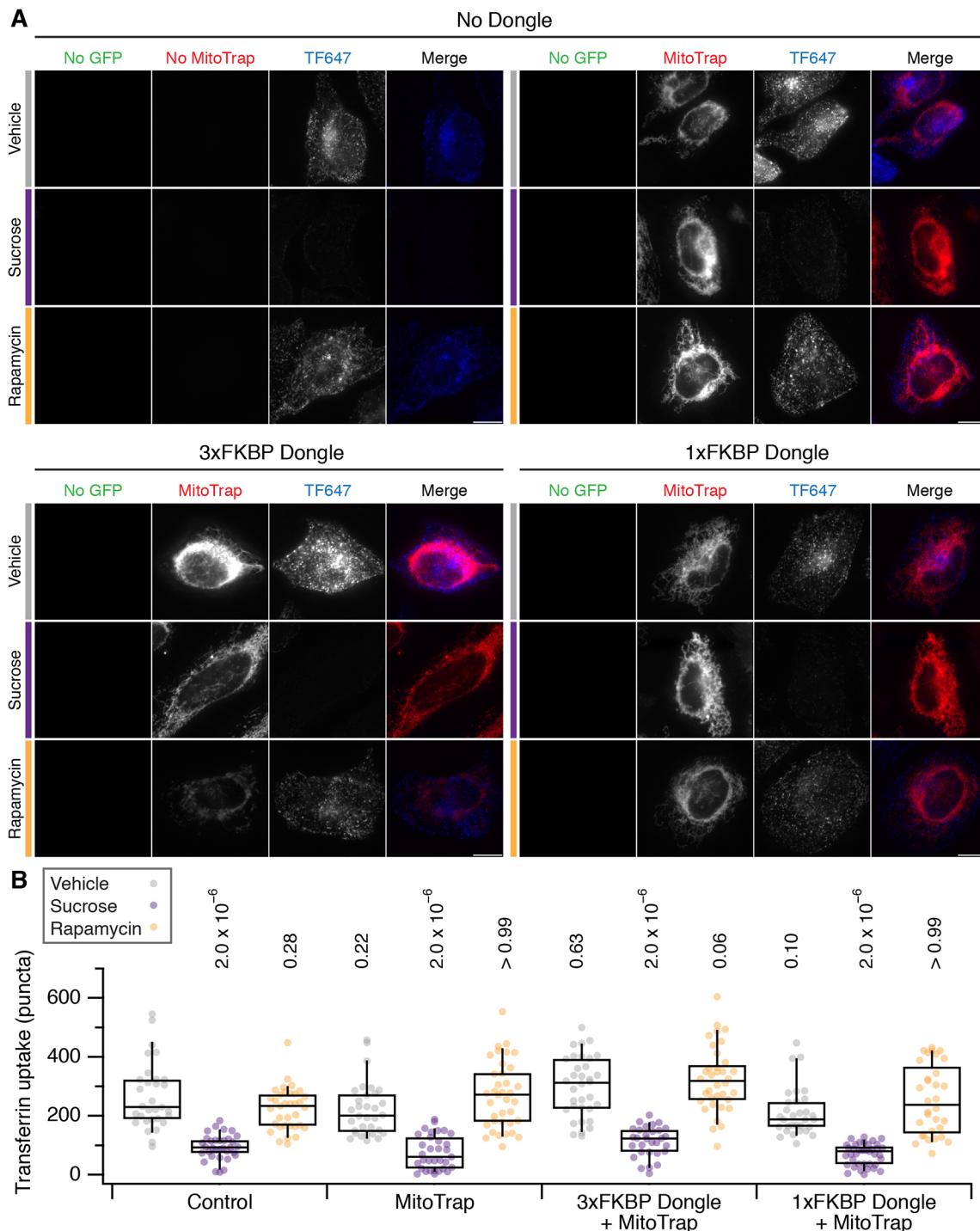


Fig. 5. Effect of dongle expression on transferrin uptake in HeLa cells. (A) Micrographs of HeLa cells treated with vehicle (gray bar), sucrose (purple bar) or 200 nM rapamycin (orange bar). Cells were untransfected (No Dongle, No Mitotrap), or expressed MitoTrap alone, or MitoTrap with 3×FKBP dongle or 1×FKBP dongle. No GFP (green), MitoTrap (red) and transferrin–Alexa Fluor 647 (TF647, blue) are displayed using the same minimum and maximum value per channel for all images in the figure. Scale bars: 10 μm. (B) Box plot to show quantification of transferrin uptake. Expression and treatments are as indicated and colored as in A. Dots represent individual cells from a single experiment. Box represents the IQR, the line the median and the whiskers the 9th and 91st percentile. One-way ANOVA *P*-values from Dunnett’s post hoc test are shown above each plot (Control vehicle as the control group).

involved in anterograde traffic and its depletion results in delayed transit of E-cadherin in a retention using selective hooks (RUSH) assay (Larocque et al., 2019; Boncompain et al., 2012). In GFP–TPD54 knock-in HeLa cells, we analysed the export of SBP–mRuby2–E-cadherin from the ER to Golgi and on to the plasma

membrane using RUSH (Fig. 6). In cells that express dark MitoTrap and 3×FKBP dongle, export from the ER to Golgi was significantly faster compared to cells expressing dark MitoTrap alone (control) (Fig. 6A–D). The kinetics of transport from the Golgi to the plasma membrane were unaffected. These experiments indicate that

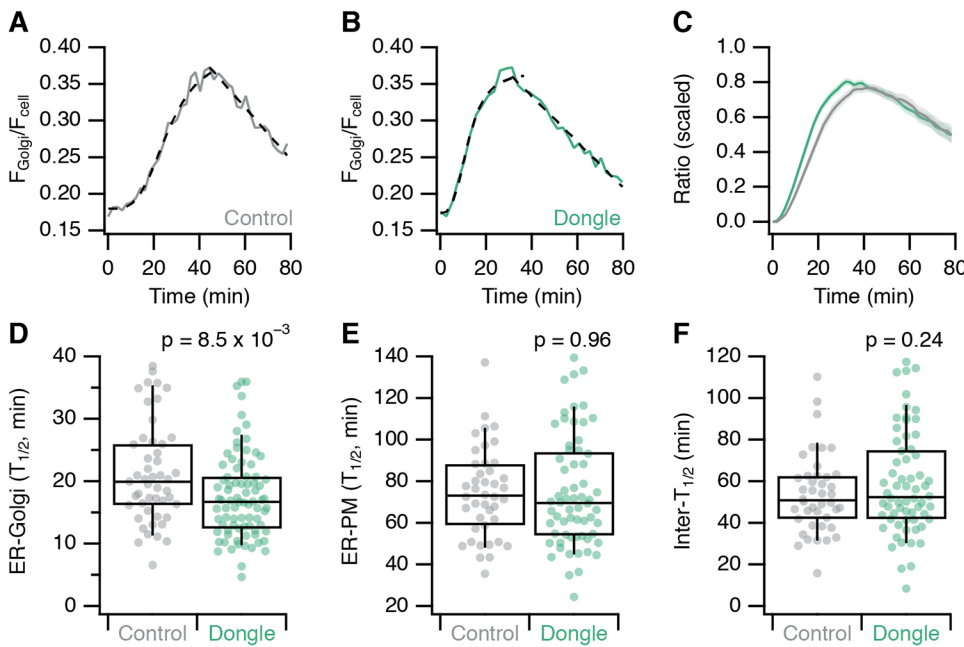


Fig. 6. Effect of dongle expression on anterograde in GFP-TPD54 knock-in HeLa cells. (A,B) Example trace of the E-cadherin fluorescence ratio following RUSH recorded from (A) a control (MitoTrap-expressing, gray) or (B) a dongle (3×FKBP dongle-expressing, green) GFP-TPD54 knock-in HeLa cell. Traces fitted with a logistic function and a line. (C) Scaled fraction of total E-cadherin fluorescence at the Golgi as a function of time, in control (gray) or dongle-expressing (green) cells. Line and shaded area represent mean ± s.e.m. (D–F) Box plots showing the half-times of E-cadherin transport from (D) ER-to-Golgi and (E) ER-to-PM in control and dongle-expressing GFP-TPD54 knock-in cells. (F) The difference in half-times represents intra-Golgi transport. Box represents the IQR, the line the median and the whiskers the 9th and 91st percentile. *P*-values from Student's *t*-test with Welch's correction. *n*_{cell}=49–82, *n*_{exp}=3.

unintended perturbation of GFP-tagged protein function is not particular to dynamin-2 but may be a general consequence of dongle expression.

DISCUSSION

In this paper, we described the development of dongles to extend the functionality of GFP for knocksideways experiments. We found that these molecular tools were effective at binding GFP and permitting the rerouting of the target protein to mitochondria. However, we discovered an unintended side effect: dongles can perturb the function of the GFP-tagged protein under study.

The use of GFP-binding proteins as an intracellular tool to manipulate protein function is becoming widespread (Prole and Taylor, 2019; Daniel et al., 2018; Ariotti et al., 2015). The appeal of the method is that proteins tagged with GFP at their endogenous loci can be adapted using dongles to enable inactivation, relocalization, recoloring or other function. This means that existing cell lines or organisms can be 'retrofitted' for additional functionality using such tools. Indeed, our initial experiments using dongles were very encouraging; the dongles expressed well, we detected no obvious perturbation of subcellular distribution of the target proteins we examined, and they permitted dongle-knocksideways which, in the case of TPD54, was very similar to knocksideways (rerouting the same protein with a fused GFP–FKBP tag). However, we found that when the dongles were expressed in cells with both copies of dynamin-2 tagged with GFP, endocytosis was inhibited. This unintended effect seemed to be due to direct inhibition of dynamin function following binding of dynamin-2–GFP by the nanobody (GBPen) portion of the dongle. Dynamins may be uniquely sensitive because they self-oligomerize, and we know that their action can be readily inhibited by simple expression of a GTPase deficient isoform (Damke et al., 1994). However, this problem was not unique to dynamin-2 since we also saw that GFP–TPD54 function in anterograde traffic was perturbed by dongle expression.

We were fortunate to test this method on dynamin-2, which has a clear functional readout as it controls the terminal step in clathrin-mediated endocytosis (Antonny et al., 2016). Other proteins do not have such unambiguous readouts, or their function can only be

measured indirectly, if at all. This would mean that if dongles were used with these proteins, perturbed function would not be revealed and potentially misleading conclusions drawn. This problem is compounded because dongles would be most useful when applied to proteins whose function is uncertain, so the perturbation of protein function caused by these tools may be hidden from the investigator. Our advice is that the same caution and functional tests should be applied when using GFP nanobodies in cells as when generating GFP-tagged proteins themselves (Snapp, 2005).

The mechanism of inhibition of dynamin-2–GFP function by dongles is unclear. The simplest explanation is that extending the GFP tag using a GFP nanobody plus additional domains results in a modification that is simply too large for dynamin to function normally; whether this is because of reduced dynamics, blocked interactions or some other mechanism. We saw similar unintended inhibition when the size of the dongle was reduced by half (from three FKBP domains to one), suggesting that the binding of the nanobody itself is inhibitory rather than there being a size limit to the tag that dynamin-2 can tolerate. It is considered that most proteins can tolerate the addition of GFP or GFP–FKBP tag, but it is perhaps underappreciated that at some level, tags will always interfere with protein function. The fact that we report perturbed protein function using dongles is perhaps not surprising.

Unintended inhibition affects experiments where the protein of interest needs to be functional (active) prior to inactivation. For other applications of dongles, inhibition may not be such a concern. First, in constitutive mislocalization experiments, where the goal is to chronically inactivate protein function by changing its cellular localization, dongles remain an important tool. We demonstrated here the use of DongleTrap to inactivate dynamin-2–GFP. Second, it is unclear whether labeling strategies based on dongles are compromised by inhibition (Ariotti et al., 2015). We saw no evidence of gross changes in subcellular localization of the two proteins we tested; however, it remains questionable whether imaging a protein of interest in its inhibited state is representative of its normal distribution. Third, in cases where investigators simply want to put a functional domain to a new location using a GFP-tagged anchor protein, such as calcium sensors at the endoplasmic reticulum (Prole

and Taylor, 2019), inhibition of the anchor may not be a concern. Fourth, our finding of nanobody-mediated inactivation of protein function may even be useful as a general purpose method for perturbing protein function in gene-edited cell lines.

What is the best strategy to extend the functionality of tags introduced with knock-in technology? First, it may be possible to reduce the inhibitory effect of dongles by mutating the GBP moiety or using different domain configurations and/or by changing the linker regions. Second, alternative GFP-binding proteins such as those based on a designed ankyrin repeat protein (DARPin) scaffold may be functionalized and used as dongles (Brauchle et al., 2014). It is possible that these reagents do not have the same inhibitory effects. Third, using split-GFP technology, proteins of interest could be tagged with GFP11 and then the fluorescence complemented with a GFP1-10 protein (Kamiyama et al., 2016), where GFP1-10 is fused to other domains to extend the functionality. A further advantage of this third method is that the fluorescence of the tagged protein can also be altered during the complementation (Kamiyama et al., 2016). However, a weakness is that this method would not take advantage of existing GFP-tagged collections, and would require new knock-ins to be generated in most cases. Finally, while GBPen is the most widely used GFP nanobody, it is possible that dongles that incorporate alternative GFP nanobodies may cause less perturbation to target protein function.

MATERIALS AND METHODS

Molecular biology

Construction of plasmids to express GFP-TPD54 and GFP-FKBP-TPD54 and mCherry-MitoTrap (pMito-mCherry-FRB) was described previously (Cheeseman et al., 2013; Larocque et al., 2019). The nanobody cDNA used in this paper, described as GBPen (GFP-binding protein enhancer), was synthesized from published sequences (Kubala et al., 2010; Kirchhofer et al., 2010). To make pMito-mCherry-FRB-IRES-FKBP(III)-GBPen, a bicistronic vector to co-express mCherry-MitoTrap and 3×FKBP-GBPen via an internal ribosome entry site (IRES), a custom insert was made using gene synthesis (GenScript) and inserted into pEGFP-C1 in place of GFP at AgeI and EcoRI. A dark version of pMito-mCherry-FRB-IRES-FKBP(III)-GBPen was also made by site-directed mutagenesis in mCherry to include the K70N mutation. To express DongleTrap, pMito-GBPen was made by amplifying GBPen from a plasmid containing FKBP(III)-GBPen (forward: 5'-cttagatccggcaCAGGTGCAGCTG-3', reverse: 5'-ggcctctagaTCAATGGTGATGGTG-3') cloning into demethylated pMito-mCherry-FRB using BamHI and XbaI. To make pMito-mCherry-FRB-IRES-FKBP(I)-GBPen, the region of IRES including the HindIII cut site and 1×FKBP was amplified using PCR from pMito-mCherry-FRB-IRES-FKBP(III)-GBPen with addition of a BglII site at the end of the amplified fragment (forward: 5'-GTTCTCTGGAAGCTTCTTGAAG-3', reverse: 5'-gcgagatctTTCCAGTTTTAGAAGCTCCACATC-3'). The product was cut with HindIII and BglII. The same vector was cut with HindIII and BglII, resulting in a vector lacking all three FKBP tags. The cut PCR product was ligated back into the cut vector. pMito-mCherry-FRB-IRES-FKBP(I)-GBPen, pMito-mCherry-FRB-IRES-FKBP(III)-GBPen and pMito-GBPen were deposited to Addgene as #128267, #128268, #128269, respectively. To make Str-KDEL-SBP-mRuby2-E-Cadherin, the FastCloning technique was used (Li et al., 2011). Briefly, EGFP was removed from the original RUSH construct Str-KDEL-SBP-EGFP-E-Cadherin (Boncompain et al., 2012) by amplifying the plasmid from either side of EGFP with the following primers: forward: 5'-GGACGAGCTGTACAGGGcggcCCAGactgggtc-3' and reverse: CGCCCTTAGACACATAC-CtgcaggTGGTTCACGTTG-3'. mRuby2 was amplified using mRuby2-N1 (Addgene, #54614) with the following primers: forward: 5'-GAACCAcct-gcaGGTATGGTGTCTAAGGGCGAAGAG-3' and reverse: 5'-ccagtcTG-GccggCCCTTGTACAGCTCGTCCATCCC-3'. Both amplicons have overlapping sequences. The insert and the vector were then digested with DpnI and transformed in DH5α cells.

Plasmids to express fluorescent proteins were either available from previous work: pDsRed-N1, pEGFP-N1, pECFP-N1, pEYFP-N1, pmRFP-N1, pmCherry-N1, pTagBFP2; from Addgene: pmScarlet-C1 (#85042), pTagRFP657-N1 (#44275), psfGFP-N1 (#54737), pEBFP2-N1 (#54595), mAzurite-N1 (#54617), mCerulean3-N1 (#54730), mTurquoise2-N1 (#60561), mVenus-N1 (#27793), mRuby2-N1 (#54614), mNeptune2-N1 (#54837), mOrange2-N1 (#54499), mCitrine2-N1 (#54594), mEmerald-N1 (#53976), pcDNA3-Clover (#40259), mAzamiGreen-N1 (#54798), mMaroon-N1 (#54554), mKO2-N1 (#54625); or from Allele Biotech: pmNeonGreen-N1 (ABP-FP-MNEONSA).

Cell biology

HeLa cells (HPA/ECACC #93021013) or GFP-TPD54 knock-in HeLa cells (Larocque et al., 2019) were cultured in DMEM+GlutaMAX (Thermo Fisher) supplemented with 10% fetal bovine serum, and 100 U ml⁻¹ penicillin/streptomycin. SK-MEL-2 hDNM2^{EN-all} or hDNM2^{EN-all}/CLTA^{EN} cells (a kind gift from David Drubin, Department of Molecular and Cellular Biology, University of California Berkeley, CA) were cultured in Dulbecco's modified Eagle's medium or nutrient mixture F-12 Ham (Sigma-Aldrich) supplemented with 10% fetal bovine serum, 1% L-glutamine, 3.5% sodium bicarbonate and 100 U ml⁻¹ penicillin/streptomycin. All cells were kept at 37°C and 5% CO₂. HeLa cells were transfected with 1.2 μg DNA (total) per 3 μl GeneJuice (Merck Millipore) according to the manufacturer's instructions. SK-MEL-2 cells were transfected with 4.8 μg DNA (total) per 850,000 cells using Neon Transfection System (Thermo Fisher) with three pulses of 1500 V, 10 ms. Cells were analyzed 2 days post-transfection.

Transferrin uptake experiments were as described previously (Clarke and Royle, 2018). Briefly, cells were serum-starved for 30 min. For knocksideways, they were exposed to 200 nM rapamycin (Alfa Aesar) or 0.1% ethanol (vehicle) for the last 10 min of starvation, and then incubated with 100 μg/ml Alexa Fluor 647-conjugated transferrin (Invitrogen) for 10 min. Hypertonic sucrose media (0.45 M) was used to inhibit transferrin uptake. All incubations were in serum-free media at 37°C with 5% CO₂ in a humidified incubator. Cells were then fixed in 3% PFA/4% sucrose in PBS and mounted on slides using Mowiol.

Microscopy

For live-cell imaging of rerouting experiments, cells were grown in 4-well glass-bottom 3.5 cm dishes (Greiner Bio-One) and media exchanged for Leibovitz L-15 CO₂-independent medium. Rerouting was triggered by addition of 200 nM rapamycin in L-15 media.

For the RUSH assay, GFP-TPD54 knock-in HeLa cells were transfected with Str-KDEL-SBP-mRuby2-E-Cadherin and either dark MitoTrap (Wood et al., 2017) alone or a plasmid that expressed 3×FKBP dongle and dark MitoTrap coupled by an IRES. mRuby2-E-cadherin was released from the ER by adding a final concentration of 40 μM D-Biotin (Sigma-Aldrich) in L-15 medium. Images were captured at a time interval of 2 min.

All cells were imaged at 37°C on a spinning disc confocal system (UltraView Vox, PerkinElmer) with a 100×1.4 NA oil-immersion objective. Images were captured using an ORCA-R2 digital CCD camera (Hamamatsu) following excitation with 488 nm and 561 nm lasers.

Imaging of fixed cells was done on a Nikon Ti-U epifluorescence microscope with 100× oil-immersion objective, CoolSnap MYO camera (Photometrics) using NIS-Elements software (Nikon).

Data analysis

Analysis of transferrin uptake was done as described previously (Wood et al., 2017). Briefly, single cells were outlined manually in Fiji. Vesicular structures were isolated by applying a manual threshold to images in the transferrin channel. Positive structures were counted using 'Analyze particles', with limits of 0.03–0.8 μm and circularity of 0.3–1.0. All analysis was done with the experimenter blind to the conditions of the experiment.

Analysis of RUSH experiments was done as previously described (Larocque et al., 2019), using custom-written code (<https://doi.org/10.5281/zenodo.3366083>).

Figures were made with Fiji or Igor Pro 8 (WaveMetrics), and assembled using Adobe Illustrator. Null hypothesis statistical tests were done as described in the figure legends.

Acknowledgements

We thank David Drubin for the kind gift of genome-edited SK-MEL-2 cell lines. Members of the lab gave constructive criticism, Penny La-Borde made the GFP-TPD54 knock-in HeLa cells and helped with early stages of the dogle project, and Miguel Hernández González critically read the manuscript. We gratefully acknowledge CAMDU (Computing and Advanced Microscopy Unit) for their support and assistance in this work.

Competing interests

The authors declare no competing or financial interests.

Author contributions

Conceptualization: N.I.C., S.J.R.; Methodology: C.K., N.I.C.; Validation: C.K.; Formal analysis: C.K., G.L., S.J.R.; Investigation: C.K., G.L.; Resources: N.I.C.; Writing - original draft: S.J.R.; Writing - review & editing: C.K., G.L., S.J.R.; Visualization: C.K.; Supervision: G.L., S.J.R.

Funding

The work was supported by the UK Medical Research Council (MR/P018947/1). C.K. was supported by University of Warwick, and the Engineering and Physical Sciences Research Council and Biotechnology and Biological Sciences Research Council Centre for Doctoral Training in Synthetic Biology (grant EP/L016494/1). Deposited in PMC for immediate release.

Supplementary information

Supplementary information available online at <http://jcs.biologists.org/lookup/doi/10.1242/jcs.234955.supplemental>

References

- Antony, B., Burd, C., De Camilli, P., Chen, E., Daumke, O., Faelber, K., Ford, M., Frolov, V. A., Frost, A., Hinshaw, J. E. et al. (2016). Membrane fission by dynamin: what we know and what we need to know. *EMBO J.* **35**, 2270-2284. doi:10.15252/embj.201694613
- Ariotti, N., Hall, T. E., Rae, J., Ferguson, C., McMahon, K.-A., Martel, N., Webb, R. E., Webb, R. I., Teasdale, R. D. and Parton, R. G. (2015). Modular detection of GFP-labeled proteins for rapid screening by electron microscopy in cells and organisms. *Dev. Cell* **35**, 513-525. doi:10.1016/j.devcel.2015.10.016
- Boncompain, G., Divoux, S., Gareil, N., de Forges, H., Lescure, A., Latreche, L., Mercanti, V., Jollivet, F., Raposo, G. and Perez, F. (2012). Synchronization of secretory protein traffic in populations of cells. *Nat. Methods* **9**, 493-498. doi:10.1038/nmeth.1928
- Brauchle, M., Hansen, S., Caussinus, E., Lenard, A., Ochoa-Espinosa, A., Scholz, O., Sprecher, S. G., Plütkthun, A. and Afholter, M. (2014). Protein interference applications in cellular and developmental biology using DARPins that recognize GFP and mCherry. *Biol. Open* **3**, 1252-1261. doi:10.1242/bio.201410041
- Caussinus, E., Kanca, O. and Afholter, M. (2011). Fluorescent fusion protein knockout mediated by anti-GFP nanobody. *Nat. Struct. Mol. Biol.* **19**, 117-121. doi:10.1038/nsmb.2180
- Cheeseman, L. P., Harry, E. F., McAnish, A. D., Prior, I. A. and Royle, S. J. (2013). Specific removal of TACC3-ch-TOG-clathrin at metaphase deregulates kinetochore fiber tension. *J. Cell Sci.* **126**, 2102-2113. doi:10.1242/jcs.124834
- Clarke, N. I. and Royle, S. J. (2018). FerriTag is a new genetically-encoded inducible tag for correlative light-electron microscopy. *Nat. Commun.* **9**, 2604. doi:10.1038/s41467-018-04993-0
- Damke, H., Baba, T., Warnock, D. E. and Schmid, S. L. (1994). Induction of mutant dynamin specifically blocks endocytic coated vesicle formation. *J. Cell Biol.* **127**, 915-934. doi:10.1083/jcb.127.4.915
- Daniel, K., Icha, J., Horenburg, C., Müller, D., Norden, C. and Mansfeld, J. (2018). Conditional control of fluorescent protein degradation by an auxin-dependent nanobody. *Nat. Commun.* **9**, 3297. doi:10.1038/s41467-018-05855-5
- Derivery, E., Seum, C., Daeden, A., Loubéry, S., Holtzer, L., Jülicher, F. and Gonzalez-Gaitan, M. (2015). Polarized endosome dynamics by spindle asymmetry during asymmetric cell division. *Nature* **528**, 280-285. doi:10.1038/nature16443
- Derivery, E., Bartolami, E., Matile, S. and Gonzalez-Gaitan, M. (2017). Efficient delivery of quantum dots into the cytosol of cells using cell-penetrating poly(disulfide)s. *J. Am. Chem. Soc.* **139**, 10172-10175. doi:10.1021/jacs.7b02952
- Doyon, J. B., Zeitler, B., Cheng, J., Cheng, A. T., Cherone, J. M., Santiago, Y., Lee, A. H., Vo, T. D., Doyon, Y., Miller, J. C. et al. (2011). Rapid and efficient clathrin-mediated endocytosis revealed in genome-edited mammalian cells. *Nat. Cell Biol.* **13**, 331-337. doi:10.1038/ncb2175
- Hansen, S. H., Sandvig, K. and van Deurs, B. (1993). Clathrin and HA2 adaptors: effects of potassium depletion, hypertonic medium, and cytosol acidification. *J. Cell Biol.* **121**, 61-72. doi:10.1083/jcb.121.1.61
- Haruki, H., Nishikawa, J. and Laemmli, U. K. (2008). The anchor-away technique: rapid, conditional establishment of yeast mutant phenotypes. *Mol. Cell* **31**, 925-932. doi:10.1016/j.molcel.2008.07.020
- Huh, W.-K., Falvo, J. V., Gerke, L. C., Carroll, A. S., Howson, R. W., Weissman, J. S. and O'Shea, E. K. (2003). Global analysis of protein localization in budding yeast. *Nature* **425**, 686-691. doi:10.1038/nature02026
- Jinek, M., East, A., Cheng, A., Lin, S., Ma, E. and Doudna, J. (2013). RNA-programmed genome editing in human cells. *eLife* **2**, e00471. doi:10.7554/eLife.00471
- Kamiyama, D., Sekine, S., Barsi-Rhyne, B., Hu, J., Chen, B., Gilbert, L. A., Ishikawa, H., Leonetti, M. D., Marshall, W. F., Weissman, J. S. et al. (2016). Versatile protein tagging in cells with split fluorescent protein. *Nat. Commun.* **7**, 11046. doi:10.1038/ncomms11046
- Kanner, S. A., Morgenstern, T. and Colecraft, H. M. (2017). Sculpting ion channel functional expression with engineered ubiquitin ligases. *eLife* **6**, e29744. doi:10.7554/eLife.29744
- Kirchhofer, A., Helma, J., Schmidthals, K., Frauer, C., Cui, S., Karcher, A., Pellis, M., Muyltermans, S., Casas-Delucchi, C. S., Cardoso, M. C. et al. (2010). Modulation of protein properties in living cells using nanobodies. *Nat. Struct. Mol. Biol.* **17**, 133-138. doi:10.1038/nsmb.1727
- Kitagawa, M., Ara, T., Arifuzzaman, M., Ioka-Nakamichi, T., Inamoto, E., Toyonaga, H. and Mori, H. (2005). Complete set of ORF clones of Escherichia coli ASKA library (a complete set of E. coli K-12 ORF archive): unique resources for biological research. *DNA Res.* **12**, 291-299. doi:10.1093/dnares/dsi012
- Kubala, M. H., Kovtun, O., Alexandrov, K. and Collins, B. M. (2010). Structural and thermodynamic analysis of the GFP:GFP-nanobody complex. *Protein Sci.* **19**, 2389-2401. doi:10.1002/pro.519
- Lambert, T. J. (2019). FPbase: a community-editable fluorescent protein database. *Nat. Methods* **16**, 277-278. doi:10.1038/s41592-019-0352-8
- Larocque, G., La-Borde, P. J., Clarke, N. I., Carter, N. J. and Royle, S. J. (2019). Tumor Protein D54 defines a new class of intracellular transport vesicles. *J. Cell Biol.* doi:10.1083/jcb.201812044
- Li, C., Wen, A., Shen, B., Lu, J., Huang, Y. and Chang, Y. (2011). FastCloning: a highly simplified, purification-free, sequence- and ligation-independent PCR cloning method. *BMC Biotechnol.* **11**, 92. doi:10.1186/1472-6750-11-92
- Nagarkar-Jaiswal, S., Lee, P.-T., Campbell, M. E., Chen, K., Anguiano-Zarate, S., Gutierrez, M. C., Busby, T., Lin, W.-W., He, Y., Schulze, K. L., (2015). A library of MiMICs allows tagging of genes and reversible, spatial and temporal knockdown of proteins in Drosophila. *eLife* **4**, e05338. doi:10.7554/eLife.05338
- Nishimura, K., Fukagawa, T., Takisawa, H., Kakimoto, T. and Kanemaki, M. (2009). An auxin-based degron system for the rapid depletion of proteins in nonplant cells. *Nat. Methods* **6**, 917-922. doi:10.1038/nmeth.1401
- Prole, D. L. and Taylor, C. W. (2019). A genetically encoded toolkit of functionalized nanobodies against fluorescent proteins for visualizing and manipulating intracellular signalling. *BMC Biol.* **17**, 41. doi:10.1186/s12915-019-0662-4
- Roberts, B., Haupt, A., Tucker, A., Grancharova, T., Arakaki, J., Fuqua, M. A., Nelson, A., Hookway, C., Ludmann, S. A., Mueller, I. A. et al. (2017). Systematic gene tagging using CRISPR/Cas9 in human stem cells to illuminate cell organization. *Mol. Biol. Cell* **28**, 2854-2874. doi:10.1091/mbc.e17-03-0209
- Robinson, M. S., Sahlender, D. A. and Foster, S. D. (2010). Rapid inactivation of proteins by rapamycin-induced rerouting to mitochondria. *Dev. Cell* **18**, 324-331. doi:10.1016/j.devcel.2009.12.015
- Rothbauer, U., Zolghadr, K., Muyltermans, S., Schepers, A., Cardoso, M. C. and Leonhardt, H. (2008). A versatile nanotrapping for biochemical and functional studies with fluorescent fusion proteins. *Mol. Cell Proteomics* **7**:282-289. doi:10.1074/mcp.M700342-MCP200
- Schornack, S., Fuchs, R., Huitema, E., Rothbauer, U., Lipka, V. and Kamoun, S. (2009). Protein mislocalization in plant cells using a GFP-binding chromobody. *Plant J.* **60**, 744-754. doi:10.1111/j.1365-3113.2009.03982.x
- Snapp, E. (2005). Design and use of fluorescent fusion proteins in cell biology. *Curr. Protoc. Cell Biol.* **21**, 21.4.1-21.4.13. doi:10.1002/0471143030.cb2104s27
- Tian, G.-W., Mohanty, A., Chary, S. N., Li, S., Paap, B., Drakakaki, G., Kopec, C. D., Li, J., Ehrhardt, D., Jackson, D. et al. (2004). High-throughput fluorescent tagging of full-length Arabidopsis gene products in planta. *Plant Physiol.* **135**, 25-38. doi:10.1104/pp.104.040139
- Wang, S. and Hazelrigg, T. (1994). Implications for bcd mRNA localization from spatial distribution of exu protein in Drosophila oogenesis. *Nature* **369**, 400-403. doi:10.1038/369400a0
- Wood, L. A., Larocque, G., Clarke, N. I., Sarkar, S. and Royle, S. J. (2017). New tools for "hot-wiring" clathrin-mediated endocytosis with temporal and spatial precision. *J. Cell Biol.* **216**, 4351-4365. doi:10.1083/jcb.201702188
- Yamaguchi, N., Colak-Champollion, T. and Knaut, H. (2019). zGrad is a nanobody-based degron system that inactivates proteins in zebrafish. *eLife* **8**, e43125. doi:10.7554/eLife.43125
- Zhao, N., Kamijo, K., Fox, P., Oda, H., Morisaki, T., Sato, Y., Kimura, H. and Stasevich, T. J. (2019). A genetically encoded probe for imaging nascent and mature HA-tagged proteins in vivo. *Nat. Commun.* **10**, 2947. doi:10.1038/s41467-019-10846-1

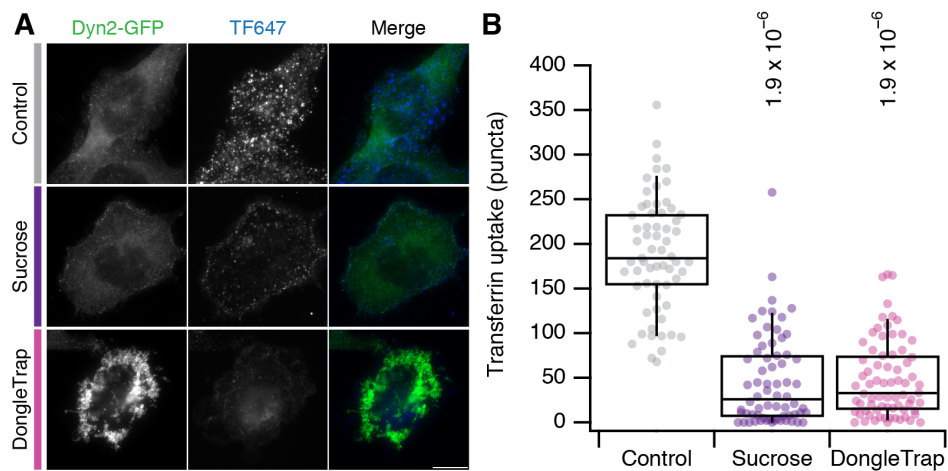


Figure S1. DongleTrap inhibits clathrin-mediated endocytosis in SK-MEL-2 hDNM2^{EN-all} cells

A, Micrographs of SK-MEL-2 hDNM2^{EN-all} cells. Untransfected cells, control (gray) or sucrose-treated (purple), or cells expressing DongleTrap (pink) are shown. DN2-GFP (green) and transferrin-Alexa647 (blue) are displayed using the same minimum and maximum value per channel for all images in the figure. Scale bar, 10 μ m.

B, Box plot to show quantification of transferrin uptake. Expression or treatments are as indicated and colored as in A. Dots represent individual cells from multiple experiments. Box represents the IQR, the line the median and the whiskers the 9th and 91st percentile. $n_{\text{cell}} = 49 - 68$, $n_{\text{exp}} = 3$. P-values from Dunnett's *post hoc* test are shown (Compared to Control).

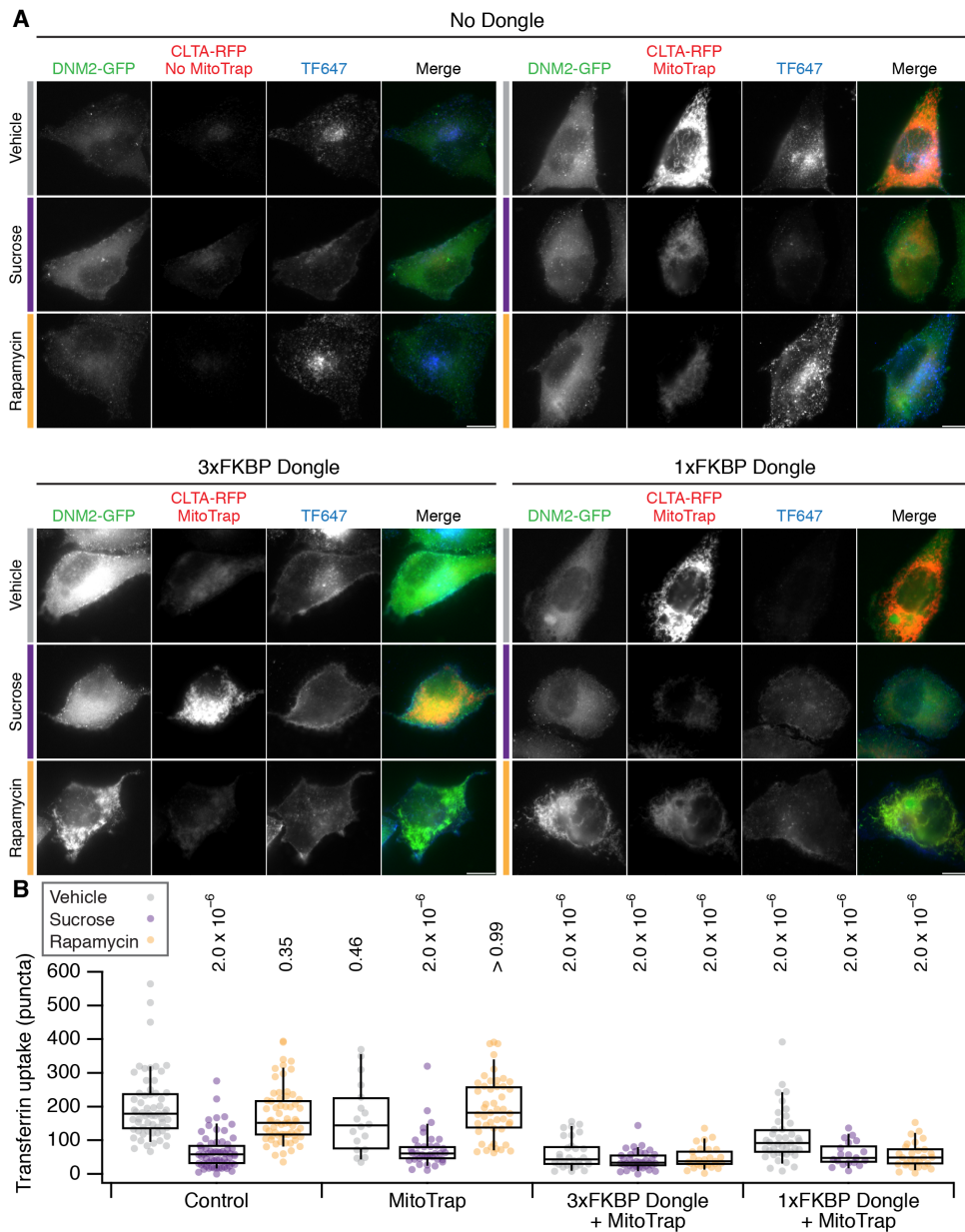
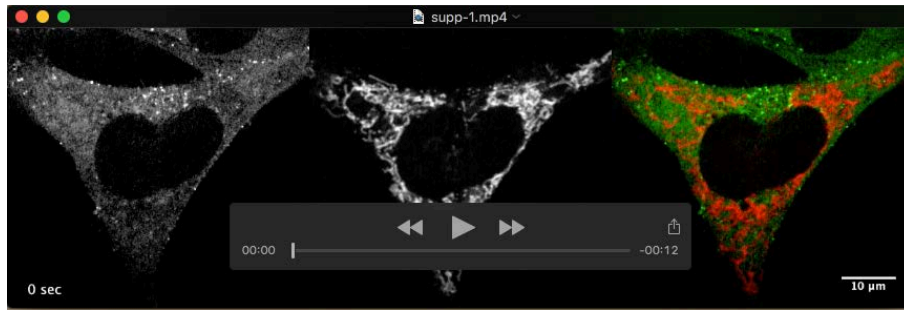


Figure S2. Effect of dongle expression on transferrin uptake in SK-MEL-2 hCLTA^{EN}/hDNM2^{EN} cells

A, Micrographs of SK-MEL-2 hCLTA^{EN}/hDNM2^{EN} cells treated with vehicle (gray), sucrose (purple) or 200 nM rapamycin (orange). Cells were untransfected (No Dongle, No Mitotrap), or expressed MitoTrap alone, or MitoTrap with 3xFKBP Dongle or 1xFKBP Dongle. DNM2-GFP (green), CLTA-RFP + MitoTrap (red) and transferrin-Alexa647 (blue) are displayed using the same minimum and maximum value per channel for all images in the figure. Note that MitoTrap and CLTA-RFP appear in the same channel. Scale bars, 10 μ m.

B, Box plot to show quantification of transferrin uptake. Expression and treatments are as indicated and colored as in A. Dots represent individual cells from multiple experiments. Box represents the IQR, the line the median and the whiskers the 9th and 91st percentile. P-values from Dunnett's *post hoc* test are shown (Control-Vehicle as the control group). $n_{\text{cell}} = 19 - 64$, $n_{\text{exp}} = 3$.



Movie 1. Knocksideways of DNM2-GFP using 3xFKBP Dongle.

Live cell confocal microscopy of dongle-knocksideways, 200 nM rapamycin is added at 10 s. Dynamin-2-GFP (left, green) and MitoTrap (middle, red) are shown together with a merge (right). Time, seconds. Scale bar, 10 μ m.

Appendix C

ARTICLE

Intracellular nanovesicles mediate $\alpha 5\beta 1$ integrin trafficking during cell migration

Gabrielle Larocque¹, Daniel J. Moore¹, Méghane Sittewelle¹, Cansu Kuey¹, Joseph H.R. Hetmanski², Penelope J. La-Borde¹, Beverley J. Wilson², Nicholas I. Clarke¹, Patrick T. Caswell², and Stephen J. Royle¹

Membrane traffic is an important regulator of cell migration through the endocytosis and recycling of cell surface receptors such as integrin heterodimers. Intracellular nanovesicles (INVs) are transport vesicles that are involved in multiple membrane trafficking steps, including the recycling pathway. The only known marker for INVs is tumor protein D54 (TPD54/TPD52L2), a member of the TPD52-like protein family. Overexpression of TPD52-like family proteins in cancer has been linked to poor prognosis and an aggressive metastatic phenotype, which suggests cell migration may be altered under these conditions. Here, we show that TPD54 directly binds membrane and associates with INVs via a conserved positively charged motif in its C terminus. We describe how other TPD52-like proteins are also associated with INVs, and we document the Rab GTPase complement of all INVs. Depletion of TPD52-like proteins inhibits cell migration and invasion, while their overexpression boosts motility. We show that inhibition of migration is likely due to altered recycling of $\alpha 5\beta 1$ integrins in INVs.

Introduction

Cell migration is important for many aspects of animal physiology, including the immune response, tissue integrity, and embryonic development. This process is tightly controlled, and any alterations can result in diseases such as inflammation or cancer (Hamidi and Ivaska, 2018; Friedl and Wolf, 2003). Membrane traffic is a key regulator of cell migration through the trafficking of cell surface receptors, including integrins, which bind the ECM. Integrins are endocytosed and recycled back to the cell surface in order to break and reestablish the cellular contacts with the ECM during migration. A prototypical example is $\alpha 5\beta 1$ integrin, which binds to fibronectin. The molecular details of integrin trafficking pathways and their influence on cell motility are under active investigation (Wilson et al., 2018).

The identity and activation state of integrin heterodimers govern their trafficking and fate (Wilson et al., 2018). Rabs are master regulators of membrane traffic with >60 different Rabs in human cells, with each one mediating a trafficking step specifically (Wandinger-Ness and Zerial, 2014). Rabs are involved in every step of integrin traffic, as well as binding integrins directly or via one of the many Rab effector proteins (Pellinen et al., 2006; Caswell et al., 2008).

A new class of intracellular transport vesicle, termed intracellular nanovesicles (INVs), has recently been described (Larocque et al., 2020). INVs are involved in recycling and

anterograde trafficking pathways. These vesicles are small (~30 nm diameter) and highly dynamic and are associated collectively with ~16 different Rab GTPases (Larocque et al., 2020). Among the Rabs present on INVs are Rab11a and Rab25, two Rabs well known for their involvement in integrin trafficking (Roberts et al., 2001; Caswell et al., 2007; Moreno-Layseca et al., 2019). INVs were discovered because of their association with TPD54, a member of the tumor protein D52-like protein family (TPD52, TPD53/TPD52L1, TPD54/TPD52L2, and TPD55/TPD52L3). How TPD54 associates with INVs and whether the other members of the TPD52-like protein family behave similarly are important open questions.

TPD52-like proteins were identified due to their overexpression in a number of cancer types (Byrne et al., 1995, 1996; Nourse et al., 1998; Cao et al., 2006). This up-regulation is often caused by gene duplication, which is tumorigenic (Balleine et al., 2000; Lewis et al., 2007). Tumorigenicity has been proposed to be due to alteration of either the cell cycle (Boutros and Byrne, 2005; Thomas et al., 2010; Lewis et al., 2007), signaling (Li et al., 2017), or DNA repair (Chen et al., 2013). Finally, TPD52-like proteins have been reported to have a role in cell migration and adhesion; however, the underlying mechanism is unknown (Ummanni et al., 2008; Mukudai et al., 2013). In breast cancer, TPD52 overexpression correlates with poor prognosis and a

¹Centre for Mechanochemical Cell Biology, Warwick Medical School, Coventry, UK; ²Wellcome Trust Centre for Cell-Matrix Research, Faculty of Biology, Medicine and Health, University of Manchester, Manchester Academic Health Science Centre, Manchester, UK.

Correspondence to Stephen J. Royle: s.j.royle@warwick.ac.uk; G. Larocque's present address is Cellular Signalling and Cytoskeletal Function Laboratory, The Francis Crick Institute, London, UK.

© 2021 Larocque et al. This article is available under a Creative Commons License (Attribution 4.0 International, as described at <https://creativecommons.org/licenses/by/4.0/>).

decrease in metastasis-free survival (Roslan et al., 2014; Shehata et al., 2008). This suggested to us that TPD52-like proteins, and the INVs they are associated with, may be involved in cell migration and invasion in cancer.

In this paper, we show how TPD52-like proteins associate with INVs and document the Rab complement of INVs decorated with TPD52, TPD53, or TPD54. We find that depletion of TPD52-like proteins inhibits cell migration and invasion, and we show that this is likely due to altered $\alpha 5\beta 1$ integrin recycling via INVs.

Results

Molecular determinants required for the association of TPD54 with INVs

We previously found that TPD54 is tightly associated with INVs and that its association with these fast-moving subresolution vesicles could be measured by spatiotemporal variance of fluorescence microscopy images (Larocque et al., 2020). Here, we asked what are the molecular determinants for the association of TPD54 with INVs. Analysis of the primary sequences of TPD52-like proteins reveals two domains: (1) a coiled-coil domain between residues 38 and 82 (Fig. 1 A) and (2) a region between residues 126 and 180 with high similarity among human TPD52-like proteins. Within this region, residues 159–171 (Fig. 1 A) are particularly well conserved across different species. With these regions in mind, we designed mCherry-FKBP-tagged TPD54 constructs to pinpoint which region of the protein was required for its association with INVs (Fig. 1, B and C). The spatiotemporal variance of fluorescence for mCherry-FKBP-TPD54 full length was much higher than that of the control mCherry-FKBP, which is to be expected due to the association of TPD54 with mobile, subresolution vesicles such as INVs (Fig. 1 B and C; and Video 1). The spatiotemporal variance of TPD54 constructs revealed that the C-terminal portion of TPD54 (155–180) was needed for INV localization (Fig. 1 B). Constructs that lacked this region (1–37, 1–82, 38–82, and 1–155) had low variance, while those that contained it (1–206, 83–206, and 1–180) had higher variance. However, while this region was necessary for localization, it was not sufficient, since 155–180, 155–206, 126–180, and 126–206 did not have high spatiotemporal variance.

The region around residues 155–180 contains several positively charged residues (Fig. 1 A), suggesting that this region could bind direct to the INV membrane. Mutation of R95, K154, R159, K165, or K175/K177 to glutamic acid reduced the spatiotemporal variance to levels similar to control (Fig. 1, B and C). A similar mutation (K15E) in the N-terminal part of TPD54 had no significant effect. These experiments establish that positively charged residues around the conserved 155–180 region of TPD54 are important for its association with INVs.

TPD54 directly binds liposomes in vitro

The association of TPD54 with INVs could either be direct or via another membrane-associated protein. We therefore investigated whether TPD54 was able to bind vesicles directly using a liposome-binding assay. From a Folch extract of brain lipids, we generated liposomes of four different sizes (30, 50, 100, and 200 nm) and tested for cosedimentation of GST, GST-TPD54, or GST-

TPD54 mutants with these liposomes (Fig. 2 A). We observed specific cosedimentation of GST-TPD54 proteins, but not GST alone, with liposomes of all sizes (Fig. 2 A). To quantify this direct membrane binding, we first measured the efficiency of liposome pelleting since smaller liposomes sediment less efficiently (Boucrot et al., 2012) and are less abundant (see Materials and methods; Fig. 2, B and C). Quantification of cosedimentation, accounting for liposome pelleting efficiency, revealed that GST-TPD54 bound 30 nm and 50 nm tighter than larger-diameter liposomes (Fig. 2, A and D). GST-TPD54(1–82) showed no binding and was indistinguishable from GST alone, indicating that the C-terminal portion of TPD54 was responsible for direct binding (Fig. 2 D). However, mutation of R169E, K154E, K175,177E, or K165E did not reduce membrane association in this assay. Indeed deletion of the C-terminal conserved region displayed similar binding to full-length TPD54 (1–155; Fig. 2 E). These results indicate that TPD54 can bind to membranes directly and that this is conferred by residues 83–155. However, the lack of effect of mutation of the C-terminal domain suggests that the liposomes in this assay are missing one or more factors that are present on INVs in cells.

Positive residues in the conserved C-terminal region of TPD54 are required for INV association

To tackle the apparent discrepancy between spatiotemporal variance measurements in cells and in vitro liposome-binding experiments, we used an alternative method to test for association of TPD54 constructs with INVs. Previously, we found that rerouting an FKBP-tagged TPD54 construct to MitoTrap on mitochondria using rapamycin causes mitochondrial aggregation due to capture of INVs (Fig. 3, A and B; Larocque et al., 2020). We therefore tested the TPD54 constructs using this method and measured mitochondrial aggregation in confocal micrographs with automated image analysis (Fig. 3, C and D). Generally, the constructs that exhibited high spatiotemporal variance caused significant mitochondrial aggregation, whereas the mitochondria were unaffected by the rerouting of constructs that had showed low variance (Fig. 3, C and D). The only exceptions were R95E and K165E; rerouting of either mutant induced mitochondrial aggregation to some extent. The results from the two cellular assays underline the importance of positive residues K154, R159, K175, and K177 in the conserved C-terminal region of TPD54 for binding INVs. Moreover, residues 83–125 are also required for binding, since 83–206, but not 126–206, was associated with INVs (Figs. 1 C and 3 D). Altogether, our results indicate that there are two regions of TPD54 that are each necessary for association with INVs, but neither region is sufficient by itself. A region between 83–125 is required for membrane binding whereas positive charge in the conserved C-terminal domain is needed for specific association with INVs in cells.

TPD52-like proteins can homo- and heteromerize via the coiled-coil domain, but multimerization is dispensable for INV binding

It is likely that TPD54 can form homomers or heteromers with other TPD52-like proteins via their coiled-coil domains (Byrne

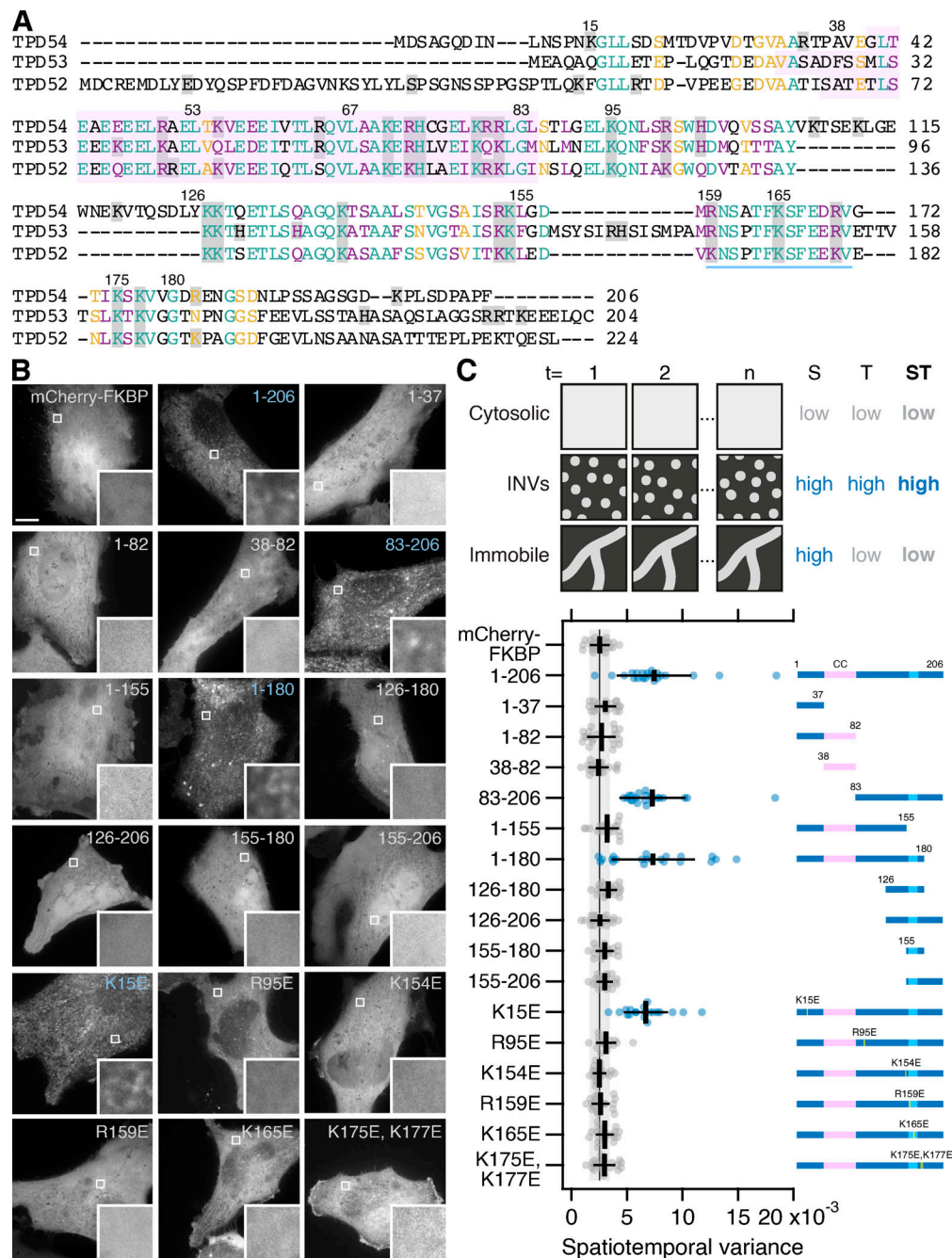


Figure 1. **Identification of the region required for the association of TPD54 with INVs.** (A) Alignment of human TPD54/TPD52L2 (UniProt accession no. O43399), TPD53/TPD52L1 (UniProt accession no. Q16890) and TPD52/TPD52L1 (UniProt accession no. P55327). Numbers indicate residue positions in TPD54. Pink highlighted area represents the coiled-coil domain (predicted with PCOILS, window size 28). Blue underlining indicates C-terminal conserved region. Gray shadowing shows positively charged residues. Lettering: teal, fully conserved residues; purple, strongly similar (>0.5 in the Gonnet PAM 250 matrix); and yellow, weakly similar (<0.5 in the Gonnet PAM 250 matrix). (B) Representative confocal micrographs of HeLa cells expressing mCherry-FKBP or mCherry-FKBP-tagged TPD54 FL (1-206) or indicated mutants. Blue labels indicate high variance measured in C. Inset: 4 \times zoom. Scale bar, 10 μ m or 1 μ m (inset). (C) Schematic diagram to show how spatiotemporal (ST) variance can be used to measure association with motile vesicular structures such as INVs. Spatial (S) and temporal (T) variance is shown for comparison. Scatter dot plot to show the spatiotemporal variance (mean variance per pixel over time) for the indicated constructs. Dots, individual cells; black bars, mean \pm SD. The mean \pm SD for mCherry-FKBP (control) is also shown as a black line and gray zone, down the plot. Dunnett's post hoc test was done using mCherry-FKBP as control; blue indicates $P < 0.05$. Right: Representation of the mCherry-FKBP-tagged TPD54 constructs analyzed. Pink region, coiled-coil domain (CC). Yellow line, position of point mutation. Light blue region, underlined area in A.

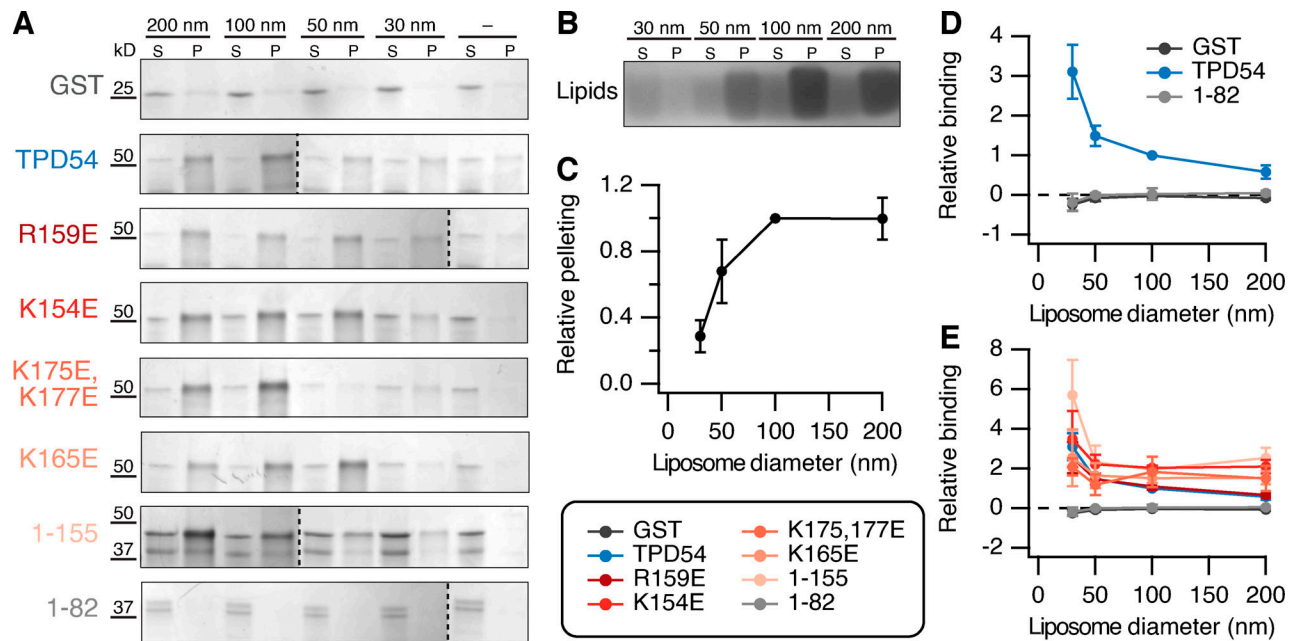


Figure 2. TPD54 directly associates with liposomes in vitro. (A) Cosedimentation of GST, GST-TPD54 WT, or GST-TPD54 mutants as indicated with differently sized liposomes (diameter indicated) or no liposomes (-), visualized on an InstantBlue-stained 4% to 12% gel. S, supernatant; P, pellet. (B) Pelleting of differently sized liposomes visualized on a Coomassie-stained Bis-Tris gel showing lipid stain. (C) Quantification of the pelleting efficiency of liposomes according to their size. Values are normalized to 100 nm liposomes. Points show mean \pm SD; $n = 3$. (D) Quantification of protein cosedimentation with differently sized liposomes. The binding of GST (dark gray), GST-TPD54 (WT, blue), or GST-TPD54 (1-82, light gray) is shown relative to TPD54 binding to 100 nm. (E) Quantification as in D, but with all mutants overlaid. Points show mean \pm SEM; $n = 3$, except $n = 6$ for GST, TPD54, and R159E.

et al., 1998; Sathasivam et al., 2001; Larocque et al., 2020). This raises the question of whether the association with INVs requires multimerization. To answer this point, we sought a TPD54 mutant that was incapable of multimerization. Mutation of two leucines to prolines is predicted to break the coiled-coil domain of TPD54 (L53P,L67P; Figs. 1 A and 4 A), and we tested whether these mutations interfered with homo- and heteromerization in cells. FLAG-tagged TPD52-like proteins were immunoprecipitated from cells coexpressing GFP-FKBP, GFP-FKBP-TPD54, or GFP-FKBP-TPD54(L53P,L67P). We found that TPD54 WT, but neither the control nor the mutant, could be coimmunoprecipitated with FLAG-tagged TPD52, TPD53, or TPD54 (Fig. 4 B). These results confirmed that the coiled-coil domain of TPD54 is responsible for homo- and heteromerization and that the L53P,L67P mutation blocks multimerization. Note that we assume that multimerization is direct between TPD52-like protein monomers, but our experiments do not rule out an intermediary protein. Next, we found that the localization of the L53P,L67P mutant was normal and its spatiotemporal variance was similar to WT TPD54, suggesting that it was associated with INVs (Fig. 4, C and D). This result is in agreement with the finding that a TPD54 construct lacking the coiled-coil region (83–206) is localized to INVs (Figs. 1 C and 3 D). Together these results indicate that monomeric TPD54 can associate with INVs and that multimerization is not required.

TPD52 and TPD53 are associated with INVs

Given the similarity of TPD52-like proteins and the conservation of the residues involved in INV association (Fig. 1 A), it is likely

that TPD52 and TPD53 are also found on INVs. Indeed, live-cell imaging indicates that they have a similar subcellular distribution and spatiotemporal variance (Video 2). The TPD54(L53P,L67P) mutant allowed us to ask whether other TPD52-like proteins are associated with INVs independently of TPD54. To do this, we used the mitochondrial INV-capture procedure using mCherry-FKBP-TPD54 or mCherry-FKBP-TPD54(L53P,L67P). We found that when GFP-TPD52 is coexpressed, it also becomes rerouted to the mitochondria (Fig. 5 A). This indicated that not only is TPD52 on INVs but also its association is likely direct and not via recruitment by TPD54. To confirm that TPD52 is an INV protein, we used correlative light EM (CLEM) to visualize the capture of INVs when GFP-FKBP-TPD52 was rerouted to mitochondria (Fig. 5 B).

To test whether TPD52 and TPD53 were bound to INVs independently of TPD54, we used the mitochondrial aggregation assay. Significant aggregation was seen for GFP-FKBP-tagged TPD52, TPD53, or TPD54 in control cells or those depleted of endogenous TPD54 by RNAi (Fig. 5, B and C). We noted that aggregation was less efficient for TPD53 compared with TPD52 or TPD54, suggesting that TPD53 is less efficiently targeted to INVs. These results confirm that TPD52-like proteins bind INVs and do so independently of TPD54.

TPD52 and TPD53 are associated with different subsets of INVs

INVs are involved in many trafficking pathways, since they collectively have a variety of Rab GTPases (Larocque et al., 2020). This was demonstrated by using mCherry-FKBP-TPD54 in a vesicle capture assay and asking which GFP-Rabs were

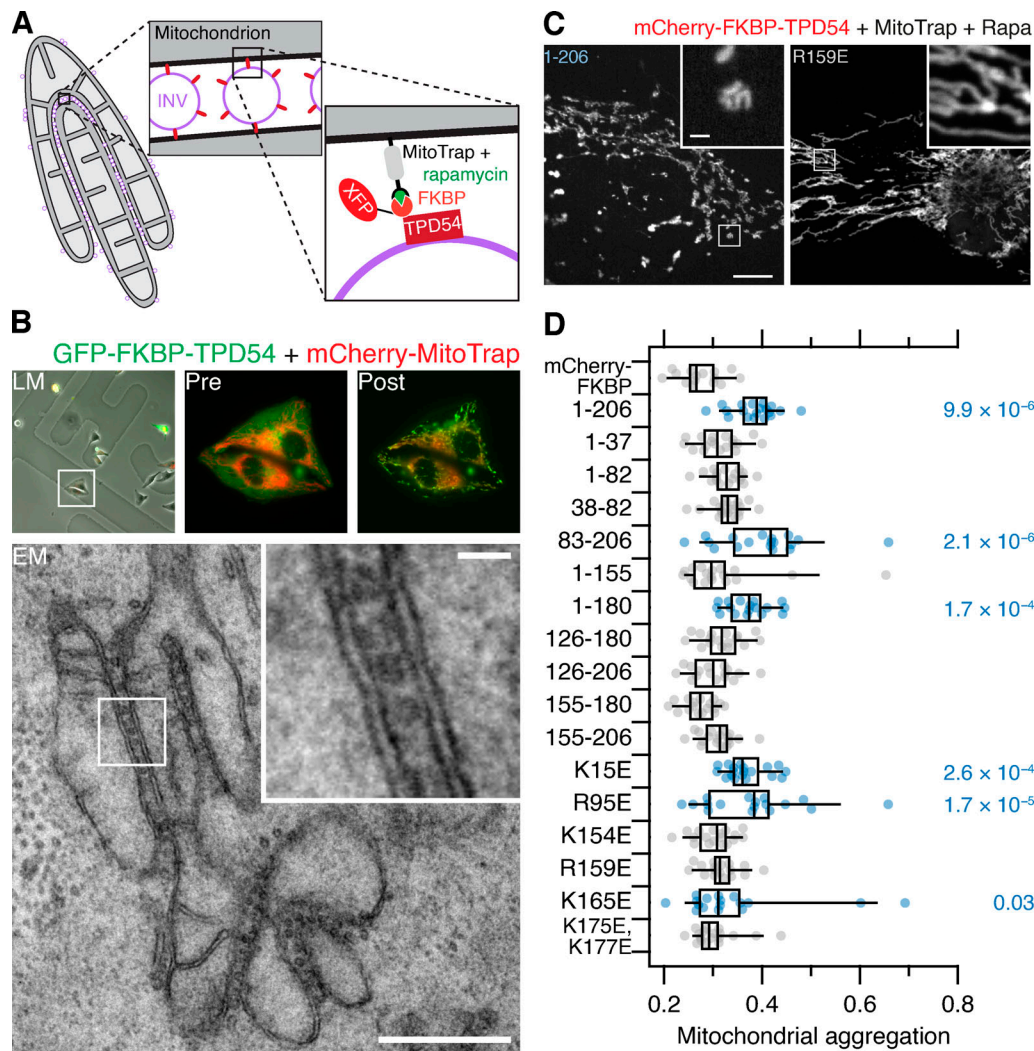


Figure 3. **INV-induced mitochondrial aggregation as an assay for TPD54 binding to INVs.** (A) Schematic diagram of vesicle capture at mitochondria and their subsequent aggregation. MitoTrap is an FRB domain targeted to mitochondria, XFP-FKBP-TPD54 (XFP is GFP or mCherry) is coexpressed, and, when rapamycin is added, the INVs associated with TPD54 become trapped at the mitochondria, eventually causing aggregation of mitochondria. (B) CLEM experiment to demonstrate INVs between aggregated mitochondria. Cells expressing GFP-FKBP-TPD54 and mCherry-MitoTrap were imaged before light microscopy (LM), before (Pre) and after (Post) rapamycin 200 nM addition for 3 min. An ultrathin section of the same cell is shown by transmission EM. Inset: 4x zoom. Scale bars, 500 nm or 50 nm (insets). (C) Representative confocal micrographs of HeLa cells expressing dark MitoTrap and either mCherry-FKBP-TPD54 WT (1-206) or R159E mutant, treated with 200 nM rapamycin. Inset: 5x zoom. Scale bars, 10 μm or 1 μm (inset). (D) Quantification of mitochondrial aggregation in cells expressing mCherry-FKBP-tagged TPD54 constructs and GFP-MitoTrap, treated with 200 nM rapamycin for 30 min. Dots show average mitochondrial shape (high values are more aggregated) per cell (see Materials and methods). Box plots show interquartile range (IQR), bar represents the median, and whiskers show 9th and 91st percentiles. Dunnett's post hoc test was done using mCherry-FKBP as control; blue indicates $P < 0.05$.

corerouted to mitochondria. Since TPD52 and TPD53 also are on INVs, we wanted to know if all INVs have TPD54 or if there are subsets of INVs with different TPD52-like proteins. To investigate this point, we performed mitochondrial vesicle capture and quantified the corerouting of GFP-Rabs to mitochondria using either mCherry-FKBP-TPD52 (Fig. 6, A and B) or mCherry-FKBP-TPD53 (Fig. 6, C and D). Of the 39 Rabs tested, 16 corerouted with TPD52 and 9 corerouted with TPD53. As with TPD54, Rab30 was the strongest hit with TPD52 (Fig. 6 B) and TPD53 (Fig. 6 D). This suggests that Rab30 is the Rab GTPase most likely to be associated with INVs and can be thought of as an "INV Rab." The other Rabs corerouted with TPD52 were Rab14, Rab26, Rab1a, Rab1b, Rab10, Rab17, Rab33a, Rab19b,

Rab4a, Rab3a, Rab25, Rab21, Rab12, and Rab43. Of these, only Rab21 had not been identified in the TPD54 screen (Larocque et al., 2020). The Rabs corerouted with TPD53 were Rab30, Rab1b, Rab26, Rab1a, Rab33b, Rab43, Rab19b, Rab14, Rab12, and Rab10; all of which also corerouted with both TPD54 and TPD52. To classify INVs in a more stringent manner, we used hierarchical clustering of the mean mitochondrial intensity change of GFP-Rabs in the TPD52 and TPD53 vesicle capture screens (Fig. 6, A and C), together with the previously published TPD54 screen (Fig. 7 A). This resulted in the classification shown in Fig. 7 B.

The GFP-Rabs that were top hits in the vesicle capture screens all had subcellular distributions at steady state that were

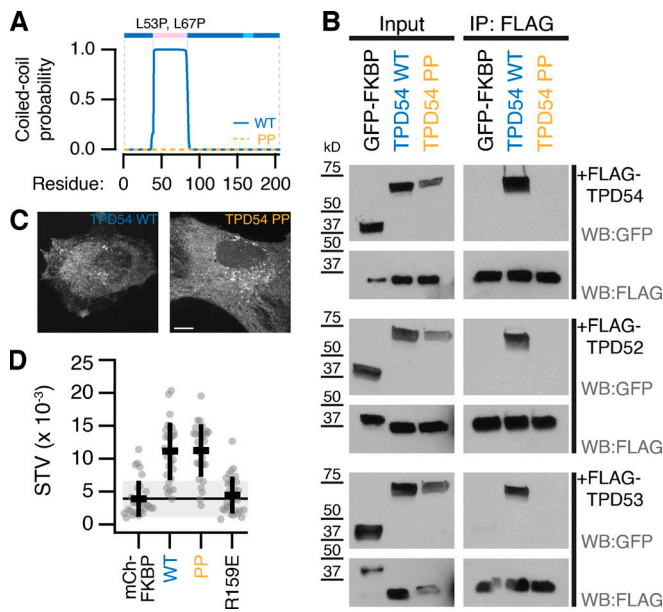


Figure 4. TPD54 homo- and heteromerizes using its coiled-coil domain. (A) Schematic representation of TPD54 and a graph showing the coiled-coil probability for WT and L53P,L67P (PP) mutant. Pink, coiled-coil domain; light blue, conserved region. For coiled-coil domain prediction, the amino acid sequences of TPD54 isoform 1 WT or TPD54(L53P,L67P) were analyzed by PCOILS with window size of 28 (Gruber et al., 2006). (B) Western blot (WB) showing immunoprecipitation (IP) of FLAG-TPDs and coimmunoprecipitation of GFP-FKBP, GFP-FKBP-TPD54 (WT) or GFP-FKBP-TPD54(L53P,L67P; PP). (C) Representative confocal image of mCherry-FKBP-TPD54 (TPD54 WT) or mCherry-FKBP-TPD54(L53P,L67P; TPD54 PP) expressed in HeLa cells. Scale bar, 10 μ m. (D) Scatter dot plot to show the spatiotemporal variance (STV) of the indicated constructs. Dots, individual cells; black bars, mean \pm SD. The mean \pm SD for mCherry-FKBP (control) is also shown as a black line and gray zone. Values for R159E are shown as a negative control. WT and PP, $P = 1.9 \times 10^{-6}$; Dunnett's post hoc test using mCherry-FKBP as control.

similar to that of TPD52-like proteins (Video 3). This suggested that if we quantify the spatiotemporal variance of individual Rabs, we could determine which Rabs are associated with INVs, to verify the results from the vesicle capture screens. Broadly, the Rabs that corerouted with one or more TPD52-like protein had high spatiotemporal variance and those that did not had lower variance (Fig. 7 C). This analysis verified that these Rabs were present on INVs that were positive for TPD52-like proteins. In theory, this approach could also be used to identify INVs that lacked TPD52-like proteins. Indeed, high variance was seen for Rab18, Rab9a, and Rab15, although none of these Rabs were corerouted with any of the three TPD52-like proteins tested (Fig. 7 C). Close inspection of these movies, however, suggest that the high variance of these Rabs is likely a false positive, since they are present on larger structures and not subresolution vesicles.

In summary, this analysis suggests that there are four INV populations. The first population has all three TPD52-like proteins and either Rab30, Rab14, Rab1a, Rab1b, or Rab26. The second population is identified by a predominance of TPD52 and Rab10 or Rab17; the third by the predominance of TPD54 and Rab4a, Rab25, or Rab3a; and the fourth by TPD53 and Rab33b or Rab19b. There are also intermediates (TPD52 and/or TPD54 with Rab11a and TPD53 and/or TPD54 with Rab12 or Rab43; Fig. 7 B).

Taken together, the data highlight the existence of different populations of INVs, marked by various Rabs, but all characterized by the presence of at least one member of the TPD52-like protein family.

Amplification of TPD52-like proteins in cancers and potential changes in cell migration

Previous work showed that TPD52-like proteins are overexpressed in several cancer types (Nourse et al., 1998; Byrne et al., 1996), which may be associated with a more metastatic phenotype (Roslan et al., 2014; Shehata et al., 2008; Ummanni et al., 2008; Mukudai et al., 2013). To provide a full picture of TPD52-like protein overexpression in cancer, we analyzed The Cancer Genome Atlas PanCancer Atlas (Fig. S1). Amplification of TPD52 and TPD54 was seen in a range of cancers including breast invasive carcinoma, ovarian and uterine cancers, and cancers of the colon and liver. Amplification of TPD53 and TPD55 was less common (Fig. S1 A). Rabs that were associated with INVs and those that were not were also analyzed. Of these, the INV-associated Rab25 had a similar amplification profile to TPD52-like proteins (Fig. S1, B and C). Analysis of the ovarian serous carcinoma dataset showed that of 398 patients, amplification of TPD54 was seen in 29 (7%), amplification of Rab25 in 20 (5%), and a significant cooccurrence in 7 patients (\log_2 odds ratio >3 , $P < 0.001$, and $q < 0.001$). These results prompted us to investigate a potential link between TPD52-like proteins and cell migration and invasion.

TPD52-like proteins are important for 2D and 3D cell migration

We imaged control RPE1 cells and those depleted of TPD54, as they migrated on two different 2D substrates, fibronectin (Fig. 8 and Video 4) or laminin (Fig. S2). Tracking cells over 12 h allowed us to generate a complete assessment of their migratory behavior (Fig. S3). We found that cells depleted of TPD54 by RNAi had a strong reduction in migration speed on both substrates, indicating that this defect is not restricted to a single integrin heterodimer (Huttenlocher and Horwitz, 2011; Figs. 8 A and S2). To check whether the TPD54 RNAi phenotype was the result of an off-target effect, we assessed migration speed on fibronectin of cells treated with a further two TPD54-targeting siRNAs (Fig. 8 B). A similar reduction was seen with all three siRNAs compared with control. We also tested whether the TPD54 RNAi phenotype could be rescued. We compared cells transfected with siCtrl expressing GFP with those transfected with siTPD54 that reexpressed GFP or RNAi-resistant GFP-TPD54 WT (Fig. 8 C). The migration defect was indeed rescued by reexpression of GFP-TPD54, but not GFP alone. More importantly, we wanted to test if the ability to bind to INVs was necessary for the role of TPD54 in migration. TPD54-depleted cells reexpressing a construct that lacked the INV-binding region (GFP-TPD54 1-155) failed to rescue the migration defect (Fig. 8 C). This shows that it is the ability to bind INVs that allows TPD54 to rescue the migration phenotype and implicates INVs in cell migration.

Since depletion of TPD54 reduced migration and overexpression is linked to disease, we next tested the effect of TPD54 overexpression. Overexpression of TPD54 caused a

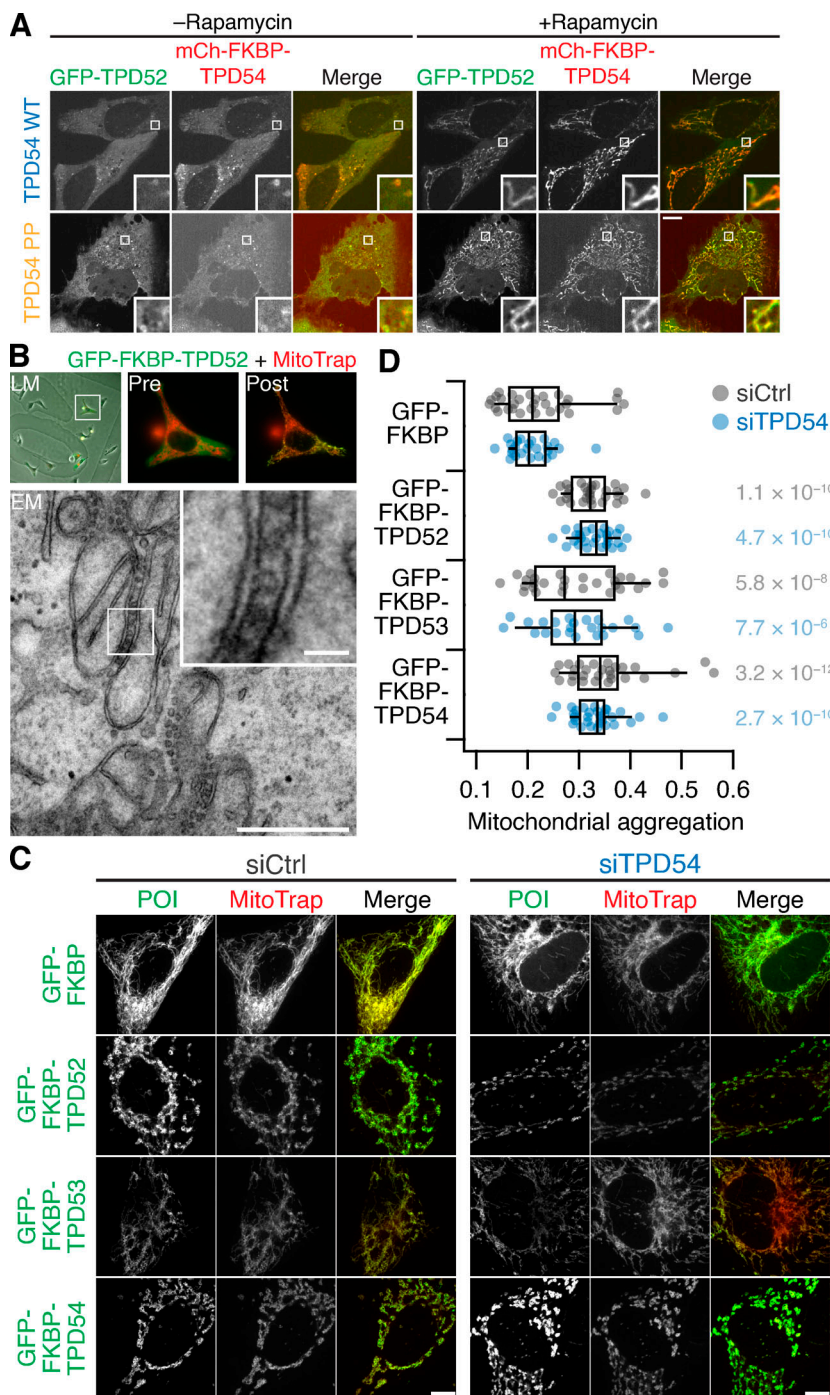


Figure 5. Vesicle capture and mitochondrial aggregation using rerouting of TPD52-like proteins. (A) Representative confocal micrographs showing the co-rerouting of GFP-TPD52 after rerouting of mCherry-FKBP-TPD54 (top) or mCherry-FKBP-TPD54(L53P,L67P; PP; bottom) to dark MitoTrap by addition of 200 nM rapamycin. Inset: 5× zoom. Scale bar, 10 μm. **(B)** CLEM experiment to test for vesicle capture using TPD52. Cells expressing GFP-FKBP-TPD52 and mCherry-MitoTrap with rapamycin 200 nM for 3 min. Insets: 4× zoom. Scale bars, 500 nm or 50 nm (inset). **(C)** Representative confocal micrographs showing rerouting and mitochondrial aggregation. GFP-FKBP (control) or GFP-FKBP-TPD52-like (POI, green) proteins were coexpressed with mCherry-MitoTrap (red) in cells treated with control siRNA (siControl) or TPD54 siRNA as indicated and treated with 200 nM rapamycin for 30 min. Scale bar, 10 μm. **(D)** Quantification of mitochondrial aggregation. Dots show average mitochondrial shape per cell. Box plots show IQR, and bar represents the median and whiskers show 9th and 91st percentiles. Right: P values from Dunnett's post hoc tests using respective GFP-FKBP as control.

significant increase in migration speed of RPE-1 cells on fibronectin compared with expression of GFP alone (Fig. 8 D). No change in speed was observed when the R159E mutant was overexpressed again, suggesting that altered migration depended on INV localization of TPD54.

As we had established that TPD52 and TPD53 are also associated with INVs, we hypothesized that their depletion would also affect migration of cells on fibronectin (Fig. 8, E-G; and Fig. S4). When compared with controls, TPD52-depleted RPE1 cells also showed a significant reduction in migration speed (Fig. 8 E). Similarly, TPD53-depleted cells show a decrease in speed, but there was more variation between experiments, which suggests

a minor role for TPD53 in cell migration in comparison with TPD52 and TPD54, which likely reflects their relative abundance (Fig. 8 F). In addition, overexpression of either TPD52 or TPD53 increased migration speed compared with expression of GFP alone (Fig. 8 G). These experiments argue for functional redundancy among the TPD52-like protein family. When compared with knockdown of TPD54, the dual knockdown of TPD52 and TPD54 or TPD53 and TPD54 did not show an additive effect on migration speed (siGL2, 0.40; si54, 0.32; si52/54, 0.35; and si53/54, 0.36 μm min⁻¹; number of experiments [*n*_{exp}] = 3), suggesting that TPD54 dominates the role of these proteins in cell migration. In summary, TPD52-like proteins have a role in

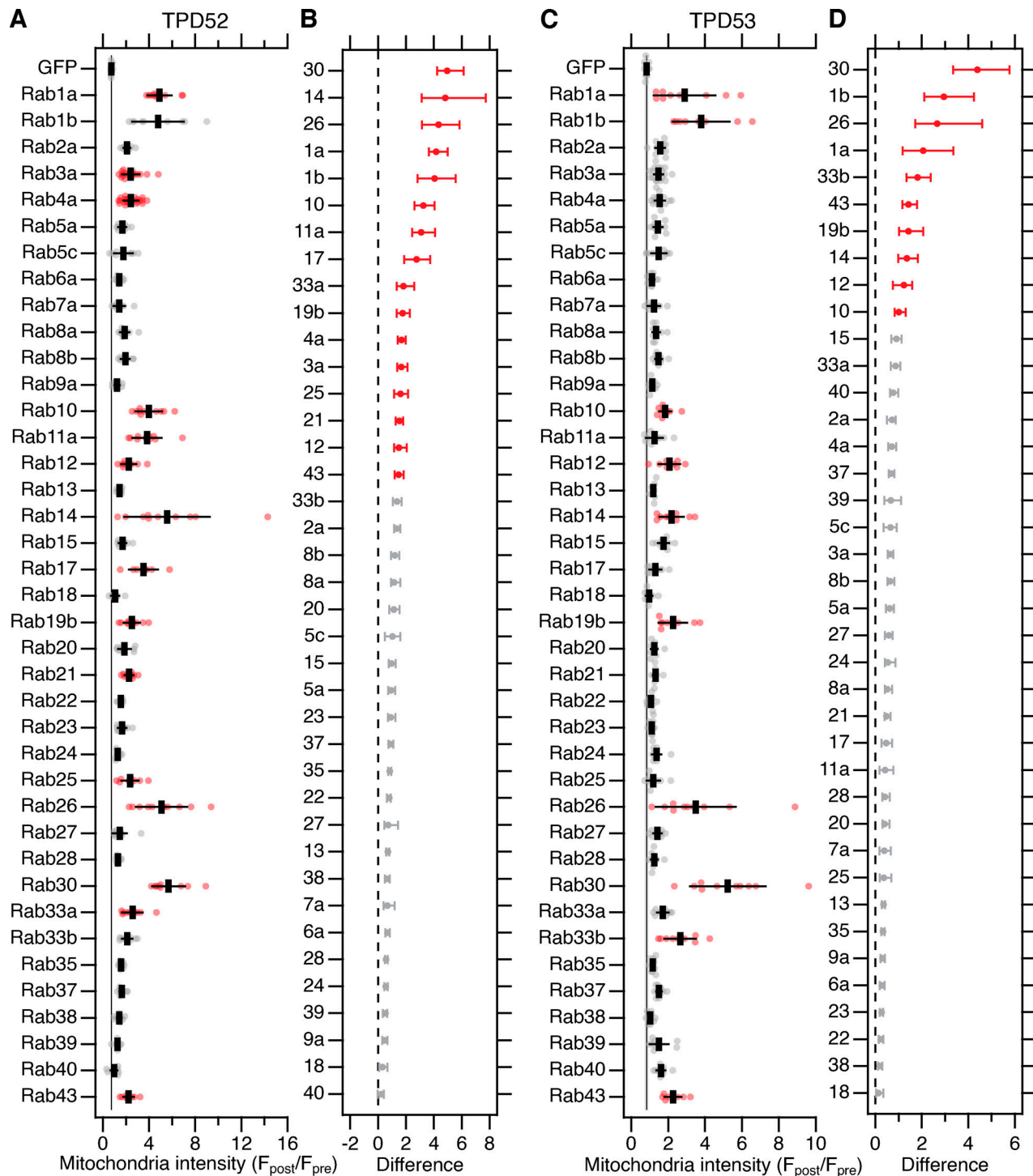


Figure 6. **Screening Rab GTPases that are associated with TPD52 and TPD53 INVs.** (A and C) Quantification of the change in mitochondrial fluorescence intensity of GFP or GFP-Rabs 2 min after rerouting of mCherry-FKBP-TPD52 (A) or mCherry-FKBP-TPD53 (C) to dark MitoTrap with 200 nM rapamycin. F_{post}/F_{pre} is the average fluorescence of indicated GFP-Rab at mitochondria after rerouting ("post") divided by the fluorescence in the same region before ("pre"). Dots represent values for individual cells across three independent trials. Black bars represent mean \pm SD. The mean \pm SD for GFP (control) is also shown as a black line and gray zone, down the plot. Red indicates $P < 0.05$; Dunnett's post hoc test, GFP as control. (B and D) Effect size and bootstrap 95% confidence interval of the data in A and C, respectively.

2D cell migration, and changes in their expression level can cause changes in migration speed; moreover, INVs are implicated in this behavior, since TPD54 mutants that cannot bind INVs are unable to modulate migration speed.

There are important differences between cells migrating on a flat substrate and those invading a 3D structure, and the latter is a more accurate model for cell movement in a cancer context. We therefore wanted to determine if TPD52-like proteins were

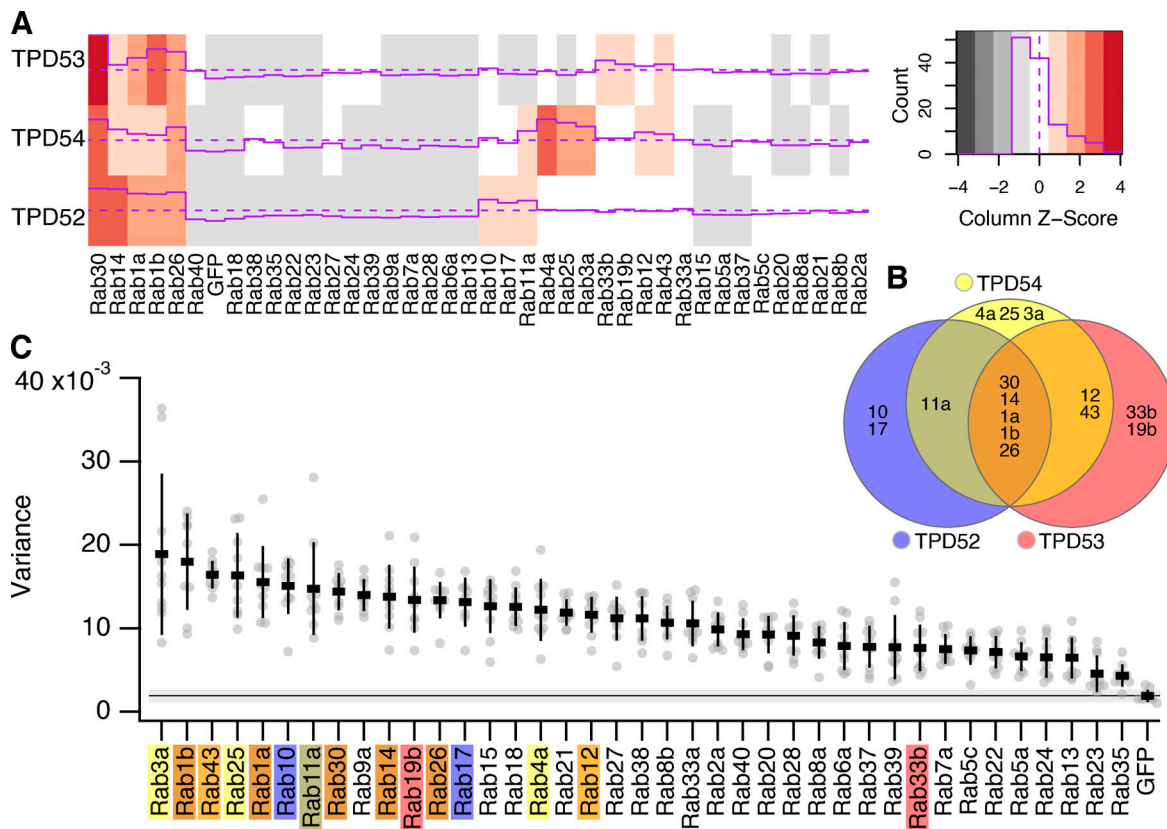


Figure 7. **Spatiotemporal variance of GFP-Rab proteins.** (A) Heatmap showing the Rab screen data for TPD52, TPD53 (from Fig. 6, A and C), and TPD54 (Larocque et al., 2020). Z-score of the values is color-coded and depicted as a purple line. Distribution of Z-values is shown in the color key. (B) Euler plot to show the Rabs identified in the screens and how they are linked to TPD52-like proteins. (C) Scatter dot plot of variance of fluorescence for the indicated GFP-Rab proteins expressed in HeLa cells. Rabs identified as present on INVs by hierarchical clustering of vesicle capture screens are indicated by the colors indicated in B. Dots represent individual cells, and bars indicates the mean \pm SD. The mean \pm SD for GFP (control) is also shown as a black line and gray zone, across the plot.

also important for cellular invasion. A2780 ovarian carcinoma cells that stably express Rab25 are an accurate model of an aggressive tumor (Cheng et al., 2004), and Rab25 increases invasion in a 3D microenvironment. First, we measured migration of these cells in cell-derived matrix (CDM), which is an elastic 3D matrix composed of fibrillar collagen and fibronectin. Depletion of TPD52 or TPD54, but not TPD53, caused a reduction in migration speed in CDM compared with control (Fig. 8 H and Video 5). Second, we tested the ability of these cells to invade a fibronectin-enriched collagen matrix for 48 h (Fig. 8 I). We quantified the invasion by measuring the total area that cells occupy deeper than 45 μ m into the matrix. Again, cells depleted of TPD52 or TPD54, but not TPD53, lost their ability to invade a dense 3D matrix (Fig. 8 J). Taken together, the data show that TPD52-like proteins are important for cell migration both in noncancerous RPE1 cells migrating on a 2D substrate and in cancer cells invading a 3D structure.

TPD54-depleted cells make larger contacts with their substrate

In addition to changes in cell motility, we observed that TPD54-depleted cells seemed morphologically different from control cells (Fig. 9 A). To quantify this difference, we analyzed a series

of cell shape parameters using a semiautomated workflow (see Materials and methods; Fig. S5). TPD54-depleted cells had much larger footprints, with an average area that was almost twice that of control cells (Fig. 9 B). Close inspection of movies of cells migrating on fibronectin revealed that the larger area and reduced speed of migration were linked. TPD54-depleted cells behaved as if they were “stuck” to the substrate; instead of having one clear lamellipodium, they made several smaller ones (Video 4). We hypothesized that these results may be due to a defect in integrin trafficking.

INVs are involved in recycling α 5 β 1 integrin

To examine the possibility that integrins are trafficked in INVs, we sought to identify them using two proteomic approaches. First, we used mass spectrometry analysis of material immunoprecipitated from RPE-1 cells expressing GFP or GFP-TPD54 lysed under nonstringent conditions. TPD52 and TPD53 were detected alongside TPD54, as well as 19 Rab GTPases that were all, with the exception Rab7A, enriched in the TPD54 sample (Fig. 10 A). Several integrins were detected by this method, including α 5 β 1, which was enriched compared with GFP. Second, identified proteins that were in close proximity to TPD54 on INVs. To do this, we compared proximity biotinylation

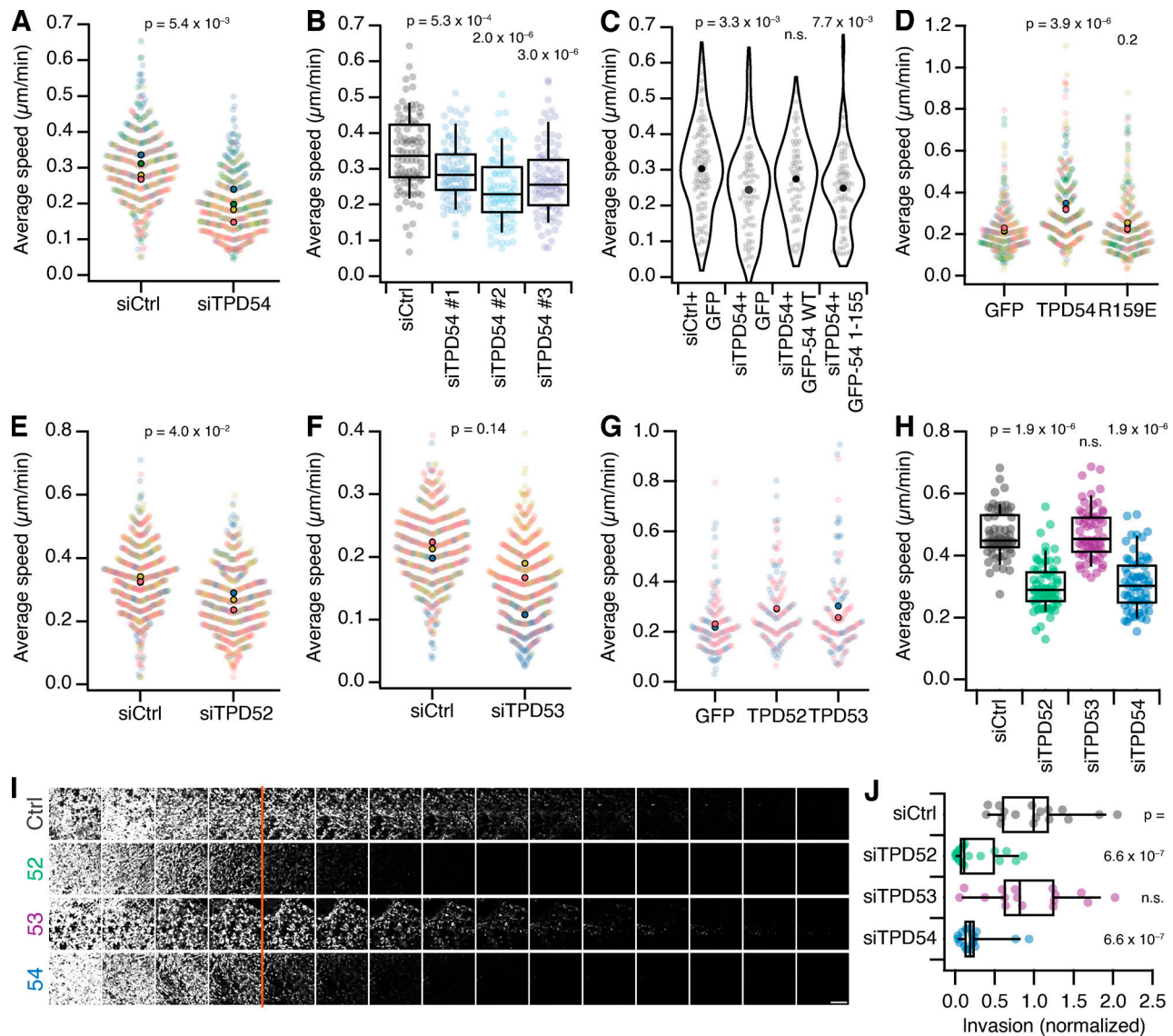


Figure 8. Role for TPD52-like proteins in cell migration and invasion. (A–G) RPE1 cell migration on a flat fibronectin substrate. **(A, E, and F)** Superplots showing migration speed of control vs TPD54- (A), TPD52- (E), or TPD53-depleted (G) cells. Dots represent individual cells, color-coded for experiments. Markers indicate mean speed for individual experiments. P value, Student's *t* test; $n_{\text{exp}} = 4$ (TPD54), 3 (TPD52 and TPD53); whereas $n_{\text{cell}} = 469$ (TPD54), 564,573 (TPD52), and 588,597 (TPD53). **(B)** Boxplot to show the migration speed of cells that were treated with siCtrl or each one of three TPD54-targeting siRNAs. Boxes show IQR, bar represents the median, and whiskers show 9th and 91st percentiles. P values from Dunnett's *post-hoc* test using siCtrl as control; $n_{\text{cell}} = 88\text{--}99$, $n_{\text{exp}} = 1$. **(C)** Violin plot showing the average speed of siCtrl- or siTPD54-treated cells expressing GFP, GFP-TPD54 WT, or GFP-TPD54 1–155 as indicated. Dots, individual cells; markers, mean speed. P values from Dunnett's *post hoc* test using siCtrl + GFP as control. $n_{\text{cell}} = 65\text{--}103$, $n_{\text{exp}} = 1$. **(D and G)** Superplots showing migration speed of cells expressing GFP, GFP + TPD54, or GFP + R159E (D) or GFP, GFP + TPD52, or GFP + TPD53 (E). P values in D from Dunnett's *post hoc* test using GFP as control. D, $n_{\text{cell}} = 247\text{--}259$, $n_{\text{exp}} = 3$. G, $n_{\text{cell}} = 129\text{--}131$, $n_{\text{exp}} = 2$. **(H–J)** Invasion of A2780 cells stably expressing Rab25 in a 3D context. **(H)** Boxplot of migration speed of cells in CDM that were treated with siRNAs as indicated. P values, Dunnett's *post hoc* test using siCtrl as control. $n_{\text{exp}} = 3$. **(I)** Representative confocal images of A2780 cells stably expressing Rab25 treated with the indicated siRNAs migrating through fibronectin-supplemented collagen type-I matrix for 72 h. Scale bar, 250 μm. **(J)** Quantification of A2780 cell invasion in confocal sections ≥ 45 μm, normalized to siCtrl. Dots, individual wells. Box plots show IQR, bar represents the median, and whiskers show 9th and 91st percentiles. P value, Kruskal–Wallis test. $n_{\text{exp}} = 3$.

profiles using either TPD54-HA-BioID2 WT or R159E mutant that does not localize to INVs. In this analysis, ITGA5 was only found in proximity with TPD54 and not the R159E mutant, while ITGB1 was enriched with TPD54 WT (Fig. 10 B). The presence of $\alpha 5 \beta 1$ integrins in INVs is consistent with the migration phenotypes observed on fibronectin or fibronectin-containing matrices.

Given the previously described role of INVs in recycling receptors, we therefore asked if recycling of $\alpha 5 \beta 1$ integrins is

affected by TPD54 depletion (Larocque et al., 2020). Using an ELISA-based recycling assay, we found that TPD54-depleted cells show a marked reduction in recycling of endocytosed $\alpha 5$ integrin heterodimers compared with control cells (Fig. 10 C). The initial surface label and uptake was similar in control and TPD54-depleted cells (98% and 84% of control, respectively). Aberrant traffic of internalized $\alpha 5$ integrin uptake in TPD54-depleted RPE-1 cells could be seen by labeling surface integrins

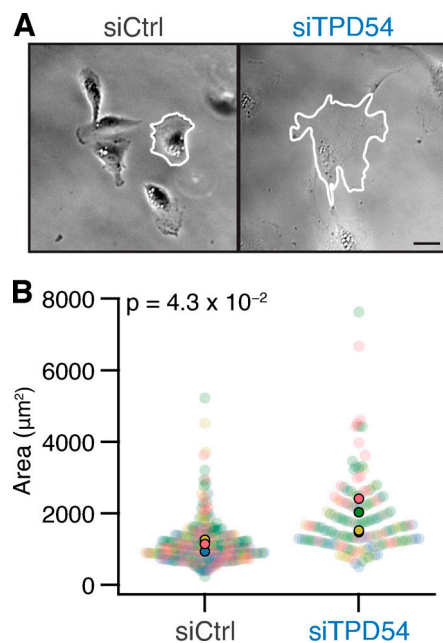


Figure 9. TPD54-depleted cells make larger contacts with their substrate. (A) Example micrographs of control and TPD54-depleted RPE1 cells migrating on fibronectin. The perimeter of the cell is outlined (white). Scale bar, 10 μm . (B) Superplot showing the area of control versus TPD54-depleted RPE1 cells migrating on fibronectin. Dots represent individual cells, colors represent different experiments, and the population mean is outlined in black. P value from Student's test. $n_{\text{cell}} = 288,151$; $n_{\text{exp}} = 4$. More statistics of cell shape are shown in Fig. S5.

and monitoring uptake and subsequent recycling (Fig. 10 D). TPD54-depleted cells showed accumulation of labeled integrins in intracellular compartments after 90 min consistent with a defect in recycling. Again, the initial surface (-30 min) and uptake (0 min) pools were similar (Fig. 10 D). These data confirm that TPD54 and the INVs are involved in trafficking of $\alpha 5\beta 1$ integrin and provide a mechanistic explanation for the cell migration and invasion phenotypes observed in cells depleted of TPD52-like proteins.

Discussion

In this study, we demonstrate the involvement of INVs in $\alpha 5\beta 1$ integrin trafficking and cell migration. We describe how the TPD52-like protein TPD54 is localized to INVs and show that other members of this family, TPD52 and TPD53, are also INV proteins. This allowed us to document the Rab GTPase complement of INVs, which included Rabs that are involved in integrin traffic and cell migration. Depletion of TPD52-like protein family members caused decreased cell migration and invasion, a phenotype that could be linked to decreased integrin recycling.

The binding of TPD52-like proteins to INVs can be explained by two molecular properties. First, residues 83–125 of TPD54 are required for direct membrane binding. Second, positively charged residues in a C-terminal region that is conserved across metazoans govern the association with INVs. Both of these properties are necessary for TPD54 to bind INVs, but they are interdependent, such that neither property by itself is sufficient

for binding. Precisely what factor TPD52-like proteins recognize on INVs is an interesting question. Our in vitro liposome-binding data allowed us to reconstitute the general interaction between TPD54 and membranes but failed to recapitulate INV binding, since mutations that prevent association with INVs in cells had no effect in vitro. It is possible that the lipid composition of Folch extract did not match that of INVs. The small size of these vesicles may be due to an unusual lipid content that assists their formation (Kozlov et al., 2014). We favor this explanation rather than a protein factor that would itself require an explanation of how it associates with INVs. Future work on the purification of INVs from cells will allow their lipid and protein composition to be determined.

We exploited the direct binding of TPD52-like proteins to INVs in a mitochondrial vesicle capture assay in order to detail the collective Rab GTPase complement of INVs. This analysis showed that the TPD52-like proteins associate with similar INVs as delineated by their Rab GTPases. The Rabs associated with INVs cover anterograde, Golgi, and recycling trafficking, with the addition of Rab21, an endocytic Rab, which was captured using TPD52 only (Simpson et al., 2004). This Rab is notable here, since it is involved in the internalization of integrins (Pellinen et al., 2006). Rab30, a Golgi-resident Rab that is not fully characterized, was our top hit in vesicle capture using TPD52, TPD53 or TPD54; by this definition it could be considered as the most likely INV Rab. Rab30 was not among the Rabs identified in our proteomic analyses of INVs in RPE-1 cells, but it could be that expression of Rab30 is below detection in this cell line. Among the Rab30 effectors identified in a screen in *Drosophila melanogaster* were the dynein adaptor Bicaudal D and the tethering factors Golgi-associated retrograde protein (GARP) and exocyst (Gillingham et al., 2014), suggesting that Rab30 is involved in membrane fusion between the endosomes and the Golgi and between the Golgi and the plasma membrane. Rab30 has been shown to bind to PI4KB in an autophagy context (Oda et al., 2016; Nakajima et al., 2019). Whether Rab30 and PI4KB are needed for the formation or transport of INVs or whether GARP and exocyst are tethering factors present on INVs remains to be determined. Although limited to the 39 Rabs tested, we found no evidence for Rab-positive INVs that had no TPD52-like protein. This suggests that TPD52-like proteins are core components of INVs and possibly should be considered the molecules that define this class of transport vesicle.

We found that depletion of TPD54, TPD52, and, to a lesser extent, TPD53 decreased cell migration and invasion. Conversely, their overexpression increased 2D migration speed. These findings echo the literature showing that TPD52-like proteins are overexpressed in various cancers and that overexpression is potentially correlated with a more invasive, migratory phenotype (Roslan et al., 2014; Shehata et al., 2008). INVs are implicated in cell migration not only because depletion of a core INV protein impaired migration speed but also because normal motility could only be rescued by WT TPD54 and not by a truncated form that cannot bind to INVs. Similarly, overexpression of WT TPD54, which can bind INVs, caused an up-regulation of migration speed, but a R159E mutant that does not bind INVs caused no up-regulation. Of the Rabs that we found

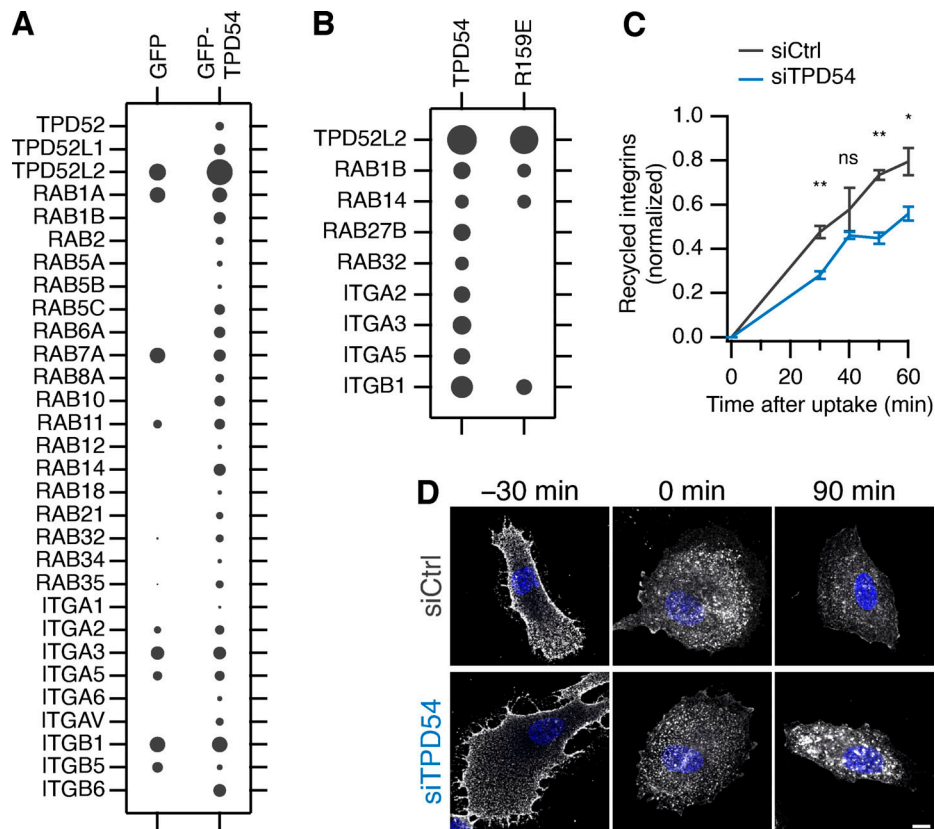


Figure 10. **INVs are involved in recycling $\alpha 5 \beta 1$ integrin.** (A) Bubble plot of total intensities from immunoprecipitates prepared from RPE-1 cells expressing GFP or GFP-TPD54 ($n_{\text{exp}} = 3$). (B) Bubble plot of total spectral counts from BioID2 experiments ($n_{\text{replicates}} = 6$, $n_{\text{exp}} = 2$). In A and B, all TPD52-like proteins, Rabs and integrins detected in the dataset are shown. Size of bubbles is normalized to the most abundant protein detected per experiment. (C) ELISA-based quantification of integrin $\alpha 5$ recycling over time in siCtrl (gray line) or siTPD54-treated (blue line) RPE1 cells. **, $P < 0.001$; *, $P < 0.05$. Bars show SD. $n_{\text{exp}} = 3$. (D) Representative confocal micrographs of integrin $\alpha 5$ recycling. RPE-1 cells (siCtrl or siTPD54 treated) were surface labeled using anti-integrin $\alpha 5$ (VC5) and allowed to recycle for the indicated times. The experiment was repeated three times, and similar results were also obtained using an alternative $\alpha 5$ antibody (SNAKA51). Scale bar, 10 μm .

associated with INVs, Rab4, Rab11, and Rab25 are all involved in integrin trafficking and cell migration (Caswell et al., 2007; Powelka et al., 2004; Roberts et al., 2001). After internalization, the integrin heterodimers are recycled back to the plasma membrane via a short, Rab4-dependent pathway or a long, Rab11-dependent pathway (Roberts et al., 2001); and in cancer cells, Rab25 sorts ligand-free integrins for recycling at the leading edge and ligand-bound integrins to lysosomes, where they reach the plasma membrane and cell rear in a CLIC3-dependent manner (Dozynkiewicz et al., 2012). Previously, we found that recycling of internalized transferrin was affected by depletion of TPD54, implicating INVs in receptor recycling (Larocque et al., 2020). Here, we showed that recycling of $\alpha 5$ integrin is impaired when TPD54 was depleted, suggesting that INVs also mediate recycling of internalized integrins. This raises an interesting question: if the size of INVs is invariant (~30 nm diameter), then how many integrin heterodimers can be trafficked in an INV? When the integrins are recycled to the plasma membrane, they are in their bent, inactive conformation. For integrin $\alpha \text{IIb} \beta 3$, this conformation extends 11 nm (Ye et al., 2008), which indicates that traffic in INVs is possible. Despite their small size, the maximum theoretical capacity of an INV is

surprisingly high (Martins Ratamero and Royle, 2019 Preprint), although for bulky cargoes such as integrins, the number traveling in each INV is likely to be low.

Materials and methods

Molecular biology

Several plasmids were available from previous work, including mCherry-FKBP-TPD54, GFP-FKBP-TPD54, mCherry-MitoTrap, and dark MitoTrap (pMito-dCherry-FRB; Larocque et al., 2020). TPD52-like protein constructs used in the paper represent the canonical UniProt sequence (TPD52, P55327-1; TPD53, Q16890-1; and TPD54, O43399-1). To make mCherry-FKBP-TPD52, human TPD52 (synthesized by GeneArt) was inserted in place of TPD54 in mCherry-FKBP-TPD54 using BglII and MfeI. FLAG-TPD52 was made by amplifying human TPD52 from the synthesized gene and inserting into pFLAG-C1 via BglII and MfeI. To make mCherry-FKBP-TPD53, TPD53 (GeneArt synthesis) was inserted into pmCherry-FKBP-C1 via HindIII and BamHI. FLAG-TPD53 was made by amplifying TPD53 from the synthesized gene and inserting into pFLAG-C1 via BglII and BamHI. The plasmid to coexpress untagged TPD54 and GFP (pIRES-EGFP-TPD54) was

made by amplifying TPD54 by PCR from human tumor protein D54 (IMAGE clone 3446037) and inserting into pIRES-EGFP-puro (Addgene; 45567) via NheI and XhoI. Similar pIRES-EGFP-TPD52 and pIRES-EGFP-TPD53 were made by amplification from respective mCherry-FKBP-tagged constructs and insertion at NheI and XhoI. The mCherry-FKBP-TPD54 deletions (1-37, 1-82, 38-82, 83-206, 1-155, 1-180, 126-180, 126-206, 155-180, and 155-206) were made by PCR from mCherry-FKBP-TPD54 and were each inserted into pmCherry-FKBP-C1 via BglII and MfeI. The mCherry-FKBP-TPD54 mutants (K15E, R95E, K154E, R159E, K165E, K175E, and K177E) and GFP-FKBP-TPD54 mutant (L53P, L67P) were created by site-directed mutagenesis. GST-tagged TPD54 constructs were made by amplification from the mCherry-FKBP-tagged version and insertion in pGEX-6P-1. Plasmids to express GFP-tagged Rabs were a gift from Francis Barr (University of Oxford, Oxford, UK), except for GFP-Rab1a and GFP-Rab5c, which were described previously (Larocque et al., 2020). Plasmids to express HA-BioID2-TPD54 WT or R159E were made by inserting HA-BioID2 in place of GFP in the GFP-TPD54 at AgeI and BglII and then subsequently lengthening the linker between BioID2 and TPD54 using insertion at BspEI and BglII, which improved biotinylation (Kim et al., 2016).

Cell culture

HeLa cells (Health Protection Agency/European Collection of Authenticated Cell Cultures; 93021013) were maintained in DMEM supplemented with 10% FBS and 100 U ml⁻¹ penicillin/streptomycin. RPE1 cells (HD-PAR-541 clone 7724) were maintained in Ham's F12 Nutrient Mixture supplemented with 100 U ml⁻¹ penicillin/streptomycin, 10% FBS, 2.3 g/liter sodium bicarbonate, and 2 mM L-glutamine. A2780 human ovarian cancer cells (female) stably expressing Rab25 (Caswell et al., 2007) were maintained in RPMI-1640 medium (Sigma-Aldrich) supplemented with 10% FCS, 1% L-glutamine, and 1% antibiotic-antimycotic (Sigma-Aldrich). All cell lines were kept at 37°C and 5% CO₂. RNAi was done by transfecting 100 nM siRNA (TPD54#1: 5'-GUCCUACCGUUAACGCAAU-3', TPD54#2: 5'-CUCACGUUUGUAGAUGAAA-3', TPD54#3: 5'-CAUGUUAGCCCAUCA GAAU-3'; TPD52: 5'-CAAUAGUUUGUGGGUAAA-3'; TPD53: 5'-GUCUCCAGCAAUAGGAUGAUUUACUA-3') with Lipofectamine 2000 (Thermo Fisher Scientific) according to the manufacturer's protocol. For DNA plasmids, cells were transfected with a total of 600 ng DNA (per well of a 4-well LabTek dish) using 0.75 µl GeneJuice (Merck Millipore) following the manufacturer's protocol. The A2780 cells were transfected by electroporation using a nucleofector (Lonza; Amaxa) using solution T, program A-23, 20 nM siRNA as per the manufacturer's instructions. Invasion experiments were performed 24 h after nucleofection.

Protein expression and purification

GST or GST-TPD54 constructs were expressed in *Escherichia coli* BL21 cells grown in double yeast tryptone media. Starter cultures of 10 ml were grown overnight at 37°C and shaken at 200 rpm. They were then diluted into 400-ml cultures and grown at 37°C, 200 rpm until an optical density at 600 nm between 0.6 and 0.8. To induce expression of the proteins, IPTG was added to

a final concentration of 0.5 mM and cells were grown for a further 5 h at 37°C, 200 rpm. The cells were harvested by centrifugation at 9,200 g for 10 min at 4°C, washed with cold PBS and pelleted again at 3,200 g for 15 min at 4°C. Pellets were stored at -80°C until purification.

For purification, pellets were resuspended in 50 ml lysis buffer (50 mM Tris, 150 mM NaCl, protease inhibitor cocktail tablet [Roche], and 0.2 mM PMSF, pH 8) and lysed by sonication. Cell debris was pelleted by centrifugation at 34,600 g for 30 min at 4°C. The supernatant was loaded onto a GSTrap column (GE Healthcare), which was then washed with 10 column volumes of wash buffer (50 mM Tris, 150 mM NaCl, protease inhibitor cocktail tablet, and 0.1 mM PMSF, pH 8) and then 10 column volumes of high-salt wash buffer (50 mM Tris, 500 mM NaCl, protease inhibitor cocktail tablet, and 0.1 mM PMSF, pH 8). The GST-tagged proteins were eluted by the addition of elution buffer (50 mM Tris, 150 mM NaCl, and 50 mM glutathione, pH 8). Purified proteins were dialyzed into binding buffer (150 mM NaCl and 20 mM Hepes, pH 7) for use in liposome-binding assays.

Protein-liposome interactions

Folch extract from bovine brain (Sigma-Aldrich) was dissolved in chloroform. The lipid mixture was dried with nitrogen flow followed by 2-h desiccation in a vacuum. The dried lipids were resuspended in binding buffer (150 mM NaCl and 20 mM Hepes, pH 7) to a final concentration of 4 mM. To generate liposomes with desired diameters, the lipid mixture was heated to 60°C and extruded 15× through polycarbonate membrane filters (Avanti Polar Lipids) with pore sizes of 200, 100, 50, or 30 nm. For 30-nm and 50-nm sizes, liposomes were produced by first extruding through a 100-nm filter, followed by extrusion through filters of a smaller pore size. Note that material is lost with each extrusion. Liposomes were stored at 4°C until used in binding assays. For the liposome pelleting assay, liposomes were centrifuged at 100,000 g for 25 min at 4°C. Pellet and supernatant samples were prepared with NuPAGE LDS Sample Buffer + reducing agent (Invitrogen) and incubated at 70°C for 10 min. Lipids were resolved on 12% Bis-Tris gels run in MES buffer and stained with 0.1% Coomassie in 10% acetic acid for 5 min (method adapted from Boucrot et al., 2012). Gels were destained in water overnight to leach the loading dye.

For the protein-liposome-binding assay, purified GST-tagged proteins were precleared before use, and then protein (2 µM) and liposomes (600 µM) were mixed with binding buffer (150 mM NaCl and 20 mM Hepes, pH 7) to a total volume of 200 µl and incubated on ice for 20 min. Samples were then centrifuged at 100,000 g for 25 min at 4°C. Bound (pellet) and free (supernatant) samples were prepared for SDS-PAGE by adding Laemmli buffer and boiling for 5 min. Proteins were resolved by SDS-PAGE on 4% to 15% Mini-PROTEAN TGX gels and visualized by staining with InstantBlue (Expedeon).

To quantify protein-liposome binding, the mean pixel density of gel bands was measured in Fiji. The background for each lane was subtracted, and the precipitation (no vesicle control band) was subtracted from the bound sample bands. These values were normalized to the amount of GST-TPD54 WT bound

to 100 nm liposomes. Liposome pelleting was quantified in the same way, and the amount of lipid pelleted for each liposome size was calculated relative to 100-nm liposome pelleting for each of three experiments. These values were used to correct the protein-binding results.

Cellular biochemistry

For FLAG immunoprecipitation, HeLa cells were seeded in 10-cm dishes. FLAG-TPD54, FLAG-TPD53, or FLAG-TPD52 was transfected with GFP-FKBP, GFP-FKBP-TPD54, or GFP-FKBP-TPD54 L53P, L67P, 10 μ g total using GeneJuice (Merck Millipore) according to the manufacturer's protocol. After 48 h, the cells were lysed with 10 mM Tris, pH 7.5, 150 mM NaCl, 0.5 mM EDTA, 1% Triton X-100, and protease inhibitors. Lysate was passed through a 23-gauge syringe and spun in a benchtop centrifuge for 15 min at 4°C. The cleared lysate was then incubated for 2 h at 4°C with 10 μ l anti-FLAG M2 magnetic beads (Sigma-Aldrich; M8823) prewashed with TBS. The beads were then washed three times with cold TBS, resuspended in Laemmli buffer, and run on a precast 4 to 15% polyacrylamide gel (Bio-Rad).

For Western blotting, the following primary antibodies were used: rabbit anti-TPD54 (Dundee Cell Products), 1:1,000; goat anti-TPD53 (Thermo Fisher Scientific; PA5-18798), 0.5 μ g/ml; mouse anti-GFP clones 7.1 and 13.1 (Roche; 11814460001), 1:1,000; and mouse anti-FLAG M2 (Sigma-Aldrich; F1804), 1 μ g/ml. HRP-conjugated secondary antibodies were used with enhanced chemiluminescence detection reagent (GE Healthcare) for detection, and manual exposure of Hyperfilm (GE Healthcare) was performed.

For GFP immunoprecipitations, three 10-cm dishes of confluent RPE-1 cells transiently expressing either GFP or GFP-TPD54 were used for each condition. Cells were scraped in lysis buffer (10 mM Tris-HCl pH 7.5, 150 mM NaCl, 0.5 mM EDTA, 0.5% NP-40, protease inhibitors [Roche]) and passed through a 23-gauge syringe and then cleared spun in a benchtop centrifuge for 15 min at 4°C. Lysates were incubated for 1 h with GFP-Trap beads (ChromoTek), washed once with exchange buffer (10 mM Tris-HCl pH 7.5, 150 mM NaCl, 0.5 mM EDTA) and three times with wash buffer (10 mM Tris-HCl, pH 7.5, 500 mM NaCl, 0.5 mM EDTA). The immunoprecipitations were run on a 4–15% polyacrylamide gel until they were 1 cm into the gel. Before excision and analysis at the University of Dundee Proteomics Facility.

For each BioID experiment, three 15-cm dishes of RPE1 cells per construct were each transfected with 9.5 μ g DNA diluted in 1.28 ml Opti-MEM with 72 μ l GeneJuice. Next day, media was replaced and supplemented with 50 μ M biotin (Sigma-Aldrich). After 16 h, biotin-fed RPE1 cells were recovered and incubated in RIPA buffer (25 mM Tris-HCl, pH 7.6, 150 mM NaCl, 1% NP-40, 0.5% sodium deoxycholate, and 0.1% SDS) for 30 min on ice, followed by 10 passages through a 23-G needle. Cleared lysates were incubated with magnetic streptavidin beads at 4°C for 2 h. Beads were washed with RIPA buffer and then PBS before storage at -20°C. On-bead trypsin digestion was performed before desalting using a C18 stage tip and analysis by nano-liquid chromatography electrospray ionization tandem mass

spectrometry in an Ultimate 3000/Orbitrap Fusion mass spectrometer (Proteomics Research Technology Platform, University of Warwick).

Integrin recycling assay

The ELISA plate (Thermo Fisher Scientific; Maxisorp 96 wells) was prepared the day before the experiment by incubating the wells with 50 μ l/well of 5 μ g/ml anti-integrin α 5 antibodies (BD Biosciences; 555651) in 0.05 M Na₂CO₃, pH 9.6, overnight at 4°C. 10-cm dishes were seeded with RPE1 cells in triplicate. Cells were serum starved for 30 min at 37°C. Following two 5 ml washes with cold PBS, the surface receptors were labeled with 0.133 mg/ml EZ-Link Sulfo-NHS-SS-Biotin (Thermo Fisher Scientific; 21331) in PBS at 4°C for 30 min. Cells were washed twice with 5 ml cold PBS on ice, and 5 ml warm serum-free medium was added. Plates were incubated at 37°C for 30 min to allow receptor internalization and then washed again with 5 ml of cold PBS on ice.

The cells were washed with cold reduction buffer (50 mM Tris, pH 7.5, and 102.5 mM NaCl, pH 8.6). Cell surface was reduced by adding 3 ml reduction buffer and 1 ml Mesna buffer (390 mg Mesna was added to 26 ml reduction buffer and mixed thoroughly, and 39 μ l of 10 M NaOH was added). Plates were agitated at 4°C for 20 min and then washed twice with cold PBS. The plates were then incubated in warm medium at 37°C to allow receptor recycling. The cell surface was then reduced again for 20 min as described above. Reduction buffer containing iodoacetamide (442 mg in 26 ml PBS) was added to the reduction buffer (1:4) to quench the reaction, for 10 min. The ELISA plate was blocked with 5% BSA in PBS-Tween at room temperature for 1 h. The cells were washed twice with cold PBS on ice. Lysates were obtained by scraping the cells with a total of 100 μ l/condition of lysis buffer (200 mM NaCl, 75 mM Tris, pH 7.5, 15 mM NaF, 1.5 mM Na₃VO₄, 7.5 mM EDTA, 7.5 mM EGTA, 1.5% Triton-X100, 0.75% Igepal, and protease inhibitors). The ELISA plate was washed twice with PBS-Tween, and 50 μ l lysate was put in each well, covered with parafilm, and incubated overnight at 4°C. Following five washes with PBS-Tween, 50 μ l of 1 μ g/ml streptavidin-HRP and 1% BSA in PBS-Tween was added to each well and incubated for 1 h at 4°C. Five more washes were performed with PBS-Tween and 50 μ l of detection reagent (0.56 mg/ml ortho-phenylenediamine dihydrochloride in ELISA buffer [25.4 mM NaHPO₄ and 12.3 mM citric acid, pH 5.4] with 0.003% H₂O₂) was added to each well. The plate was incubated at room temperature in the dark for 15 min before reading on a plate reader using 450-nm light.

Microscopy

For confocal imaging, cells were grown in four-well, glass-bottom, 3.5-cm dishes (Greiner Bio-One), and medium was exchanged for Leibovitz L-15 CO₂-independent medium for imaging at 37°C on a spinning disc confocal system (PerkinElmer; Ultraview Vox) with a 100 \times 1.4 NA oil-immersion objective. Images were captured using an ORCA-R2 digital charge-coupled device camera (Hamamatsu) following excitation with 488-nm and 561-nm lasers. For some experiments a Nikon CSU-W1 spinning disc confocal system with SoRa upgrade (Yokogawa)

was used with a Nikon 100×, 1.49, oil, CFI SR HP Apo total internal reflection fluorescence objective (Nikon) and 95B Prime camera (Photometrics). Rerouting of mCherry-FKBP-TPD52 or mCherry-FKBP-TPD53 to the mitochondria (dark MitoTrap) was induced by addition of 200 nM rapamycin (Alfa Aesar). For the Rab GTPase corerouting experiments, an image before rapamycin and an image 2 min after rapamycin were taken of live cells. For spatiotemporal variance analysis, cells were imaged for 30 frames with a 300-ms exposure.

For widefield imaging of 2D migration, 4-well LabTek dishes were incubated 30 min at 37°C with 10 µg/ml fibronectin or O/N at 37°C with 20 µg/ml laminin (Sigma-Aldrich; L2020-1MG). RPE1 cells were then plated at low density in the dishes and imaged the next day in L15 medium supplemented with 10% FBS and 100 U ml⁻¹ penicillin/streptomycin. Cells were imaged at 37°C on a Nikon Ti epifluorescence microscope with a 20× 0.50 NA air objective, a heated chamber (OKOlabs) and CoolSnap MYO camera (Photometrics) using NIS Elements AR software. Movies were recorded over 12 h (one frame/10 min or one frame/20 min) with phase contrast. Cells in CDM were imaged for 16 h using an Eclipse Ti inverted microscope (Nikon) with a 20×/0.45 SPlan Fluor objective and the Nikon filter sets for bright field and a pE-300 LED (CoolLED) fluorescent light source with imaging software NIS Elements AR.5.20.02. Images were acquired using a Retiga R6 (Q-Imaging) camera.

For the invasion assay, 5 mg/ml collagen-I supplemented with 25 µg/ml fibronectin was polymerized in inserts (Corning; Transwell) at 37°C for 1 h. The inserts were inverted, and A2780 cells stably expressing Rab25 were seeded on the opposite side of the filter. The inserts were then put in 0.1% serum medium supplemented with 10% FCS, and 100 ng hepatocyte growth factor and 30 ng/ml EGF were added on top of the matrix. After 72 h, cells were stained with Calcein-AM and visualized with an inverted Leica SP8 confocal microscope using a 20× objective. Cells were considered invasive above 45 µm, and slices were taken every 15 µm.

Imaging recycling of immunolabeled integrins was done by incubating RPE-1 cells (control or TPD54 depleted) in serum-free medium for 30 min. Cell surface integrins were labeled on ice for 30 min using either clone VC5 anti-human CD49e (BD PharMingen; 1:500, 555651) or clone SNAKA51 (Sigma-Aldrich; 1:500, MABT201). Following three washes with cold serum-free medium, coverslips were transferred to warm serum-free medium and incubated for 0, 30, or 120 min at 37°C. Finally, cells were fixed in 3% PFA and 4% sucrose in PBS for 15 min at RT, permeabilized with 0.1% Triton X-100 in PBS, and blocked and stained with goat anti-mouse Alexa Fluor 568-conjugated secondary antibodies (1:500 in blocking solution). Coverslips were mounted and imaged by confocal microscopy.

CLEM

Analysis of vesicle capture and mitochondrial aggregation was by CLEM following the methods outlined previously (Larocque et al., 2020). Briefly, transfected cells were plated onto gridded dishes (MatTek; P35G-1.5-14-CGRD). Cells were imaged at 37°C in Leibovitz L-15 CO₂-independent medium supplemented with 10% FBS. Rapamycin (200 nM, final concentration) was added

for 3 min before the cells were fixed in 3% glutaraldehyde and 0.5% paraformaldehyde in 0.05 M phosphate buffer, pH 7.4, for 1 h. Aldehydes were quenched in 50 mM glycine solution and then postfixed in 1% osmium tetroxide and 1.5% potassium ferrocyanide for 1 h and then in 1% tannic acid for 45 min to enhance membrane contrast. Cells were rinsed in 1% sodium sulfate and then twice in H₂O before being dehydrated in grade series ethanol and embedded in EPON resin (TAAB). Correlation of light images allowed the cell of interest to be identified for sectioning, and 70-nm ultrathin sections were cut and collected on formvar-coated hexagonal 100-mesh grids (EM resolutions). Sections were poststained with Reynolds lead citrate for 5 min. Electron micrographs were recorded using a JEOL 1400 transmission EM operating at 100 kV using iTEM software.

Data analysis

Analysis of spatiotemporal variance of fluorescence signals in live-cell movies was done using five 20 × 20-pixel excerpts of 30 frames from GFP-Rab live-cell imaging captured at 0.1775 s per frame. The excerpts were positioned in the cytoplasm away from bright structures. Each frame was first normalized to the mean pixel intensity for that frame and then the variance per pixel over time was calculated, resulting in a 20 × 20 matrix of variances. The mean of the five matrices is presented as the “spatiotemporal variance” for that cell. The analysis of the mCherry-FKBP-TPD54 constructs was measured in the same way, except that one region of interest of 50 × 50 pixels was taken per cell.

Mitochondrial aggregation was measured using a workflow that segmented postrapamycin images and extracted the area and perimeter of objects above threshold. These data were then fed into Igor Pro, where, for objects greater than 0.2 µm², the compactness of mitochondria was approximated using a circularity formula:

$$f_{\text{circ}} = \frac{4\pi A}{P^2},$$

where *A* is area and *P* is perimeter. The median circularity per cell was used to compare conditions.

For the Rab screen, corerouting of Rab GTPases was quantified by averaging for each cell, the pixel intensity in the green channel in 10 regions of interest of 10 × 10 pixels on the mitochondria, before and after rapamycin. This mitochondrial intensity ratio ($F_{\text{post}}/F_{\text{pre}}$) for every Rab was compared with the ratio of GFP in TPD52- or TPD53-rerouted cells. Estimation statistics were used to generate the difference plot shown in Fig. 6. The mean difference is shown together with bias-corrected and accelerated 95% confidence intervals calculated in R using 1×10^5 bootstrap replications. The heatmap was generated in R (see Data and software availability) using mitochondrial intensity ratio data. Note that when constructing the heatmap, we reanalyzed data for Rab3a and Rab4a from the original TPD54 screen (Larocque et al., 2020), and this has slightly altered the Rab profile for TPD54.

For the 2D migration assay, cells were tracked using the Fiji plugin Manual Tracking by using the center of the nucleus as guide. The data were saved as CSV files and fed into

CellMigration 1.14 in IgorPro for analysis (Royle, 2021). Superplots were used to show experimental effects across experimental repeats (Lord et al., 2020).

Invasion was quantified using the area calculator plugin in Fiji, measuring the fluorescence intensity of cells invading 45 μm or more and expressing this as a percentage of the fluorescence intensity of all cells within the plug. The data were normalized to siCtrl to show relative invasion.

For the cell shape analysis, a scientist blind to the experimental conditions drew with a stylus the outline of each cell in a frame halfway through the migration movies. The coordinates of all cell contours were fed into CellShape 1.01 in IgorPro for analysis (Royle, 2020).

Figures were made with Fiji or Igor Pro 9 (WaveMetrics) and assembled using Adobe Illustrator. Null-hypothesis statistical tests were as described in the figure legends.

Online supplemental material

[Fig. S1](#) shows the amplification of TPD52-like proteins in cancer. [Fig. S2](#) shows the effect of TPD54 depletion on migration of RPE1 cells on laminin. [Fig. S3](#) shows the effect of TPD54 depletion on the migratory behavior of RPE1 cells on fibronectin. [Fig. S4](#) shows the effect of TPD52 or TPD53 depletion on migration of RPE1 cells. [Fig. S5](#) shows the effect of TPD54 depletion on the shape of migrating RPE1 cells on fibronectin. [Video 1](#) demonstrates spatiotemporal variance of a selection of TPD54 mutants. [Video 2](#) shows TPD52-like proteins on subresolution vesicles. [Video 3](#) compares the spatiotemporal variance of GFP-tagged Rab GTPases. [Video 4](#) shows the effect of TPD54 depletion on RPE1 cell morphology and migration. [Video 5](#) shows the effect of TPD54 depletion on migration of A2780 cells in CDM.

Data availability

The two software packages that are described in this paper, CellMigration (Royle, 2021) and CellShape (Royle, 2020), are freely available. All code that is specific to this paper is available at <https://github.com/quantixed/p054p031>.

Acknowledgments

The authors thank Laura Cooper, Erick Martins Ratamero, and Claire Mitchell of CAMDU (Computing and Advanced Microscopy Unit) for their support and assistance in this work. We would like to thank Francis Barr (University of Oxford, UK) for reagents and Darius Koester for advice and assistance with liposome production. We would also like to thank Miguel Hernández González and Joseph Cockburn for valuable discussion.

This work was supported by the UK Medical Research Council (MR/P018947/1). G. Larocque was supported by Fonds de Recherche du Québec (Nature et technologies) and University of Warwick Chancellor's Award. D.J. Moore was funded by the Medical Research Council Doctoral Training Partnership (MR/N014294/1).

The authors declare no competing financial interests.

Author contributions: G. Larocque performed experimental work, analyzed data, and wrote the paper. D.J. Moore did the

liposome-binding assays and BioID2 experiments and helped with the Rab screens. M. Sittewelle carried out additional migration and immunofluorescence experiments. C. Kuey extended the spatiotemporal variance and mitochondrial aggregation analyses. P.J. La-Borde performed the original liposome-binding assays. B.J. Wilson and P.T. Caswell performed the original invasion assays, which were extended by J.H.R. Hetmanski. N.I. Clarke did the vesicle capture CLEM experiments. S.J. Royle analyzed data, wrote computer code, and wrote the paper.

Submitted: 4 September 2020

Revised: 29 May 2021

Accepted: 30 June 2021

References

- Balleine, R.L., M.S. Fejzo, P. Sathasivam, P. Basset, C.L. Clarke, and J.A. Byrne. 2000. The hD52 (TPD52) gene is a candidate target gene for events resulting in increased 8q21 copy number in human breast carcinoma. *Genes Chromosomes Cancer*. 29:48–57. [https://doi.org/10.1002/1098-2264\(2000\)9999:9999<::AID-GCC1005>3.0.CO;2-O](https://doi.org/10.1002/1098-2264(2000)9999:9999<::AID-GCC1005>3.0.CO;2-O)
- Boucrot, E., A. Pick, G. Çamdere, N. Liska, E. Evergren, H.T. McMahon, and M.M. Kozlov. 2012. Membrane fission is promoted by insertion of amphipathic helices and is restricted by crescent BAR domains. *Cell*. 149:124–136. <https://doi.org/10.1016/j.cell.2012.01.047>
- Boutros, R., and J.A. Byrne. 2005. D53 (TPD52L1) is a cell cycle-regulated protein maximally expressed at the G2-M transition in breast cancer cells. *Exp. Cell Res.* 310:152–165. <https://doi.org/10.1016/j.yexcr.2005.07.009>
- Byrne, J.A., C. Tomasetto, J.M. Garnier, N. Rouyer, M.G. Mattei, J.P. Bellocq, M.C. Rio, and P. Basset. 1995. A screening method to identify genes commonly overexpressed in carcinomas and the identification of a novel complementary DNA sequence. *Cancer Res.* 55:2896–2903.
- Byrne, J.A., M.G. Mattei, and P. Basset. 1996. Definition of the tumor protein D52 (TPD52) gene family through cloning of D52 homologues in human (hD53) and mouse (mD52). *Genomics*. 35:523–532. <https://doi.org/10.1006/geno.1996.0393>
- Byrne, J.A., C.R. Nourse, P. Basset, and P. Gunning. 1998. Identification of homo- and heteromeric interactions between members of the breast carcinoma-associated D52 protein family using the yeast two-hybrid system. *Oncogene*. 16:873–881. <https://doi.org/10.1038/sj.onc.1201604>
- Cao, Q., J. Chen, L. Zhu, Y. Liu, Z. Zhou, J. Sha, S. Wang, and J. Li. 2006. A testis-specific and testis developmentally regulated tumor protein D52 (TPD52)-like protein TPD52L3/hD55 interacts with TPD52 family proteins. *Biochem. Biophys. Res. Commun.* 344:798–806. <https://doi.org/10.1016/j.bbrc.2006.03.208>
- Caswell, P.T., H.J. Spence, M. Parsons, D.P. White, K. Clark, K.W. Cheng, G.B. Mills, M.J. Humphries, A.J. Messent, K.I. Anderson, et al. 2007. Rab25 associates with $\alpha 5 \beta 1$ integrin to promote invasive migration in 3D microenvironments. *Dev. Cell*. 13:496–510. <https://doi.org/10.1016/j.devcel.2007.08.012>
- Caswell, P.T., M. Chan, A.J. Lindsay, M.W. McCaffrey, D. Boettiger, and J.C. Norman. 2008. Rab-coupling protein coordinates recycling of $\alpha 5$ - $\beta 1$ integrin and EGFR1 to promote cell migration in 3D microenvironments. *J. Cell Biol.* 183:143–155. <https://doi.org/10.1083/jcb.200804140>
- Chen, Y., A. Kamili, J.R. Hardy, G.E. Goblewski, K.K. Khanna, and J.A. Byrne. 2013. Tumor protein D52 represents a negative regulator of ATM protein levels. *Cell Cycle*. 12:3083–3097. <https://doi.org/10.4161/cc.26146>
- Cheng, K.W., J.P. Lahad, W.L. Kuo, A. Lapuk, K. Yamada, N. Auersperg, J. Liu, K. Smith-McCune, K.H. Lu, D. Fishman, et al. 2004. The RAB25 small GTPase determines aggressiveness of ovarian and breast cancers. *Nat. Med.* 10:1251–1256. <https://doi.org/10.1038/nm1125>
- Dozynkiewicz, M.A., N.B. Jamieson, I. Macpherson, J. Grindlay, P.V.E. van den Berghe, A. von Thun, J.P. Morton, C. Gourley, P. Timpson, C. Nixon, et al. 2012. Rab25 and CLIC3 collaborate to promote integrin recycling from late endosomes/lysosomes and drive cancer progression. *Dev. Cell*. 22:131–145. <https://doi.org/10.1016/j.devcel.2011.11.008>

- Friedl, P., and K. Wolf. 2003. Tumour-cell invasion and migration: diversity and escape mechanisms. *Nat. Rev. Cancer*. 3:362–374. <https://doi.org/10.1038/nrc1075>
- Gillingham, A.K., R. Sinka, I.L. Torres, K.S. Lilley, and S. Munro. 2014. Toward a comprehensive map of the effectors of rab GTPases. *Dev. Cell*. 31: 358–373. <https://doi.org/10.1016/j.devcel.2014.10.007>
- Gruber, M., J. Söding, and A.N. Lupas. 2006. Comparative analysis of coiled-coil prediction methods. *J. Struct. Biol.* 155:140–145. <https://doi.org/10.1016/j.jsb.2006.03.009>
- Hamidi, H., and J. Ivaska. 2018. Every step of the way: integrins in cancer progression and metastasis. *Nat. Rev. Cancer*. 18:533–548. <https://doi.org/10.1038/s41568-018-0038-z>
- Huttenlocher, A., and A.R. Horwitz. 2011. Integrins in cell migration. *Cold Spring Harb. Perspect. Biol.* 3:a005074. <https://doi.org/10.1101/cshperspect.a005074>
- Kim, D.I., S.C. Jensen, K.A. Noble, B. Kc, K.H. Roux, K. Motamedchaboki, and K.J. Roux. 2016. An improved smaller biotin ligase for BioID proximity labeling. *Mol. Biol. Cell*. 27:1188–1196. <https://doi.org/10.1091/mbc.E15-12-0844>
- Kozlov, M.M., F. Campelo, N. Liska, L.V. Chernomordik, S.J. Marrink, and H.T. McMahon. 2014. Mechanisms shaping cell membranes. *Curr. Opin. Cell Biol.* 29:53–60. <https://doi.org/10.1016/j.ccb.2014.03.006>
- Larocque, G., P.J. La-Borde, N.I. Clarke, N.J. Carter, and S.J. Royle. 2020. Tumor protein D54 defines a new class of intracellular transport vesicles. *J. Cell Biol.* 219:e201812044. <https://doi.org/10.1083/jcb.201812044>
- Lewis, J.D., L.A. Payton, J.G. Whitford, J.A. Byrne, D.I. Smith, L. Yang, and R.K. Bright. 2007. Induction of tumorigenesis and metastasis by the murine orthologue of tumor protein D52. *Mol. Cancer Res.* 5:133–144. <https://doi.org/10.1158/1541-7786.MCR-06-0245>
- Li, J., Y. Li, H. Liu, Y. Liu, and B. Cui. 2017. The four-transmembrane protein MAL2 and tumor protein D52 (TPD52) are highly expressed in colorectal cancer and correlated with poor prognosis. *PLoS One*. 12:e0178515. <https://doi.org/10.1371/journal.pone.0178515>
- Lord, S.J., K.B. Velle, R.D. Mullins, and L.K. Fritz-Laylin. 2020. SuperPlots: Communicating reproducibility and variability in cell biology. *J. Cell Biol.* 219:e202001064. <https://doi.org/10.1083/jcb.202001064>
- Martins Ratamero, E., and S.J. Royle. 2019. Calculating the maximum capacity of intracellular transport vesicles. *bioRxiv*. (Preprint posted February 20, 2019) <https://doi.org/10.1101/555813>
- Moreno-Layseca, P., J. Icha, H. Hamidi, and J. Ivaska. 2019. Integrin trafficking in cells and tissues. *Nat. Cell Biol.* 21:122–132. <https://doi.org/10.1038/s41556-018-0223-z>
- Mukudai, Y., S. Kondo, A. Fujita, Y. Yoshihama, T. Shirota, and S. Shintani. 2013. Tumor protein D54 is a negative regulator of extracellular matrix-dependent migration and attachment in oral squamous cell carcinoma-derived cell lines. *Cell Oncol. (Dordr.)*. 36:233–245. <https://doi.org/10.1007/s13402-013-0131-y>
- Nakajima, K., T. Nozawa, A. Minowa-Nozawa, H. Toh, S. Yamada, C. Aikawa, and I. Nakagawa. 2019. RAB30 regulates PI4KB (phosphatidylinositol 4-kinase beta)-dependent autophagy against group A Streptococcus. *Autophagy*. 15:466–477. <https://doi.org/10.1080/1548627.2018.1532260>
- Nourse, C.R., M.G. Mattei, P. Gunning, and J.A. Byrne. 1998. Cloning of a third member of the D52 gene family indicates alternative coding sequence usage in D52-like transcripts. *Biochim. Biophys. Acta*. 1443:155–168. [https://doi.org/10.1016/S0167-4781\(98\)00211-5](https://doi.org/10.1016/S0167-4781(98)00211-5)
- Oda, S., T. Nozawa, A. Nozawa-Minowa, M. Tanaka, C. Aikawa, H. Harada, and I. Nakagawa. 2016. Golgi-Resident GTPase Rab30 Promotes the Biogenesis of Pathogen-Containing Autophagosomes. *PLoS One*. 11: e0147061. <https://doi.org/10.1371/journal.pone.0147061>
- Pellinen, T., A. Arjonen, K. Vuoriluoto, K. Kallio, J.A.M. Fransén, and J. Ivaska. 2006. Small GTPase Rab21 regulates cell adhesion and controls endosomal traffic of β 1-integrins. *J. Cell Biol.* 173:767–780. <https://doi.org/10.1083/jcb.200509019>
- Powelka, A.M., J. Sun, J. Li, M. Gao, L.M. Shaw, A. Sonnenberg, and V.W. Hsu. 2004. Stimulation-dependent recycling of integrin β 1 regulated by ARF6 and Rab11. *Traffic*. 5:20–36. <https://doi.org/10.1111/j.1600-0854.2004.00150.x>
- Roberts, M., S. Barry, A. Woods, P. van der Sluijs, and J. Norman. 2001. PDGF-regulated rab4-dependent recycling of α v β 3 integrin from early endosomes is necessary for cell adhesion and spreading. *Curr. Biol.* 11: 1392–1402. [https://doi.org/10.1016/S0960-9822\(01\)00442-0](https://doi.org/10.1016/S0960-9822(01)00442-0)
- Roslan, N., I. Bièche, R.K. Bright, R. Lidereau, Y. Chen, and J.A. Byrne. 2014. TPD52 represents a survival factor in ERBB2-amplified breast cancer cells. *Mol. Carcinog.* 53:807–819. <https://doi.org/10.1002/mc.22038>
- Royle, S. 2020. quantixed/CellShape: CellShape v1.01. *Zenodo*. 3931238. <https://doi.org/10.5281/ZENODO>. <https://zenodo.org/record/3931238>
- Royle, S. 2021. quantixed/CellMigration: CellMigration v1.14. *Zenodo*. 4850277. <https://doi.org/10.5281/ZENODO>. <https://zenodo.org/record/4850277>
- Sathasivam, P., A.M. Bailey, M. Crossley, and J.A. Byrne. 2001. The role of the coiled-coil motif in interactions mediated by TPD52. *Biochem. Biophys. Res. Commun.* 288:56–61. <https://doi.org/10.1006/bbrc.2001.5721>
- Shehata, M., I. Bièche, R. Boutros, J. Weidenhofer, S. Fanayan, L. Spalding, N. Zeps, K. Byth, R.K. Bright, R. Lidereau, and J.A. Byrne. 2008. Nonredundant functions for tumor protein D52-like proteins support specific targeting of TPD52. *Clin. Cancer Res.* 14:5050–5060. <https://doi.org/10.1158/1078-0432.CCR-07-4994>
- Simpson, J.C., G. Griffiths, M. Wessling-Resnick, J.A. Fransén, H. Bennett, and A.T. Jones. 2004. A role for the small GTPase Rab21 in the early endocytic pathway. *J. Cell Sci.* 117:6297–6311. <https://doi.org/10.1242/jcs.01560>
- Thomas, D.D.H., C.L. Frey, S.W. Messenger, B.K. August, and G.E. Groblewski. 2010. A role for tumor protein TPD52 phosphorylation in endo-membrane trafficking during cytokinesis. *Biochem. Biophys. Res. Commun.* 402:583–587. <https://doi.org/10.1016/j.bbrc.2010.10.041>
- Ummanni, R., S. Teller, H. Junker, U. Zimmermann, S. Venz, C. Scharf, J. Giebel, and R. Walther. 2008. Altered expression of tumor protein D52 regulates apoptosis and migration of prostate cancer cells. *FEBS J.* 275: 5703–5713. <https://doi.org/10.1111/j.1742-4658.2008.06697.x>
- Wandinger-Ness, A., and M. Zerial. 2014. Rab proteins and the compartmentalization of the endosomal system. *Cold Spring Harb. Perspect. Biol.* 6:a022616. <https://doi.org/10.1101/cshperspect.a022616>
- Wilson, B.J., J.L. Allen, and P.T. Caswell. 2018. Vesicle trafficking pathways that direct cell migration in 3D matrices and in vivo. *Traffic*. 19:899–909. <https://doi.org/10.1111/tra.12605>
- Ye, F., J. Liu, H. Winkler, and K.A. Taylor. 2008. Integrin α IIb β 3 in a membrane environment remains the same height after Mn²⁺ activation when observed by cryoelectron tomography. *J. Mol. Biol.* 378: 976–986. <https://doi.org/10.1016/j.jmb.2008.03.014>